

# **Investigation of a Novel High Temperature Solid Oxide Electrolyzer for Solar Hydrogen Production**

by

**Abdullah A. AlZahrani**

A Thesis Submitted in Partial Fulfillment  
of the Requirement for the Degree of

Doctor of Philosophy

in

Faculty of Engineering and Applied Science Program  
University of Ontario Institute of Technology  
Oshawa, Ontario, Canada

© Abdullah A. AlZahrani

April 2017

## **Abstract**

This thesis proposes and investigates a new generation of photoelectrochemical cells for solar hydrogen production based on high temperature Solid Oxide Electrolysis Cells. Therefore, a set of experiments are designed to develop and select the most promising materials and configurations. Furthermore, the study includes a design of a novel testing station built to accommodate the various parameters to be tested in order to assess the performance of the proposed Photoelectrochemical Solid Oxide Cell (PSOC). As part of the design process, a material survey was conducted to screen potential semiconductors that are capable of operating at high temperatures. Subsequently, promising materials are selected and applied through specific chemical processes which can provide the required structure and surface properties. The material processing strategies to develop a light absorbing surface are made on commercial button cells; which has been tested and its performance is well-characterized under different operating conditions. Thus, improvements brought about by the developed photoactive layer can be detected under different types of light.

The research further includes the thermodynamic and electrochemical modeling of a Solid Oxide Electrolysis Cell (SOEC). In this regard, the energy and exergy aspects of a single cell performance, as well as the performance of Solid Oxide Electrolysis (SOE) stack, are investigated. The exergoeconomic aspects of utilizing SOE plant at a large-scale is also considered through a detailed exergoeconomic analysis. Last, the models are used to examine the SOE performance sensitivity to variation in operating parameters and conduct an exergetic optimization to highlight the trade-offs between economic and technical performance optimums. In addition, the integration of SOE in solar tower power plant for hydrogen production is examined considering continuous operating by using thermal energy storage and a high efficiency supercritical carbon dioxide (S-CO<sub>2</sub>) power cycle. The findings of this thesis are expected to make a new solar hydrogen production pathway that is efficient, environmentally friendly, and in near-future expected to be economically competitive.

**Keywords:** Solid Oxide Electrolysis, SOFC, SOEC, Photoelectrochemical Cell, Hydrogen production, Exergy, Energy, Exergoeconomic, PSOC, High temperature Electrolyzer.

## **Dedication**

*To the soul of my father Ali bin Rashed Al Tahisi*

## **Acknowledgments**

All praise due to Allah, for His mercy, blessings, and guidance during the course of this research and throughout my entire life.

First and foremost, I sincerely thank my supervisor, Professor Ibrahim Dincer, for his continuous and unlimited support, mentorship, and inspiration. Indeed, working in Professor Dincer's group is as enjoyable and fruitful as much as it is challenging.

I thank my external examiner, Dr. Emin Caglan Kumbur, and my university examiner, Dr. Franco Gaspari. Special thanks go to my supervisory committee, Professor Bale Reddy and Dr. Atef Mohany, for their time while reviewing my thesis, and for their comments and suggestions. Special thanks also to go to Professor Bekir Yilbas for his support and for providing me with insightful suggestions and recommendations. Dr. Calin Zamfirescu's technical support and recommendations regarding the experimentations is greatly acknowledged. Dr. Ghaus Rizvi also provided great help by opening the electrospinning lab facilities for my research.

I acknowledge with gratitude Umm Al-Qura University for sponsoring my education and supporting my research. The kind support from KACST, in particular, Dr. Yousef Al Yousef, the Director of KACST Energy Research Institute, in providing access to the SOFC lab and the material characterization facilities is greatly acknowledged.

During the time spent in UOIT, as part of Professor Dincer's research group in ACE3030 or the CERL Lab, I have met generations of great friends and exceptional minds, some of whom have already graduated while others are finishing in a few months. To all of those, I sincerely thank you for your friendship and kind support. We will always remember the great times we spent together.

Finally, I want to express my deep thanks and appreciation to my family, especially my mother and my grandmother, for their boundless enthusiasm and continuous encouragement to see the fruitful completion of my studies. I also thank my wife for her patience and support during my Ph.D. journey.

# Table of Contents

Abstract .....	ii
Dedication .....	iii
Acknowledgments .....	iv
Table of Contents .....	v
List of Figures .....	x
List of Tables .....	xv
Nomenclature .....	xvii
Chapter 1: Introduction .....	1
1.1. Motivation .....	2
1.2. Objectives .....	3
1.3. Thesis Outlines .....	4
Chapter 2: Background .....	6
2.1. Hydrogen as a Fuel of Future .....	6
2.1.1. The Global Energy Challenge .....	8
2.1.2. The Role of Renewable Energy .....	10
2.1.3. The Potential of Hydrogen Storage .....	14
2.2. The Current Demand for Hydrogen .....	19
2.3. Fossil-Based Hydrogen Production .....	20
2.3.1. Steam Methane Reforming .....	21
2.3.2. Partial Oxidation .....	22
2.3.3. Gasification .....	22
2.4. Water Electrolysis Hydrogen Production .....	23
2.4.1. Alkaline Electrolysis .....	26
2.4.2. Proton Exchange Membrane Electrolysis .....	31
2.4.3. Solid Oxide Electrolysis .....	36
2.5. Solar Hydrogen Production .....	40
2.5.1. Concentrated Solar Systems .....	40
2.5.2. Photovoltaic Systems .....	42
2.6. Thermochemical Cycles .....	42

2.6.1.	Sulfur-Iodine (S-I) Cycle .....	42
2.6.2.	Hybrid Sulfur Cycle .....	43
2.6.3.	Copper-Chlorine (Cu-Cl) Cycle.....	43
2.7.	Other Hydrogen Production Methods .....	44
2.7.1.	Photobiological Hydrogen Production.....	44
2.8.	Types of Fuel Cell.....	44
2.8.1.	Alkaline Fuel Cell (AFC).....	45
2.8.2.	Proton Exchange Membrane Fuel Cell (PEMFC) .....	45
2.8.3.	Phosphoric Acid Fuel Cell (PAFC) .....	45
2.8.4.	Molten Carbonate Fuel Cell (MCFC).....	46
2.8.5.	Solid Oxide Fuel Cell (SOFC).....	46
Chapter 3:	Literature Review.....	47
3.1.	Thermal Analysis of Solid Oxide Electrolysis.....	47
3.1.1.	Solar Hydrogen Production Applications .....	48
3.1.2.	Nuclear Hydrogen Production Applications .....	48
3.1.3.	Modeling of Solid Oxide Electrolysis.....	49
3.2.	Materials of Solid Oxide Cells .....	51
3.2.1.	Electrolyte Materials.....	53
3.2.2.	Fuel Electrode Materials .....	53
3.2.3.	Oxygen Electrode Materials .....	54
3.2.4.	Interconnect and Sealing Materials.....	55
3.3.	Testing of Solid Oxide Electrolysis .....	55
3.4.	Photoelectrochemical Hydrogen Production.....	58
3.5.	Research Gaps in Literature and Key Contributions.....	61
Chapter 4:	Experimental Apparatus and Methodology .....	63
4.1.	Experimental Apparatus.....	63
4.1.1.	High Temperature Furnace Design.....	63
4.1.2.	Humidifier Unit.....	67
4.1.3.	Cell Fixture .....	68
4.1.4.	Cell Type and Dimensions.....	70
4.1.5.	Cell Installation.....	71

4.2.	Instrumentation.....	72
4.2.1.	Thermocouple Probes .....	72
4.2.2.	Potentiostat.....	72
4.2.3.	Pressure gauges.....	73
4.2.4.	Mass Flow Controllers.....	74
4.2.5.	Data Acquisition System.....	75
4.3.	Measurement Procedure.....	75
4.3.1.	Full Testing Station.....	75
4.3.2.	Testing Procedure .....	79
4.4.	Development of Photo-Solid Oxide Cell .....	80
4.4.1.	Photoactive Material Selection .....	80
4.4.2.	Methods of Material Application.....	82
4.4.3.	Sol-Gel Coating .....	82
4.4.4.	Electrospinning .....	83
4.5.	Uncertainty Analysis .....	85
4.5.1.	Random Error Uncertainties .....	85
4.5.2.	Systematic Error Uncertainties .....	86
4.5.3.	Combination of Uncertainties and Error Propagation .....	87
Chapter 5:	Development of SOE Systems .....	88
5.1.	SOE for Hydrogen Production .....	88
5.1.1.	SOE for Hydrogen Production.....	88
5.1.2.	SOE for Compressed Hydrogen Production.....	91
5.2.	Solar Tower Powered SOE .....	92
5.2.1.	Solar Tower.....	93
5.2.2.	Thermal Energy Storage .....	93
5.2.3.	S-CO <sub>2</sub> Brayton Power Cycle.....	95
Chapter 6:	Analysis, Modeling and Optimization .....	97
6.1.	Analyses of Solar Concentrator .....	97
6.2.	Thermodynamic Analyses.....	99
6.2.1.	Energy and Exergy Efficiencies of SOEC .....	102
6.2.2.	Energy and Exergy Efficiencies of SOE.....	103

6.3.	Electrochemical Analysis.....	105
6.4.	Exergoeconomic Analysis.....	107
6.5.	SOE System Optimization .....	108
6.6.	Scale-up Analysis.....	111
Chapter 7: Results and Discussion.....		112
7.1.	Experimental Results.....	112
7.1.1.	Cell Performance .....	112
7.1.2.	Cell Characterization .....	128
7.1.3.	Coated Samples.....	130
7.2.	Modeling Results.....	131
7.2.1.	SOEC Thermal and Electric Energy Requirements.....	132
7.2.2.	SOEC Model Validation.....	133
7.3.	Single Electrolysis Cell Parametric Analysis Results .....	134
7.4.	Overall SOE System Performance Results .....	137
7.4.1.	Comparison with Conventional Electrolyzers .....	141
7.4.2.	Effects of Stack Temperature.....	142
7.4.3.	Effects of Stack Pressure .....	145
7.4.4.	Effects of Operating Current Density .....	148
7.4.5.	Sensitivity Analysis and Performance Optimization Results .....	150
7.4.6.	Exergoeconomic Analysis Results.....	152
7.5.	Solar Tower Powered SOE Results.....	157
7.5.1.	Solar Tower Results .....	157
7.5.2.	TES Results.....	159
7.5.3.	Performance of S-CO <sub>2</sub> Brayton Power Results .....	161
7.5.4.	Performance of SOE Results .....	163
7.5.5.	Overall Integrated System Performance Results .....	164
7.6.	SOE Plant Scale-up Results .....	164
Chapter 8: Conclusions and Recommendations .....		168
8.1.	Conclusions.....	168
8.2.	Recommendations.....	171
References.....		173

Appendix 1: Fixture Designs .....	184
Appendix 2: Uncertainty Calculation Example .....	187

## List of Figures

Figure 2.1 Annual global fossil fuel carbon emission (data from [5]).....	8
Figure 2.2 Global annual temperature anomalies from land and ocean observations, from 1880 to 2014 (data from [6]).....	9
Figure 2.3 World total energy supply in 2014 from various resources (data from [4])...	11
Figure 2.4 Distribution of the world total renewable energy supply in 2014, based on resource type (data from [4]). .....	12
Figure 2.5 The increase in the world total renewable energy capacity from 2007 to 2016 (data from [11]).....	13
Figure 2.6 Total investment in renewables worldwide (data from [12]). .....	14
Figure 2.7 Volumetric energy densities ( $\text{GJ m}^{-3}$ ) and specific energies ( $\text{GJ tonne}^{-1}$ ) for various fuels used in transportation (data from [1]).....	16
Figure 2.8 Energy density of compressed hydrogen.....	17
Figure 2.9 Comparison between electrochemical and mechanical hydrogen compression from ambient conditions of 298 K and 0.1 MPa to 70 MPa. ....	18
Figure 2.10 Distribution of hydrogen consumption shares in the different industries. ...	19
Figure 2.11 Schematic representation of the Haber-Bosch ammonia synthesis process.	20
Figure 2.12 Schematic representation of the main components of an electrolysis cell and the movement directions of the various species with respect to electrodes.....	24
Figure 2.13 Classification of water electrolyzers based on electrolyte type.....	25
Figure 2.14 Schematic representation of the working principle of the various water electrolysis types, illustrating the moving species and the produced gases with respect to either the cathode or anode side.....	26
Figure 2.15 Schematic representation of an alkaline water electrolyzer with KOH as an electrolyte.....	28
Figure 2.16 Unipolar or tank electrolyzer configuration. ....	29
Figure 2.17 Bipolar or filter-press electrolyzer stack configuration.....	29
Figure 2.18 Schematic representation of a Proton Exchange Membrane (PEM) electrolyzer.....	32
Figure 2.19 Chemical structure of NAFION <sup>®</sup> membrane. ....	33
Figure 2.20 Schematic representation of bipolar plate design for a PEM electrolyzer stack [29].....	34
Figure 2.21 Schematic representation of SOEC operating principle and electrode arrangement.....	37
Figure 2.22 Schematic diagram of solar hydrogen production methods, including feedstock and by-products (modified from [35]).....	41
Figure 3.1 Schematic representation of water splitting mechanism utilizing a semiconductor material (modified from [94]). .....	58

Figure 3.2 Illustration of the photo-derived electron and hole pair and the subsequent redox reaction.....	59
Figure 3.3 Schematic representation of the band gap energies of semiconductor relative to energy level for redox reactions in water (modified from [103])......	60
Figure 4.1 Schematic representation of the furnace electric circuit and control unit. ....	64
Figure 4.2 Representation of the furnace electric circuit made of MiCr80 heating coils.....	65
Figure 4.3 High temperature furnace heating coils test. ....	65
Figure 4.4 Setup within the fume hood structure showing the furnace, control unit, and air flow line. ....	66
Figure 4.5 Schematic diagram of the humidifier unit. ....	67
Figure 4.6 Cell casing: the reactant/product passages (for a sealed cell design). ....	69
Figure 4.7 Cell casing design for burnout products (Non-sealed cell). ....	69
Figure 4.8 Lower cell fixture with a button cell installed for testing. ....	70
Figure 4.9 New <i>NextCell</i> : the green side is the hydrogen electrode; and the black side is the oxygen electrode. ....	70
Figure 4.10 Exploded schematic diagram of the SOEC testing installation with all the components. ....	71
Figure 4.11 Mass flow controller used for hydrogen line.....	74
Figure 4.12 Schematic representation of the experimental setup for SOEC testing (without light). ....	76
Figure 4.13 Hydrogen and steam line to the lower fixture and the wiring. ....	77
Figure 4.14 Lower cell fixture with internal porous nickel foam for gas distribution.....	77
Figure 4.15 Schematic representation of the experimental setup testing for the PSOC (with light). ....	78
Figure 4.16 The complete SOC station testing. ....	78
Figure 4.17 All-quartz PSOC fixture for cell test under light.....	79
Figure 4.18 Rectangular samples of nickel foam and stainless steel mesh samples.....	83
Figure 4.19 Schematic representation of the electrospinning process. ....	84
Figure 5.1 Schematic representation of the SOE hydrogen production plant.....	89
Figure 5.2 The SOE system layout including a hydrogen compression unit.....	91
Figure 5.3 Schematic representation of the solar tower powered SOE for hydrogen production [40].....	92
Figure 5.4 T-s diagram of the CO <sub>2</sub> Brayton power cycle, according to the numbering system presented in Fig. 5.1.....	96
Figure 6.1 Schematic flow chart of the GA optimization.....	110
Figure 7.1 The layout of the button cell installation in the testing fixture.....	113
Figure 7.2 The J-V-P curve measurement of the SOFC operating at 100% H <sub>2</sub> and 750°C. ....	115
Figure 7.3 The J-V-P curve measurement of the SOFC operating at 50% H <sub>2</sub> - 50% H <sub>2</sub> O and a temperature of 750°C. ....	115

Figure 7.4 The J-V-P curve measurement of the SOEC operating at 50% H <sub>2</sub> - 50% H <sub>2</sub> O and a temperature of 750°C. ....	116
Figure 7.5 The J-V-P curve measurement of the SOFC operating at 20% H <sub>2</sub> - 80% H <sub>2</sub> O and a temperature of 750°C. ....	117
Figure 7.6 The J-V-P curve measurement of the SOEC operating at 20% H <sub>2</sub> - 80% H <sub>2</sub> O and a temperature of 750°C. ....	117
Figure 7.7 The J-V-P curve measurement of the SOFC operating at 50% H <sub>2</sub> - 50% H <sub>2</sub> O and a temperature of 850°C. ....	118
Figure 7.8 The J-V-P curve measurement of the SOEC operating at 50% H <sub>2</sub> - 50% H <sub>2</sub> O and a temperature of 850°C. ....	118
Figure 7.9 The J-V-P curve measurement of the SOFC operating at 20% H <sub>2</sub> - 80% H <sub>2</sub> O and a temperature of 850°C. ....	119
Figure 7.10 The J-V-P curve measurement of the SOEC operating at 20% H <sub>2</sub> - 80% H <sub>2</sub> O and a temperature of 850°C. ....	119
Figure 7.11 The OCV measurements at stable conditions of different reactant gas compositions. ....	120
Figure 7.12 The J-V-P curve measurement while operating in a fuel cell mode at a temperature of 750°C. ....	121
Figure 7.13 Comparisons between the J-V-P of two typical cells tested at exact conditions of 50% H <sub>2</sub> – 50% H <sub>2</sub> O gas compositions and temperatures of 750°C and 850°C ....	122
Figure 7.14 J-V curves of the tests performed on cell no. 1 showing the relative changes associated with temperature and composition changes as well as the with associated uncertainties. ....	122
Figure 7.15 The J-V-P curve measurements of a SOFC test at a temperature of 750°C reactants compositions of 50% H <sub>2</sub> - 50% H <sub>2</sub> O, 10% H <sub>2</sub> - 90% H <sub>2</sub> O, and 5% H <sub>2</sub> - 95% H <sub>2</sub> O. ....	124
Figure 7.16 The J-V curve measurements of a SOEC test at a temperature of 750°C reactants compositions of 50% H <sub>2</sub> - 50% H <sub>2</sub> O, 10% H <sub>2</sub> - 90% H <sub>2</sub> O, and 5% H <sub>2</sub> - 95% H <sub>2</sub> O. ....	124
Figure 7.17 J-V curves of the tests performed on cell no. 2 showing the relative changes associated with temperature and composition changes as well as the with associated uncertainties. ....	125
Figure 7.18 The electrochemical impedance spectra at different reactant concentrations while operating at temperature of 750°C. ....	125
Figure 7.19 The electrochemical impedance spectra at different reactant concentrations while operating at a temperature of 850°C. ....	126
Figure 7.20 Nyquist curve fitting to the EIS measurements to a representative equivalent circuit model. ....	127
Figure 7.21 A layout of the equivalent circuit model components. ....	127

Figure 7.22 A cross sectional view of the cell structure showing the different electrode layers. ....	128
Figure 7.23 The bilayer used in between the electrolyte and electrodes. ....	128
Figure 7.24 Analysis of the material compositions for each layer of the electrolyte. ...	129
Figure 7.25 Analysis of the material compositions within each electrode. ....	129
Figure 7.26 OCV reading showing the TiO <sub>2</sub> coated SS mesh under on/off UV light. ..	130
Figure 7.27 Magnified photos of the surface structure of Ni sample coated with ZnS through the electrospinning process and annealed at a temperature of 450 ± 5°C. ....	131
Figure 7.28 Variations in the SOEC subsystem thermal, electrical, and total energy demand over a range of electrolyzer operating temperature.....	132
Figure 7.29 Model validation through comparison with the published experimental data [78]......	134
Figure 7.30 Variations in SOEC voltage and power with current density different operating temperatures.....	135
Figure 7.31 Variations in ohmic, activation, and concentration polarizations when electrolysis operates at 1073 K. ....	136
Figure 7.32 Variations in ohmic, activation, and concentration polarizations when electrolysis operates at 973 K. ....	136
Figure 7.33 Variations in SOEC energy and exergy efficiencies with changing current density. ....	137
Figure 7.34 The energy and exergy efficiencies of the SOE system with and without hydrogen compression storage.....	138
Figure 7.35 Distribution of exergy output and exergy destruction compared with total exergy input and the relative shares of exergy destruction per main components. ....	140
Figure 7.36 The variations in total power input to the SOE system, the stacks power and power consumed for heating with variations in the stacks operating temperature. ....	143
Figure 7.37 The variations in energy and exergy efficiencies of SOE system of the two cases. ....	144
Figure 7.38 Effects of changing the stacks operating temperature on the exergy destruction rates occurs within the stacks and the BOP. ....	144
Figure 7.39 Effects of variations in the stack operating pressure on SOE system energy and exergy efficiencies. ....	145
Figure 7.40 Effects of variations in stack pressure on stacks' heat and power demand.	146
Figure 7.41 Variations exergy distraction rates within the stacks and the BOP with the variation in the stacks operating pressure. ....	147
Figure 7.42 Effect of pressure on electric power required for steam generation and total system's electric power demand. ....	147
Figure 7.43 Effect of pressure drop within the stacks on the overall SOE system energy and exergy efficiencies. ....	148

Figure 7.44 Variations in total system electric power demand and hydrogen production with variation in operating current density. ....	149
Figure 7.45 Variations in the stacks' heat and power demand with the variations in the operating current density.....	149
Figure 7.46 Effects of variations in operating current density on exergy destruction rates per stacks and BOP. ....	150
Figure 7.47 Effect of changing the operating current density on the cost of hydrogen produced and on the exergoeconomic factor of the SOE. ....	153
Figure 7.48 Effect of changing the operating temperature on the cost of hydrogen produced and on the exergoeconomic factor of the SOE. ....	154
Figure 7.49 Effect of changing the operating current density on the cost of hydrogen produced and on the exergoeconomic factor of the SOE. ....	155
Figure 7.50 Effect of changing the operating current density on the cost of hydrogen produced and on the exergoeconomic factor of the SOE. ....	155
Figure 7.51 Effect of changing the number of cells (scale) on the cost of hydrogen produced and on the exergoeconomic factor of the SOE. ....	156
Figure 7.52 Effect of changing the plant life time on the cost of hydrogen produced and on the exergoeconomic factor of the SOE. ....	156
Figure 7.53 Variations in solar tower exergy efficiency and mass flow rate with changing receiver outlet temperature. ....	158
Figure 7.54 Variation in solar tower exergy efficiency and heliostats field exergy destruction ratio with changing ambient temperature.....	158
Figure 7.55 Exergy destruction ration for the heliostats field and central receiver, and the total net-exergy output from solar tower. ....	159
Figure 7.56 The change in the TES temperature over the discharging time as well as the corresponding TES energy and exergy efficiencies.....	160
Figure 7.57 The effects of changing the solar tower temperature on the s-CO <sub>2</sub> power cycle performance as illustrated in terms of energy efficiency and BWR for different operating pressures.....	161
Figure 7.58 The effects of changing the compressor inlet pressure and temperature on the s-CO <sub>2</sub> power cycle performance as illustrated in terms of energy efficiency and BWR.	162
Figure 7.59 Exergy destruction ratios of the s-CO <sub>2</sub> Brayton power cycle components.	163
Figure 7.60 Effects of electrolyzer operating temperature and current density on cell potential and total hydrogen production rate. ....	163
Figure 7.61 The process flow diagram of the large-scale hydrogen production. ....	165
Figure A1.1 Design no. 1A.....	184
Figure A1.2 Design no. 2A.....	185
Figure A1.3 Design no. 1B. ....	186

## List of Tables

Table 2.1 Comparison of different hydrogen storage mechanisms [2].....	15
Table 2.2 Current status of different electrolysis technologies [22].....	26
Table 2.3 Comparison between alkaline and PEM electrolyzers [25].....	35
Table 3.1 Comprehensive list of SOC materials corresponding to the fuel electrode, electrolyte, and oxygen electrode (modified from [72]).....	52
Table 4.1 Material and dimensions of the <i>NextCell 2.5</i> (data from [108]).....	71
Table 4.2 Specifications of thermocouples used for temperature measurement and control. ....	72
Table 4.3 Specifications of Gamry Reference 3000 [110]. ....	73
Table 4.4 Pressure gauge specifications [111].....	74
Table 4.5 The specifications of Alicat MC-Series flow controllers [112].....	75
Table 4.6 Main parameters of the electrospinning nanopowder coating. ....	85
Table 5.1 List of BOP components and their performance merits. ....	90
Table 5.2 Main parameters used for solar tower modeling. ....	93
Table 5.3 Composition and heat transfer properties of selected high temperature molten salt (LiF-NaF-KF) at 973 K [136]. ....	94
Table 6.1 List of objective function constraints.....	109
Table 7.1 The combination of tests performed on two typical cells.....	112
Table 7.2 The ohmic and polarization resistances obtained from Fig. 7.18. ....	125
Table 7.3 The ohmic and polarization resistances obtained from Fig. 7.19. ....	126
Table 7.4 The Equivalent circuit parameters used for model fitting in Fig. 7.20.....	127
Table 7.5 Main parameters used for the base case SOEC model. ....	133
Table 7.6 Comparison between the results of the current model and the experimental measurements reported by Ebbesen et al. [78] for SOEC tests at reactants gas composition of 50% H <sub>2</sub> O – 50% H <sub>2</sub> . ....	133
Table 7.7 The reference case solution listing for each state point the mass flow rate, temperature, pressure, specific enthalpy, specific entropy, and specific exergy. ....	139
Table 7.8 Sensitivity of the exergy efficiencies to ±10% variations in stack operating temperature, pressure, and current density. ....	151
Table 7.9 Results of conjugate directions-based optimization of SOE exergy efficiency and optimum efficiency sensitivity to ±10% variations in operating conditions.....	151
Table 7.10 Results of genetic algorithm optimization of SOE exergy efficiency and optimum efficiency sensitivity to ±10% variations in operating conditions. ....	152
Table 7.11 The financial parameters of the reference case.....	152
Table 7.12 Capital cost of the SOE system components. ....	153
Table 7.13 Summary of the integrated system energy and exergy efficiencies.....	164
Table 7.14 List of equipment and their installed cost based on Aspen Plus.....	166

Table 7.15 List of stream number and their solution based on Aspen Plus flowsheet given in Fig.7.63. ....	166
Table A2.1 List of stream number and their solution based on Aspen Plus flowsheet given in Fig.7.63. ....	166

## Nomenclature

A	Area ( $\text{m}^2$ )
C	The compressor; Cost rate ( $\$ \text{h}^{-1}$ )
c	Speed of light in vacuum ( $300 \times 10^6 \text{ m s}^{-1}$ )
$c_p$	Heat capacity ( $\text{J kg}^{-1} \text{ K}^{-1}$ )
D	Effective diffusion coefficient ( $\text{m}^2\text{s}^{-1}$ )
E	Cell potential (V)
$\dot{E}$	Energy rate (W)
$\dot{E}_x$	Exergy rate (W)
F	Faraday's constant, $F = 96\,487 \text{ (C mol}^{-1}\text{)}$
G	Gibbs free energy ( $\text{J kmol}^{-1}$ )
h	Specific enthalpy ( $\text{J kg}^{-1}$ )
I	Direct solar radiation ( $\text{W m}^{-2}$ )
J	Current density ( $\text{A m}^{-2}$ )
$\dot{m}$	Mass flow rate ( $\text{kg s}^{-1}$ )
N	Number of measurements
n	Number of transferred electrons
P	Pressure (Pa); Power density ( $\text{W m}^{-2}$ )
$\dot{Q}$	Heat rate (W)
Q	Specific heat ( $\text{J kg}^{-1}$ )
R	Universal gas constant, $R = 8.31446 \text{ (J mol}^{-1} \text{ K}^{-1}\text{)}$ ; Resistance ( $\Omega$ )
S	Standard deviation
$\dot{S}$	Entropy rate ( $\text{W K}^{-1}$ )
s	Specific entropy ( $\text{J kg}^{-1} \text{ K}^{-1}$ )
T	Temperature (K); the turbine
t	Time (s)
U	Utilization factor; Uncertainty
u	Unified atomic mass unit ( $1.660539040(20) \times 10^{-27} \text{ kg}$ )
W	Work rate or power (W)
X	Physical quantity

### *Greek Letters*

$\alpha$	Symmetry factor
$\varepsilon$	Effectiveness
$\gamma$	Pre-exponential for electrode exchange current density ( $\text{A m}^{-2}$ )
$\delta$	Thickness (m)
$\eta$	Efficiency; Polarizations (V)
$\lambda$	Wavelength ( $\mu\text{m}$ )
$\nu$	Frequency ( $\text{s}^{-1}$ )
$\rho$	Resistivity ( $\Omega \text{ m}$ )
$\psi$	Exergy efficiency

### *Subscripts*

0	Exchange current density; initial
A	Anode

a	Average
abs	Absorbed
act	Activation
C	Compressor
c	Cathode
ch	Charging
COL	Cooler
conc	Concentration
dis	Discharging
E	Voltage
elec	Electric
en	Energy
ex	Exergy
f	Final
h	Heliostat
HE	Heat exchanger
i	Species
IHE	Internal heat exchanger
L	Limiting current
max	Maximum
net	Net work
ohm	Ohmic
p	Pressure
r	Reversible
rec	Receiver
s	Solar; isentropic state
st	Storage
sun	Sun temperature
T	Turbine
tot	Total

***Superscripts***

CH	Chemical
CL	Capital cost
eff	Effective
OM	Operation and maintenance
PH	Physical

***Acronyms***

AFC	Alkaline fuel cell
AKE	Alkaline electrolyzer
ASR	Area Specific Resistance
BOP	Balance of plant
BWR	Back work ratio
CB	Conduction band
CCS	Carbon capture and storage
CERL	Clean Energy Research Lab

CFD	Computational Fluid Dynamic
CIPM	The International Committee for Weights and Measures
COL	The cooler
CoMo	cobalt-molybdenum
CSP	Concentrating solar power
CTE	Coefficient of thermal expansion
DC	Direct Current
DoE	Department of Energy
EC	Electrolysis cell
EDS	Energy-dispersive X-ray spectroscopy
EES	Engineering Equation Solver
EIS	Electrochemical impedance spectroscopy
FC	Fuel cell
GA	Genetic Algorithm
GHG	Greenhouse gas
HE	The heater
HHV	Higher Heating Value
HT	High temperature
HTF	Heat transfer fluid
HTGR	High temperature gas-cooled reactors
IAHE	International Association for Hydrogen Energy
IEA	International Energy Agency
IHE	The internal heat exchanger
IJHE	International Journal of Hydrogen Energy
KACST	King Abdulaziz City for Science and Technology
LHV	Lower heating value ( $\text{J kg}^{-1}$ )
LSCF	Lanthanum strontium cobalt ferrite
LSCuF	Lanthanum Strontium Copper Ferrite
LSF	Lanthanum Strontium Ferrite
LSM	strontium-doped lanthanum
LT	Low temperature
MCFC	Molten carbonate fuel cell
MEA	Membrane electrode assembly
MFC	Mass gas flow controllers
MMTCDE	Million metric tons of carbon dioxide equivalent
OCV	Open Cell Voltage
OECD	The Organization of Economic Co-operation and Development
PAFC	Phosphoric acid fuel cell
PEC	Photoelectrochemical cell
PEM	Proton exchange membrane
PEMFC	Proton exchange membrane fuel cell
PSOC	Photoelectrochemical Solid Oxide Cell
PV	Photovoltaic cell
SG	steam generator
S-I+	Sulfur-Iodine
SLM	Standard liter per minute

SMR	Steam methane reforming
SOC	Solid oxide cell
SOE	Solid Oxide Electrolysis
SOEC	Solid Oxide Electrolysis Cell
SOFC	Solid Oxide Fuel Cell
SPE	solid polymer electrolyzer
STE	Solar thermal energy
TES	Thermal Energy Storage
THEME	The First Hydrogen Economy Miami Energy Conference
TPB	The triple phase boundary
VB	Valence band
YSZ	Yttria (Y <sub>2</sub> O <sub>3</sub> ) stabilized zirconia

## **Chapter 1: Introduction**

The evolving development of humans is a consequence of intellectual abilities. As a result of sincere efforts and brilliant ideas, humans have been able to overcome many challenges and produce innovative solutions that have created today's convenient lifestyle. A few centuries ago, one of the major challenges faced by global communities was finding reliable and economical energy resources. For a time, the discovery and expansion of fossil fuels appeared to solve the energy challenge and the industry started a revolutionary era. However, people very quickly started realizing the negative consequences of their increasing dependence on fossil resources not just limited to health and lifestyle, but as it extended further to the climatic and environmental system. This has resulted in a more intense energy challenge that manifests in finding economical, sustainable, and environmentally benign energy resources.

Renewable energy resources, such as solar, hydro, wind, geothermal, and ocean energy, are continuously renewed in contrast to fossil fuels that have finite depleting resources. Therefore, renewables are promising resources that have the potential to meet global energy demands without compromising the environment. However, for these renewable resources to be reliable and commercially competitive, several limitations have to be resolved. For example, many renewables, such as solar and wind, have an intermittent nature which causes the energy supplied by these resources to fluctuate, based on the availability of energy. Therefore, it is a current priority to overcome this intermittent characteristic through the development of a reliable energy storage system. Thus, the energy harvested based on resource availability can be efficiently stored and uniformly dispatched in accordance with end-user demand. Furthermore, innovative alternatives, such as the development of a single energy capturing and storing unit, are envisioned to efficiently solve this renewable energy challenge.

The present thesis investigates a novel way of capturing and utilizing solar energy in hydrogen production as an integral solution to energy and environment challenges. Thus, solar hydrogen production allows better use of solar energy resources and delivers stable and clean energy to users. This energy can be conveniently and efficiently used to power

transportation or stationary systems utilizing fuel cell technology. In this way, a carbon-free energy cycle can be achieved which will lead to CO<sub>2</sub> emissions reduction and ultimately preserve the environment.

In this chapter, the motivation to undertake this research subject is presented in the context of the current global energy and environmental challenges. Furthermore, the potential outcomes based on the targeted objectives are outlined, listing the detailed task-based objectives. The chapter concludes with a presentation of the thesis outline.

## **1.1. Motivation**

Considering the increasing demand for hydrogen, either as a clean energy carrier or as an integral part of many industries, the crucial need to find alternative hydrogen production methods can be realized. These methods should be more efficient and sustainable in order to replace hydrocarbon-based methods which currently produce more than 95% of the world hydrogen demand. For example, steam methane reforming (SMR), one of the most popular hydrogen production methods, contributes 80–85% of the hydrogen derived from natural gas. The major disadvantage of this technology is not only its dependence on finite fossil hydrocarbons, but also the significant amounts of CO<sub>2</sub> emissions released by these processes and the relatively low purity of the produced hydrogen.

A promising alternative method for hydrogen production is water electrolysis in a high temperature solid oxide electrolyzer. Numerous studies have outlined the increasing potential of this technology, especially in the context of large-scale applications that can be integrated into solar or nuclear power plants to produce hydrogen from the surplus energy which can be used as storage or to meet industrial demand and replace conventional methods such as SMR.

The current study aims to experimentally examine the Solid Oxide Electrolysis Cell (SOEC) performance of producing hydrogen and to further explore the fabrication of a Photoelectrochemical Solid Oxide Cell (PSOC) which is expected to utilize sunlight energy, in addition to thermal and electric energy, in order to increase hydrogen production efficiency. Therefore, the cost of hydrogen produced by high temperature electrolyzers can

be reduced, specifically if inexpensive materials are successfully utilized to modify current state-of-the-art electrodes and produce the desired PSOC characteristics.

## **1.2. Objectives**

The primary objective of this research is to develop a novel solar electrolyzer system based on improving the current SOECs. This improvement is expected if inexpensive photoactive materials are successfully deposited on the cathode side to capture and utilize sunlight, in addition to electric and heat energies.

The main objectives of this research project are summarized in the following points:

- To design an experimental test setup for the SOEC, starting by identifying the key parameters that influence cell performance, then listing all parameters to be measured, and materials and devices to be used.
- To build a SOEC testing and characterization station while considering the different cases that will be included in this research. The setup will accommodate two cases: one for a conventional SOEC test, and the other for a proposed PSOC test.
- To investigate the development of Solid Oxide-based PSOC for hydrogen production.
- To develop a novel PSOC by fabricating a photoactive cathode; this will enable the utilization of light energy (photons). This includes: (1) Designing the PSOC casing using quartz glass to allow light to shine on the new cathode; and (2) Improving the PSOC cathode through electro-deposition of a photoactive semiconductor, primarily  $\text{TiO}_2$  and/or  $\text{ZnS}$ . In addition, other materials will be examined based on research outcomes.
- To test the SOCs and PSOCs performance at different operating temperatures and with different reactant compositions, with and without light.
- To compare the performance of conventional SOEC, with PSOC, with and without light.
- To model the performance of the SOEC and PSOC, including thermodynamic and electrochemical analyses of the cell.

- To optimize the performance of the SOE based on exergy efficiency under the constraints of operating temperature, pressure, and current density. The SOE, is then to be integrated with solar tower technology for efficient solar hydrogen production.
- To examine SOE scale-up options to meet commercial large-scale hydrogen production capacities.

### **1.3. Thesis Outlines**

This thesis is presented in eight chapters. The first chapter concisely presents the motivation to undertake this research subject and introduces the objectives to be achieved as a result of the research.

In Chapter 2, the broad background of hydrogen production technologies is discussed in the context of environmental challenges and renewables opportunities with a focus on water electrolysis. Furthermore, related topics, such as hydrogen storage and utilization in fuel cells, are highlighted.

Chapter 3 is dedicated to the literature review where the research on solid oxide cells in general, and the electrolysis cell in particular, is traced from early developments to the current state-of-the-art. The presented review is based on two main pathways: (1) theoretical and modeling studies; and (2) material and experimental studies. An additional section is devoted to photoelectrochemical hydrogen production due to its relevance to the thesis subject.

Chapter 4 presents the experimental apparatus and methodology under five sections that describe the SOCs testing equipment, the sol-gel and electrospinning coating procedures, and the measuring instrumentations. The chapter includes a section on uncertainties analysis.

Chapter 5 describes two systems that have been proposed and optimized for large-scale hydrogen production using solid oxide electrolysis. One system considers a Solid Oxide Electrolyzer (SOE) unit for hydrogen and compressed hydrogen production, while the other includes a solar tower power plant to power the high temperature electrolysis process.

Chapter 6 deals with an analysis of the systems proposed in Chapter 5. Thus, the modeling and formulation is presented in view of thermodynamics, electrochemistry, and economics in order to evaluate the system's performance under various operating conditions. The chapter concludes with an optimization to establish an informative discussion on setting the systems' operating parameters for optimum economic and technical performance.

In Chapter 7, the results of this thesis are presented and discussed. The experimental results are first discussed, emphasizing the performance changes in response to changes in operating parameters. Moreover, the cell is characterized by Energy-dispersive X-ray spectroscopy (EDS) and Scanning Electron Microscopy (SEM) techniques before and after testing. The results of the coating processes to create photoactive surfaces on conductive current collectors are also reported for nickel and stainless steel samples. The modeling and optimization results are then presented, starting with principle single cell model validation. More detailed parametric analyses are discussed for the SOE model, considering the two cases of hydrogen production with and without hydrogen compression and the integrated solar tower hydrogen production plant.

Chapter 8 presents the conclusion and recommendations, and is where the main findings of the thesis are reported. The chapter includes the thesis contributions and a list of recommendations for future directions.

## Chapter 2: Background

This chapter discusses the involvement of hydrogen in the energy-environment paradox as a critical commodity that can be either part of the problem or part of the solution. The fact that hydrogen is currently an essential element of many modern industries is first highlighted, confirming that hydrogen does not exist in nature in its elemental form but is produced through an energy consuming process. Furthermore, the concept of the “hydrogen economy” is presented, examining the promising potential of using hydrogen as an efficient energy carrier and storage media that can be used to overcome the inherited limitation of renewable energy resources due to their intermittence. The various hydrogen production technologies are next introduced and classified according to the two primary sources of hydrocarbons and water. Accordingly, these categories are: fossil-based hydrogen production and water electrolysis hydrogen production. Additionally, the new hydrogen production methods that are currently under early research are briefly presented. The chapter concludes with an overview of the types of fuel cells and their operating principles as efficient and environmentally friendly means of converting hydrogen fuel to power.

### 2.1. Hydrogen as a Fuel of Future

Hydrogen as a chemical element has an atomic number of 1, and an atomic weight of 1.007794 u. Thus, it is placed first in the periodic table. At standard temperature and pressure, hydrogen is a colorless, odorless, nonmetallic, and nontoxic highly combustible gas. Hydrogen is the most abundant chemical substance in the universe but it is rarely found on earth in its elemental diatomic form. However, hydrogen has a substantial presence as part of the molecular structure of many compounds such as water, hydrocarbons, and organics.

In addition to the various modern industry uses of hydrogen, such as ammonia synthesis, petroleum upgrading, and food processing, many scientists recognize hydrogen potential as an energy carrier that can be relied on in the future to store surplus energy and harmonize energy production and demand. In spite of hydrogen’s low volumetric energy density of 10 MJ m<sup>-3</sup> at a pressure of 100 kPa, it has the highest energy density of 120 MJ kg<sup>-1</sup>, based

on the lower heating value (LHV). Furthermore, hydrogen reacts with oxygen to release energy that can be utilized in the transportation sector and in residences, and eventually in meeting different energy needs in a clean and carbon-free manner. For these reasons, hydrogen has been of prime interest to many research institutions. This interest led to the realization of what later became known as the “hydrogen economy.”

The concept of the hydrogen economy was initially proposed in the 1970s as a response to the oil crises at that time [1]. The hydrogen economy suggests that hydrogen can be produced from renewable resources to meet diverse energy demands. Thus, hydrogen can eventually drive the economy towards the ultimate goal of replacing the current petroleum-dependent economy. As a result, several institutions and scientific initiatives have been commenced, including: the International Association for Hydrogen Energy (IAHE); the First Hydrogen Economy Miami Energy Conference (THEME); and the International Journal of Hydrogen Energy (IJHE) [2]. However, with the oil market regaining stability, inexpensive hydrocarbons have continued to dominate the world energy mix. To date, more than 96% of world hydrogen demands are met by hydrogen derived from hydrocarbon-based methods while alternative methods for hydrogen production, such as water electrolysis, have failed to be economically competitive for the majority of applications at current electricity rates [3]. The significant contribution of hydrocarbon-based methods in meeting the global hydrogen demand demonstrates the remarkable impact of hydrogen production on the environment due to carbon emissions. Nevertheless, the burden of carbon and pollutant emissions produced by hydrocarbon-based energy systems in general, and hydrogen production in particular, faces progressive restrictions as a result of international awareness of their long-term environmental effects. Thus, the world has witnessed the introduction of regulations and limitations on emissions to mitigate climate change. These regulations may include carbon taxation and governmental emission charges as well as incentives for renewables, which favor alternative pathways to hydrogen. Eventually, more environmentally benign methods, such as water electrolysis, may become competitive. In contrast, water electrolysis is a mature hydrogen production method that can efficiently produce hydrogen in a carbon-free process. Furthermore, many renewable hydrogen production methods, which are currently being investigated by researchers in order to develop other sustainable hydrogen production methods, contribute towards the realization

of the hydrogen economy. Hence, it must be emphasized that for the hydrogen economy era to flourish, three pillars must be equally established: (1) sustainable hydrogen production; (2) storage and distribution infrastructure; and (3) successful development and commercialization of fuel cell systems. Due to their crucial role in hydrogen solution development, each of these trio pillars will be further discussed in the following sections.

### 2.1.1. The Global Energy Challenge

Ongoing dependence on fossil fuels for energy supply has created two major challenges that face our world today. The first challenge is related to the massive amount of greenhouse gas (GHG) that is being emitted into the atmosphere, mostly by conventional energy systems as a consequence of burning hydrocarbons to meet growing global energy demand. These GHG emissions have been increasing, reaching levels that threaten the entire ecosystem, leading to permanent climate change. According to the International Energy Agency (IEA), the world primary energy supply in 1971 was approximately 86% from fossil resources and 14% from non-fossil resources. In 2014, fossil fuels contributed 80.8%, while non-fossils contributed 19.02%. The alarming fact, as advised by these figures, is that the world still relies on fossil fuels to supply more than 80% of its primary energy [4].

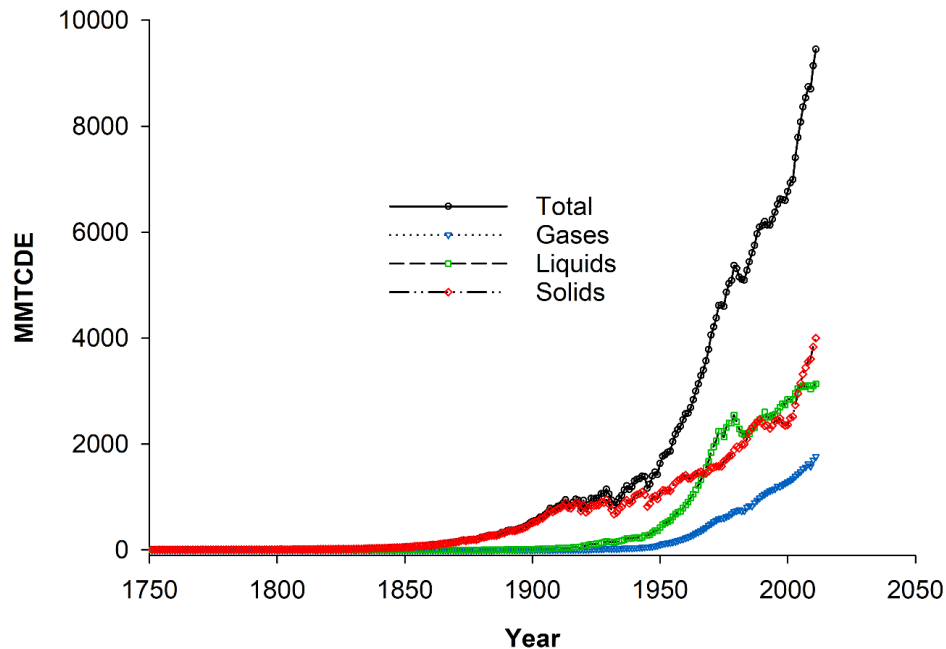
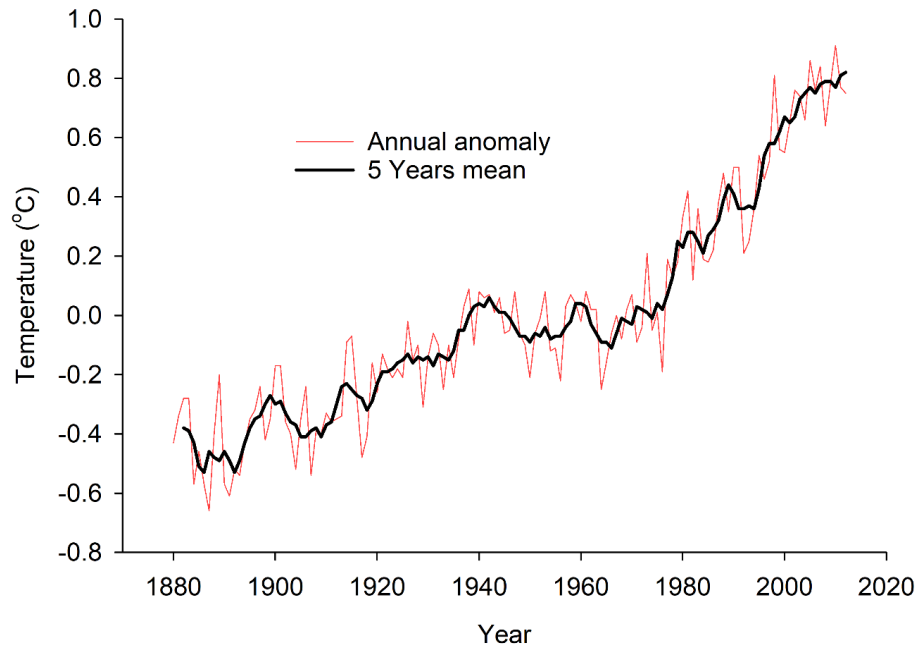


Figure 2.1 Annual global fossil fuel carbon emission (data from [5]).

The cost of this reliance on fossil fuels appears in the increase in carbon emissions, as shown in Fig. 2.1, which illustrates the change in annual global fossil fuel carbon emissions over the period from 1750 to 2010. It is noticeable that the dramatic increase in annual fossil fuel carbon emission, from zero in 1750 to approximately 9,500 million metric tons of carbon in 2010, is connected to the global industrial revolution and energy consumption. As a consequence of GHG accumulation in the atmosphere, the earth's average surface temperature has increased.



**Figure 2.2 Global annual temperature anomalies from land and ocean observations, from 1880 to 2014 (data from [6]).**

Fig. 2.2 shows the variations in the annual global anomaly and the five year mean temperatures from land and ocean observations [6]. The analogy between trends in global fossil fuel carbon emission and global average surface temperature shows the impact that carbon emission has on the environment. The second energy challenge, in addition to climate change, is that these hydrocarbon fuels are limited and subject to increasing consumption, driving global energy security to significant uncertainty. In the meantime, unless more effort is dedicated to resolving these challenges, the international community will suffer severe environmental and economic consequences. These consequences are observed in extreme and frequent weather events, as the anomalies presented in Fig. 2.2 indicate. These anomalies are usually encountered in territories around the world as: heavy

snow, severe rains, hurricanes, and droughts; also in other locations it causes ice melt, and rising sea levels [7]. Thereby, human existence on earth, in addition to many species, is endangered by these climate changes.

### **2.1.2. The Role of Renewable Energy**

Multiple solutions have been proposed to moderate climate change without compromising sustainable development. These solutions include diversifying energy mix, increasing energy efficiency, utilizing carbon capture and storage, and encouraging wise energy consumption. However, for an effective long-term carbon dioxide mitigation, an increase in renewable energy shares as a replacement for fossil fuels is the most promising option due to the carbon-free nature of most renewables and the fact that they are inexhaustible resources [8]. Solar energy (including thermal systems, concentrated solar power, and photovoltaic), and wind, geothermal, hydro, ocean and biomass energy are examples of renewable energy resources. These resources are abundant and considered sustainable as they produce no emissions and have only a minor environmental effect compared with fossil fuels [9]. The increase in the share of energy supplied by renewables is expected to stabilize the current levels of carbon emission and, in the future, higher renewable deployment is predicted to achieve safe carbon concentration levels compared with the pre-industrial era [8]. Furthermore, the distributed nature of these sources enables renewables to penetrate rural areas with limited access to conventional energy sources, which enhances energy security and leads to overall community development. Currently, renewable energy technologies are the focus of active research and development, leading some of these technologies to mature commercial status while others are on the verge of commercialization.

The potential of combined renewable sources is estimated to be an order of magnitude higher than the total world energy demand [10]. The renewable energy supply in 2014 was limited to 1,894 Mtoe, which accounts for 13.8 % of the world total energy supply of 13,700 Mtoe [4] while fossil fuels provided a total of about 80.8 %, distributed as 31.3 % from oil, 28.3 % from coal, and 21.2 % from natural gas. The nuclear energy share was about 4.8 %, and other resources such as wastes, oil shale, and chemical processes are noted

to have a marginal share of 0.3 %. Fig. 2.3 shows the relative distribution of these resources' share in the world energy supply mix in 2014.

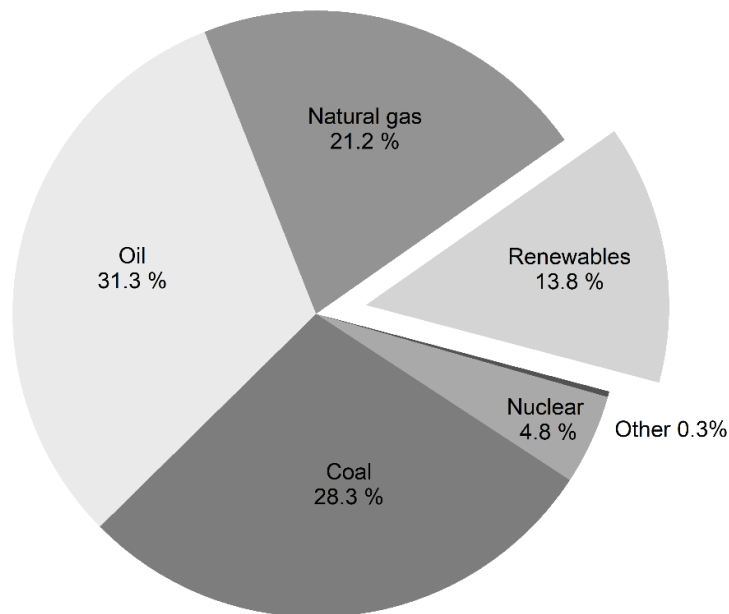


**Figure 2.3 World total energy supply in 2014 from various resources (data from [4]).**

The largest share provided by renewables noticeably came from biofuels, estimated to be approximately 10.1% of the total world supply. (This includes a considerable share of non-electrical applications such as cooking and residential heating.) The second largest renewable energy share was provided by hydropower, which was about 2.4% of the total world supply. The combined contributions of solar, wind, and geothermal provided the least, at approximately 1.3% of the total world supply.

Fig. 2.4 presents the relative share of the different renewable resources in the world total renewable supply in 2014. In spite of a reported renewable energy average growth rate of 2.2 % from 1990 to 2014, Fig. 2.3 shows the limited contribution of essential resources such as solar and wind. However, over the same period, these resources grew at the remarkably high rates of 46.2 % for solar PV, 24.3 % for wind, and 11.7% for solar thermal [4] when the total world energy supply was growing at a rate of 1.9 %. This growth in solar and wind energy has been reported in different countries around the world, with considerable contribution from OECD countries and China.

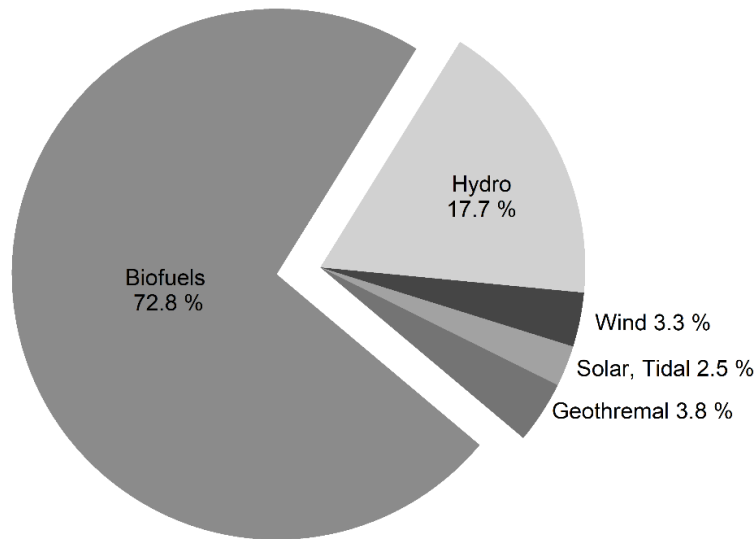


**Figure 2.4 Distribution of the world total renewable energy supply in 2014, based on resource type (data from [4]).**

Focusing on the electric power capacity produced by renewable resources as a primary form of energy, Fig. 2.5 presents the increase in total renewable capacity over the last decade. Fig. 2.5 shows that, in 2007, world total installed renewable capacity was 989.2 GW, which steadily doubled by 2006 [11]. This progressive growth in renewable technologies is derived by increasing investments and is supported by some recent environmental policies. One research study [8] claimed that, if strong environmental policies were already in place, renewables would have played a greater if not dominant role, especially in electricity generation.

The total investments in renewable energy (excluding large hydro) worldwide are presented, for the years from 2004 to 2016, in Fig. 2.6. The figure also shows the annual investment growth rates. The investments in renewables increase hitting a record of over \$300 billion in 2015; however, in 2016 the total investments fell by 23% to reach \$241.6 billion which is the lowest since 2013 [12]. Despite the considerable reduction in the total investments in 2016, solar, wind, geothermal, biomass, and tidal sources managed a capacity increase from 127.5 GW in 2015 to 138.5 GW. Furthermore, the reduction in investment in renewable technology may partially attribute to the reduction in the capital cost of solar energy one of the fastest growing technologies.

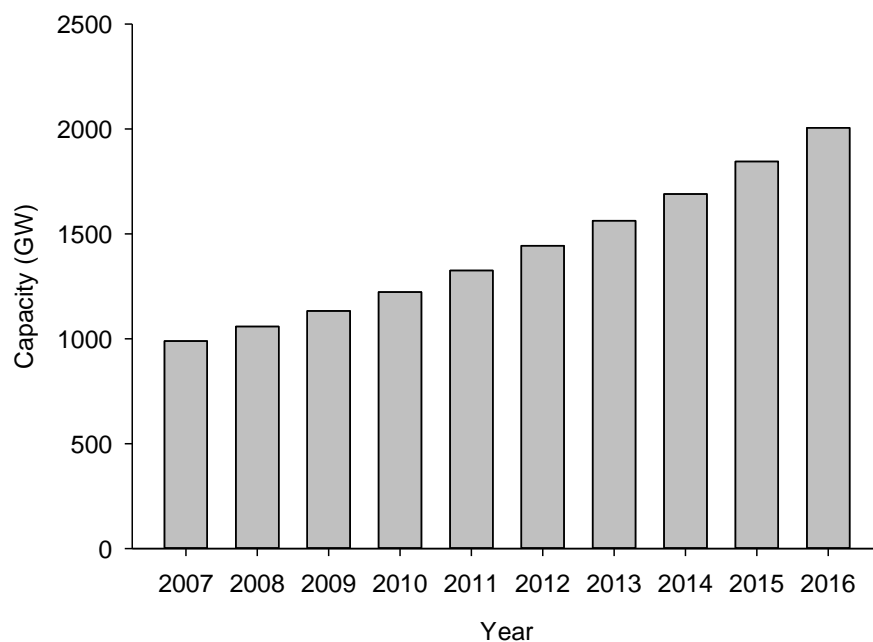


**Figure 2.5** The increase in the world total renewable energy capacity from 2007 to 2016 (data from [11]).

In contrast to fossil fuel sources which bear a continuous fuel cost, renewable sources are harvested freely, but involve a relatively higher capital investment. The current cost of renewable technologies is a significant constraint for larger renewable deployment. In addition to cost, other limiting factors are: (1) economic competitiveness with other sources, such as nuclear energy; (2) the geographical diversity of these sources; and (3) storage, transportation, and integration challenges. Regarding the first factor, many believe that fossil fuel scarcity, alongside limited social acceptance of nuclear energy, will result in favoring renewable energy sources. The second and third factors are interrelated; i.e., a solution to the third challenge will reduce the intensity of the second. In other words, if renewables can demonstrate efficient storage and transportation technologies, the effect of their geographical diversity will be moderate. Energy storage in hydrogen, as an excellent energy carrier, is one of the most promising options for resolving this problem.

Renewably produced hydrogen can serve as reliable storage to tackle a major drawback of renewables, namely their intermittent nature. This hydrogen can be efficiently stored and dispatched, or transported according to energy demands. Water electrolysis, thermal electrolysis, and photolysis are examples of hydrogen production technology that can be

used for renewable hydrogen production. Some of these have not yet reached a competitive commercial status, but are more environmentally friendly in terms of carbon emissions. The different hydrogen production methods have been reviewed by Dincer [13]. This review focuses on environmentally friendly hydrogen production methods. More comprehensive coverage of the various topics related to sustainable hydrogen production can be found in the recently published work by Dincer and Zamfirescu [1].

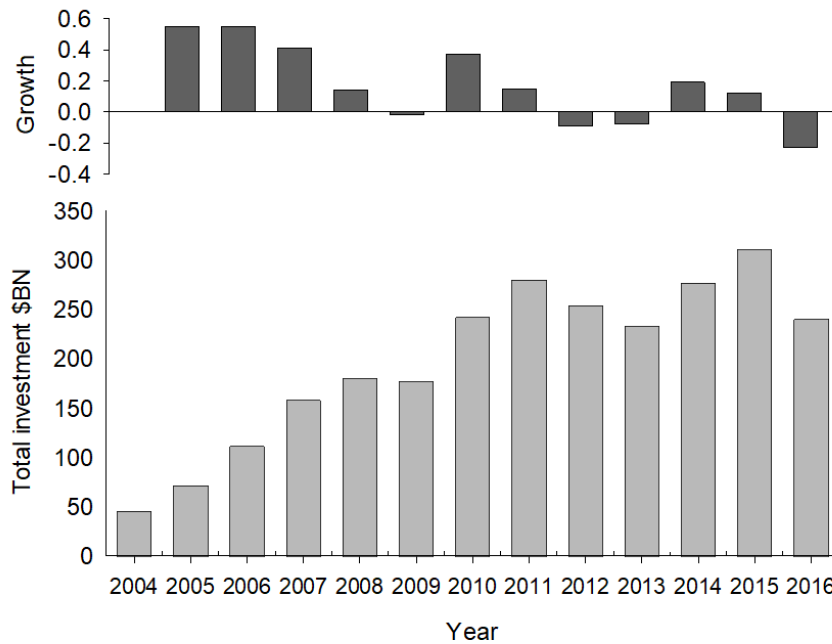


Figure 2.6 Total investment in renewables worldwide (data from [12]).

### 2.1.3. The Potential of Hydrogen Storage

The potential use of hydrogen as an energy carrier and storage medium for renewable energy involves a minimum of two conversion processes, charging and discharging, while in some cases a storing period takes place between these two processes. The first process is the conversion from the primary energy source to hydrogen, commonly from electricity to hydrogen in an electrolyzer, while the second is the conversion of stored hydrogen fuel to electricity in fuel cells. Although these two conversion processes are considered satisfactorily well-developed, the mechanisms for storing hydrogen during the intermediate stage (the storing process) are still being developed to overcome some technical challenges that prevent larger market penetration of the hydrogen storage option.

**Table 2.1 Comparison of different hydrogen storage mechanisms [2].**

Storage mechanism	Energy density (MJ kg <sup>-1</sup> )	wt.% H <sub>2</sub> /tank	wt.% H <sub>2</sub> /kg system	g H <sub>2</sub> /tank	g H <sub>2</sub> /L-system
Compressed hydrogen (35 MPa)	10.2	6	4-5	20	15
Liquid hydrogen	28-45	20	15	63	52
Low temperature hydrides (T<100°C)	10-12	2	1.8	105	70
High temperature hydrides (T>300°C)	20-25	7	5.5	90	55

At ambient temperature and pressure conditions, hydrogen gas occupies a large space, thus storing hydrogen in the gaseous phase requires compression to high pressures. Other hydrogen storage options also require a low temperature, e.g., liquefaction or advanced materials. Thus, all these mechanisms involve additional energy consumption, which varies from one to another and may in some cases become prohibitive. Table 2.1 shows a comparison of different hydrogen storage options. In this figure, the weight ratios of stored hydrogen to the storage system are compared for various hydrogen storage mechanisms.

Hydrogen density at atmospheric conditions is 0.0408 kg m<sup>-3</sup>. The three storage mechanisms currently available are: a compressed gas; cryogenic liquid; and hydrogen storage in metal hydrides. Hydrogen storage mechanisms have relatively lower volumetric and gravimetric energy density than conventional fuels such as diesel, gasoline, ammonia, and biodiesel, as presented in Fig. 2.7.

The energy content of 1 kg of gasoline is equivalent to approximately 1/3 kg of hydrogen, (specifically 0.324 kg), considering the hydrogen Higher Heating Value (HHV). From a volume perspective, at standard conditions, the volume occupied by 1 kg of gasoline is approximately 1.3 L, but the volume required by 0.324 kg of hydrogen is 3.932 m<sup>3</sup>. Therefore, minimizing hydrogen storage volume is a critical issue that must be addressed for the broad realization of hydrogen storage. For example, a major obstacle that limits hydrogen penetration in the transportation sector is that currently available onboard hydrogen storage options cannot achieve a driving range of 500 km without refueling at a reasonable cost [14].

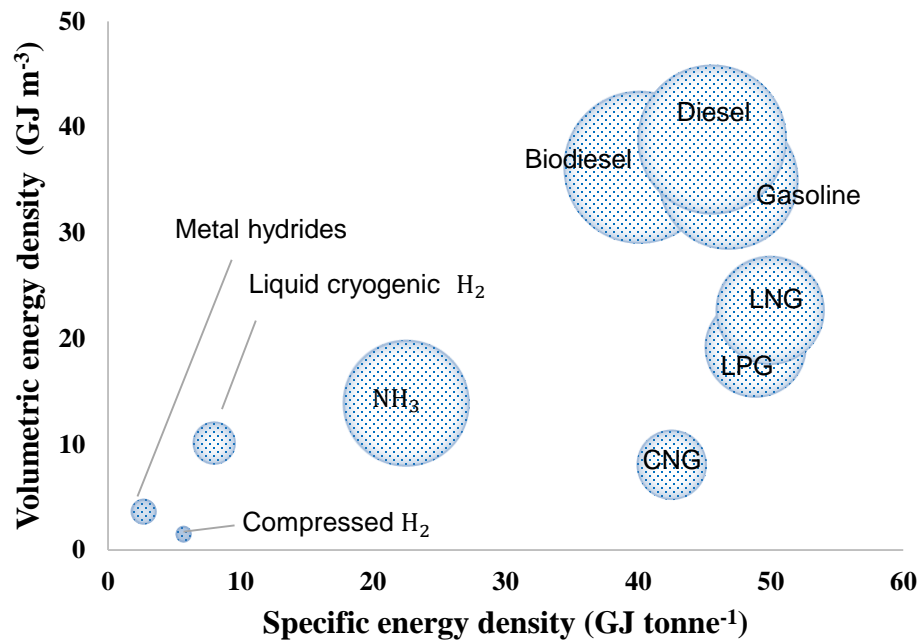


**Figure 2.7 Volumetric energy densities (GJ m<sup>-3</sup>) and specific energies (GJ tonne<sup>-1</sup>) for various fuels used in transportation (data from [1]).**

Considering the option of hydrogen liquefaction and storing hydrogen as a cryogenic liquid, hydrogen has to be brought to a temperature below the boiling point of  $-252.9^{\circ}\text{C}$ , at 100 kPa, where the liquid hydrogen density is  $70.77\text{ kg m}^{-3}$ . Thus, the volume of 0.324 kg of hydrogen (1 kg of gasoline equivalent) is about 4.58 L. However, the liquefaction process involves extensive energy demand in addition to some system complexity. The energy needed to liquefy 1 kg of hydrogen is estimated to be about 50 MJ, which is about one third of the energy content in that 1 kg of hydrogen.

Another option is compressed hydrogen gas to reduce system volume. In this case, at standard temperature and a pressure of 40 MPa, hydrogen gas density is about  $26\text{ kg m}^{-3}$ . Accordingly, the volume of 0.324 kg of hydrogen becomes 12.5, i.e., 9.6 times that of equivalent gasoline. Current compressed hydrogen storage technology, developed for onboard hydrogen storage, reaches as high as 70 MPa. Thus, 5 kg of hydrogen requires a volume of 125 L [2]. The variations in energy density of compressed hydrogen storage and hydrogen gas density are presented in Fig. 2.8 as a function of storage pressure. For example, at a pressure of 40 MPa, the hydrogen volumetric energy density is about  $4\text{ MJ m}^{-3}$ .

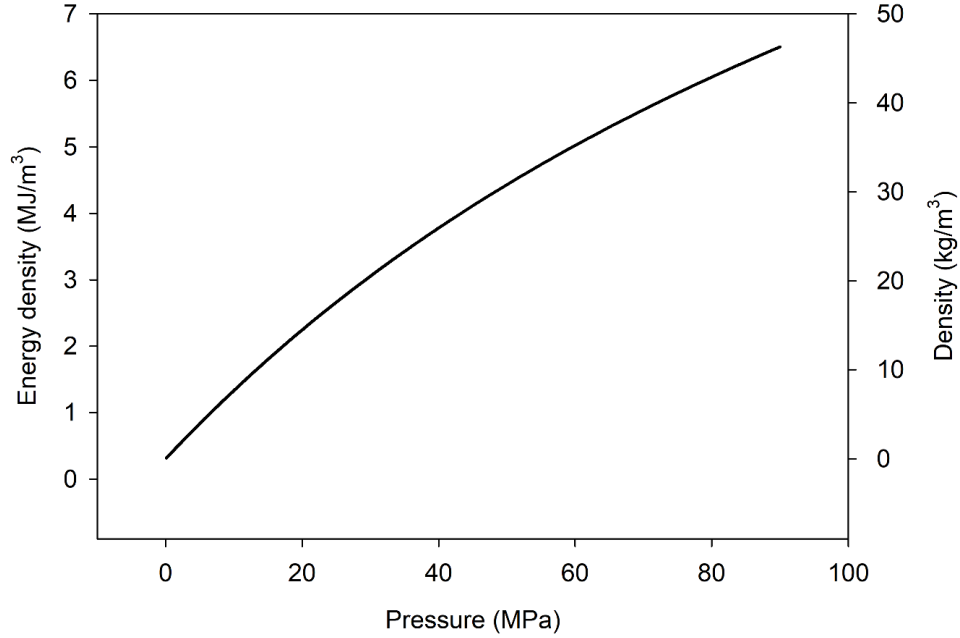


**Figure 2.8 Energy density of compressed hydrogen.**

The power required to compress hydrogen, assuming hydrogen as an ideal gas, can be evaluated using the adiabatic compression and the compressor isentropic efficiency relations given by:

$$w_{mc} = \frac{\gamma}{(\gamma - 1)\eta_{comp}} RT \left[ \left( \frac{P_2}{P_1} \right)^{\frac{\gamma}{\gamma-1}} - 1 \right] \quad (2.1)$$

Here,  $\gamma$  is the specific heat ratio given as  $C_p/C_v$ , and  $\eta_{comp}$  is the compressor isentropic efficiency.

The electrochemical hydrogen compression is another hydrogen compression method. The specific work in this process follows an isothermal compression relation given by:

$$w_{ec} = RT \ln \left( \frac{P_2}{P_1} \right) \quad (2.2)$$

Here,  $P_1$  is the low-pressure side (the anode compartment), and  $P_2$  is the high pressure side (the cathode compartment). Electrochemical hydrogen compression, which has been known for decades [15], has recently drawn considerable attention [16], [17], consistent with the development of PEM fuel cells and due to the significant reduction in compression

power that this technology achieves. Furthermore, electrochemical compression eliminates moving parts and can integrate some purification processes, thus high pressure and high purity hydrogen can be produced from a reformer or other hydrogen production technologies.

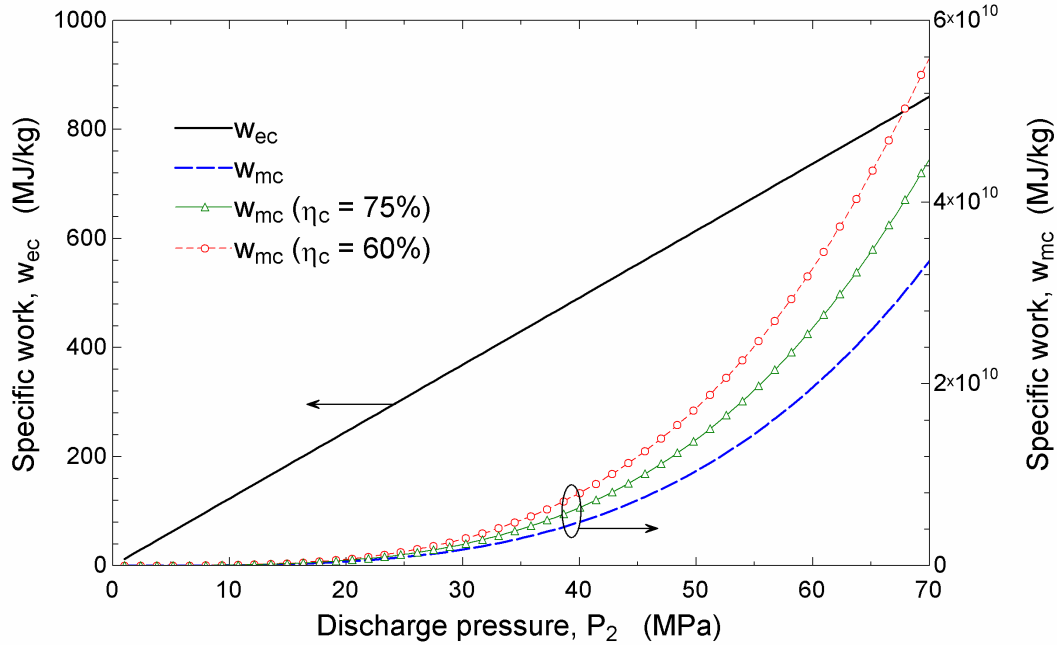


**Figure 2.9 Comparison between electrochemical and mechanical hydrogen compression from ambient conditions of 298 K and 0.1 MPa to 70 MPa.**

Fig. 2.9 compares the electrochemical and mechanical specific works required to compress hydrogen from 0.1 MPa to 70 MPa. For mechanical compression, two isentropic compressor efficiencies are considered, with 60% representing the lower end and 75% representing the higher end, in addition to an ideal adiabatic compression curve.

The third storage option is utilizing some chemical elements that can create hydrides thus store hydrogen in the material solid structures such as nanostructured materials. This mechanism involves either physisorption or chemisorption process, for example, some types of materials such as metals, intermetallic materials, and alloys can absorb hydrogen at low temperatures and moderate pressure to form metal-hydrogen compound [18]. The absorbed hydrogen can later be released in an endothermic reaction operating at temperatures comparable to that of low-temperature fuel cells. Thus, these formed metal hydrides can store hydrogen in what is considered safer storage method compared with,

the above mentioned, mechanical mechanisms. This because of stored hydrogen is not in its diatomic structure. Also, the metal hydride hydrogen storage has an advantage of high volumetric energy density compared with other methods. However, it has few major drawbacks such as the heavyweight, slow reaction kinetics, and high (discharging) dehydrogenation temperatures.

## 2.2. The Current Demand for Hydrogen

Total worldwide hydrogen consumption by industries is approximately 50 million tons per year [19], mainly for ammonia synthesis and fertilizer production, methanol synthesis, and for oil product upgrading, as shown in Fig. 2.10, where the distribution of hydrogen consumption by these industries is presented.

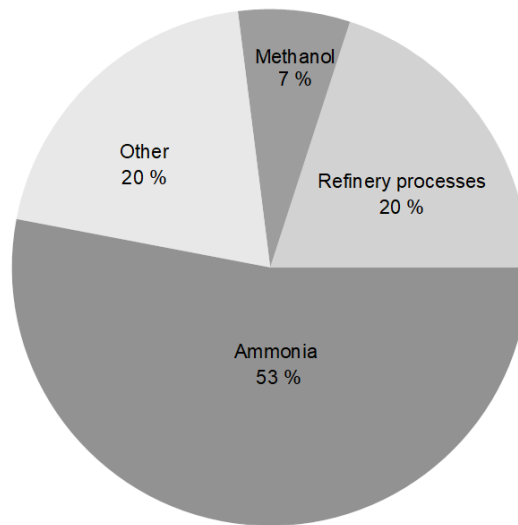


**Figure 2.10** Distribution of hydrogen consumption shares in the different industries.

Additionally, other processes, such as metal fabrication, the plastics and glass industry, food processing, and the pharmaceutical industry, all depend on hydrogen. It is expected that the global demand for hydrogen will continue increasing by 5-6% over the next five years [20]. The estimated size of the hydrogen production market in 2013 was 255.3 billion cubic meters, valued at USD 96.6 billion. The predicted growth in the hydrogen production market by 2020 is expected to reach 324.8 billion cubic meters, valued at USD141.4 billion, in terms of investment. Initially, hydrogen demand was derived by the expansion of ammonia synthesis through the Haber–Bosch process (see Fig. 2.11).

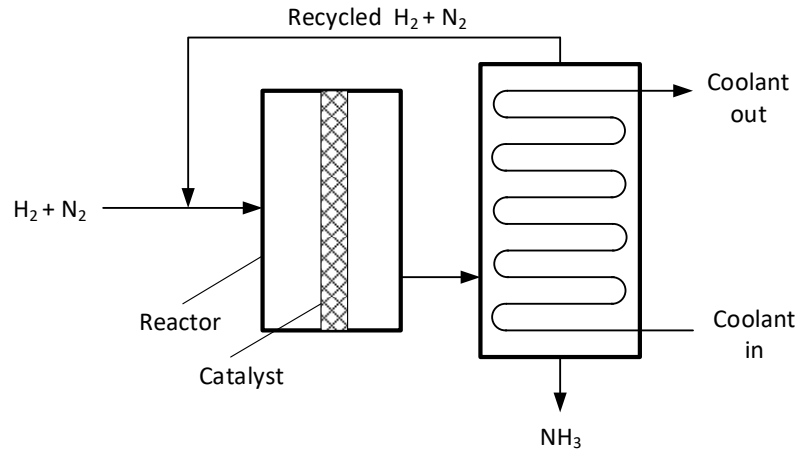
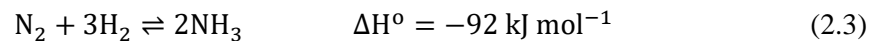


**Figure 2.11 Schematic representation of the Haber-Bosch ammonia synthesis process.**

In the Haber–Bosch process, as shown in Fig. 2.11, hydrogen and nitrogen are fed into a reactor operating at a temperature and pressure of approximately 450°C and 25 MPa, respectively, in order to produce ammonia. The process reaction is given by:



The enthalpy change associated with this reaction is  $-92 \text{ kJ mol}^{-1}$ . Hence, the reaction is an exothermic reaction. For an optimized forward rate, the reaction’s temperature and pressure are increased.

Hydrogen demand for petroleum refining currently dominates the hydrogen markets, which have experienced a significant increase over the last few years. This increase in refinery hydrogen demand came as a response to the progressive tightening of governmental regulations on vehicle emissions. As a consequence, further fuel upgrading and desulfurization has been added to hydrogen demand. Other chemical processes that have participated in raising the demand for hydrogen are methanol production, metal processing, and the food and pharmaceutical industries.

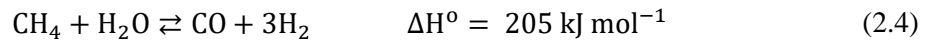
### **2.3. Fossil-Based Hydrogen Production**

A substantial amount of hydrogen is currently derived from fossil-based sources, namely natural gas, coal, and liquid hydrocarbons. Therefore, it is imperative to understand how these technologies operate and how much hydrogen they produce, in order to evaluate the hydrogen shortages that may be encountered as well as the carbon emissions that can be

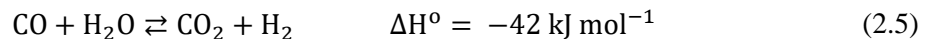
prevented, if any of these methods were to be replaced with environmentally friendly alternatives. In this section, the different fossil-based hydrogen production methods are presented and discussed.

### 2.3.1. Steam Methane Reforming

Steam methane reforming (SMR) is currently the primary method used worldwide to produce hydrogen as it contributes about 48% of total hydrogen production. The reforming process involves a chemical reaction which restructures hydrocarbon molecules such as methane to form hydrogen and carbon monoxide. In this process, as the largest constituent of natural gas, methane undergoes several processes, starting with a multi-stage desulfurization process, which occurs at a temperature in the range of 340°C, to remove the sulfur. The sulfur removal process utilizes a catalyst, such as cobalt-molybdenum (CoMo), to convert the sulfur contents into H<sub>2</sub>S. The produced low sulfur methane is then introduced into a steam reformer reactor to produce hydrogen and carbon monoxide, utilizing a Ni catalyst. The following equation gives the overall reforming reaction:



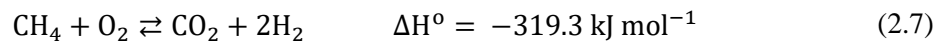
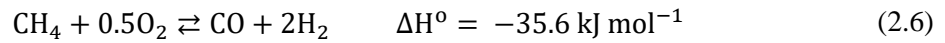
This reaction has a standard enthalpy change of 205 kJ mol<sup>-1</sup>. This indicates that the reforming reaction is endothermic and nonspontaneous, thus requires heating and a reduced pressure environment to make the forward reaction favorable. Subsequently, a steam shift reaction is performed to oxidize the carbon monoxide resulting from the reforming process to carbon dioxide. This will lead to more hydrogen production. The steam shift overall reaction is given as:



However, in contrast to a reforming reaction, a steam shift reaction is an exothermic reaction having a standard enthalpy change of -42 kJ mol<sup>-1</sup>. In practical applications, the reaction operating temperature is usually optimized to maintain high reaction kinetics and integrated process synchronization. The produced hydrogen, carbon dioxide, and carbon monoxide can be further treated to yield the desired purity [21]. Catalyst selection plays a vital role in achieving the required reaction rate at reasonably minimized resource consumption.

### 2.3.2. Partial Oxidation

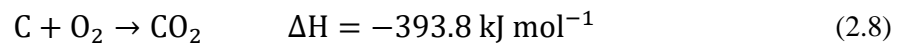
The process of partial oxidation involves controlled combustion of hydrocarbons to produce syngas. The produced syngas is then allowed to undergo a shift reaction to produce hydrogen and carbon dioxide [21]. Several modifications are usually introduced on the partial oxidation process to account for feedstock composition and quality of fuel. Partial oxidation is an exothermic process that can be performed with or without catalysts. However, operating without catalysts increases reaction temperature, i.e., in the range (1100–1500°C), especially for dense residual oils and coal feeds. Introducing the catalysts reduces the operating temperatures to about 600–900°C. The reaction of partial oxidation of the methane is given by the following equations:



The fact that both methane oxidation reactions are exothermic implies that an external heat source may not be required.

### 2.3.3. Gasification

In a gasification process, coal and biomass are used as solid feedstock that is combusted at a controlled high temperature and pressure environment to produce syngas. For the feedstock reactants to form syngas as a product, a number of processes, such as combustion, pyrolysis, and gasification, have to take place. The critical step in a gasification process is the partial oxidation of coal where a limited amount of oxidant is allowed (about one-third to one-fifth stoichiometry). Thus, the energy generated by the combustion process is used to drive the process [22]. Based on the type and design of gasification reactor, the temperature profile is formed, typically the oxidation reaction takes place at the reactor's highest temperature. This reaction is given by:



This reaction is the rate determining step based on which the pace of the entire gasification process is determined. The heat generated by this reaction is transferred by produced gases to drive the endothermic gas shift and Boudouard reactions as given by:



Thus, the steam and produced  $\text{CO}_2$  are reduced to  $\text{CO}$  and  $\text{H}_2$  by the concentrated carbon in the char. The produced gases travel to the far end of the gasification reactor, to the lower temperature end, to dry the intake biomass. At this zone, the pyrolysis of the dried biomass takes place where low molecular weight compounds are produced.

The main limitations, worthy of mention, of the gasification process, are: (1) feedstock requires further pretreatment; (2) a significant amount of tar and ash is formed; and (3) the product gas requires further purification steps.

## 2.4. Water Electrolysis Hydrogen Production

The water electrolysis process is an electrochemical process in which electricity is used to decompose water molecules into its main constituent elements of hydrogen and oxygen. The total worldwide electrolysis capacity is currently about 8 GW, which accounts for 4% of total hydrogen production [23]. Water electrolysis reaction is a nonspontaneous electrochemical reaction which requires electrical and thermal energy to proceed and produce hydrogen and oxygen. Electrolysis reaction is the reverse reaction that takes place in fuel cells where reactants such as hydrogen and oxygen/air are consumed to produce electricity and water. The minimum electrical energy required to drive the electrochemical reactions is equivalent to Gibbs free energy of the electrolysis reaction.

A schematic representation of an electrolysis cell is shown accordingly in Fig. 2.12. This figure primarily illustrates the three main components of an electrolysis cell (the two electrodes, an anode, and a cathode) in addition to an electrolyte. Fig. 2.12 also shows the operating principle of a water electrolysis cell.

The overall chemical reaction of liquid water electrolysis is given, at standard conditions, as:



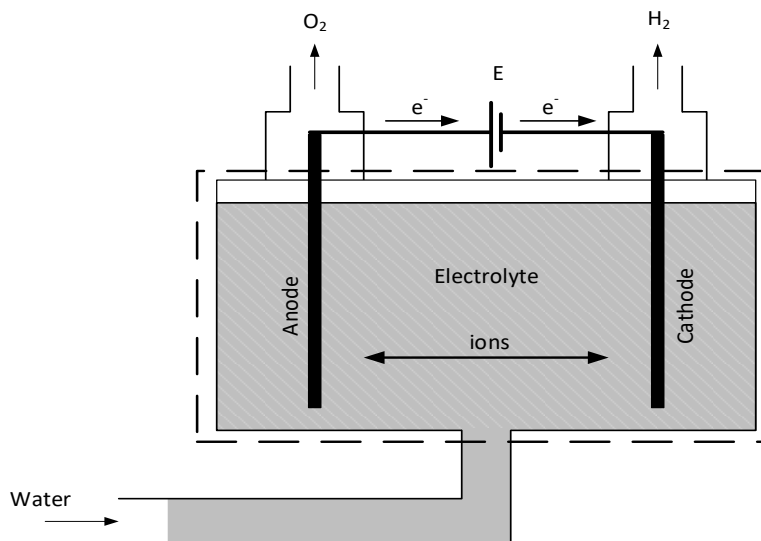


**Figure 2.12 Schematic representation of the main components of an electrolysis cell and the movement directions of the various species with respect to electrodes**

This reaction equation shows that electrolysis of 1 mole of water results in a formation of 1 mole of hydrogen and half a mole of oxygen. As this reaction occurs in the vicinity of the two electrodes, the reaction can be split into two half-cell reactions based on the electrode at which they occur. At the negatively charged electrode (the cathode), a hydrogen reduction reaction takes place:



At the positively charged electrode (the anode), an oxygen oxidation reaction takes place:



In the context of an electrochemical reaction, the electrolysis cell's three components (the cathode and anode electrodes, and the electrolyte) fall under two types of conductors. For an instance, electrodes are fabricated of composite metals, semiconductors, or both, such that they function as an electron conductor. In contrast, the electrolyte conducts ion species and, for an electrolysis reaction to proceed, a closed electric circuit must form in which electronic current passes through an external circuit from the anode electrode to the cathode electrode. However, both ion (internal circuit) and electron (external circuit) currents must be equal. At the electrode-electrolyte interface, an electrochemical reaction occurs where electrons directly react with molecules and atoms in the vicinity of a catalyst.

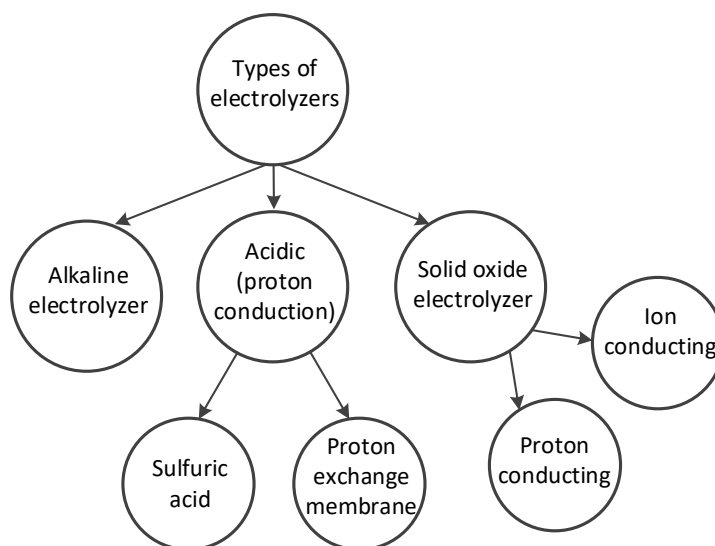


**Figure 2.13 Classification of water electrolyzers based on electrolyte type.**

Various characteristics have been used to categorize the different types of electrolysis technologies, such as the electrolyte phase, electrolyte composition/type, and operating temperature and pressure. However, the most widely accepted classification of electrolysis processes is either based on the electrolyte type or on the operating temperature. Accordingly, three main types that are well-established are classified, according to electrolyte type, into: (1) alkaline electrolyzer; (2) proton exchange membrane (PEM) electrolyzer; and (3) solid oxide electrolyzers. The classification of electrolyzers is presented in Fig. 2.13.

In a typical electrolysis reaction, such as that which occurs in one of the various types of electrolyzers shown in Fig. 2.14, hydrogen evolves at the cathode electrode while oxygen is produced at the anode electrode.

Furthermore, Fig. 2.14 illustrates the working principles of the different types of electrolyzers. The direction of moving species and the evolving gases with respect to the electrodes can be seen for each type. The figure also shows the electrons moving from the anode, and through an external circuit, to the cathode, respectively. The current status, operating conditions and conversion efficiencies of the various electrolysis technologies are presented in Table 2.2. Further detail regarding each of the water electrolysis technologies are discussed, according to each type, in the following sections.

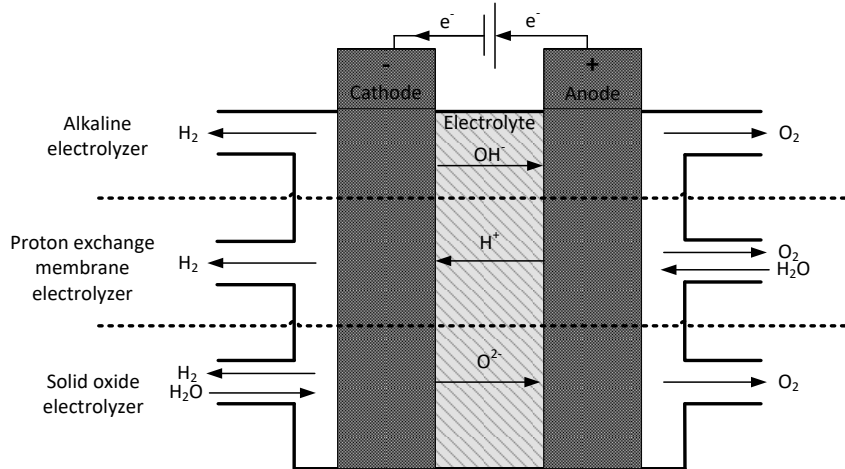


**Figure 2.14** Schematic representation of the working principle of the various water electrolysis types, illustrating the moving species and the produced gases with respect to either the cathode or anode side.

**Table 2.2** Current status of different electrolysis technologies [24].

Technology	Alkaline large-scale	Alkaline high-pressure	Advanced alkaline	PEM	SOEC
Status	Commercial	Commercial	Pre-commercial	Pre-commercial	Prototype
T (°C)	70–90	70–90	80–140	80–150	900–1000
P (kPa)	100 – 2500	Up to 69000	Up to 12000	Up to 40000	Up to 3000
kWh kg <sup>-1</sup> H <sub>2</sub>	48–60	56–60	42–48	40–60	28–39

### 2.4.1. Alkaline Electrolysis

Alkaline electrolysis is one of the earliest industrial techniques used for hydrogen production, mainly in the ammonia synthesis industry. It was also the first electrolysis technology to reach demonstration status. Therefore, alkaline electrolysis is the most mature and commercially proven method for hydrogen production from water. The alkaline electrolysis cell is composed of two electrodes operating in a liquid alkaline electrolyte solution of potassium hydroxide (KOH) or sodium hydroxide (NaOH). These electrodes are technically separated by a diaphragm which prevent mixing the product gases and transports the hydroxide ions from one electrode to another. The electrolyte concentrations typically range from 25 to 30 wt.% and can be as high as 40 wt.% in order to enhance electrolyte electrical conductivity. However, the drawback of a high electrolyte concentration is that it causes a higher corrosion rate of the electrolysis cell components. The electrodes are usually made of metallic materials such as nickel and copper due to their

high conductivity and low cost. Furthermore, catalytic coating layers, such as platinum, are commonly applied for the cathode electrode while metal oxides are used for the anode electrode. As an example, steel mesh has also been used for the cathode electrode, specifically low carbon steel or nickel coated low carbon steel. Other materials that have been used for the cathode are cobalt, zinc, lead, palladium, platinum, and gold while nickel, platinum, cobalt, iridium, and rhodium have been used for the anode. The porous diaphragm separator, historically made of asbestos (a natural silicate mineral), has recently been replaced by other alternatives due to the toxicity of asbestos which may cause lung cancer if the asbestos fibers are inhaled [25]. Alternative materials, such as high-polymer composites (e.g., polyphenylene-sulfide), are being investigated. The operating temperature of the alkaline electrolyzer is in the range of 70–90°C.

In the alkaline electrolysis process, water is supplied to the cathode side where it decomposes to hydrogen ions ( $H^+$ ) and hydroxide ions ( $OH^-$ ). The internal potential difference induced by the direct current (DC) connected to the anode and the cathode influences these ions, thus they are attracted, according to their charges, to the opposite electrode. The electrons flow from the negative electrode (the anode) to the positive electrode (the cathode) in order to balance the electron consumption at the cathode as the hydrogen ion ( $H^+$ ) coming from the electrolyte combines with the electrons to form hydrogen. The cathode side half-cell reaction is given as:



The hydroxide ions migrate through a diaphragm separator (see Fig. 2.14) to the anode electrode at which these hydroxide ions release electrons to form oxygen and water while the released electrons return to the DC source. The anode side half-cell reaction is given as:



The overall alkaline electrolysis cell reaction can be written as:



The operating principle of the alkaline electrolyzer is illustrated in the schematic diagram shown in Fig. 2.15. The figure shows the direction of electron movement and the opposite movement of the hydroxide ions through the diaphragm separator which is made of a material with a porous structure and which is electrolyte-impregnated to prevent the recombination of produced  $H_2$  and  $O_2$ .

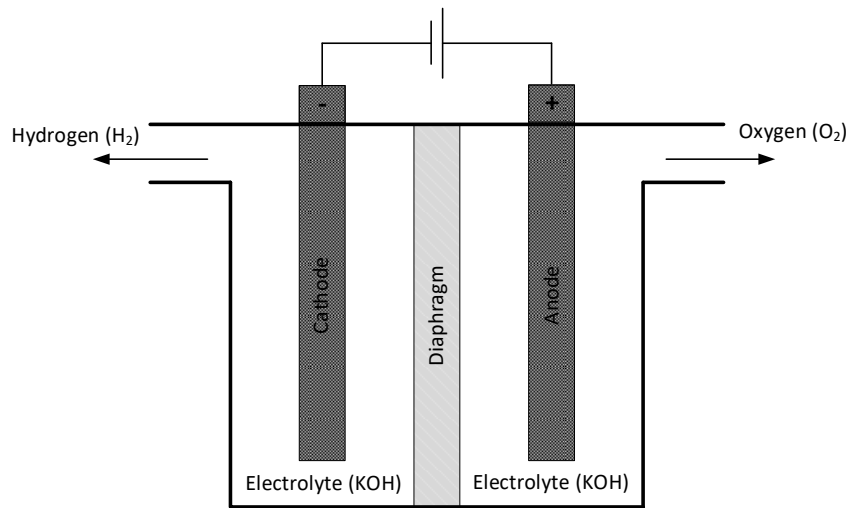


**Figure 2.15** Schematic representation of an alkaline water electrolyzer with KOH as an electrolyte.

As water is being consumed with the progress of the electrolysis process and the production of hydrogen and oxygen, a water supply must be provided to the cell to maintain the reaction progress and to maintain the electrolyte concentration at the desired design value. Although traces of electrolyte and water vapor may be carried away with the produced hydrogen and oxygen, the final produced hydrogen is characterized by high purity of about 99.9%.

Alkaline electrolysis stacks are currently produced in two designs: unipolar (tank) or bipolar (filter press) configuration. In the unipolar configuration, electrodes are arranged alternately separated by porous diaphragms and immersed in a single electrolyte tank [26]. The cathodes are connected to the negative terminal of the DC source, and the anodes are connected to the positive terminal. Fig. 2.16 shows a schematic diagram of the unipolar, also known as tank stack, configuration.

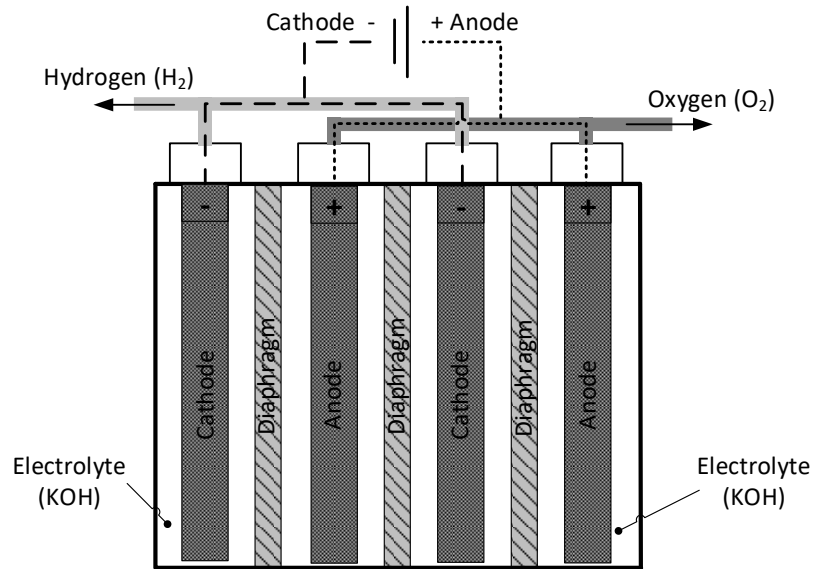


**Figure 2.16 Unipolar or tank electrolyzer configuration.**

The other alkaline electrolysis stack design is the bipolar configuration, which employs bipolar electrodes where the anodes and cathodes are connected back-to-back and separated by a porous diaphragm, as shown in Fig. 2.17. By this arrangement, the hydroxide ions transfer through the separator, and the electrons move from one electrode to the next cell through oppositely connected electrodes.

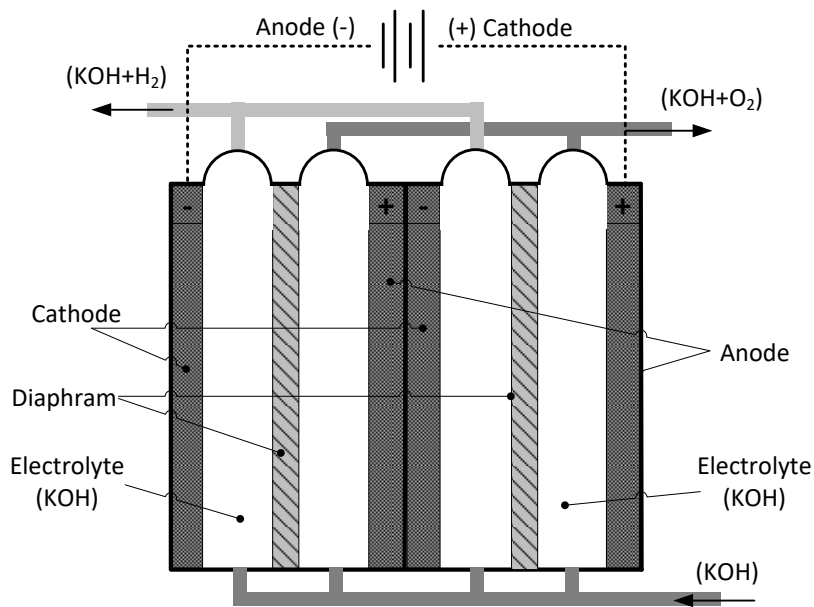


**Figure 2.17 Bipolar or filter-press electrolyzer stack configuration.**

In this design, the electrolyte is circulated through the electrode-separator spaces. Hydrogen is produced from the cathode-electrolyte interface. Thus, an electrolyte and hydrogen mixture leaves the channel between the separator and cathode while oxygen is produced from the anode-electrolyte interface. Accordingly, the mixture of oxygen and electrolyte leaves the anode separator channel. The produced gases are then separated from the electrolyte in an external step while the purified electrolyte is circulated through the bottom to the electrolyzer stack. The electrolyte may be cooled or heated to maintain the desired operating electrolyzer temperature. In the bipolar stack configuration, the individual cells are connected in series, thus the voltage of the cells adds up and can be calculated based on the number of cells  $n_c$  as:

$$V_{stack} = V_{cell}N_{cell} \quad (2.17)$$

Comparing both the unipolar and the bipolar stack designs, several advantages and disadvantages can be recognized for each. In regard to the unipolar design, simplicity and cost-effectiveness, as well as the elimination of parasitic currents, are among the major advantages of this design. Furthermore, the unipolar configuration does not require circulation pumps, and is easier to maintain. In contrast, the major disadvantages of this design are high power consumption, low operating pressure, and temperature limits. Operator attention is also required.

For the bipolar stack design, the main advantages are the lower cell voltage and high operating current densities, the higher pressure and temperature operation, as well as the compact stack. The disadvantages of this configuration are the necessity for pumps and gas separators (for produced hydrogen and oxygen separation) and the increased parasitic current. Additionally, the maintenance and fault diagnosis are relatively complicated and mandate the entire stack shutdown.

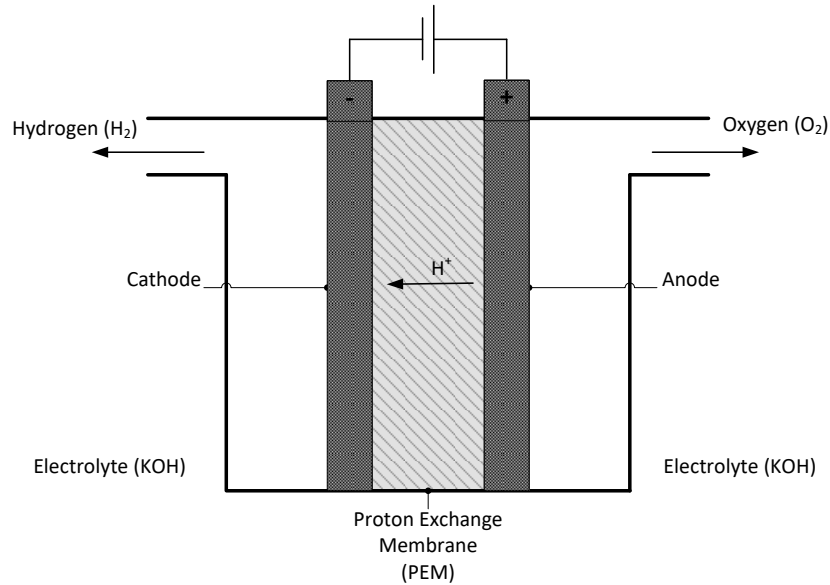
Compared with other water electrolysis technologies, alkaline electrolyzers are characterized by the following advantages: (1) low capital cost due to the inexpensive materials required for electrode and separator manufacturing; (2) mature technology that has already demonstrated long-term operation feasibility; (3) commercial large-scale capacity units; and (4) tolerance to raw feed water, thus complex water purification systems are not required.

However, in contrast to these advantages, there are several major limitations which can be summarized as follows: (1) low partial load range; (2) low operating current density partial; and (3) low operating pressure [27]. In addition, the use of asbestos as a separator diaphragm between the anode and cathode compartments raises health concerns related to the toxicity of the asbestos, which mandates finding alternative materials. Another issue related to the use of the porous separator diaphragm is that it does not completely prevent the product gases from penetrating through to the opposite gas compartment, which reduces hydrogen purity, electrolyzer efficiency, and safety. This issue is more persistent at low load operating conditions, potentially leading to a fast increase of hydrogen to oxygen concentration approaching the explosion lower limit of 4 mol.% H<sub>2</sub>. Furthermore, in the gap-cell design, the electrodes are installed such that they sandwich the separator at a few millimeters' gap within which the product hydrogen and oxygen evolve at their respective electrode. The evolution of these gases depends on the applied current density thus, at a higher current density, a higher gas bubble rate creates a continuous gas film which becomes very resistive and limits the electrolyte conductivity. Therefore, in most practical applications, the maximum operating current density is about 700 mA cm<sup>-2</sup>. Finally, the liquid electrolyte limits the high-pressure operation and contains the electrolyzer geometry configuration.

#### **2.4.2. Proton Exchange Membrane Electrolysis**

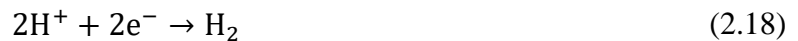
Proton exchange membrane (PEM) electrolyzers are considered one of the most promising hydrogen production technologies. A PEM electrolysis cell consists of two electrodes that sandwich a proton conducting electrolyte (as the name indicates). These three components of the anode, electrolyte, and cathode are assembled into a single unit known as a membrane electrode assembly (MEA). PEM electrolyzers are also known as solid polymer electrolyzers (SPE) since a solid electrolyte is used.

Fig. 2.18 shows the structure, polarity, and species movement direction of a PEM electrolysis cell. The operating temperature of PEM electrolyzers is in the range of 25–90°C. The pure water to be electrolyzed is supplied to the PEM electrolysis cell such that the MEA is entirely submerged. Thus, the polymer electrolyte allows proton mobility from one electrode–electrolyte interface to another.



**Figure 2.18 Schematic representation of a Proton Exchange Membrane (PEM) electrolyzer.**

Upon application of a DC to the electrode terminals, an internal potential is developed, causing hydrogen protons to flow through the electrolyte from the anode-electrolyte interface to the cathode-electrolyte interface while an opposite balancing electron flow develops from the DC source to the cathode, where these electrons eventually combine with the hydrogen protons to produce hydrogen. The half-cell reaction for the cathode side can be written as:



For the anode side, feed water is oxidized into hydrogen ions, oxygen, and electrons where the released electrons flow through the anode to the DC source and the hydrogen ions transfer to the cathode through the PEM electrolyte. The anode half-cell reaction can be written as:



Thus, the overall reaction is given as:



The rise of the PEM water electrolyzer dates back to the 1960s, following the development of proton-conducting acid polymers, including mainly perfluoro sulfonic acid polymer

among which is the well commercially established NAFION<sup>®</sup>. The structural formula of the NAFION<sup>®</sup> membrane is shown in Fig. 2.19.

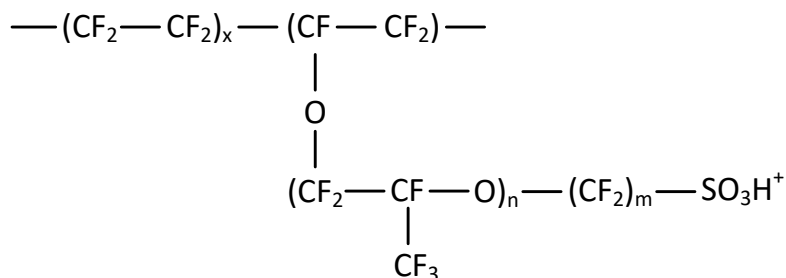


**Figure 2.19** Chemical structure of NAFION<sup>®</sup> membrane.

The sulfonic acid groups in the polymeric structure make the electrolyte acidity very high, such that only a noble metal catalyst, e.g., Pt, is able to sustain such an environment. Therefore, a noble catalyst requirement is the major contributor that increases PEM electrolyzer capital cost. For the membrane to be ionic conductive, it must be wet. Furthermore, backward penetration of oxygen molecules may occur, which accounts for about 5% electric current consumption. PEM electrolyzers are currently viewed as the safest and the most promising hydrogen production technology for the near future.

A typical PEM electrolyzer consists of a membrane electrolyte and two electrodes. The proton conducting electrolyte is an essential part of a PEM electrolyzer and, by the introduction of this electrolyte, a PEM fuel cell first existed. Sulfonated polystyrene was initially used but, as previously mentioned, it was replaced by perfluorinated phosphonic acid copolymers in order to enhance electrolyte chemical stability and improve overall cell performance. NAFION (the chemical structure is shown in Fig. 2.16), which is currently produced by DuPont de Nemours Co., is considered the most widely-accepted membrane. These membranes are perfluorinated membranes and fabricated into thin solid films (about 20–50 μm), thus the internal ion movement resistance is significantly reduced. In terms of electrodes, they are typically fabricated of two distinct layers: the first in contact with an electrolyte made of an approximately 5–50 μm porous layer coated with a catalyst while the second is the backing layer or what may be called a gas-diffusion layer, which is usually thicker (about 100–300 μm) to support the assembly (MEA) structure. The MEA is produced by hot pressing the two electrodes into the membrane such that the catalyst layers bond to the membrane.

The bipolar PEM electrolyzer configuration is a widely adapted design for stacking electrolysis cells. The bipolar plates are made of electrically conductive material which has one or two sides facing the MEA on which flow channels are grooved or milled to allow for a gas-water mixture to flow into and out of the stack. The bipolar plates also function as electrical current distributors and MEA mechanical supporters. The bipolar plates in a PEM electrolyzer stack are shown in Fig. 2.14. To achieve the required hydrogen production capacity by an electrolyzer unit, numerous electrolysis cells, comprised of MEA, are placed between two bipolar plates, thus the cells are in series connection. Parallel connection is also possible, based on the specific design requirements and the input power's voltage and current. The currently popular bipolar plate material is graphite as it has a sufficient electric conductivity and can withstand electrode operating conditions. However, thick plates may be required to provide the necessary MEA support. As shown in Fig. 2.20, a repeating electrolysis cell unit, composed of MEA and two bipolar plates, makes a stack, based on the number of included units. Since the thickness of the MEA is very small (usually less than 1 mm), and the bipolar plates are much thicker, the latter make up as much as 80% of the stack mass and subsequently share as much as 60% of the stack capital cost [28]. Thus, although bipolar plates are considered a significant challenge, they are expected to offer numerous potential improvements in PEM electrolyzer technology.

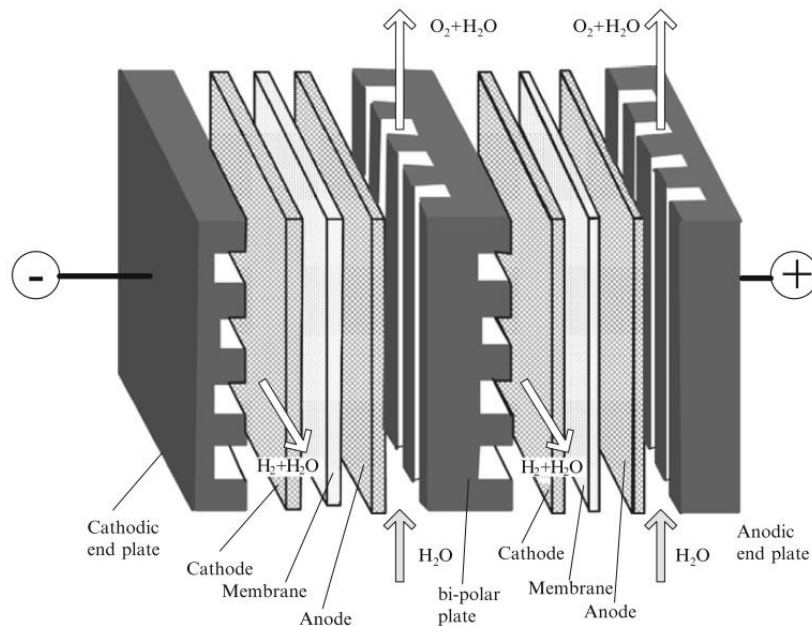


**Figure 2.20 Schematic representation of bipolar plate design for a PEM electrolyzer stack [29].**

The introduction of the solid membrane has resulted in numerous advantages among which is the ability to obtain higher performance due to the reduced electrolyte thickness. Furthermore, when compared with alkaline electrolyzers, PEM electrolytes eliminate the use of the corrosive liquid electrolytes and allow for more design compactness and orientation flexibility. The manufacturing processes are also much simpler. The electrolyzer operating pressure becomes higher, thus higher produced gas pressure can be possible, eliminating the need for an external unit for hydrogen compression. Since the membrane acidity is a result of the sulfonic acid groups attached to the polymer chain structure (as presented in Fig. 2.19), which is fixed upon the manufacturing of the membrane, the electrolyte concentration is independent of operating conditions and does not reduce by extended operating hours or rate of hydrogen production. This characteristic limits the need for regular maintenance of PEM electrolyzers, especially compared with alkaline electrolyzers. Another merit of PEM electrolyzers is that the low operating temperature significantly reduces the startup time, hence offering an instantaneous hydrogen production which makes this technology a promising solution for storing energy produced from renewable energy sources in the form of hydrogen. Thus, PEM electrolyzers can accommodate the intermittent nature of renewable energy resources.

**Table 2.3 Comparison between alkaline and PEM electrolyzers [27].**

Specifications	Alkaline electrolyzer	PEM electrolyzer
Operating temperature (°C)	60 – 80	50 – 80
Operating pressure (bar)	<30	<30
Current density (mA cm <sup>-2</sup> )	0.2 – 0.4	0.6 – 2.0
Cell potential (V)	1.8 – 2.4	1.8 – 2.2
Power density (mW cm <sup>-2</sup> )	<1	<4.4
Voltage efficiency based on HHV (%)	62 – 82	67 – 82
Specific energy consumption: stack (kWh Nm <sup>-3</sup> )	4.2 – 5.9	4.2 – 5.9
Specific energy consumption: electrolyzer system (kWh Nm <sup>-3</sup> )	4.5 – 7.0	4.5 – 7.5
Lower partial load range (%)	20 – 40	0 – 10
Cell area (m <sup>2</sup> )	>4	<0.03
Hydrogen production rate: Stack/System (Nm <sup>3</sup> h <sup>-1</sup> )	<760	<10
Stack lifetime (h)	<90,000	<20,000
System lifetime (y)	20 – 30	10 – 20
Degradation rate (μV h <sup>-1</sup> )	<3	<14

From a contrary perspective, the high acidity of the electrolytes, along with the low operating temperature, mandates the use of noble metals, such as Pt, which makes the PEM electrolyzer an expensive technology. In addition, polymer membrane conductivity depends on humidity conditions. Therefore, when the membrane is entirely humidified, it is conductive. However, conductivity decreases when the membrane dries, and therefore it is unstable at high operating temperatures. Local heating may develop as a result of Joule heating. These issues limit the lifetime of the membrane and subsequently the electrolyzer. As the two low-temperature electrolysis hydrogen production technologies, a comparison between alkaline and PEM electrolyzers is presented in Table 2.3.

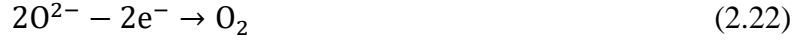
### 2.4.3. Solid Oxide Electrolysis

Compared with other electrolyzer technologies, the solid oxide electrolyzer is the most recent technology. Nevertheless, the solid oxide electrolyzer theoretically has the highest conversion efficiency in terms of total input energy or electrical energy. Therefore, ambitious efforts have been dedicated to bringing this technology to market.

Solid oxide electrolysis takes place at high temperatures in the range of 500–1000°C. A high temperature is required for the oxygen ion electrolyte to reach a practical conductivity. The solid oxide cell electrolyte is made of a dense ceramic layer fabricated of materials such as the commonly used yttria-stabilized zirconia (YSZ). The electrolyte is positioned between two electrodes: an oxygen electrode, which is the anode electrode with respect to the electrolysis process, and a hydrogen electrode, which is the cathode electrode. The typical oxygen electrode is fabricated from strontium-doped lanthanum (LSM) while the cathode is made of nickel/yttria-stabilized zirconia (Ni/YSZ) cermet. Upon connecting the DC power source to the solid oxide electrode terminals, the water vapor, fed to the cathode side, is reduced to hydrogen and oxygen ion by electron consumption, as shown in the following half-cell reaction:



The oxygen ions  $\text{O}^{2-}$ , produced at the cathode side, migrate through the electrolyte to the anode side, creating an internal balancing ion current whereas, at the anode, oxygen ions are oxidized, releasing electrons and forming oxygen, as shown in the following half-cell reaction:



A schematic representation of the operating principle of the solid oxide electrolysis cell is shown in Fig. 2.21. The figure also shows a schematic representation of the electrodes' porous structure that allows reactants and product gases to permeate to the reaction sites. These reactions, at the microscopic level, occur at the triple phase boundary (TPB), which is where electrons, ions, and reactant gas intersect. At the TPB, electrolyte and catalyst particles are connected and able to electrochemically interact with the gas reactants. Therefore, the performance and size of an electrolysis cell depend on the active cell area, which in turn depends on the total area of TPBs.

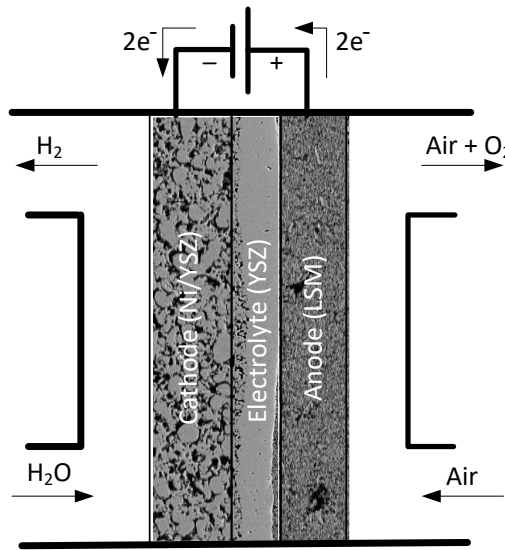


**Figure 2.21 Schematic representation of SOEC operating principle and electrode arrangement.**

Hydrogen leaves the cathode in a mixture with residual steam molecules that have not been utilized by the reaction. This mixture is then separated in order to produce pure hydrogen and recycle the remaining water to the system. At the anode side, oxygen is produced, and if no sweeping air is used, then pure oxygen is the product. However, in practice, such as high oxidizing conditions (of pure oxygen and high temperature) are avoided to prevent electrolysis component corrosion and any subsequent short-term failure. The practical operating current density is usually in the range of 0.5–0.7 A cm<sup>-2</sup>, although some experimental studies investigated as high as 2 A cm<sup>-2</sup>. The operating cell potential is in the range of 1.1–1.6 V.

Electrolyte conductivity, which is a function of temperature, significantly reduces at low operating temperatures (below 600°C) [30]. Nevertheless, YSZ (the most widely accepted electrolyte material) has a higher ohmic resistance ( $\sim 30 \Omega \text{ cm}$ ) than both an alkaline solution and proton exchange membrane even at as high a temperature as 900–1000°C. Therefore, and in an effort to reduce the electrolysis cell operating temperature, a thin electrolyte layer (as low as 10–50  $\mu\text{m}$ ) has been fabricated to optimize the tradeoff between cell performance and operating temperature. However, the positive side of the high operating temperature of solid oxide electrolyzers is that, at such a high temperature, the electrochemical kinetics is high and thus no expensive catalyst materials are required. Some precious metals, such as platinum, gold or silver, are still in use as interconnect materials for current collection and distribution within the electrodes as they can withstand a high temperature and electrode environment.

Three electrolyte-electrode assemblies are possible, based on the supporting substrate that is usually made thicker to provide support to the assembly structure. Accordingly, these three assembly configurations are: (1) electrolyte supported; (2) anode supported; or (3) cathode supported electrolysis cell. However, due to the previously explained electrolyte resistance, the first option is avoided in most designs. The typical material used for SOCs electrolyte is YSZ is usually composed of zirconium oxide ( $\text{ZrO}_2$ ) doped with 8–10 mol.% yttrium oxide ( $\text{Y}_2\text{O}_3$ ).

Apart from a high operating temperature, solid oxide electrolyzers are characterized, in comparison with low-temperature electrolyzers, by the fact that all the cell components are solids, which grants them excellent design flexibility. As a consequence, more cell designs and geometries are produced. As an example, a tubular solid oxide electrolysis cell was fabricated and tested as early as the 1970s, by Dornier Systems Co. [25]. A tubular electrolysis cell is composed of a supporting porous tube with one closed end. On this supporting tube, the anode, the electrolyte, and the cathode are painted as successive layers. The electrode terminals, the current distributing interconnects, are also connected to a DC source. Thus, one gas (sweeping air) can be blown through the tube's open end where it eventually permeates the porous structure to the internal electrode while the other gas (steam) is arranged to flow over the external electrode.

In addition to a tubular design, solid oxide electrolysis cells are produced in planar cell structure. The tubular design is considered more mature compared with other designs. However, a planar cell design is currently being extensively pursued, due to the simple manufacturing and installation procedures.

An outstanding advantage of SOEs is their higher conversion efficiency compared with low-temperature electrolyzers. SOEs efficiency can theoretically reach over 75% but electrical to hydrogen conversion efficiency can be as high as 100% [31]. Experimental investigations showed a maximum efficiency of 52.7% achieved by a 30-cell stack [32]. Furthermore, solid oxide electrolyzers allow for more cell designs due to the all solid components. The high temperature offers great advantage from both thermodynamic and electrochemical perspectives as, thermodynamically, the higher operating temperature offers higher energy efficiency and greater integration opportunities due to the high energy quality that may be produced as a byproduct. From an electrochemical perspective, the high operating temperature eliminates the need for the expensive catalyst materials that increase cell cost. Also, solid oxide electrolysis cells can electrolyze CO<sub>2</sub> molecules to produce CO and electricity. This process can be conducted separately or in the same electrolysis cell for steam and CO<sub>2</sub> in what is known as co-electrolysis, which recently received considerable attention from numerous researchers.

Conversely, numerous challenges limit the commercialization of solid oxide electrolyzers. The first challenge is the high operating temperature, which limits the possible material options to be used in the cell component manufacturing and assembly. This has led to increasing the cost of SOEs due to their requirement for materials and connecting wires that can withstand such high temperatures. Furthermore, the cell components are vulnerable to corrosion, especially at the anode electrode where oxygen gas evolves at the cells' high operating temperature. The issue of degradation rate is also a vital factor, especially at high steam content rate, thus a small percentage of hydrogen (~10 vol.%) is fed with the steam intake to eliminate or at least reduce the cathode oxidation rate. Another challenge is the sealing mechanism of a SOE stack, which depends on glass and glass-based ceramics. These materials may not endure the thermal cyclic nature of the stack operation.

The long-term performance and cell durability of electrolyzers are crucial factors that must demonstrate accepted reliability in order to attract large-scale industrial investments. Degradation rates and long-term studies have shown that current state-of-the-art cells encounter degradation rates between 15–20 %/1000 h of stack operation at temperatures between 800–900°C [33]. Some studies reported lower degradation rates as low as 1.7%/1000 h for individual cells (e.g., [34]), which is comparable with that which occurs in solid oxide fuel cells. However, stacks encounter higher rates due to interconnect degradation and pollution from tubing and sealing components.

The topic of high temperature electrolysis will be discussed in further detail in the literature review in Chapter 3.

## **2.5. Solar Hydrogen Production**

Solar hydrogen production falls under the subject of solar fuels, which is one of three active solar energy research themes: solar photovoltaic (PV) cells; solar thermal plants; and solar fuels. Solar hydrogen production achieves a sustainable pathway to hydrogen, therefore the development of this technology is expected to significantly impact the future of the economy, the environment, and global energy security.

Solar hydrogen production includes various methods in which solar energy is used as a primary resource to directly or indirectly derive hydrogen from hydrocarbon, or non-hydrocarbon compounds such as natural gas or water. Three primary conversion processes are commonly involved in solar hydrogen production technologies: thermochemical, photochemical, and electrochemical [35]. In all of these processes, solar energy is the primary driving energy, which may be utilized as direct light, absorbed heat, or electricity as the final solar cell product. Fig. 2.22 illustrates the various pathways to hydrogen, utilizing solar energy in both hydrocarbon- and water-based methods.

### **2.5.1. Concentrated Solar Systems**

Solar tower technology is gaining more acceptance as a cost-effective solar energy harvesting method, especially in large-scale applications [36]. It has been shown that, at locations with solar radiation of  $\sim 2 \text{ MWh/m}^2/\text{yr}$ , solar tower technology is approaching commercial viability [37].

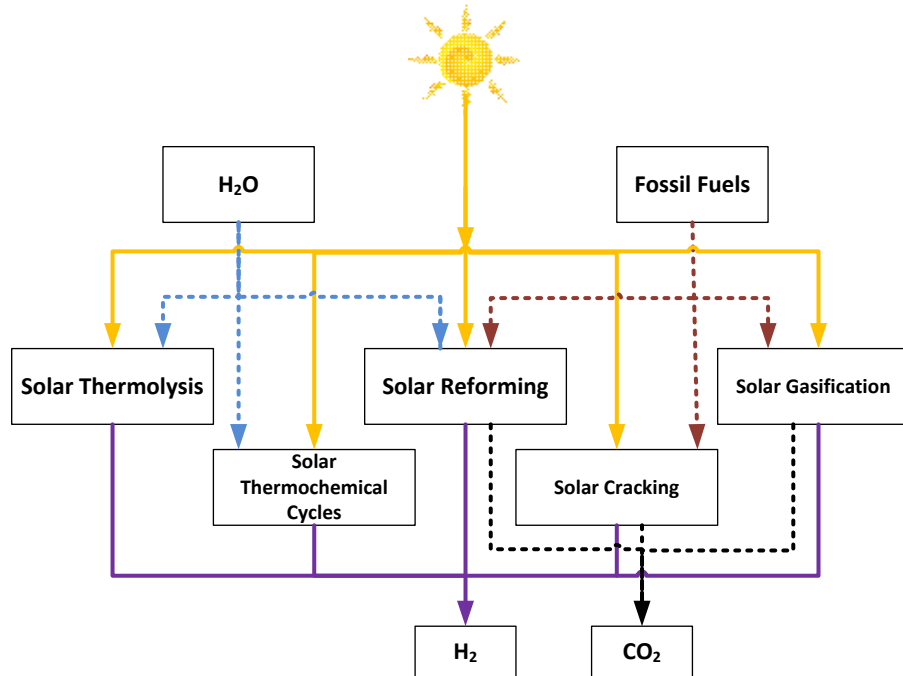


**Figure 2.22 Schematic diagram of solar hydrogen production methods, including feedstock and by-products (modified from [35]).**

This optimistic assessment is based on three decades of extensive research and development efforts, leading to the successful commissioning and operation of over 13 demonstration plants with thermal power as large as 30 MW and an expected lifetime of 45 years. Moreover, the US Department of Energy (DoE) has adopted the integration of solar tower technology with thermochemical water splitting processes to achieve a hydrogen production goal of \$2–3/kg by 2025 [38]. The use of concentrated solar energy as a primary energy source to produce low-cost hydrogen from electrolysis has been discussed by McConnel [39], where the aspects of electricity pricing, solar concentration, and conversion efficiencies are outlined.

The potential of integrating high temperature SOEs into solar tower technology has been recently investigated by AlZahrani et al. [40], who proposed an integrated power plant to produce power, heat, and hydrogen. The energy and exergy performance of the integrated system examined the case of hydrogen production utilizing locally produced power. Furthermore, the impact of using high temperature Thermal Energy Storage (TES) on the plant is highlighted through the assessment of energy and exergy efficiencies at different modes of operation.

### 2.5.2. Photovoltaic Systems

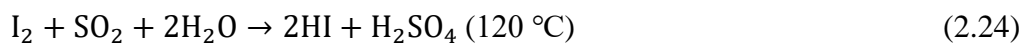
Solar hydrogen can also be produced using PV cells as a primary energy source where the generated electricity is utilized in a low-temperature electrolyzer. However, the main challenge of such a system is a limited solar-to-hydrogen conversion efficiency of about 13%, which is estimated considering a product of the efficiencies of commercial PV cells of 19% and an electrolyzer of 70%. Therefore, researchers pursued different approaches to maximize solar energy utilization. As an example, Zamfirescu et al. [41] examined utilizing an optical system to split sunlight into a high, middle, and low energy spectrum based on wavelength range. The high energy spectrum is used directly to generate hydrogen in a photolysis process, while the middle spectrum is used for electricity generation in a PV system, and the low energy is utilized in the form of heat to drive a Rankine power cycle.

## 2.6. Thermochemical Cycles

In a thermochemical hydrogen production cycle, water is split into hydrogen and oxygen through a sequence of physical and chemical processes, where chemical compounds involved in the intermediate processes are internally recycled. Thereby, thermochemical cycles require heat as primary energy input and only consume water as feedstock while producing hydrogen and oxygen without GHG emissions [42]. These cycles require a heat source temperature in the range of 500–1100°C. Thermochemical cycles were first suggested in the 1960s to utilize heat instead of electricity to produce hydrogen from water as a cheaper alternative to water electrolysis [43]. Over 100 cycles have been theoretically proposed to produce hydrogen, but only a few cycles were considered to be practically realistic and further investigated. These selected cycles have been under active research, targeting experimental demonstration, upscaling, and system integration. The following section offers a brief description of the cycles presented as promising in the literature.

### 2.6.1. Sulfur-Iodine (S-I) Cycle

The S-I cycle, which has been the focus of many research institutions, was demonstrated at a pilot plant scale and achieved a hydrogen production capacity of 30 L h<sup>-1</sup>. The S-I cycle is comprised of the following three reactions:





The maximum cycle temperature is 840°C, which is one of the major limitations of this cycle in addition to the corrosive nature of the intermediate compounds. Nevertheless, this cycle has numerous advantages, such as all reactants are fluids which facilitates process integration. The S-I cycle is capable of producing hydrogen at high pressures up to 5 MPa, thus the subsequent hydrogen compression stage is eliminated. It is estimated that the S-I cycle achieves as high as 44% thermal efficiency if powered by a heat source temperature of 950°C [44].

### 2.6.2. Hybrid Sulfur Cycle

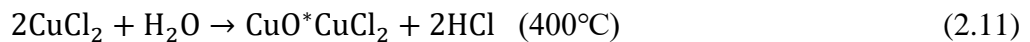
The hybrid sulfur cycle is a reduced version of the S-I cycle where an electrolysis step is introduced, resulting in the following two reactions:



This cycle, proposed and investigated during the 1970s by the Westinghouse Electric Co., is referred to by many as the Westinghouse cycle. Many research institutions, including the US DoE, are currently pursuing further development of both the S-I and hybrid sulfur cycles as promising hydrogen production technologies.

### 2.6.3. Copper-Chlorine (Cu-Cl) Cycle

The Cu-Cl cycle is characterized by its relatively low maximum temperature of 500°C compared with other cycles. The chemical reactions that take place in the Cu-Cl cycle are given by



This cycle is currently under active research as a promising hydrogen production method. As an example, significant research efforts have been dedicated at the University of Ontario Institute of Technology to demonstrate this cycle and investigate the integration potential of the Cu-Cl cycle with Canada's generation IV reactor [45]–[47]. It was reported that this integration could produce hydrogen at an overall net energy conversion efficiency of 30%, while electric efficiency can reach up to 42% [48].

## **2.7. Other Hydrogen Production Methods**

In this section, the different methods for generating hydrogen are discussed. Some of these methods are well-established while others are still in the research stage and feature in the more recent literature. However, active research on these new methods indicates future potential that may impact hydrogen production.

### **2.7.1. Photobiological Hydrogen Production**

In photobiological hydrogen production, a photosynthesis process takes place in which two types of microbes, oxygenic and anoxygenic, convert water to hydrogen and oxygen utilizing sunlight and some organic substances. The following reactions describe this process. The photosynthesis reaction to yield hydrogen ions is given by:



Moreover, the hydrogen ion reduction reaction to produce hydrogen is as follows:



Micro-organisms, such as green algae and cyanobacteria, are currently being studied for the long-term goal that these processes can be a future sustainable hydrogen production method. Despite being in its early stages, low capital cost makes this method attractive to many.

## **2.8. Types of Fuel Cell**

A fuel cell is an electrochemical device that can directly convert the chemical energy of fuel to electricity. Due to the direct conversion process, fuel cells have a high conversion efficiency compared with heat engines such as internal combustion engines. Though fuel

cells have some similarities with batteries, there are major differences. As in the case of a battery, the chemical reactants are stored inside the battery, thus the battery life is significantly dependent on the volume of stored reactants. However, in the case of a fuel cell, the cell structure only contains the major components of an electrolyte, an anode, and a cathode, and all reactants are supplied to the cell while in operation. Accordingly, as long as the reactants are being supplied, the fuel cell continues producing electricity. Since the fuel cell lifetime mainly depends on the electrode and electrolyte degradation rate, the fuel cells retain a longer lifetime compared with batteries. Growth of the fuel cell global market between 2008 and 2013 has been estimated to have been as high as 400%, of which about 80% was fuel cell installations for stationary applications such as micro-cogeneration and remote power stations [23].

Fuel cells are commonly classified according to electrolyte material operating temperature. A brief description of the various fuel cells types and their operating conditions are provided in the following sections.

### **2.8.1. Alkaline Fuel Cell (AFC)**

The electrolyte material used in alkaline fuel cells is a potassium hydroxide (KOH) water solution and molten potassium hydroxide with a thickness of about 0.5 mm [28]. The operating temperature and pressure of alkaline fuel cells are in the range of 60–80°C and 100–300 kPa, respectively. The primary fuel is hydrogen, and the cell is poisoned by CO<sub>2</sub>, SO<sub>2</sub>, H<sub>2</sub>S, and Hg species. The cell potential is ~ 0.85 V and operates at current densities in the range of 400–470 mA cm<sup>-2</sup>.

### **2.8.2. Proton Exchange Membrane Fuel Cell (PEMFC)**

PEM fuel cells operate at low temperatures ~ 80°C while the operating pressure can be as high as 300 kPa. An ions-semipermeable-membrane, e.g., Nafion, is used in thicknesses of 50–175 μm as an electrolyte. The poisoning species are CO and H<sub>2</sub>S, and the operating cell potential and current densities are about 0.65 V and 300–500 mA cm<sup>-2</sup>, respectively.

### **2.8.3. Phosphoric Acid Fuel Cell (PAFC)**

The electrodes are fabricated in the form of paper or cloth from graphite-carbon materials. For the electrolyte, Phosphoric acid (H<sub>3</sub>PO<sub>4</sub>) is used with a minimum concentration of 95%.

The operating temperature and pressure of PAFCs is in the range of 170–210°C and 100–800 kPa, respectively. The operating cell potential is about 0.65 V at a current density in the range of 150–350 mA cm<sup>-2</sup>. The poisoning species are sulfur compounds and carbon monoxide.

#### **2.8.4. Molten Carbonate Fuel Cell (MCFC)**

MCFCs rely on natural gas or coal-derived syngas as a primary fuel. The electrolyte is made of a matrix of LiAlO<sub>2</sub>. The typical operating temperature of MCFC is 600–700°C. The nominal cell potential is around 0.75 V, and the current density is 100–200 mA cm<sup>-2</sup>.

#### **2.8.5. Solid Oxide Fuel Cell (SOFC)**

SOFCs have the highest tolerance to fuel impurities compared to other types of fuel cells, which is mainly attributed to the high operating temperature of about 1000°C. The primary fuels for SOFCs are hydrogen and carbon monoxide, which can react electrochemically to produce electricity without any pretreatment process. However, other fuels such as coal-derived syngas, natural gas, and carbon dioxide are also used but either reforming or shifting reactions must occur internally in order to yield hydrogen or carbon monoxide. Furthermore, SOFCs are characterized by their all-solid-state components, which has led to the development of different cell configurations, such as tubular, monolithic, and planar designs. The typical SOFC potential is about 0.75 V at current densities of 160 mA cm<sup>-2</sup> or higher. The material of SOCs will be further explained in Chapter 3 as part of the literature review of solid oxide cells.

## **Chapter 3: Literature Review**

In this chapter, the broad subject of Solid Oxide Cells (SOCs) is discussed in the context of the recent advances and progress of both fuel cell and electrolysis cell operating modes. However, despite the conventional materials and methods used in fabrication, more emphasis is given to electrolysis testing and operation for hydrogen production. Therefore, SOC materials, manufacturing, and modeling are reviewed. Furthermore, the testing and characterization methods are discussed with a focus on SOEC experimental studies.

Recent research activity in the direction of the developing a high temperature photoelectrochemical cell (PEC), is highlighted. This includes a conceptual description of the photoelectrochemical cell and the most promising semiconductors for light utilization in SOCs. The chapter concludes with a concise description of the research gap and the key contribution of this thesis.

Historically, the discovery of the solid oxide electrolyte in 1853 marks the dawn of the SOC. By the end of the 19th century, Nernst demonstrated the high conductivity of the (15YSZ) at elevated temperatures [49]. In 1905, the solid oxide fuel cell (SOFC) came into existence through the patent of Haber [50]. However, a major landmark in high-temperature water electrolysis hydrogen production was made through the initiation of the “HOT ELLY” project, which stands for High Temperature Electrolysis. Dornier initiated this project in 1975 [51], [52]. Several research institutions have launched similar programs to pursue hydrogen production using high temperature water electrolysis.

### **3.1. Thermal Analysis of Solid Oxide Electrolysis**

Thermodynamic analysis, including the energy and exergy analyses of high temperature electrolysis, is an active research area. Due to the high temperature requirement, many studies investigated the integration of high temperature electrolysis with other high temperature renewable resources, such as solar and nuclear plants, for hydrogen production. In these studies, a common motivation towards using high temperature electrolysis was the high conversion efficiency that these systems achieve while producing carbon-free hydrogen. The produced hydrogen can then be sold to end-users, fed to a chemical process or stored as an energy carrier.

### **3.1.1. Solar Hydrogen Production Applications**

Solar tower technology is one of the most promising venues for high temperature electrolysis integration as this technology offers a high temperature which enables hydrogen production at a conversion efficiency of about 86% [36].

Arashi et al. [53] experimentally examined solar hydrogen production using a tubular 8YSZ with two porous Pt electrodes placed in the focal point of a solar concentrator. The experiment was conducted at a temperature of 1000°C where the conversion efficiency, defined as the ratio of the produced hydrogen energy to the consumed electrical power, is estimated to reach 71%. Others have considered solar energy as an energy source for high temperature SOE integration. As an example, Zhang et al. [54] proposed a solar-driven SOE for hydrogen production where a solar concentrating system is optimized for providing the necessary heat and power for steam electrolysis in SOE. Similarly, Houaijia et al. [55], who studied hydrogen production using SOE powered by an 80 MW<sub>th</sub> solar concentrating power plant, reported a solar-to-hydrogen conversion efficiency of 18%.

### **3.1.2. Nuclear Hydrogen Production Applications**

In particular, during off-peak hours, the surplus electricity generated by nuclear power plants can be used to produce hydrogen at a relatively competitive cost. Therefore, several research and industrial institutions have contributed to the advancement of high temperature SOEC research and development. For example, the Idaho National Laboratory conducted numerous theoretical and experimental studies as part of an ongoing effort to integrate high temperature electrolysis with nuclear power. For instance, some studies investigated the thermodynamic performance of SOE considering integration with high temperature gas-cooled reactors (HTGRs) to provide power and heat at temperatures in the range of 500–900°C, utilizing HTGR outlet temperatures of up to 750–950°C, and at pressures in the range of 1–5 MPa [56], [57]. The reported overall system thermal efficiency is in the range of 48–59%. Bo et al. [58] reported on research in China into hydrogen production using high temperature electrolysis coupled with HTGRs as an efficient means of hydrogen production. These integrated nuclear-powered hydrogen production plants are justified through the potential utilization of off-peak low price

electricity production while, during peak power demand, electricity can be directly connected to the grid to meet high power demands.

### **3.1.3. Modeling of Solid Oxide Electrolysis**

Motivated by the rigorous results provided by well-established SOFC models, e.g., [59], numerous SOEC modeling studies were published to predict SOEC performance in a hydrogen production process. Various models have been developed, implementing thermodynamics, electrochemistry, and heat and mass transfer laws to, firstly, enhance overall understanding of the detailed sub-processes that influence SOEC performance and, secondly, to explore the different opportunities that may arise through the optimization of the operating and design conditions. Furthermore, the knowledge gained through the numerical studies is expected to guide the research into the fabrication processes of SOEC for better performance and durability.

Ni et al. [60] conducted a parametric analysis of SOEC. In their study, a detailed model was developed through which activation, ohmic, and concentration polarizations were evaluated over a range of operating current density levels for different cell operating temperatures and pressures. The effects of changes in electrode porosity, as well as reactant concentrations, were also examined. The reported results showed improved electric efficiency with operation at higher temperatures and steam inlet concentration. In another study [61], the authors assessed the performance of SOEC as part of a hydrogen production plant in terms of energy and exergy efficiencies. The variations in both energy and exergy efficiencies over a range of operating conditions were evaluated. Zhang et al. [62] studied three different energy efficiency expressions that are commonly used in the literature to determine the performance of SOECs. However, considering the variations in operating conditions that a system may experience, it is deemed difficult to propose a generalized efficiency expression; rather, the concept of hydrogen energy output over energy input should be followed. Nieminen et al. [63] thermodynamically modeled a SOE to compare its performance with a low-temperature proton exchange membrane (PEM) electrolyzer.

Laurencin et al. [64] investigated the parametric performance of a SOE stack using a two-dimensional multi-physics model. It was found that the anode concentration overpotentials were limited regardless of the variation in possible operating conditions. However, the

cathode concentration overpotentials showed more sensitivity at high current density, in particular in the case of the cathode supported cell. Hawkes et al. [65] developed a three dimensional model for a stack consisting of 60 planar SOECs. The model was based on the SOFC model provided by Fluent Computational Fluid Dynamic (CFD) software which includes a coupled code for mass, momentum, energy, species and transport equations, in addition to chemical reactions and electric current distribution. This model was adjusted to solve all the required conservation and electrochemical equations for the electrolysis mode. The results show the detailed distribution of temperature and gas compositions over the different parts of the stack. In addition, the Nernst and operating potential profiles were predicted for various operating conditions.

A high stack pressure operation is preferred for meeting high-pressure hydrogen gas delivery. Thus, the after-production pressurization stage can be eliminated to improve overall plant efficiency and reduce production cost. In this regard, high-pressure operation attracted the attention of many researchers who have considered the effect of the operating pressure on performance at the levels of both a single cell and a stack. At the cell, the scope was primarily to examine the kinetics of different electrode-electrolyte compositions and durability while, at the stack level, other issues such as sealing, degradation rate, and system optimization were discussed. A high-pressure operation was investigated by Henke et al. [66]. Todd et al. [67] theoretically determined the performance of SOEC at extreme high pressure conditions reaching up to 100 MPa. They concluded that electrolysis cell pressurization reduces the required energy inputs (work and heat). Furthermore, Cacciuttolo et al. [68] used a two-dimensional model in addition to three reference electrodes in an experiment to evaluate the impact of increasing the operating pressure on a SOEC with a composition of Ni<sub>8</sub>YSZ/3YSZ/LSCF. The experimental results are used to validate the model which has been used for extended parametric analysis. The J-V and the EIS curves are reported at various pressures. At high current density, the high pressure operation showed a positive impact on overall cell performance. No major negative impact was noted on the LSCF oxygen electrode.

O'Brien et al. [69] reported one of the earliest high-pressure tests in which a 10-cell stack was examined under pressures of up to 1.5 MPa. It was claimed that the test had confirmed

an anticipated improvement in the stack Open Cell Voltage (OCV). Furthermore, a reduction in the Area Specific Resistance (ASR) was observed and attributed to the enhanced gas diffusion caused by high pressure. Similarly, stack performance under high-pressure conditions was tested by Jensen et al. [70] in an attempt to increase power density and reduce system auxiliaries. The tested stack was made up of 11 planar cells and tested at pressures ranging from 0.12–2.5 MPa. The results show an improvement in the OCV and reaction kinetics with high pressure. In another study Jensen et al. [71] reported an energy efficiency improvement in the stack performance from 76.0% to 81.5% as a result of increasing pressure from 1–20 bar.

### **3.2. Materials of Solid Oxide Cells**

SOCs represent the conventional cell structure and compositions that include both fuel and electrolysis cells that, in principle may operate in fuel or electrolysis cell modes. SOC are made of three major components: dense solid electrolyte ceramics and two porous electrodes that sandwich the electrolyte. From a material perspective, SOC can operate in both fuel cell and electrolysis cell modes, with some material-related variations in the cells performance and durability.

A detailed review on each component, focusing on the most widely used materials, is given in the following sections while a comprehensive list of the materials that have been proposed or tested in the literature is presented in Table 3.1.

The solid-state nature of the SOC supports the great flexibility that SOC offer. Thus, three main cell configurations are currently available: planar, tubular and monolithic. The manufacturability and the fabrication cost are critical factors in favoring one design over the other. Additionally, stacking and sealing of the cells are of primary importance. The planar cell design is characterized by high power density compared with the tubular cells. Therefore, planar cells are perceived to have more economic competitiveness potential due to the higher power production and lower material cost [72]. Nevertheless, tubular SOC are known for a short current path with lower interconnect losses. Tubular cells are considered a reliable power source, remarkably for stationary application where space is not a major constraint. In this thesis, emphasis is placed on planar design, which requires one of the electrodes to provide the mechanical strength to support the cell structure. As a

result, three cell designs are evolved: an anode supported cell, a cathode supported cell, and an electrolyte-supported cell. As an SOC active research area, each of these three designs comes with some pros and cons. The detailed fabrication processes and the challenges associated with the production of planar SOCs are reviewed by Mahmud et al. [72] while the environmental impact of planar SOC fabrication is examined by Karakoussis et al. [73].

**Table 3.1 Comprehensive list of SOC materials corresponding to the fuel electrode, electrolyte, and oxygen electrode (modified from [74]).**

Fuel Electrode		Electrolyte		Oxygen Electrode				
Nickel-based	NiO/YSZ	Zirconia-based	YSZ	Lanthanum-based	LSM			
	NiO/SSZ		SSZ		LSC			
	NiO/GDC		CaSZ		LSMC			
	Copper-based	NiO/SDC	Cerium-based		GDC	LCM		
		NiO/YDC			SDC	LSF		
Cu/CeO <sub>2</sub> /YSZ		YDC			LSCF			
Lanthanum-based		La <sub>1-x</sub> Sr <sub>x</sub> CrO <sub>3</sub>	Lanthanum-based		CDC	LSMC		
					CuO <sub>2</sub> /YSZ	LSMCr		
	Cu/YST	LSGMC			LCM			
	CuO <sub>2</sub> /CeO <sub>2</sub> /SDC	LSGMF			LSFN			
		LSGMCF			LNF			
Other materials	La <sub>1-x</sub> Sr <sub>x</sub> Cr <sub>1-y</sub> M <sub>y</sub> O <sub>3</sub>	Other materials	LaAlO <sub>3</sub>		LSCN			
			BCY		LBC			
			YSTh		LNC			
	YSHa		LSAF					
	Bismuth oxide-based		LSCNCu					
	Bismuth oxide-based Pyrochloro-res-based		LSFNCu					
Other materials	LST	Barium and strontium	Lanthanum-based	LNO				
				LAC	Pyrochloro-res-based Barium and strontium	GSC		
	CeO <sub>2</sub> /GDC					Barium and strontium	Gadolinium-based	GSM
				TiO <sub>2</sub> /YSZ	Praseodymium-based			PCM
								Cobalt-based
Platinum-based	PBC							
	SSC							
Ru/YSZ	Yttria-based	NSC						
		BSCCu						
				YSCF				
		YCCF						
		YBCu						

### 3.2.1. Electrolyte Materials

A typical SOC electrolyte material is yttria-stabilized zirconia (YSZ), composed of  $\text{ZrO}_2$  doped with 8–10 mol.%  $\text{Y}_2\text{O}_3$  making a dense ceramic layer. This layer can be thermally activated to allow for oxygen ionic conductivity. The flow of oxygen ions depends on vacant sites on the crystal lattice moving from one lattice to an adjacent one. In general, for any material to be considered as an electrolyte material, a set of requirements have to be satisfactorily met. These requirements are: (1) efficient ionic transport; (2) limited electronic conductivity; (3) high thermal and chemical stability; and (4) minimal thermal expansion mismatch with electrode materials. YSZ is currently the most widely accepted electrolyte material that seems to meet most of the requirements, with the one major limitation of a high operating temperature. This is due to the significant reduction in YSZ conductivity at low temperatures (below  $600^\circ\text{C}$ ). The YSZ electrolyte conductivity ( $\Omega\text{ cm}$ ) is given as a function of absolute temperature (K), by the following equation [30]:

$$\sigma = 0.00294 \exp\left(\frac{10350}{T}\right) \quad (3.1)$$

Thus, electrolyte ohmic resistance becomes so prohibitively high that a low-temperature operation is impossible unless YSZ is replaced with an alternative electrolyte material such as ceria fluorites and  $\text{LaGaO}_3$  perovskites. Nevertheless, YSZ has a higher ohmic resistance ( $\sim 30\ \Omega\text{ cm}$ ) than either an alkaline solution and a proton exchange membrane even at as a high-temperature as  $900\text{--}1000^\circ\text{C}$ . Therefore, and in an effort to reduce the operating temperature, thin electrolyte layers as low as  $10\text{--}50\ \mu\text{m}$  have been used in new cells.

Additionally, other dopants, such as  $\text{CaO}$ ,  $\text{MgO}$ , and  $\text{Sc}_2\text{O}_3$ , have been used. The persisting domination of YSZ, in spite of high temperature operation, is due to the following advantages: (1) the high conductivity for  $\text{O}_2$  partial pressure, ranging from  $1\text{--}10^{-20}\text{ atm}$ ; (2) low electronic leakage, (3) low reactant gas permeability; and (4) the very high chemical and thermal stability at both electrode environments.

### 3.2.2. Fuel Electrode Materials

The fuel electrode (cathode electrode in electrolysis) is made of Nickel (Ni), Zirconia (Zr) or a combination of Ni/YSZ cermet which is widely used with a composition of about 40 vol.% Ni/YSZ. This ratio is set to optimize the trade-off between the difference in

coefficient of the thermal expansion between the cathode and electrolyte and the electronic conductivity. Fuel electrode porosity varies with an average of 35%. Nickel functions as a catalyst as well as an electron conductor. The chemical and electrochemical heterogeneous reactions that occur within the electrode-electrolyte interface depend not only on the catalytic and conductance of the constituting materials but also on the electrode microstructure and the distribution of triple-phase boundaries (TPBs), which are electrochemically reactive sites. For an efficient fuel electrode performance, the TPBs have to be maximized for optimum mass transfer, and electronic and ionic conductivity. Thus, reactant gaseous species and electrons have better access to reaction sites, leading to a reduction in electrode activation and concentration polarizations. Another property to consider is the coefficient of thermal expansion (CTE) match with the cell electrolyte. Mismatch in the CTE between cell components is one of the primary causes of cell degradation and failure. Furthermore, in fuel-electrode supported cells, the fuel electrode is required to provide a structural support to the cell. More detailed literature on the selection process of fuel electrode material is provided in the review article by Shaikh et al. [75].

Numerous research studies have been conducted on fuel electrode material, fabrications, and performance characterization. Most of these studies target SOFC performance optimizations, while few consider the electrolysis mode of operating. For example, the oxidation of Ni to NiO during the electrolysis reaction is one of the major limitations of the Ni/YSZ fuel electrode.

### **3.2.3. Oxygen Electrode Materials**

An oxygen electrode is commonly fabricated of perovskite-structure oxides, notably strontium-doped manganite ( $\text{La}_{(1-x)}\text{Sr}_x\text{MnO}_3$ ,  $x = 0.1-0.15$ ) (LSM) and Lanthanum strontium cobalt ferrite (LSCF), in addition to many other compositions that have been identified for potential use as an oxygen electrode. These perovskites are made into a porous structure with high conductivity to allow for electron transfer to reaction sites and to reduce ohmic losses. The catalytic activity of this material is considered suitable for electrolysis. However, since it has a relatively higher coefficient of thermal expansion compared with electrolyte material, using multilayers with slightly different compositions

to reduce these expansion variations is required. To overcome these limitations, other materials have been proposed, including Lanthanum Strontium Ferrite (LSF) and Lanthanum Strontium Copper Ferrite (LSCuF). The effect of variation in oxygen partial pressure on the performance of composites of LSM/YSZ and LSM/SDC electrodes was experimentally investigated by Thomsen et al. [76] for a pressure range from 0.1 to as high as 10 MPa. Languna-Bercero et al. [77] tested LSCF and LSM as oxygen electrodes in Scandia and Ceria Stabilized Zirconia (10Sc1CeSZ), with the fuel electrode maintained as Ni/YSZ, and at an operating temperature of 800°C and using 70% H<sub>2</sub>O. They reported that LSCF achieved lower polarization resistances. The measured ASR of LSCF was 0.79 Ω cm<sup>2</sup> where, in the case of LSM, it was 0.93 Ω cm<sup>2</sup>.

#### **3.2.4. Interconnect and Sealing Materials**

Despite the great advantage that SOC has over other low-temperature fuel and electrolysis cells where no precious catalyst materials are required, some precious metals, such as platinum, gold or silver, are still in use as interconnect materials for current collection and distribution within the electrodes as they can withstand a high temperature and electrode environment. Furthermore, the interconnect materials are necessary to satisfy the following requirements: (1) chemical and thermal stability under high temperature oxidizing/reducing conditions; (2) high electronic conductivity; (3) compatible CTE; and (4) high stability in processing environments. There has been a recent increase in alternative materials, such as nickel and stainless steel, which have been tested or proposed through research studies. For instance, Mori et al. [78] examined the use of SrTi<sub>1-x</sub>Co<sub>x</sub>O<sub>3</sub> perovskites ( $0 \leq x \leq 0.2$ ).

In regards to cells and stack sealing, glass is widely used, but researchers are actively investigating new alternatives due to the shortcomings of glass sealing, especially in applications which may require replacement of the cell component and reassembly.

### **3.3. Testing of Solid Oxide Electrolysis**

Despite the numerous studies dedicated to lab testing and experimental measurements of SOFC performance, which include some long-term degradation and durability records [79], less attention is given to the reverse operation of SOFCs. However, in the last decade, the interest in SOECs for hydrogen production has gained momentum as observed through

the number of studies dedicated to high temperature SOECs. One of the limitations that mandates further SOEC testing studies is the lack of standardized testing procedures, as indicated by researchers [79]. The development of a standard procedure will reduce any uncertainty of flawed results due to an ill procedure and will subsequently reduce discrepancies among different researchers.

Ebbesen et al. [80] tested a hydrogen electrode (Ni/YSZ) supported planar cell in an electrolysis mode for synthetic fuel production from steam and carbon dioxide. Different ratio combinations of a mixture of H<sub>2</sub>O, H<sub>2</sub>, and CO<sub>2</sub> were supplied to a Ni/YSZ electrode active area of 16 cm<sup>2</sup> at temperatures between 750–850°C. The current density-voltage (J-V) curves were then measured, in addition to the durability and characterization tests that were performed. The reported results showed a feasible operation of a Ni/YSZ electrode with these mixtures and also indicated a long-term degradation of 0.003–0.006 mV h<sup>-1</sup>, detected while operating at -0.25 A cm<sup>-2</sup>. Moreover, Brisse et al. [81] experimentally measured the performance of a SOEC consisting of Ni/YSZ as a hydrogen electrode, YSZ as an electrolyte, and LSM as an oxygen electrolyte. This study revealed a considerable influence in the change in absolute humidity, which may be attributed to the steam diffusion at the hydrogen electrode. The degradation rate over 160 hours of continuous operation was observed to be minimal. Zheng et al. [82] examined the performance degradation for three different oxygen electrodes of SOECs. The composition of the examined electrodes is LSM-YSZ, LSC-GDC, and LSCF-GDC with an active area of 63 cm<sup>2</sup> per cell. The experiment intended to investigate a large-scale application of SOECs. Delamination was reported around the steam and air inlets in the case of LSM and LSC. Agglomeration of Ni was also reported in the hydrogen electrodes of the LSM and LSCF cells, which led to a reduction in the active electrode area.

The use of electrochemical impedance spectroscopy (EIS) techniques in a SOEC analysis was reviewed by Nechache et al. [83] who explained EIS principles and demonstrated EIS characterization mechanisms. This review reported some EIS-based studies and analysis techniques that have been used to explain the degradation phenomena for a single electrode as well as for a cell or stack. It was also concluded that systematic EIS studies are needed in order to investigate the influence of the different operating parameters on SOEC

performance. Furthermore, comprehensive modeling of SOEC polarizations in terms of equivalent impedance was conducted by Shin et al. [84].

Li et al. [32] measured the performance of a single cell, as well as 2 and 30 cell stacks, and reported that conversion efficiencies varied between 16.1% up to 52.7%. Kim et al. [85] built and tested a SOEC-based electrolyzer stack and obtained a high electric-to-hydrogen conversion efficiency of about 97%.

Floriane et al. [86] tested a SOEC operating in transient and steady-state conditions. The reported results showed that no detrimental failure occurred over 600 hours of cyclic operation, which indicates the viability of operating a SOEC under on-off conditions. Laguna-Bercero et al. [87] measured the performance of a SOEC with electrodes of LSM/YSZ and LSCF. They also used the EIS method to characterize electrodes. The ASR is evaluated for LSM/YSZ and LSCF/YSZ while operating at 800°C and 70% steam concentration; the ASR values are 0.93 and 0.79  $\Omega \text{ cm}^2$ , respectively.

Menon et al. [88] focused on the syngas production process through the co-electrolysis of H<sub>2</sub>O and CO in a high temperature SOEC. Similarly, Aicart et al. [89], [90] studied the co-electrolysis of H<sub>2</sub>O and CO<sub>2</sub> in a Ni-YSZ supported cell where the resulting gases are experimentally analyzed using gas chromatography at an OCV to validate the kinetic related parameters used in numerical modeling such as exchange current density. They also attempted to identify the operating conditions for optimum performance of a co-electrolysis cell through a simulation approach.

The high operating temperature of SOCs limits the material options that can be used to fabricate the cell and support its structure. This limitation increases the cell manufacturing cost and subsequently constrains SOC commercialization. Knibbe et al. [33] reviewed the durability of SOCs, including electrolytes and electrodes. The different materials, structure and operating aspects were discussed. The main degradation mechanisms of Ni-YSZ as a hydrogen/steam electrode in SOFC are discussed by Khan et al. [91]. A metal supported SOEC was fabricated in DLR and tested by Schiller et al. [92]; the tested cell showed a 3.2% degradation rate over 1000 h. Lay-Grindler et al. [93] used a 3D reconstruction technique to the volumetric microstructures of Ni-YSZ SOEC to evaluate microstructural

properties after 1000 h of operation at a current density of  $-0.8 \text{ A cm}^{-2}$  and a temperature of  $800^\circ\text{C}$ . At these conditions, the reported degradation rate is observed in terms of a considerable reduction in the triple phase boundary length.

Li et al. [32] measured the performance of a single cell, as well as 2 and 30 cell stacks, and reported that conversion efficiencies varied between 16.1% up to 52.7%. Kim et al. [85] built and tested a SOEC-based electrolyzer stack and obtained a high electric-to-hydrogen conversion efficiency of about 97%.

### 3.4. Photoelectrochemical Hydrogen Production

The concept of water-splitting using sunlight was first demonstrated by Fujishima and Honda in 1972 [94]. In their experiment, an n-type  $\text{TiO}_2$  was used as a photoanode immersed in an aqueous electrolyte with a Pt as a counter electrode. They illuminated the cell using a 500W xenon lamp and observed the evolution of hydrogen and oxygen gases.

The sunlight-driven electrochemical process gained increasing interest as a potential sustainable method of hydrogen production. In this process, semiconductor photo-catalyst materials are used to absorb light energy and promote separation of the electron and hole pair excited by photon energy. Schematic representation of this process is shown in Fig. 3.1. Therefore, through the photoelectrochemical cell (PEC) process, capturing solar energy and splitting water using a single semiconductor device is possible [95]. Fig. 3.1 illustrates the operating principle of a PEC, and role of a semiconductor. For a photon to be absorbed and to generate an electron-hole pair, it must have energy larger than the band gap of the semiconductor to be used [96].

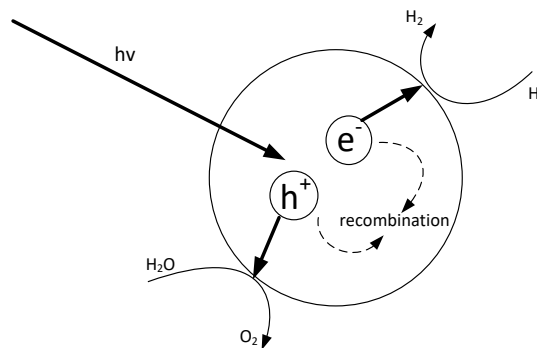


**Figure 3.1 Schematic representation of water splitting mechanism utilizing a semiconductor material (modified from [94]).**

Fig. 3.2 illustrates the band gap energy and the relative redox reaction. Archer conducted a comparative study between PVs and PECs [97]. A major differentiation is made based on the device state. Therefore, PV cells are known as all solid-state devices while PEC contain an electrolyte through which ion may move from an electrode interface to another. Furthermore, Gratzel discussed PV and PEC cells from different perspectives, including operating principle, conversion efficiency, commercialization status, cost, and future potential [98].

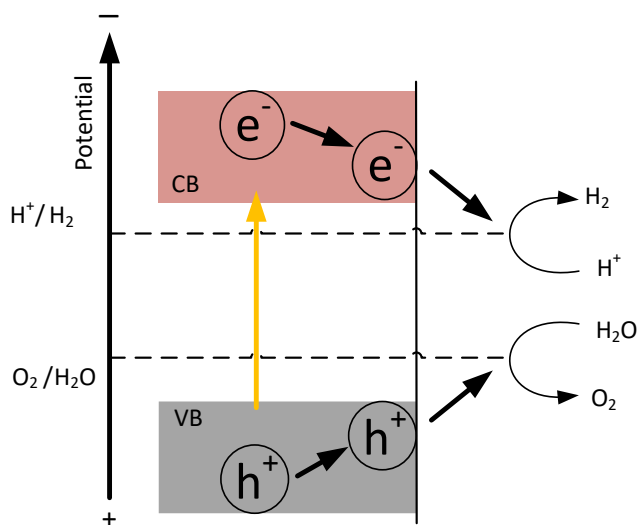


**Figure 3.2 Illustration of the photo-derived electron and hole pair and the subsequent redox reaction.**

The use of nanostructured metal oxides in a photoelectrochemical device for water splitting and hydrogen production, using direct sunlight, is discussed by Krol et al. [99]. The use of bismuth vanadate-decorated tungsten trioxide helix nanostructures in PEC for hydrogen production is investigated by Shi et al. [100]. Carlos et al. [101] used  $\text{Cu}_2\text{O}$  to examine PEC hydrogen production in an alkaline solution. Preethi et al. [102] reviewed the different nanomaterials used in photocatalytic processes for hydrogen production, including liquid and gas hydrogen produced from water or hydrogen sulfide as feedstock.

A significant number of research articles investigate the PECs in aqueous electrolytes. However, few studies have examined photoelectrochemical cells in a high temperature gaseous reactive medium, such as the case of photoelectrochemical solid oxide electrolysis cells (PSOCs), which involves light photon absorptions as well as an electrochemical reaction leading to steam separation into hydrogen and oxygen.

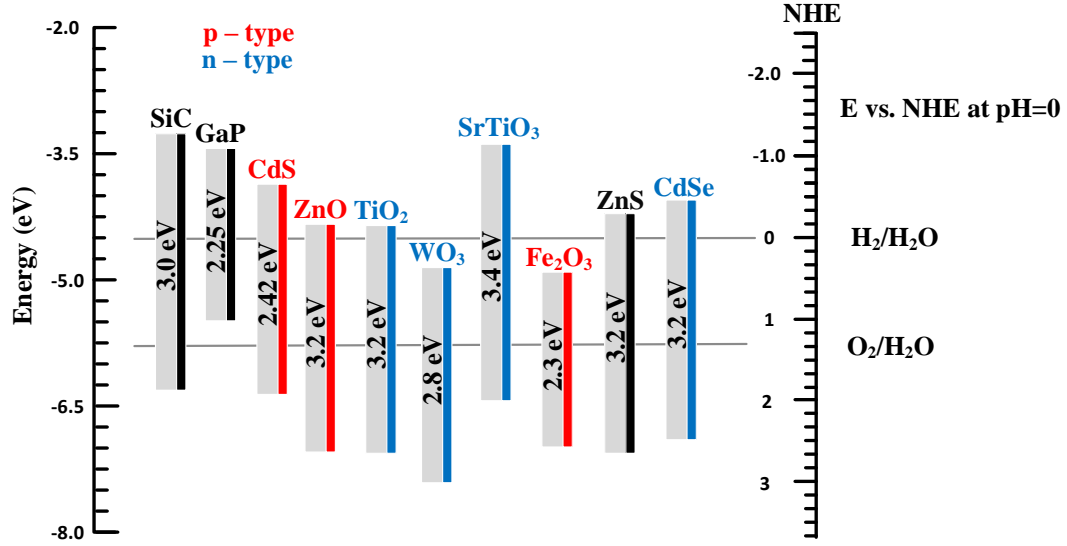


Figure 3.3 Schematic representation of the band gap energies of semiconductor relative to energy level for redox reactions in water (modified from [103]).

In an attempt to use sunlight to split water at high temperature, Ye et al. [104] proposed using a mixed ion and electron conductor in conjunction with light absorber semiconductor oxides for a single-step solar to hydrogen conversion. They evaluated a single cell efficiency as a function of operating temperature, solar radiation, and material optical properties. The predicted efficiency dropped with increasing temperature, from 17% at 723 K to 11% at 872 K, respectively. Similarly, in an attempt to develop a high-temperature PEC, Zhou et al. [105] studied some semiconductor compositions in order to harvest visible light. Their study included Ag/TiO<sub>2</sub>, LSM/TiO<sub>2</sub>, LSC/TiO<sub>2</sub>, and LSCF/TiO<sub>2</sub> over temperatures from ambient to 500°C. The rectifying properties of LSM/TiO<sub>2</sub> were reported to exhibit a feasible performance up to 450°C and thus claimed to be deserving of further investigation. It was observed that, since the increase in operating temperature will result in a reduction of the band gap of the semiconductors used, materials with a high/wide band gap can be used and the reduction in the band gap can be evaluated according to Varshni equation [106], as:

$$E_g(T) = E_g(0) - \frac{\alpha T^2}{T + \beta} \quad (3.2)$$

Here,  $E_g(0)$  is the band gap at an absolute zero temperature.  $\alpha$  and  $\beta$  are both constant, determined by experiments. Based on this equation, Zhou et al. [105] reported that TiO<sub>2</sub>

will narrow down to 1.7–2.3 eV at a temperature of 1000 K. Thus, they fall properly in the visible spectrum. Fleig et al. [107] examined the behavior of mixed conducting oxides under ultraviolet light at temperatures ranging from 350–500°C.

Walch et al. [108] examined a YSZ-based cell under a UV light and at temperatures in the range of 360–460°C. In their test, two cells were with a 900 nm YSZ manufactured, where one had a photoactive electrode made of a 100 nm single crystalline SrTiO<sub>3</sub> while the other had a 100 nm electrode of TiO<sub>2</sub>. For both cells, a Pt paste was used as a second electrode. These cells were produced in dimensions of 5 × 5 × 0.5 mm and 10 × 10 × 0.5 mm. The authors reported a time-dependent voltage response to UV-light illumination in the order of a hundred millivolts, which is interpreted as a generation of two types of voltages: a PV-type and a battery-type.

### **3.5. Research Gaps in Literature and Key Contributions**

Reflecting on the literature review, it can be clearly concluded that considerable research has been recently conducted or initiated on the subject of utilizing high temperature solid oxide electrolyzers for hydrogen production. However, few studies have considered solid oxide electrolyzer performance at the cell level as well as at the integrated system scale. Furthermore, limited experimental studies have been conducted on the SOECs to examine the effect of critical operating parameters on performance such as hydrogen feed concentration. As a key contribution of this thesis, the concept of the photo-solid oxide electrolysis cell is proposed and investigated. According to the best knowledge of the author, this has never yet been proposed in the literature. Thus, the results revealed by this research are expected to be a breakthrough in linking high temperature electrolysis with PECs. In this regard, the background of the relevant branches is reviewed and an experimental setup is designed to test the performance of a commercial SOCs under fuel cell and electrolysis modes.

Another objective of this thesis is to narrow down a list of potential semiconductor materials that have a promising potential to successfully achieve the desired absorption of light while in a fuel electrode operating environment. Although the ultimate purpose is to examine the performance of the designed PSOC under light and verify the effect of high temperature on the photocatalytic materials, the appropriate methods of fabrication and cell

arrangement have yet to be established. The result will shed light on the future application of this technology in the context of solar concentrators and large-scale solar hydrogen production. The potential cell performance improvement in terms of sunlight harvesting in a single cell, and the contributions in water splitting reaction, will be highlighted.

Additionally, broader studies have been performed targeting SOE system integration, including energy, exergy, and exergoeconomic analysis and optimization. The objective behind following two different levels is to comparatively examine two main pathways towards achieving a reliable solar hydrogen technology.

## **Chapter 4: Experimental Apparatus and Methodology**

Despite the fact that SOEC models are well developed and provide reliable results for the various types of SOCs, the importance of the experimental investigation of SOECs arises when new materials or fabrication procedures are implemented. In this case, experimental techniques provide the diagnostics and characterizations that are needed to measure cell performance and limitations under actual operating conditions. In this chapter, the design of the experimental apparatus is presented and discussed. The approach pursued for the development of the Photoelectrochemical Solid Oxide Cell (PSOC) is elaborated. The chapter concludes with a presentation of a relevant uncertainty analysis.

### **4.1. Experimental Apparatus**

An experimental apparatus is designed, manufactured and assembled as part of this research work. This includes the design and assembly of a high temperature furnace with customized features and a control unit that enables the desired measurements and specifications. Moreover, a control panel with mass flow controllers, pressure, and temperature sensors is constructed to adjust the gaseous reactant lines that feed the cell. A humidification unit is also added to adjust the moisture content of the reactant streams that flow into the cell fixture.

In an attempt to optimize the measurements and reduce the reactant leakage from the cell fixture, several fixture designs are developed and produced. The production process of these fixtures is presented. The commercial set of cells that have been tested and characterized are presented, and their specification described. Lastly, the specifications of the different instrumentations used for measurements are reported.

#### **4.1.1. High Temperature Furnace Design**

Due to the specialty of the experimental procedure that was determined as necessary for accurate and successful measurements, a furnace design was not readily available from vendors at an economically feasible price. Therefore, a primary task in this research was to identify the set of requirements based on which the furnace could be designed. A problem was formulated, researched, analyzed, and solved. Relevant heat transfer references were utilized in accordance with the manufacturers' recommendations and

standards. The following primary requirements were identified: (1) the furnace capacity required  $\sim 4.5$  kW; (2) the maximum temperature  $1200^{\circ}\text{C}$ ; and (3) insulation to achieve a maximum surface temperature of  $50^{\circ}\text{C}$ , with an internal diameter of 6 inches and a vertical height of 12 inches. A lab power outlet provided a maximum power of about 2.3 kW ( $\sim 115\text{V} \times 20\text{A}$ ) per circuit. Accordingly, a split furnace was designed, each with two halves with a maximum power of 2.3 kW. The primary schematic representation of the furnace circuit is shown in Fig. 4.1.

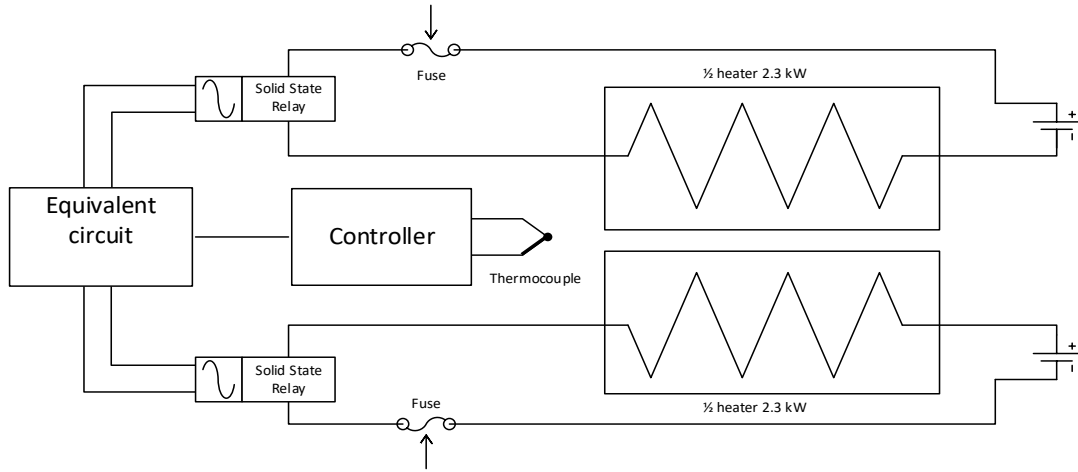


**Figure 4.1 Schematic representation of the furnace electric circuit and control unit.**

A detailed electric circuit was designed based on the heating coil provided by Omega (Coiled Nickel-Chromium Alloy Resistance Wire MiCr80) with a gauge rating of 28 [109]. The coil was selected to meet the required maximum temperature while achieving the maximum power rate. For each half, seven coils were cut, based on the specifications provided by the manufacturer's catalog and connected in parallel, as shown in Fig. 4.2. All the coils, arranged in parallel with an equivalent resistance, can be calculated as follows:

$$R_t = \frac{1}{\left(\frac{1}{R_1} + \frac{1}{R_2} + \frac{1}{R_3} + \dots + \frac{1}{R_N}\right)} \quad (4.1)$$

Thus, to achieve an equivalent resistance  $R_t = 6.14 \pm 0.7 \Omega$ , each of the resistances  $R_1$  to  $R_7$  is designed and installed to be  $R_N = 43 \pm 0.5 \Omega$ . Accordingly, the circuit has a maximum rated power of  $P = 2154 \pm 25 \text{ W}$ .

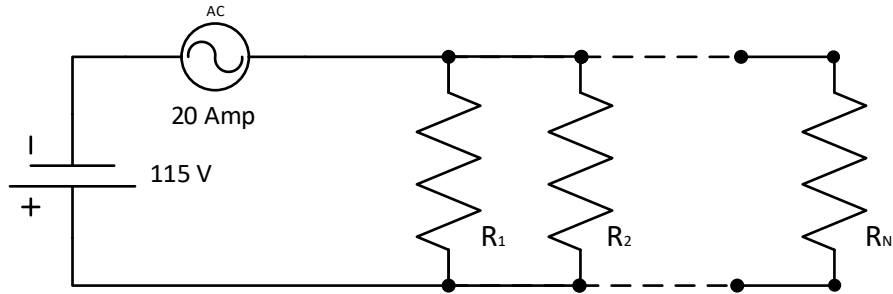


**Figure 4.2 Representation of the furnace electric circuit made of MiCr80 heating coils.**

Other components of the circuit shown in Fig. 4.1, such as the solid-state relays (SSRL240AC10 by Omega ®), fuses, thermocouple and temperature controller, were also ordered. The inner structure of the furnace was then cast of Lite Kastite 2300 (Alumina, Calcium Oxide, and Silica) high temperature insulation castable ceramic, provided by Allied Mineral Products, Inc. [110].



**Figure 4.3 High temperature furnace heating coils test.**

The casting product, which was made during several steps, started with the preparation of the casting mold and the wire connections, and ended with gradual curing in order to eliminate cracking. After installing the wires and thermocouples, the outer structure was

covered by a layer of high temperature insulation board (K-FAC® 19). Several tests and calibrations were conducted before installing the furnace into the final structure within the hydrogen lab fume hood. Initially, the testing was performed for every coil to ensure accurate response and measurement before assembly and insulation. Fig. 4.3 shows one-half of the furnace while being tested.

Fig. 4.4 shows the full furnace structure after being installed in the fume hood and connected to the temperature controller. The structure is also customized to support the reactant lines and allow for flexible cell fixture mounting, i.e., different cell sizes and geometries can be tested.

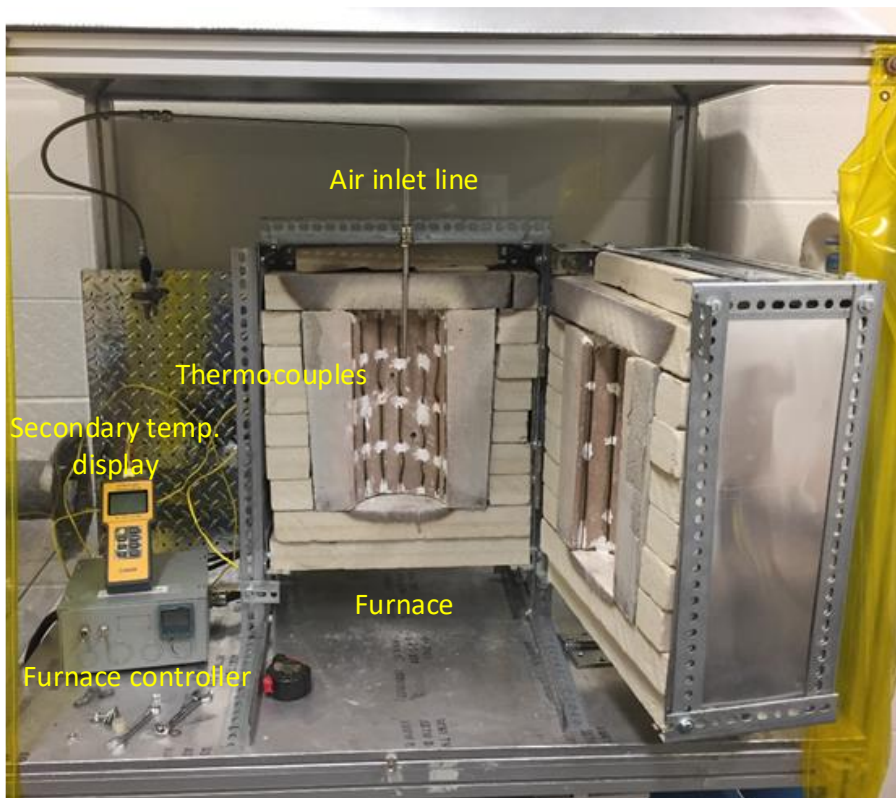


**Figure 4.4** Setup within the fume hood structure showing the furnace, control unit, and air flow line.

In addition, a Eurotherm 2116 PID temperature controller was installed to monitor and control the furnace temperature. The controller features include several operating and control modes, such as the ramp and dwell mode that enable setting the required heating rate. A K-type thermocouple is used to measure the furnace temperature and feed the temperature measurements to the controller. For example, to prevent high thermal

expansion rate, a low heating rate is usually set for SOCs, i.e., in the range of  $\sim 1^{\circ}\text{C min}^{-1}$ . The controller utilizes auto-tuned PID parameters to maintain this rate until the desired temperature is reached, then holds for the specified dwell time.

#### 4.1.2. Humidifier Unit

In order to meet the moisture content required by the cell, a humidification unit is installed. This unit consists of a glass container, a heater, a thermocouple, an inlet stream for the reactant and inert species (i.e., hydrogen and nitrogen), and an outlet stream where the reactant species leave the humidifier with the adjusted moisture content based on the set humidifier temperature. Fig. 4.5 shows a schematic representation of the humidifier. The thermocouple is connected to a temperature controller in order to monitor and maintain the humidifier at the desired set temperature.

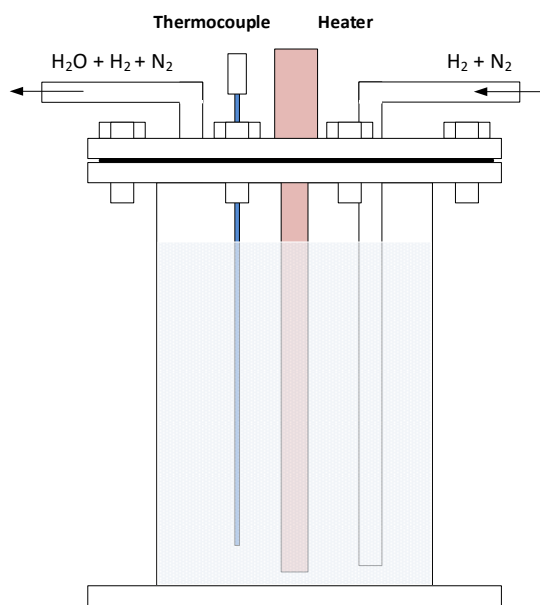


**Figure 4.5 Schematic diagram of the humidifier unit.**

The amount of water vapor that a gas flow can hold depends significantly on the temperature of that water-gas mixture. Thus, the higher the temperature, the more water vapor the gas can hold up to saturation state. The parameters that are commonly used to identify the water vapor content in gas are many. As an example, relative humidity RH%, and absolute humidity (also called humidity fraction or ratio  $\omega$ ) are the most widely used terminologies. Absolute humidity is defined as:

$$\omega = \frac{m_v}{m_g} \quad (4.2)$$

Utilizing the ideal gas relations,  $\omega$  can be written as:

$$\omega = \frac{\dot{m}_v}{\dot{m}_g} = \frac{P_v \dot{V} / R_v T}{P_g \dot{V} / R_g T} = \frac{P_v / R_v}{P_g / R_g} \quad (4.3)$$

Knowing the gas flow rate composition, and the universal gas constant  $R_g$ , the  $P_v$  can be adjusted through the setting of the humidifier temperature. These equations can be used to conduct an online processing in a LabVIEW environment to read or log the evaluated absolute humidity. Alternatively, for a fixed gas flow input, the temperature can be correlated with the vapor pressure to set the temperature that produces the outlet stream with the desired absolute humidity.

#### 4.1.3. Cell Fixture

The cell casing is designed to allow sufficient flow of the reactants over the electrodes at the same time in order to maintain good contact and uniform pressure on the cell structure. For the current experimental project, the cell fixtures were cast of Aluminum Oxide ( $\text{Al}_2\text{O}_3$ ) provided by Aremco Products, Inc. under the commercial powder name of 567N. Several casing designs were developed to meet the specific experiment requirements. For example, in some cases, fixtures are designed for sealed cell operation while in others an open cell design is preferred. A schematic representation of the two designs: sealed and the non-sealed (open cells) are presented in Fig. 4.6 and Fig. 4.7, respectively. Due to the critical role of the cell fixture design, many alternative designs were proposed and some have been successfully tested, the detailed drawings of these designs are given in Appendix 1.

For all of the designs, the same casting procedure is used and can be summarized as: (1) A mixture of 100 wt.% to 14 wt.% ceramic powder to water is combined to create the casting slurry. (2) The slurry mixture is thoroughly mixed to achieve the required homogenous texture before being poured into the designed models. (3) The wire connections and current collecting meshes are already in place in the model. (4) After pouring the ceramic into the

models, it is allowed to dry at room temperature for 10 hours. (5) The casts are then cured in a furnace at 80°C for 2 hours and at 120°C for 4 hours.

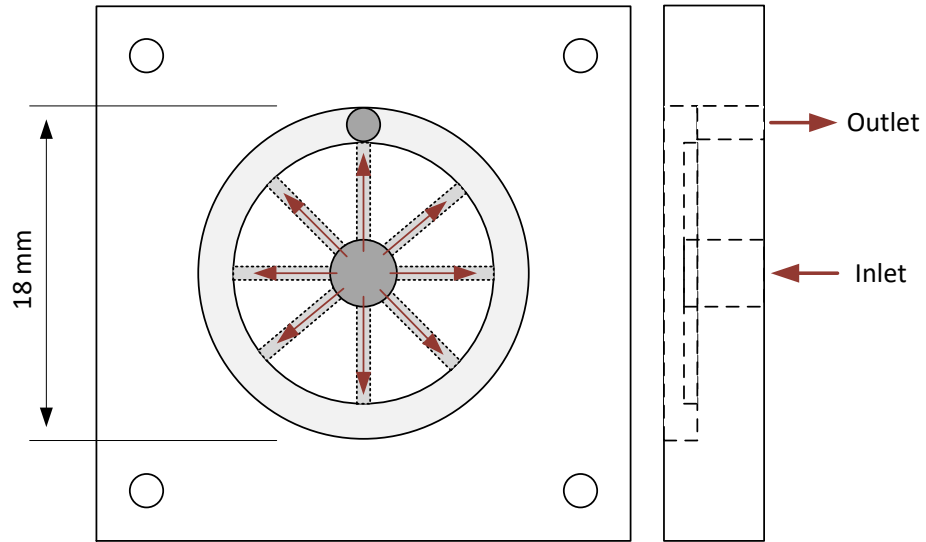


**Figure 4.6 Cell casing: the reactant/product passages (for a sealed cell design).**

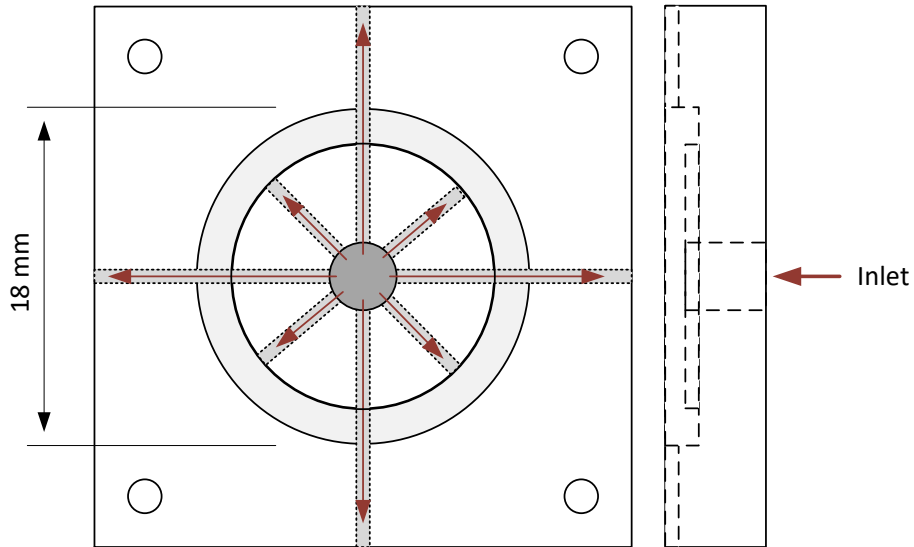


**Figure 4.7 Cell casing design for burnout products (Non-sealed cell).**

An illustration of the final lower-side cell fixture is shown in Fig. 4.8. Using Inconel® tubing, the fixture is connected to the fuel line coming from the humidifier. Inconel® can withstand high temperature conditions within the furnace. Furthermore, the reactant line coming from the humidifier may require insulation and trace heating to eliminate any condensation. Inconel tubes are able to tolerate trace heating.



Figure 4.8 Lower cell fixture with a button cell installed for testing.

#### 4.1.4. Cell Type and Dimensions

The cell used for testing is a planar SOC, usually called a button cell. A *NextCell 2.5*, provided by *NexTech Materials*, is used in the current experimental work. This cell is an electrolyte-supported cell, the design of which is advantageous for sealed operations. The cell specifications are listed in Table 4.1. A photo of the actual cell, showing the size and the two electrodes, is shown in Fig. 4.9.

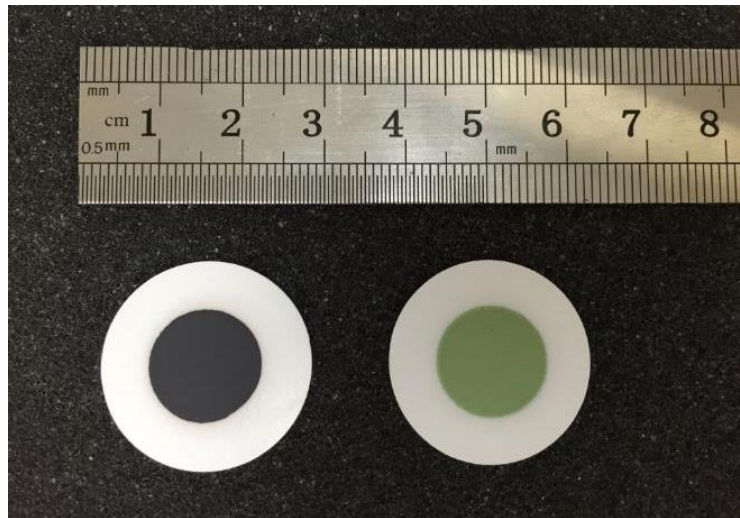


Figure 4.9 New *NextCell*: the green side is the hydrogen electrode; and the black side is the oxygen electrode.

**Table 4.1 Material and dimensions of the *NextCell 2.5* (data from [111]).**

Component	Diameter	Thickness	Material
Electrolyte	25 mm	0.13-0.17 mm	YSZ
Hydrogen electrode	12.5 mm	~50 $\mu\text{m}$	NiO-GDC/NiO-YSZ
Oxygen electrode	12.5 mm	~50 $\mu\text{m}$	LSM/LSM-GDC

#### 4.1.5. Cell Installation

The installation of the cell within the casing is shown in Fig. 4.10. The cell is sandwiched between two meshes to allow for uniform gas distribution over the electrodes' active area. At the oxygen electrode, precious metals (commonly Pt) are used for current collection. The selection usually depends on the operating temperature as well as the desired conductivity. Ni mesh can be used for current collection at the hydrogen electrode. Platinum wires are preferred for current transmission and voltage measurements, but nickel wire can also be used. An exploded schematic view of the cell installation is shown in Fig. 4.10, presenting the main arrangement of components in the cell fixture. High temperature gaskets are used to reduce or eliminate gas leakage from the cell fixture.

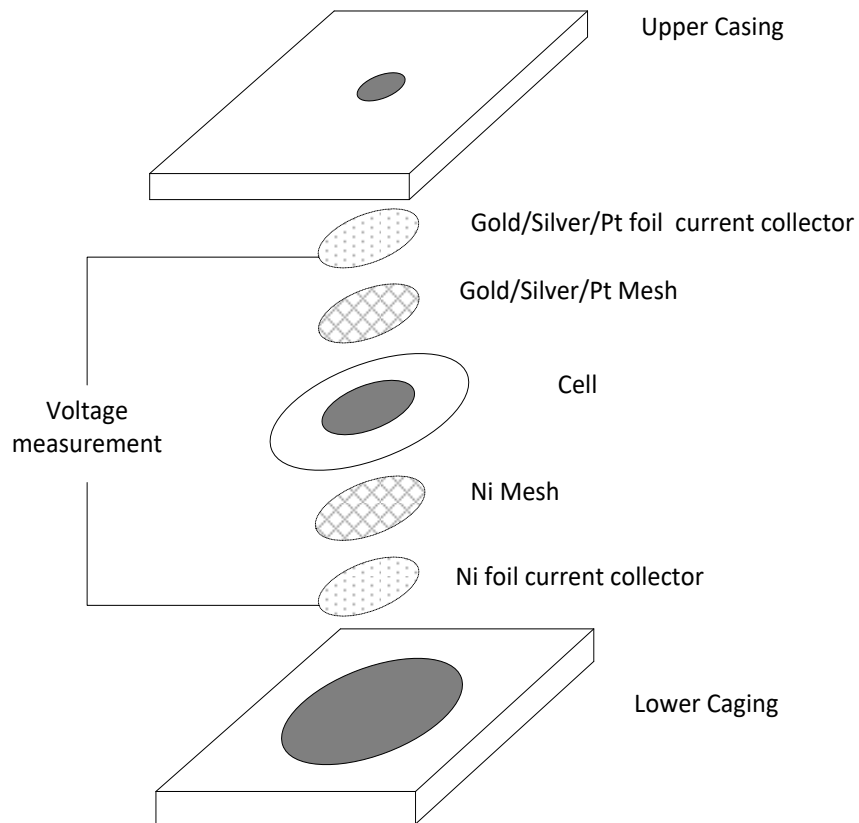


**Figure 4.10 Exploded schematic diagram of the SOEC testing installation with all the components.**

## 4.2. Instrumentation

In this section, a list of all instrumentations used for measurement and data collection is provided. The accuracy of this equipment and other relevant properties is also highlighted.

### 4.2.1. Thermocouple Probes

During experimentation, two types of thermocouples have been used for temperature measurement, namely K-type and T-type. The K-type thermocouple is used to measure the temperature inside the furnace and provide feedback to the temperature controller to close the control loop while the T-type is used to measure the temperature inside the furnace in a location as close as possible to the cell fixture. Hence, the cell temperature can be correlated according to systematic measurements and evaluated based on the reading from this thermocouple. The T-type thermocouple is used to measure and monitor the temperature of the water in the humidifier, and is also connected to the temperature control to maintain the desired temperature. The specifications of the K-type and T-type thermocouples are listed in Table 4.2.

**Table 4.2 Specifications of the thermocouples used for measurements.**

Type	Parameter	Specification
K	Temperature range	0 – 1260°C
	Length	12 inch
	Diameter	1/4 inch
	Accuracy	±0.75%
	Response time	5 sec
	Connection type	Wire Leads
	Probe material	Nickel
T	Temperature range	-250 – 662°C
	Length	6 inch
	Diameter	1/8 inch
	Accuracy	±0.5°C or 0.4%*
	Response time	5 sec
	Connection type	Nylon connector
	Probe material	Stainless steel

\*whichever greater

### 4.2.2. Potentiostat

A Potentiostat is a lab equipment used to read and control voltage difference between a working electrode and a reference or counter electrode in an electrochemical cell [112]. In

order to control voltage, the Potentiostat passes the appropriate amount of current to a cell using either an auxiliary electrode or a counter electrode. A Gamry Instrument Reference 3000 and Reference 30 K Booster (Potentiostat/Galvanostat/ZRA) are used for electrochemical measurements and analysis in the current experimental cell. The relevant specifications of the Gamry Potentiostat are presented in Table 4.3. Further detail can be found in the manufacturer's manual [113].

**Table 4.3 Specifications of the Potentiostat instrument [113].**

Component	Parameter	Specifications
Manufacturer	Gamry	Gamry Reference 3000
System	Control modes	Pstat, Gstat, ZRA, FRA
	Cell connections	2, 3, or 4 electrode
	Max. current	$\pm 3$ A
	Min. voltage resolution	1 $\mu$ V
	Max. current resolution	100 aA
EIS measurement	Frequency range	10 $\mu$ Hz – 1 MHz
	Impedance accuracy	see manuf. accuracy map
High resolution electrometer	Max. measured potential	$\pm 11$ V
	Input impedance	$>10^{14} \Omega \parallel < 0.2$ pF
	Input current	$<10$ pA
High voltage electrometer	Accuracy	$\pm 4$ mV $\pm 0.3\%$ or reading
	Full-scale ranges	$\pm 12$ V, 1.2 V, 120 mV
	Resolution	400 $\mu$ V, 40 $\mu$ V, 4 $\mu$ V
Applied signal (Potentiostat)	Accuracy	$\pm 1$ mV $\pm 0.2\%$ of setting
	Resolution	12.5 $\mu$ V, 50 $\mu$ V, 200 $\mu$ V/bit
	Scan range	$\pm 0.4$ V, $\pm 1.6$ V, $\pm 6.4$ V
Applied signal (Galvanostat)	Accuracy	$\pm 10$ pA $\pm 0.3\%$ of setting
	Resolution	0.0033% full-scale/bit
Measured Current	Accuracy	$\pm 0.3\%$ range $\pm 10$ pA
	Resolution	0.0033% of full-scale/bit
	Offset range	$\pm 1X$ full-scale

#### 4.2.3. Pressure gauges

A Swagelok stainless steel pressure gauge (C Model) is used to read the pressure in the hydrogen/steam line before the humidification unit. The line is open to the humidifier, and the pressure reading is used as the humidifier internal pressure. The details and specification of the pressure gauge are presented in Table 4.4.

**Table 4.4 Pressure gauge specifications [114].**

Parameter	Specification
Dial range	0 to 60 psi
Accuracy	63 mm (2 1/2 in) $\pm$ 1.5% of span
Configurations	Center-back mount
Operating temperature	Ambient: -40–60°C
	Media: 100°C

#### **4.2.4. Mass Flow Controllers**

Three Alicat mass flow controllers (MFC) have been installed to measure and control the mass flow rates of gases into the cell fixture. These devices are capable of controlling the mass flow rate for a wide range of gases and measuring the pressure and temperature. One MFC, MC-Series with a range of 0–5 standard liters per minute (SLM) is used for hydrogen streamline (see Fig. 4.11). The other has a range of 0–50 SLM, and is used for the nitrogen line that is to be mixed with hydrogen and humidified before being fed to the fuel electrode compartment. The third controller is used for the air or nitrogen line that feeds the anode (oxygen electrode) compartment. The relevant specifications of these flow controllers are given in Table 4.5.



**Figure 4.11 Mass flow controller used for hydrogen line.**

**Table 4.5 The specifications of the mass flow controllers [115].**

Parameter	Specification
Manufacturer	Alicat MC-Series
Mass reference conditions (STP)	25°C and 14.696 psia
Operating temperature	-10 to +50°C
Humidity range (non-condensing)	0 to 100%
Max. internal pressure (static)	145 psig
Proof pressure	175 psig
Valve type	Normally closed
Accuracy at calibration condition	± (0.8% of reading + 0.2% of full scale)
High accuracy at calibration condition	± (0.4% of reading + 0.2% of full scale)
Repeatability	±0.2% full scale
Zero shift and span shift	0.02% full scale/°C/Atm
Maximum flow rate	102.4% full scale
Typical response time	100 ms (adjustable)
Warm-up time	<1 second

#### **4.2.5. Data Acquisition System**

National instrumentation compact cDAQ is used to collect and monitor the different temperature sensors and pressure transducers. The NI-DAQ system is made up of an NI cDAQ-9172 chassis in addition to several modules used for specific signal processing and acquiring. For example, an NI 9211 module is used for thermocouples, and a current signal module NI 9203 is used for the pressure transducer. These components are interfaced with the computer for measurement reading and logging through the NI software Labview.

### **4.3. Measurement Procedure**

This section includes two main parts, in the first of which the full test station is presented. The testing and measurement procedure is then outlined.

#### **4.3.1. Full Testing Station**

The apparatus that has been developed for testing is schematically illustrated in detail in Fig. 4.12. This figure shows the reactant gases, such as Air, Nitrogen (N<sub>2</sub>) and Hydrogen (H<sub>2</sub>), which are required to conduct the experiments deionized water is also heated in the humidifier to adjust the required moisture content leaving the humidification unit. A mixture of H<sub>2</sub>, N<sub>2</sub>, and steam is fed to the cathode side of the SOEC.

As the operating temperature of the cell varies within 600–800°C, the mass flow rate, temperature, and pressure are measured at each stream in order to accurately evaluate the

gas compositions. For high flow rates, the reactant gas mixture can be circulated in a coil heat exchanger inside the furnace before introducing it to the cell. Thus, uniform cell temperature is maintained. The furnace temperature is measured at two locations using thermocouples.

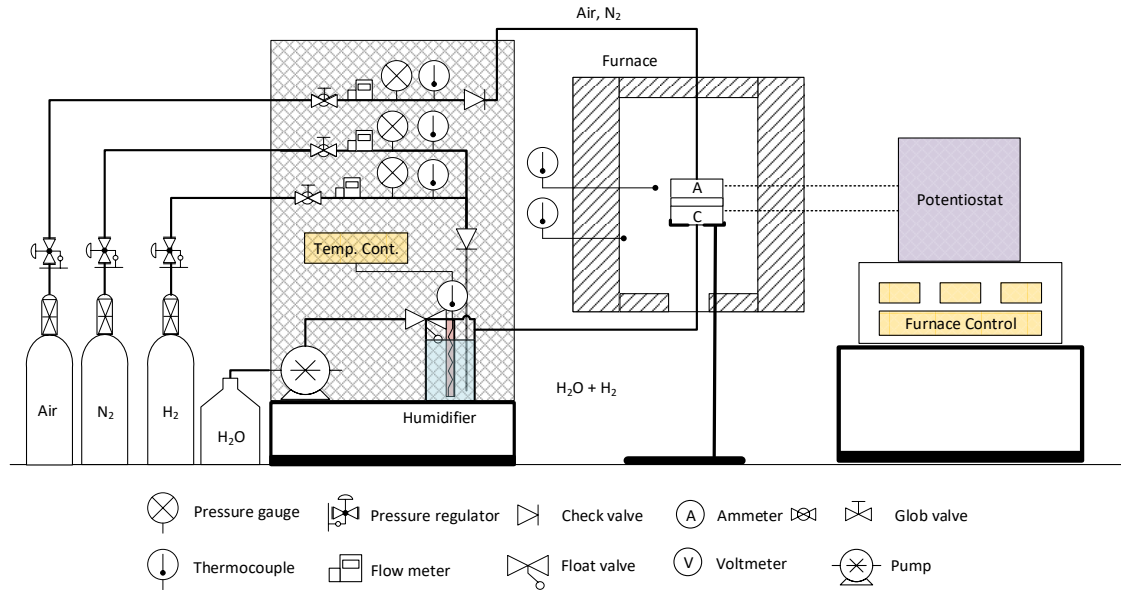


**Figure 4.12 Schematic representation of the experimental setup for SOEC testing (without light).**

The produced  $H_2$ , while operating in electrolysis mode, can be cooled and sent to a gas analyzer to determine the different concentrations of the output stream, otherwise it can be burnt within the furnace as in the case of open cell design. At the anode side,  $N_2$  gas is usually blown, at a rate of about 100–200 sccm, to sweep the generated oxygen while in the case of a fuel cell mode test, air is fed to the anode side to supply the required oxygen at the same rate. The Potentiostat is connected to continuously measure and collect the cell voltage and current. The cell lower fixture, with the connecting Ni wires, is shown in Fig. 4.13. The tubing inside the furnace is Inconel.

The reactants flow through the tubing into the cell electrode through a conductive Ni foam which allows for gas distribution and current collections. The lower fixture, with the conductive Ni foam, is shown in Fig. 4.14.



**Figure 4.13 Hydrogen and steam line to the lower fixture and the wiring.**



**Figure 4.14 Lower cell fixture with internal porous nickel foam for gas distribution.**

In the case of the PSOC, the cells can be tested in the same setup by altering the furnace lower side opening to accommodate light access to the photoactive electrode. Utilizing the lower side for shining light on the cell provides two advantages. Firstly, it eliminates the need for an opening at the top side of the furnace, thereby reducing the convective heat losses from the furnace to the surroundings. Secondly, placing the light source at the lower side reduces the risk of burning or overheating the light source due to natural convection from the furnace. The schematic representation of the setup modified for light testing of the PSOC is illustrated in Fig. 4.15.

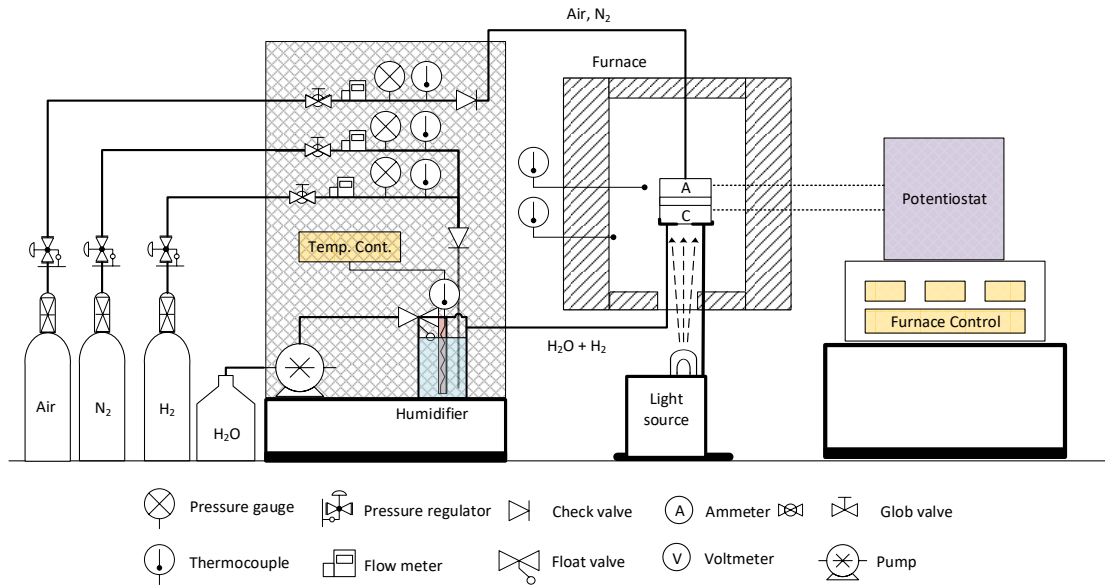


**Figure 4.15 Schematic representation of the experimental setup testing for the PSOC (with light).**

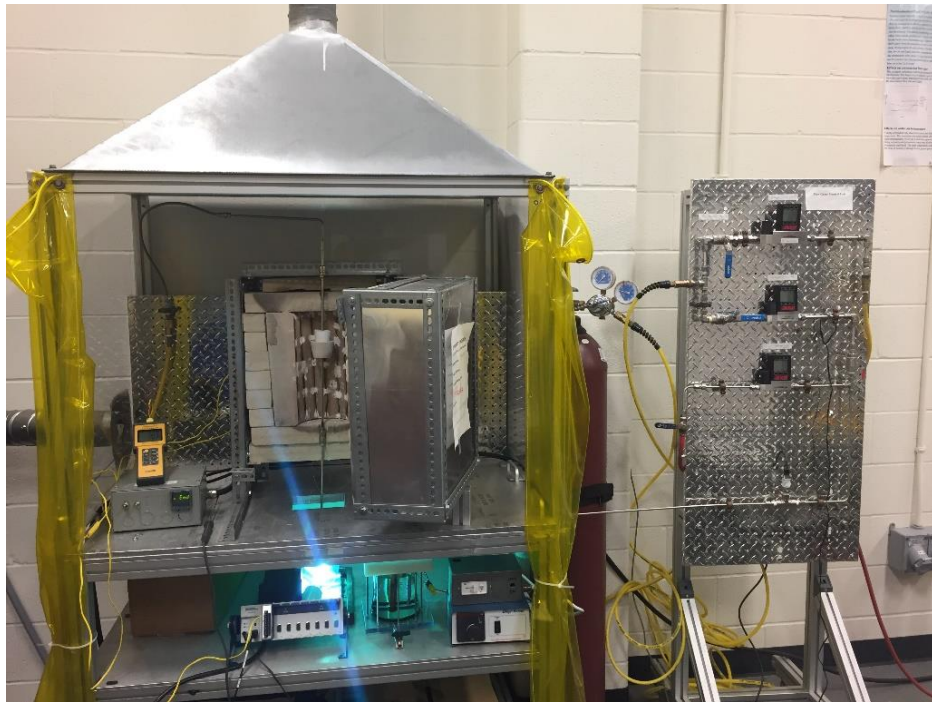


**Figure 4.16 The complete SOC station testing.**

The actual setup is shown in Fig. 4.16. The various components of the testing station are shown in this figure. One of the major challenges encountered in the current research project is to construct a cell fixture which can withstand high temperature test conditions and allows light and reactant gases access to electrodes' active area. Therefore, a number

of novel cell fixtures were proposed and designed. A successful example is the all-quartz lower cell fixture which has been designed by the author and specifically manufactured for this project. Fig. 4.17 illustrates the all-quartz cell fixture used for light testing the PSOCs.



**Figure 4.17 All-quartz PSOC fixture for cell test under light.**

The main features of this fixture are the ability to withstand high operating temperatures, the very high thermal shock resistance, and the excellent UV light transmittance of quartz. Thus, even semiconductors that are known to be active only under UV light, such as  $\text{TiO}_2$ , can be tested using this device.

#### **4.3.2. Testing Procedure**

Considering the button cell described in section 4.1.4, the SOC testing procedure can be summarized as: (1) The cell is inspected and installed in the cell fixture. (2) The conductivity of the connecting wires is examined and connected to the Potentiostat. (3) After the cell installations, a flow of an inert gas, e.g., Ar, or  $\text{N}_2$ , is set to feed the fuel electrode and purge the piping line. (4) Air is fed to the oxygen electrode at a rate of 200 sccm. (5) The gas flow rate into each compartment is maintained at 200 sccm, regardless of the compositions. (6) The furnace temperature is set to a heating ramp of  $1^\circ\text{C min}^{-1}$  until it reaches the desired testing temperature. (7) While the temperature of the furnace increases, the hydrogen concentration in the fuel line is raised with 5% steps to reach 20%. (8) Once the desired temperature is reached, the hydrogen concentration can be increased with steps of 5% to reach 95%. (9) The cell is then allowed to be reduced, thus non-conductive green NiO is reduced to Ni, causing the fuel electrode to become conductive

and catalytically active. (10) The continuous monitoring of cell potential (OCV) using the Gamry Potentiostat shows the OCV stability when the cell is fully reduced. (11) An EIS measurement is taken to record the cell resistance spectra under OCV condition. (12) Linear sweep voltammetry is then conducted to record the cell J-V curve from OCV to a minimum of 0.5 V. (13) The next step is to change the parameter to be investigated, e.g., temperature, gas compositions, or load. (14) The changes should be gradually introduced and the cell is allowed to reach steady state operation. (15) Steps (8–13) can be repeated to record the cell performance.

#### **4.4. Development of Photo-Solid Oxide Cell**

For the development of the PSOC, multiple design choices have been proposed. Of the several designs identified as feasible, the most promising ones are considered. To make use of efficiently available and well-established SOEC technology, photocatalytic materials can be applied to a conductive layer of meshes, foam or foil with openings for gas flow. These layers are used for current collecting and to provide a photoactive surface without impacting the electrode structure and compositions. The addition of this layer should not compromise electrode porosity or catalytic activity. High surface exposure to light can be achieved by utilizing the free side of the current collecting layer. Other challenges associated with reactant gas access to the active electrode area are still to be addressed through different fixture designs.

##### **4.4.1. Photoactive Material Selection**

The relevant literature and recent developments in the photoelectrochemical cell have been introduced and discussed in section 3.4, including some recent efforts on high temperature PSOCs. In this section, the rationale behind the selection process of a semiconductor is discussed. Many semiconductors have been characterized as photocatalysts capable of hydrogen production, e.g.,  $\text{TiO}_2$ ,  $\text{SrTiO}_3$ ,  $\text{NaTi}_6$ ,  $\text{TaO}_5$ ,  $\text{KTaO}_3$ . However, most of these catalysts have a larger band gap, thus are only active under UV light and poorly active under visible light [116]. Therefore, research efforts have been dedicated towards the development of photocatalysts that can efficiently operate under visible light.

In the context of the high temperature PSOC, a different set of requirements evolves to shape an ideal semiconductor candidate for such an application. For example, a primary

requirement is the chemical and thermal stability of the semiconductor under electrode conditions, either in fuel reducing or oxygen oxidizing environments. Another critical parameter is the band gap of the photoactive materials; that is, for the envisioned PSOC to operate under sunlight, the band gap should be suitable for visible sunlight absorption. It must be emphasized here that some semiconductors that are characterized with a wide band gap at low temperatures should be considered for high temperature applications due to the reduction in the band gap with increasing operating temperature. This reduction in the band gap may result in favorable changes that allow for visible light absorption. Based on the band gap and temperature relation given by equation (3.2), Zhuo et al. [104] reported that the TiO<sub>2</sub> band gap is expected to reduce from 3 eV at a temperature of 25°C to 1.7–2.3 eV at a temperature of about 730°C, which makes it suitable for visible light absorption. However, the photoactivity of TiO<sub>2</sub> at high temperatures is still to be verified due to the limited number of studies conducted under such high operating conditions.

Furthermore, some perovskites reported to exhibit photoactivity such as SrTiO<sub>3</sub> and LaCrO<sub>3</sub>. These materials have already been tested and demonstrated as SOC electrodes, and their physical stability during the processing and testing conditions was documented. Accordingly, it is expected that optimizing such an electrode for testing under light conditions is a promising direction and worth investigating.

Concerning the current study, a list of the most promising semiconductors is prepared based on the aforementioned requirements being integrated into the cell structure to form a PSOC. As a next step, different possible configurations of semiconductors and cell structures will be tested under the light in addition to the typical cell operating conditions.

The selected semiconductors are ZnS, CdS, and TiO<sub>2</sub>. The primary aim is to successfully apply a photoactive coating of these semiconductors onto a conductive material that can function as a current collector in the PSOC and as a photoactive surface. The optimistic outcome anticipated is that a photocurrent would be generated as a result of light absorption which can be observed in changes in the cell OCV, or current detection through the electrochemical measurements. The method of application of these semiconductors and the integration into the cell are described in the following sections.

#### **4.4.2. Methods of Material Application**

Advanced technologies are now available for the manufacturing of the SOCs. These methods vary in terms of component, scale, and cost of production. For example, electrolytes are commonly produced by the tape casting (doctor blade) method while screen printing and sputtering are the most common methods for electrode production. These components may also be laminated by a warm pressing and then sintered to make the final cell structure. Further detail on the fabrication of SOCs and recent advances can be found in the review article by Mahmud et al. [72].

In regards to the synthesis of the photocatalytic layer, several methods are considered more economically and technically feasible than others based on the scope of the current research and the desired output. Therefore, two different methods, electrospinning and sol-gel, have been selected and used while other methods such as screen priming and spraying are considered for future research. The following sections focus on these methods for the development of a photoactive surface for future use in PSOCs as current collectors and photoactive surfaces for radiation absorption.

#### **4.4.3. Sol-Gel Coating**

The sol-gel process is a well-established low temperature synthesis process with many applications in the fabrication of ceramic oxides and glass fiber materials. A number of parameters play a critical role in determining the properties of the final product. These parameters are: temperature, mixing speed, pH level, and the condensation process. The sol-gel process, as the name indicates, involves two initial steps: (1) solution preparation; and (2) gel formation through heating and condensation [72].

In the current study, the sol-gel process was used to prepare and coat samples of nickel foam and stainless steel mesh with a TiO<sub>2</sub> photoactive layer. The procedure for preparing the sol-gel and deposition process have been described in previous studies, e.g., [117]. In order to produce the solution, 25 ml Titanium(IV) isopropoxide (%97, CAS # 546-68-9) [118] was mixed with 5 ml acetic acid (%99.7, CAS #64-19-7) [119], then added to 500 ml of deionized water. 3.5 ml Nitric acid (%70, CAS # 7697-37-2) [120] was then added to the solution before heating for 30 minutes at a temperature of 80°C. Using a magnetic

stirrer, the solution was stirred for two hours at a constant temperature to form sol-gel with a pH concentration of 1.

Having prepared the sol-gel, two samples of nickel foam and two stainless steel meshes were prepared into rectangular samples, as shown in Fig 4.18. The samples were coated with TiO<sub>2</sub> using a low-cost dip-coating method where a dip-coating machine was used to maintain a dipping and withdrawal speed of 2.5 mm s<sup>-1</sup>. All samples were dipped 60 times at a constant speed and at room temperature.



**Figure 4.18** Rectangular samples of nickel foam and stainless steel mesh samples.

The samples were then allowed to dry for 2 hours at room temperature and 4 hours at 120°C, then annealed at 500°C for 2 hours. The annealing process was carried out at air with constant heating and cooling ramps of 10°C min<sup>-1</sup>. The samples were tested in an electrolytic cell made for a graphite counter electrode against the coated sample.

#### **4.4.4. Electrospinning**

Electrospinning is a nanofiber production technology that uses high voltage to draw thin thread from a charged injection needle. The product is a layer of fiber deposited on a collecting drum which is oppositely charged. Fig. 4.19 shows a schematic representation of the electrospinning process. This method is selected because it achieves a high level of dispersion and causes no changes to the composition of the target substrate or metal mesh. For the purpose of this research, a porous nickel (Ni) foam was used on which the

electrospinning was made. This Ni foam was subjected to the collecting drum and a solution was then prepared from the selected photocatalytic material (ZnS). The polymer solution was used as a carrier to efficiently distribute the ZnS particle across the Ni porous structure.

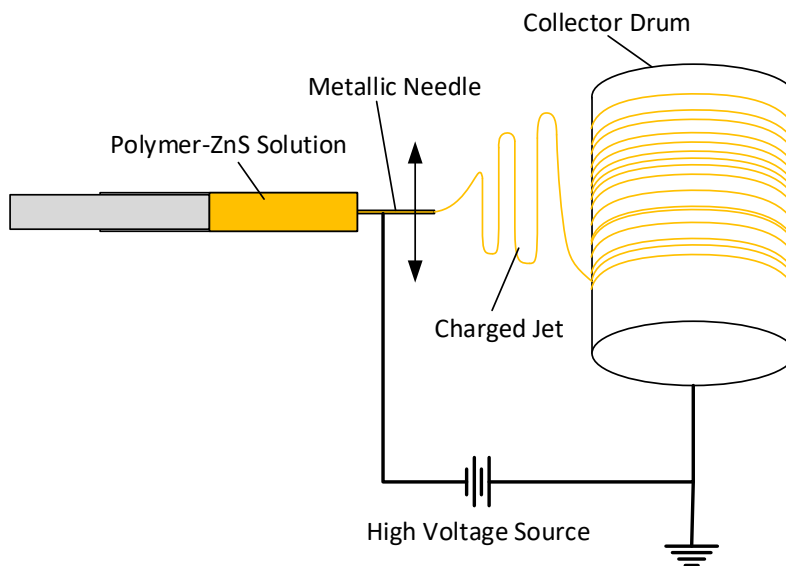


**Figure 4.19 Schematic representation of the electrospinning process.**

After the required layer thickness was achieved, the Ni sample was removed from the collector drum and annealed in the furnace to remove the organic polymer. The sample was heated to a temperature of 450°C for about 3 hours to ensure the complete combustion of the polymer material.

The polymer-based solution was prepared from 11 wt.% PVA (Sigma-Aldrich), 1wt.% ZnS (Alfa Aesar), and 88 wt.% deionized water. The water was first weighed (22 g) to which the PVA material was then added (2.97 g). The mixture was stirred for 2 hours at a temperature of 50°C. When the solid particles were completely dissolved in the water, the ZnS nanopowder was added (0.03 g). The mixture was stirred overnight at 200 rpm. Several tests were performed to optimize the solution's viscosity and concentration, but the same procedure was maintained for all prepared solutions.

The main parameters of the electrospinning procedure that determine the produced nanofibers are the solution concentration, polymer concentration, applied voltage, drum

speed, type of injection needle, feed rate, and needle distance from the drum. These parameters are set in our test as in Tables 4.6.

**Table 4.6 Main parameters of the electrospinning nanopowder coating.**

Parameter	Set value
Solution concentration	1%
Polymer (PVA) concentration	12%
Voltage	10kV
Drum speed	1000 rpm
Needle type	25 gauge
Feed rate	0.6 ml hr <sup>-1</sup>
Needle distance from the drum	7 cm

## 4.5. Uncertainty Analysis

An uncertainty analysis, which is conducted to quantify the range of possible errors associated with measured values and the propagation of these errors in the final results, is an essential factor in determining the quality of the collected data and how it is representative of the targeted facts to be measured. Furthermore, knowledge of the uncertainty concept advises experimentalists on the design and selection of the instrumentation required to conduct accurate measurements that meet expectations [121].

Various sources of errors can influence measured value such that the measured value deviates from the true value. This deviation (or error) can be classified as bias error and precision error. These errors may also be referred to as systematic error and random error. These two categories are components of the uncertainty of a measured value. The difference between systematic and random errors is that systematic error, caused by one source, does not vary for multiple readings. This type of error can be evaluated through a calibration process. In contrast, random error exhibits variations around an average value, which can be statistically treated. In cases where the number of samples is so small that statistical error limits cannot be established, other methods such as experience and judgment are used to set error limits [122].

### 4.5.1. Random Error Uncertainties

For an  $N$  number of measurements of an  $X$  physical quantity, the mean value of  $X$  is given as:

$$\bar{X} = \frac{1}{N} \sum_{i=1}^N X_i \quad (4.4)$$

The variance  $S_X^2$ , is a measure of precision independent of sample size, and calculated as:

$$S_X^2 = \frac{1}{N-1} \sum_{i=1}^N (X_i - \bar{X})^2 \quad (4.5)$$

The standard deviation (square root of the variance) is then calculated as:

$$S_X = \left[ \frac{1}{N-1} \sum_{i=1}^N (X_i - \bar{X})^2 \right]^{0.5} \quad (4.6)$$

The standard deviation is a key parameter in indicating the precision of a certain measurement which is widely used method. For example, in the case where systematic error is assumed to be negligible, the uncertainty can be written as:

$$U_X = S_X \quad (4.7)$$

Accordingly, the measured  $X$  value can be written with associated uncertainties as:

$$X = \bar{X} \pm U_X \quad (4.8)$$

It is important to note that the magnitude of the random error can be reduced by increasing the number of measurements.

#### 4.5.2. Systematic Error Uncertainties

Unlike random error that can be quantified through a well-established statistical procedure, systematic error is more difficult to evaluate. Furthermore, systematic error is not affected by increasing the number of measurements. Thus, it cannot be reduced or eliminated by repetitions due to the nature of the systematic error pertaining to the method, the instrument, or data processing. Therefore, the accuracy of measured value depends significantly on the appropriate assessment of the systematic error uncertainty. The agreement of two completely independent measurement methods is the primary indicator of low systematic error [122]. Finally, it must be emphasized that systematic uncertainty should be reduced as much as possible but shall never be higher than the random error, otherwise estimation of random error becomes meaningless.

### 4.5.3. Combination of Uncertainties and Error Propagation

Combinations of both random and systematic error components are used to quantify the uncertainty in a measured value. The International Committee for Weights and Measures (CIPM) recommends that uncertainty of measurement be grouped into two types based on the methods of estimating these uncertainties: A type, which includes the method of statistical treatment and B type, which includes any other means of estimation [123]. Accordingly, the use of calibration data and manufacturer's specifications fall under B type. Therefore, considering a systematic uncertainty  $U_B$ , a total combined uncertainty can be written as:

$$U_i = (U_B^2 + U_X^2)^{0.5} \quad (4.9)$$

In the case of an  $F_x$  value to be determined from  $X_1, X_2, X_3, \dots$  primary measured values, the error propagated to the determined value as a result of uncertainties in measured values can then be estimated as follows:

$$\delta F = \left\{ \sum_{i=1}^N \left( \frac{\partial F}{\partial X_i} \delta X_i \right)^2 \right\}^{0.5} \quad (4.10)$$

Here,  $\delta X_i$  is the uncertainty associated with measured value  $X_i$  and the  $\delta F$  is the determined uncertainty in the value of  $F_x$ , calculated as shown above. The Engineering Equation Solver (EES) software [124] is used to calculate the propagated errors based on the provided error limit. A detailed example on uncertainty calculation is provided in Appendix 2.

## **Chapter 5: Development of SOE Systems**

In this chapter, large-scale hydrogen production through high-temperature solid oxide electrolyzers (SOEs) is investigated under two main objectives: (1) to examine the energy, exergy and exergoeconomic performance of a modular SOE unit for hydrogen production; and (2) to examine the integration opportunities of high temperature SOEs into a solar tower power plant for hydrogen production. In this regard, the system layout of an independent SOE is first presented, showing the different components and stream lines into and out of the SOE stacks. The issue of compressed hydrogen storage is addressed through a consideration of a second case that takes into account the energy required for hydrogen storage. Secondly, the integration of the SOEs for efficient solar hydrogen production is examined by considering a concentrating solar power (CSP) technology, namely a solar power tower.

### **5.1. SOE for Hydrogen Production**

Thermal design concepts are utilized to develop the proposed systems and to optimize their thermal performance for maximum exergy efficiency and minimum hydrogen production cost.

#### **5.1.1. SOE for Hydrogen Production**

The layout of the proposed SOE system is illustrated in Fig. 5.1. The main components of the system are shown as part of the overall system according to the reactant flow streams. The system is designed for hydrogen production utilizing two input streams, electricity and water. This electrolysis system can be employed to meet industrial hydrogen demands in many applications and at various capacities. Hence, the scale of the proposed SOE is 1 MW<sub>e</sub> input capacity.

The different SOE system components are classified into two categories: the stacks and the balance of plant (BOP). The stack-related components are the solid oxide cells, interconnects, sealing, and reactant manifolds while, under the BOP, the equipment required to provide the reactants to the stack at the desired conditions includes the pump, heat exchangers, compressor, heaters, converter and hydrogen separator.

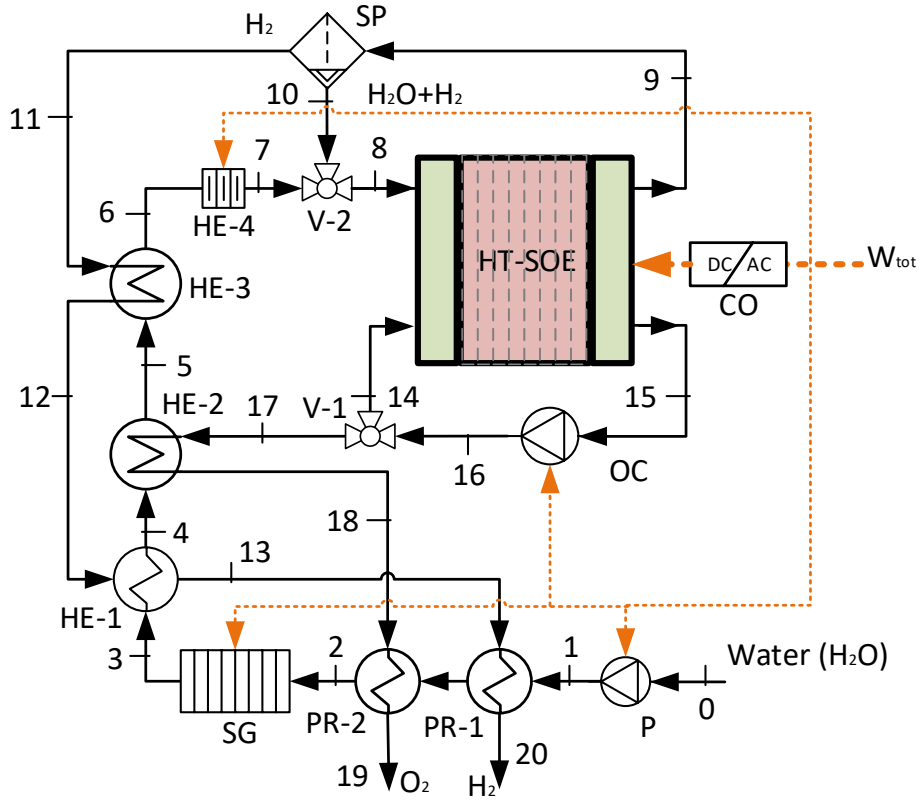


**Figure 5.1 Schematic representation of the SOE hydrogen production plant.**

Table 5.1 provides the component list of the BOP and their relevant specifications. A pump is used to adjust the feed water pressure to the stack operating pressure. The heat exchangers (recuperators) are integrated to heat the entering feedwater/steam while cooling the exiting hydrogen and oxygen streams, to minimize heat losses and electricity demand and increase SOE system efficiency. An electric heater is used to provide any additional heat required to ensure the inlet stream to the stack is at the stack operating temperature. An oxygen circulation blower is also employed to circulate the oxygen through the stacks' anode manifolds. The continuous circulation of oxygen through the stack oxygen electrodes enhances temperature uniformity. Further details on oxygen handling in the context of SOE can be found elsewhere [125]. Since an SOE stack operates on DC, an AC/DC converter is used to convert the AC power, provided by the distribution grid, to high current DC power that matches the SOE stack requirements. In this study, a conservative efficiency of 95% is assumed while in the literature [126] an efficiency of 98% is used.

**Table 5.1 List of BOP components and their performance merits.**

The balance of plant components	Parameter	Reference
Water pump (P) efficiency	70%	[127]
Steam generator (SG) efficiency	98%	[128]
Electric heater (EH) efficiency	98%	[128]
Heat exchangers (HE) effectiveness	95%	[129]
AC/DC converter (CO) efficiency	95%	[130]
Oxygen circulation blower (OC) efficiency	75%	[131]
Hydrogen compressors (HC)	75%	[132]

Under steady state operation of the SOE system, electricity and water are the only inputs for hydrogen and oxygen production. Water is pumped from ambient conditions through preheaters before it is introduced to an electric steam generator, which is used to produce steam. This steam is subsequently heated in multiple recuperators (as shown in Fig. 5.1) before it is injected into the stack. The steam temperature may require further superheating by an electric heater to match the stack temperature. Just before injection to the stack, the steam is mixed with about 10 mol.% hydrogen, to prevent excessive cathode oxidation [133], utilizing a hydrogen recycling feed. The hydrogen recycling system, which has been experimentally proven to be effective, eliminates external hydrogen supply requirements [134]. The electrochemical reaction takes place within the stack at active cell areas, and the produced hydrogen, mixed with the remaining steam, will leave the stack. In the current analysis, the steam utilization factor is set to about 85%. Thus, the remaining unreacted steam is circulated back from the separator with the required hydrogen percentage to maintain the desired stack inlet steam/hydrogen composition. At the anode side of the solid oxide cells, where oxygen evolves, a portion of the produced oxygen is circulated to maintain uniform temperature distribution and to sweep the produced oxygen from the stacks. Since the produced hydrogen and oxygen streams leave the stacks at high temperature, their heat is recovered, before being compressed and stored for end-use. The stack design in the present SOE model is assumed to be of 50-cells that are planar SOECs of  $20 \times 20 \text{ cm}^2$  square-shaped, with a total active area of  $3240 \text{ cm}^2$  [134]. Each cell is made of a cathode, an electrolyte and an anode made of nickel yttria-stabilized zirconia (NiYSZ), yttria-stabilized zirconia (YSZ), and lanthanum strontium manganite (LSM), respectively. The cells are cathode-supported (hydrogen electrode) with a thickness of  $312 \text{ }\mu\text{m}$ . The electrolyte and the anode (the oxygen electrode) have average thicknesses of  $12.5 \text{ }\mu\text{m}$  and

17.5  $\mu\text{m}$ , respectively [80]. Different SOE stack designs can be found in the literature, some of which are proposed and modeled [65] while others are experimentally tested [134]. An approximate total of 34 stacks, with a total of 1700 cells, is required to meet the targeted capacity.

### 5.1.2. SOE for Compressed Hydrogen Production

In another case, the produced hydrogen is compressed to a pressure of 15 MPa for storage. The layout of the SOE system, with the hydrogen compression storage, is presented in Fig. 5.2.

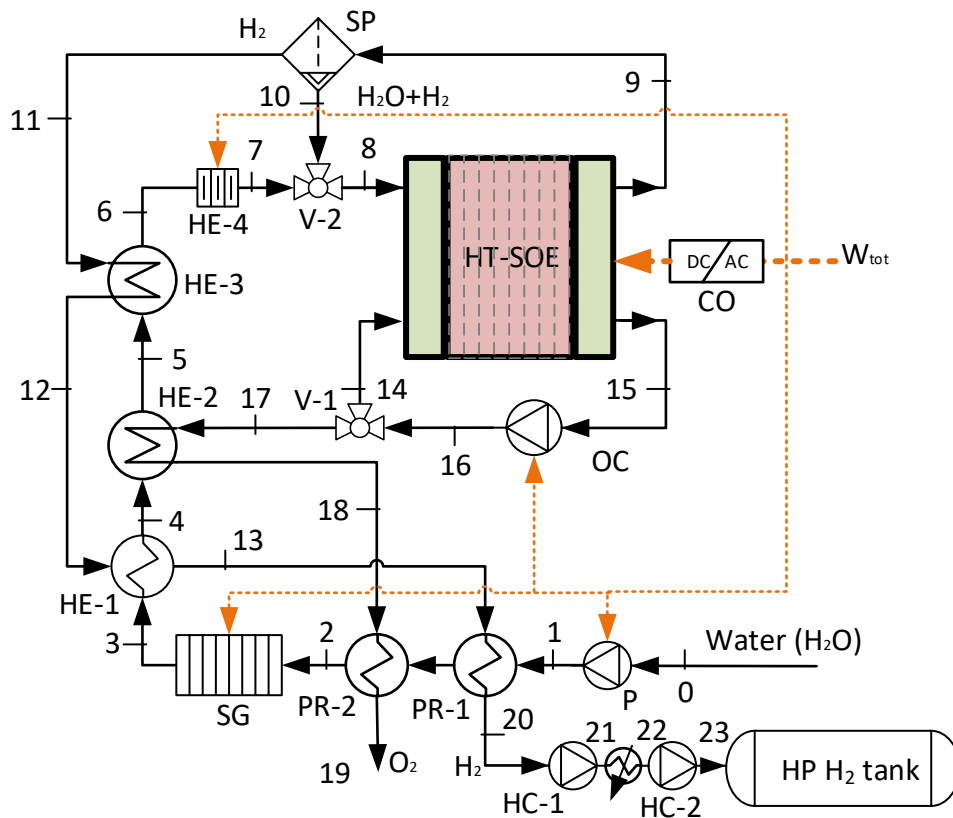


**Figure 5.2** The SOE system layout including a hydrogen compression unit.

The high pressure storage of hydrogen is one of the most convenient methods of hydrogen storage [135], but the energy required for compression can be prohibitive. Therefore, the system performance, including the compression work, is included in the analysis in order to provide a practically reasonable assessment. The compressor isentropic efficiency is assumed to be 75%, about an average of 65–80% that has been used by Parks et al. [132].

In this case, the effect of utilizing an additional hydrogen compression unit can be investigated and compared with high pressure stack operation which produces hydrogen at a relatively high pressure. Furthermore, trade-offs between a compressed system and after-production compression can be examined. Thus, the advantages brought by increasing the stack operating pressure do not compromise stack durability and cost due to stack and system upgrading requirements to withstand high pressure stresses. Similarly, the benefit of design simplicity will not be compromised by the extensive energy required for compressing the final hydrogen product.

## 5.2. Solar Tower Powered SOE

A solar tower SOE integrated system consists of four subsystems: (1) a solar tower; (2) thermal energy storage (TES); (3) an SOE and (4) an S-CO<sub>2</sub> Brayton cycle. A full schematic representation of the proposed integrated system is illustrated in Fig. 5.3.

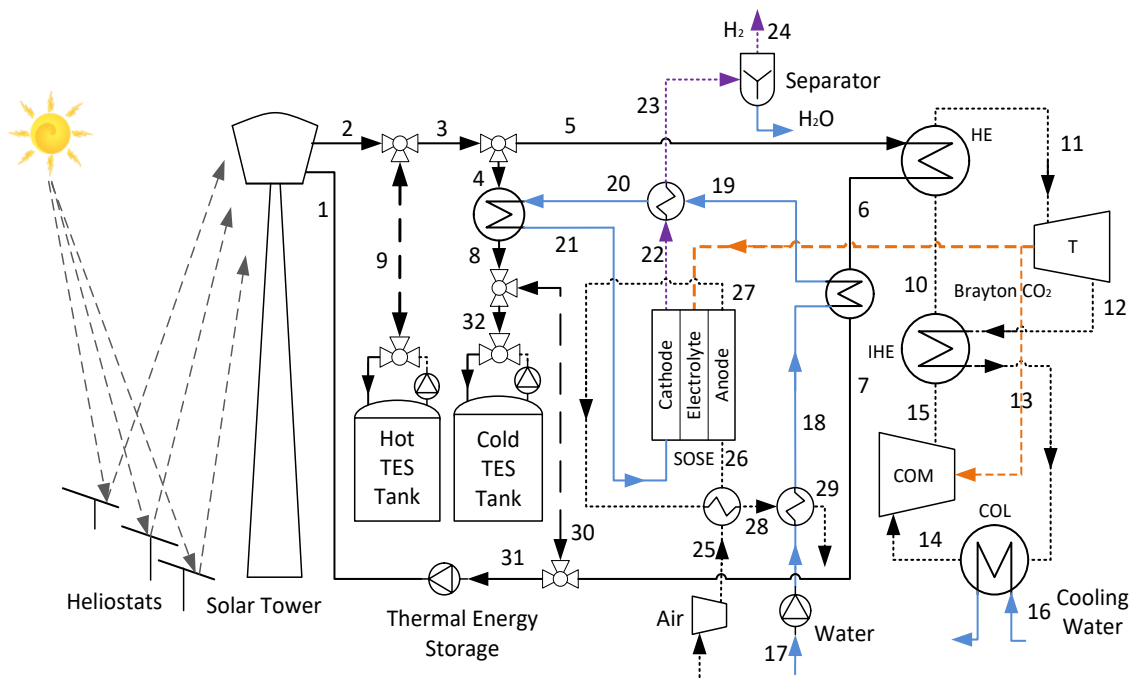


**Figure 5.3 Schematic representation of the solar tower powered SOE for hydrogen production [40].**

A heliostats and solar tower subsystem is used to collect solar energy and to bring a heat transfer fluid (HTF) to a high temperature for use in a power cycle subsystem for power generation. A major portion of the thermal energy, as well as the power produced by the S-CO<sub>2</sub> Brayton power cycle, is used to power a high temperature SOE in order to produce

hydrogen. Furthermore, to maintain continuous operation, a TES, which utilizes and stores peak solar production for later use during cloudy days or at night time, is incorporated. A further explanation of each subsystem is provided in the sections that follow.

### 5.2.1. Solar Tower

The heliostats and solar tower subsystem consists of a number of mirrors distributed in circular arrays to reflect and concentrate solar radiation into a central receiver, which is placed at the top of the solar tower. The solar tower is centered in an optimized location to intercept as much as possible of the reflected radiation by the heliostat mirrors. The HTF is circulated through the receiver to absorb radiation heat and transport it either to the hot tank TES or directly to the power cycle and steam heating heat exchanger. Solar tower technology is capable of providing high temperatures up to 2200 K [136], which makes it a promising integration option, particularly with systems such as the S-CO<sub>2</sub> Brayton cycle and high temperature SOE, since these systems demonstrate optimum performance at high operating temperatures. The numerical values and assumptions used for the reference case modeling are listed in Table 5.2. A detailed description and thermodynamic analysis of the solar tower can be found in [40].

**Table 5.2 Main parameters used for solar tower modeling.**

Parameter	Value
Heliostats optical efficiency	75% [137]
Receiver efficiency. Xu et al. [137] study suggested 90%	87.5% [138]
Heliostats field area (m <sup>2</sup> )	6000
Design direct radiation (W m <sup>-2</sup> )	850
Solar multiple	~2

### 5.2.2. Thermal Energy Storage

The TES subsystem, which has two tanks of hot TES and cold TES, is integrated between the solar tower subsystem and the power cycle, and the SOE subsystems. Thereby, the TES subsystem can play an intermediate role according to solar availability and can eliminate any fluctuation that may arise from clouds or weather changes. The working principle of the current TES subsystem is as follows: during normal operation, the heliostats field is designed to produce enough energy for day and night operation as well as peak production hours, which are mainly around noon time when a large portion of the HTF mass is pumped into the hot TES tank in addition to the other portion that is sent to the power and SOE

subsystems. However, when the thermal energy coming from the solar field begins to decline, the hot TES starts discharging in order to maintain stable operation. When the sun is not available, the HTF that is discharged from the hot tank and used in the power and SOE subsystems is then stored in the cold TES tank.

**Table 5.3 Composition and heat transfer properties of selected high temperature molten salt (LiF-NaF-KF) at 973 K [139].**

Parameter	Value
Salt composition (mol.%)	46.5-11.5-42
Formula weight (kg kmol <sup>-1</sup> )	41.3
Melting point (K)	727
Boiling point (K) (estimated by extrapolation)	1843
Vapor pressure (mm Hg) at (1173 K)	~ 0.7
Density (g cm <sup>-3</sup> )	2.02
Volumetric heat capacity (Cal cm <sup>-3</sup> K)	0.91
Viscosity (cP)	2.9
Thermal conductivity (W m <sup>-1</sup> K <sup>-1</sup> )	0.92

In the current system, fluoride salt (LiF-NaF-KF) is used as an HTF and as a sensible heat storage medium. Therefore, this fluoride salt is circulated between the four subsystems transporting heat from the central receiver to the power cycle and SOE passing through the TES. Molten salts, such as binary nitrate salt, commercially known as Hitec solar salt, (60 wt.% NaNO<sub>3</sub>- 40 wt.% KNO<sub>3</sub>) has been successfully implemented in a number of operating plants, e.g., the (GemSolar) Thermosolar Plant in Andalusia, Spain, with a turbine capacity of 19.9 MW [140]. In this plant, 2-tank direct TES, with 15 hours of storage capacity, is installed. However, these plants are limited to a maximum operating temperature below 580°C (the maximum temperature that nitrate salts may withstand before decomposition) which limits the plant's conversion efficiency. The selection of fluoride molten salt is driven by the high temperature operation requirements (>700°C) to increase power cycle conversion efficiency and reduce SOE ohmic losses. Moreover, Forsberg et al. [141] proposed fluoride molten salts as an HTF between a solar tower and a Brayton cycle to raise the cycle conversion efficiency to about 50%. The chemical composition and heat transfer properties of the selected eutectic fluoride molten salt are listed in Table 5.3. It can be clearly noticed that this salt has low vapor pressure and good heat transfer properties, making it very suitable for the current system. Further detail of the fluoride salt properties, corrosion tests and performance relative to other candidate molten

salts is presented in the literature [139], [142], [143]. A thermodynamic analysis and the performance of this TES, including the energy and exergy efficiencies, are presented in [40].

### **5.2.3. S-CO<sub>2</sub> Brayton Power Cycle**

The S-CO<sub>2</sub> Brayton power cycle is selected for power provision because of the advantages that this cycle has to offer compared with steam power cycles. These advantages are: high efficiency, especially for elevated operating temperatures, and relatively small volume. For example, Dostal [144] predicted that regenerative S-CO<sub>2</sub> achieves over 50% conversion efficiency. The Sandia National Laboratory tested the practical processes of CO<sub>2</sub> cycles [145] while AlZahrani et al. [40], [146]–[148] examined different configurations of transcritical CO<sub>2</sub> cycles as part of integrated renewable energy systems. In addition, Santini et al. [149] highlighted the power plant volume reduction that can be achieved by adopting S-CO<sub>2</sub> power cycles.

In the present study, the power subsystem has five components: (1) a primary heat exchanger; (2) a turbine; (3) an internal heat exchanger; (4) a cooler; and (5) a compressor. CO<sub>2</sub> is used as a working fluid in a closed loop in which CO<sub>2</sub> gas is heated to a high temperature in the primary heat exchanger and allowed to expand in a CO<sub>2</sub> turbine where the high velocity CO<sub>2</sub> drives the turbine blades generating a shaft work. Subsequently, the CO<sub>2</sub> leaves the turbine at a low pressure and a relatively high temperature. Therefore, it is sent to an internal heat exchanger to further reduce the temperature and recover energy contents before passing to a cooling unit. The cooling unit reduces the CO<sub>2</sub> gas temperature to facilitate and reduce the compression power needed by the compressor. The high pressure CO<sub>2</sub> leaves the compressor to be heated in two stages: in the internal heat exchanger by the hot CO<sub>2</sub> stream and in the primary heat exchanger by the HTF. The T-s diagram of the s-S-CO<sub>2</sub> Brayton cycle is illustrated in Fig. 5.4. Further detail on the analysis and the performance of this subsystem can be found in [38].

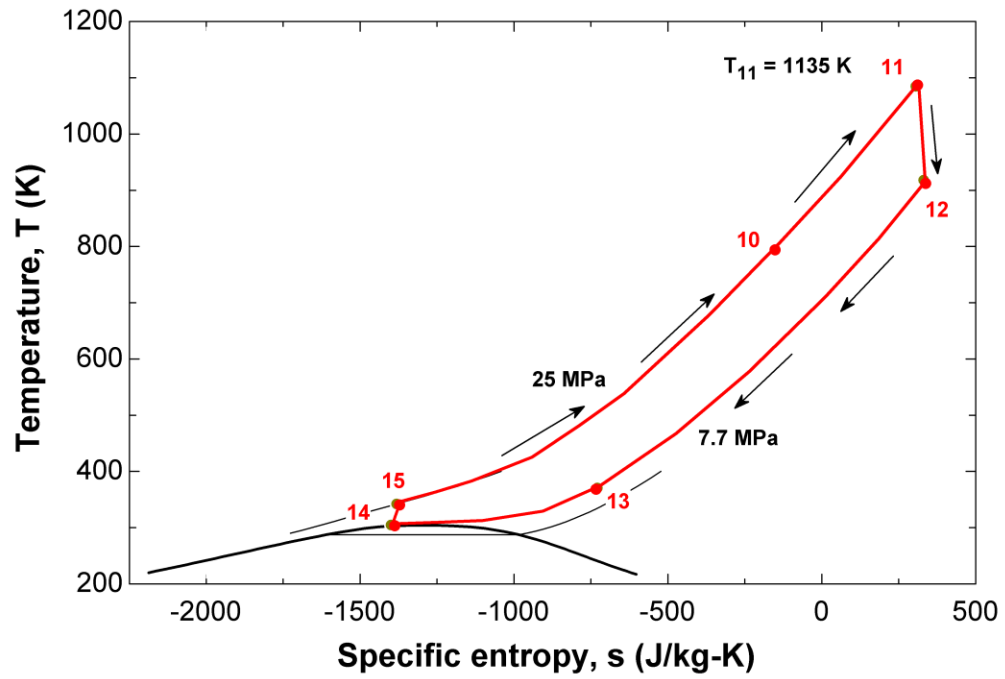


Figure 5.4 T-s diagram of the CO<sub>2</sub> Brayton power cycle, according to the numbering system presented in Fig. 5.1.

## Chapter 6: Analysis, Modeling and Optimization

In this chapter, analyses of the systems described in Chapter 5 are presented. Due to both the integrated nature of the proposed systems and the multidisciplinary nature of some components, this chapter is organized in five sections following the modeling approach. First, the photonic nature of sunlight is treated according to the thermodynamic approach in attempting to define the energy and exergy efficiencies of a concentrator. A Classical thermodynamic analysis follows, including both the energy and exergy performance of each component. The subsequent section is dedicated to the electrochemical analysis of the SOEC.

The economic aspects of the proposed SOE system are then considered, where an exergoeconomic analysis is presented following the well-established “exergy-costing” approach in order to identify the cost of produced hydrogen through a detailed accounting trace of cost buildup through the various involved streams, leading to the final product.

The final section is dedicated to optimization, where both deterministic and stochastic optimization methods are used to suggest the designs and operating parameters that yield optimal efficiency and lower cost.

### 6.1. Analyses of Solar Concentrator

Considering a solar concentrator for harvesting solar radiation, it is recognized that sunlight first hits a reflective mirror before hitting the PSOC. In order to track the radiation energy flow and evaluate the different losses, the microscopic approach of effective photon temperature, as presented in [41], [150], will be adapted in the current analysis. Accordingly, and as an implication of the notion that photon interaction with matter is a form of work, photon energy is considered as an equivalent to photon exergy and given as:

$$E = h\nu \quad (6.1)$$

where  $h$  is Planck constant and  $\nu$  is the frequency which is related to wavelength  $\lambda$  through the formula:

$$\nu = \frac{c}{\lambda} \quad (6.2)$$

Furthermore, thermal radiation illustrates an important aspect of photon interaction with matter that photons behave thermal energy carriers; however there is no established relation can put this photo thermal energy in the context of temperature based on the photon characteristics parameters such as wavelength  $\lambda$ , energy  $h\nu$ , and mass  $h/\lambda c$ .

In an effort to fill this gap Chen et al. [150] defined two additional parameters, an effective photon temperature  $T_\lambda$  given as:

$$T_\lambda = \frac{c_\lambda}{\lambda} \quad (6.3)$$

Here,  $c_\lambda = 0.00533026$  mK, based on the assumption introduced by Chen et al. [150] that for any photon  $c_\lambda = T_\lambda \lambda$ . The other parameter is an entropy constant  $S_{ph}$  defined as:

$$S_{ph} = \frac{hc}{c_\lambda} \quad (6.4)$$

Accordingly, Carnot energy conversion factor can be defined for at a reference temperature  $T_0$  as:

$$\eta_\lambda = 1 - \frac{T_0}{T_\lambda} \quad (6.5)$$

Further details on the derivation and conceptual justification are available in [150]. In the context of treating photon interactions as thermal radiation transfer processes rather than work. A reference spectrum is assumed  $I_\lambda$ , based on which solar radiation exergy and energy are determined as:

$$\dot{S} = \int_0^\infty \frac{I_\lambda}{T_\lambda} d\lambda = \frac{1}{T_{rad}} \int_0^\infty I_\lambda d\lambda \quad (6.7)$$

Here, the radiation temperature  $T_{rad}$  depends on the assumed reference spectrum  $I_\lambda$ . Now, for each point  $i$  within our system we can define energy rate:

$$\dot{E}_i = \int_0^{\infty} \dot{E}_{i,\lambda} d\lambda \quad (6.8)$$

where  $\dot{E}_{i,\lambda}$  is evaluated as  $\dot{E}_{i,\lambda} = A_i I_{DNI\lambda}$ .

Also entropy rate is written as:

$$\dot{S}_i = \int_0^{\infty} \frac{\dot{E}_{i,\lambda}}{T_\lambda} d\lambda \quad (6.9)$$

and photonic temperature as:

$$T_i = \frac{\dot{E}_i}{\dot{S}_i} \quad (6.10)$$

This lead to the exergy rate definition as:

$$\dot{E}x_i = \left(1 - \frac{T_0}{T_i}\right) \dot{E}_i \quad (6.11)$$

Having energy and exergy rates evaluated at all state points of the system; we can define as energy and exergy efficiency of solar tower as:

$$\eta_s = \frac{\dot{E}_{out}}{\dot{E}_{in}} \quad (6.12)$$

$$\psi_s = \frac{\dot{E}x_{out}}{\dot{E}x_{in}} \quad (6.13)$$

## 6.2. Thermodynamic Analyses

The principles of thermodynamics provide the framework of the current analysis, considering a steady state operating the mass, energy and entropy rate balance equations can be written over a control volume, assumed around component, as:

$$\sum_i \dot{m}_i - \sum_e \dot{m}_e = 0 \quad (6.14)$$

$$\dot{Q}_{cv} - \dot{W}_{cv} + \sum_i \dot{m}_i h_i - \sum_e \dot{m}_e h_e = 0 \quad (6.15)$$

$$\sum_j \frac{\dot{Q}_j}{T_j} + \sum_i \dot{m}_i s_i - \sum_e \dot{m}_e s_e + \dot{S}_{gen} = 0 \quad (6.16)$$

Now, the exergy balance equation for steady state operation can be written as:

$$\sum_j \left(1 - \frac{T_0}{T_j}\right) \dot{Q}_j - \dot{W}_{cv} + \sum_i \dot{m}_i ex_i - \sum_e \dot{m}_e ex_e - \dot{E}x_D = 0 \quad (6.17)$$

Here,  $ex$  represents the specific exergy at each of the system streams, which combines both physical and chemical specific exergies:

$$ex_j = ex_j^{PH} + ex_j^{CH} \quad (6.18)$$

The physical specific exergy at any state point  $j$  in the system is given as:

$$ex_j^{PH} = (h_j - h_0) - T_0(s_j - s_0) \quad (6.19)$$

The chemical specific exergy is commonly evaluated for different species and tabulated in a number of thermodynamics books. For a stream containing a mixture of  $k$  species:

$$ex^{CH} = \sum x_k ex_k^{CH} \quad (6.20)$$

The exergy destruction rate is given in terms of entropy generation rate per component and ambient temperature as:

$$\dot{E}x_D = T_0 \dot{S}_{gen} \quad (6.21)$$

In the context of an electrolysis cell, the energy and entropy balance equations can be used to write the following equation:

$$\dot{W}_{cv} = -\Delta\dot{H} + T\Delta\dot{S} - T\dot{S}_{gen} \quad (6.22)$$

Knowing that Gibbs free energy is given, in rate of change form, as:

$$\Delta\dot{G} = \Delta\dot{H} + T\Delta\dot{S} \quad (6.23)$$

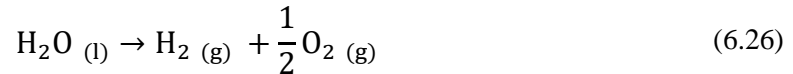
the cell work can be written as:

$$\dot{W}_{cv} = -\Delta\dot{G} - T\dot{S}_{gen} \quad (6.24)$$

According to the second law of thermodynamics any real process involves some entropy generation ( $\dot{S}_{gen} \geq 0$ ), and only for reversible processes entropy generation can be assumed equal zero. In this idealized case, irreversibilities which commonly associated with heat generation/consumption are minimal and set equal to zero. The cell work is then, the maximum work and given as:

$$\dot{W}_{cv} = -\Delta\dot{G} \quad (6.25)$$

Water decomposition reaction is an endothermic reaction with change in Gibbs free energy of  $\Delta G = 238 \text{ kJ mol}^{-1}$ .



Accordingly, this reaction is a nonspontaneous reaction and unless this energy is externally supplied this reaction is impossible. The total theoretical energy required to derive the electrochemical reaction in an SOEC is given as:

$$\Delta h = \Delta g + T \Delta s \quad (6.27)$$

where  $\Delta G$  is change in Gibb's free energy, and represents the electric energy; while  $T \Delta S$  (product of change in Entropy and absolute temperature) represents the thermal energy.

The reversible cell potential, is then determined at standard T and P conditions as:

$$E_r = \frac{\Delta g}{nF} \quad (6.28)$$

At any operating pressure or temperature, the SOEC reversible cell potential at equilibrium is given by Nernst equation as:

$$E_r(T, P_i) = E_r - \frac{RT}{nF} \ln \left( \frac{P_{H_2} P_{O_2}^{1/2}}{P_{H_2O}} \right) \quad (6.29)$$

Then, the practical cell potential is evaluated as the summation of the activation, ohmic, and concentration polarizations, in addition to reversible cell potential, and written as:

$$E = E_r + \eta_{act} + \eta_{ohm} + \eta_{conc} \quad (6.30)$$

### 6.2.1. Energy and Exergy Efficiencies of SOEC

The energy and exergy efficiencies are defined for SOEC as given in [59] as:

$$\eta_{en,SOEC} = \frac{\dot{m}_{H_2} LHV_{H_2}}{\dot{W}_{SOEC} + Q_{SOEC}} \quad (6.31)$$

$$\eta_{ex,SOEC} = \frac{\dot{m}_{H_2} ex_{H_2}}{\dot{W}_{SOEC} + Ex_{Q_{SOEC}}} \quad (6.32)$$

Here,  $ex_{H_2}$  is the produced hydrogen specific exergy and calculated as:

$$ex_{H_2} = ex_{H_2}^{PH} + ex_{H_2}^{CH} \quad (6.33)$$

where  $ex_{H_2}^{PH}$  is the physical specific exergy of hydrogen at the exist state.

$$ex_{H_2}^{PH} = h_{24} - h_0 - T_0(s_{24} - s_0) \quad (6.34)$$

and the chemical specific exergy is given as  $ex_{H_2}^{CH}=236,100 \text{ kJ kmol}^{-1}$ , according to Bejan et al. [151].

### 6.2.2. Energy and Exergy Efficiencies of SOE

The power density consumed by a single SOEC is determined as:

$$W_{cell} = EJ \quad (6.35)$$

The AC power converter to the stack is now given as:

$$\dot{W}_{st} = (W_{cell}A_{cell}N_{cells})/\eta_{co} \quad (3.36)$$

However, the total AC power consumed by the SOE system is evaluated as the summation of power consumed by the stacks and the BOP; i.e., the water pump, steam generator, oxygen circulation blower, and the electric heater:

$$\dot{W}_{tot} = \dot{W}_{st} + \dot{W}_P + \dot{W}_{SG} + \dot{W}_{OC} + \dot{Q}_{EH} \quad (3.37)$$

For the case of hydrogen compression storage, an additional term is added to account for hydrogen compression power. Thus, the total power becomes:

$$\dot{W}_{tot} = \dot{W}_{st} + \dot{W}_P + \dot{W}_{SG} + \dot{W}_{OC} + \dot{W}_C + \dot{Q}_{EH} \quad (3.38)$$

The energy and exergy efficiencies of the SOE system can be defined by considering the various possible operating conditions, i.e., exothermic and endothermic conditions where the stacks produce or consume heat, respectively. Accordingly, based on the heat direction, the energy efficiency is defined as:

$$\eta_{en} = (\dot{m}_{H_2}LHV)/(\dot{W}_{tot} + \dot{Q}_{SG}) \quad \text{for } \dot{Q}_{st} < 0 \quad (3.39)$$

$$\eta_{en} = (\dot{m}_{H_2} LHV) / (\dot{W}_{tot} + \dot{Q}_{SG} + \dot{Q}_{st}) \quad \text{for } \dot{Q}_{st} > 0 \quad (3.40)$$

The exergy efficiency is similarly defined as:

$$\eta_{ex} = [\dot{m}_{H_2} (ex_{H_2}^{CH} + ex_{H_2}^{PH})] / (\dot{W}_{tot} + \dot{Q}_{SG}) \quad \text{for } \dot{Q}_{st} < 0 \quad (3.41)$$

$$\eta_{ex} = [\dot{m}_{H_2} (ex_{H_2}^{CH} + ex_{H_2}^{PH})] / (\dot{W}_{tot} + \dot{Q}_{SG} + \dot{Q}_{st}) \quad \text{for } \dot{Q}_{st} > 0 \quad (3.42)$$

For the second case presented in Fig. 5.2, where hydrogen compression to 15 MPa for storage is included as part of the SOE system electric power requirement, the energy and exergy efficiencies are defined, respectively, as:

$$\eta_{en,c} = (\dot{m}_{H_2} LHV) / (\dot{W}_{tot} + \dot{Q}_{SG} + \dot{W}_c) \quad \text{for } \dot{Q}_{st} < 0 \quad (3.43)$$

$$\eta_{en,c} = (\dot{m}_{H_2} LHV) / (\dot{W}_{tot} + \dot{Q}_{SG} + \dot{Q}_{st} + \dot{W}_c) \quad \text{for } \dot{Q}_{st} > 0 \quad (3.44)$$

$$\eta_{ex,c} = [\dot{m}_{H_2} (ex_{H_2}^{CH} + ex_{H_2}^{PH})] / (\dot{W}_{tot} + \dot{Q}_{SG} + \dot{W}_c) \quad \text{for } \dot{Q}_{st} < 0 \quad (3.45)$$

$$\eta_{ex,c} = [\dot{m}_{H_2} (ex_{H_2}^{CH} + ex_{H_2}^{PH})] / (\dot{W}_{tot} + \dot{Q}_{SG} + \dot{Q}_{st} + \dot{W}_c) \quad \text{for } \dot{Q}_{st} > 0 \quad (3.46)$$

From the physical perspective, equations (3.39-3.46) relate the SOE performance to the actual operating mode and operating conditions. For example, equations (3.39) and (3.40) assess the SOE system energy performance by relating the rate of hydrogen production to the total energy input, which involves two cases covering both endothermic and exothermic operating modes. Equations (3.41) and (3.42) are similar to equation (3.39) and (3.40) with one difference: the formers consider, as part of the energy input, the compression power required to store hydrogen at 15 MPa. Equations (3.43–46) examine exergy performance while considering the chemical and physical exergy output of produced hydrogen over the total exergy inputs, which vary according to either endothermic or exothermic modes as well as whether a compression power is included.

### 6.3. Electrochemical Analysis

The thermodynamic analysis of the electrolysis cell provides valuable information such as whether a reaction will occur spontaneously or not, and if not how much energy is needed to drive that reaction. Through the thermodynamic analysis, the cell potential is calculated. However, further cell performance related details such internal cell reactions and losses cannot be obtained from a thermodynamic analysis alone and an electrochemical analysis is required to investigate the different processes that occur in an electrolysis cell.

The activation polarization is given by the Butler-Volmer equation as:

$$J = J_0 \left[ \exp\left(\frac{\alpha n F \eta_{a,act}}{RT}\right) - \exp\left(-\frac{(1-\alpha) n F \eta_{c,act}}{RT}\right) \right] \quad (6.47)$$

The activation polarization attributed to electrodes: anode and cathode is given as:

$$\eta_{act,i} = \frac{RT}{nF} \sinh^{-1} \left( \frac{J}{2J_{0,i}} \right) \quad (6.48)$$

where

$$J_{0,i} = \gamma_i \exp\left(-\frac{E_{act,i}}{RT}\right) \quad (6.49)$$

Here,  $i$  can be either  $a$  or  $c$  corresponding to anode and cathode, respectively. The ohmic polarization is calculated as:

$$\eta_{ohm} = \rho \delta J \quad (6.50)$$

where  $\rho$  is the material resistivity and  $\delta$  is the element thickness. Accordingly, the contribution of each of cell components may be written as:

$$\eta_{ohm} = (\rho_a \delta_a + \rho_c \delta_c + \rho_e \delta_e) J \quad (6.51)$$

where the resistivity and thickness are written corresponding to the anode, cathode, and electrolyte materials as given in literature [30], [152].

The concentration polarization is determined based on evaluating the limiting current densities at each electrode as:

$$J_{L,a} = \frac{2 F P_{H_2,e} D_a^{\text{eff}}}{R T \delta_a} \quad (6.52)$$

and

$$J_{L,c} = \frac{4 F P_{O_2,e} D_c^{\text{eff}}}{\left(\frac{P - P_{O_2,e}}{P}\right) R T \delta_c} \quad (6.53)$$

where  $J_{L,a}$ ,  $D_a^{\text{eff}}$ ,  $J_{L,c}$  and  $D_c^{\text{eff}}$  are the limiting current density and effective diffusion coefficient at the anode and cathode, respectively. Thus, the total concentration polarization calculated as:

$$\eta_{\text{conc}} = -\frac{R T}{2 F} \ln\left(1 - \frac{J}{J_{L,a}}\right) + \frac{R T}{2 F} \ln\left(1 + \frac{P_{H_2} J}{P_{H_2 O} J_{L,a}}\right) - \frac{R T}{4 F} \ln\left(1 - \frac{J}{J_{L,c}}\right) \quad (6.54)$$

The steam utilization factor is defined as the number of moles of steam consumed over the total number of moles fed to the cell as:

$$U_{H_2 O} = \left[ (N_{H_2 O})_{in} - (N_{H_2 O})_{out} \right] / (N_{H_2 O})_{in} \quad (6.55)$$

The entropy generation can be evaluated as:

$$s_{gen} = nF(\eta_{act} + \eta_{ohm} + \eta_{conc})/T \quad (6.56)$$

Thus, the heat that the SOE cell/stack may require or produce (based on the mode of operating endothermic or exothermic) is given by:

$$q = T(s_{out} - s_{in}) - T s_{gen} \quad (6.57)$$

The area specific resistance (ASR) of the cell is determined as:

$$ASR = \frac{\Delta V}{\Delta J} \quad (6.58)$$

#### 6.4. Exergoeconomic Analysis

The exergoeconomic analysis is developed based on cost accounting for each stream either entering or exiting the system in addition to the system total cost  $\dot{Z}_k$ . The system total cost is defined the sum of capital cost and operating and maintenance cost, and written as:

$$\dot{Z}_k = \dot{Z}^{CL} + \dot{Z}^{OM} \quad (6.59)$$

Now, a costing rate can be assigned to each stream, based on which the cost of the product can be evaluated. This equation is given as:

$$\sum_e \dot{C}_{e,k} + \dot{C}_{w,k} = \dot{C}_{q,k} + \sum_i \dot{C}_{i,k} + \dot{Z}_k \quad (6.60)$$

Where each of these terms can be broken down into a product of an average cost per unit of exergy and an exergy rate as follows:

$$\dot{C}_e = c_e \dot{E}x_e \quad (6.61)$$

$$\dot{C}_w = c_w \dot{W} \quad (6.62)$$

$$\dot{C}_i = c_i \dot{E}x_i \quad (6.63)$$

$$\dot{C}_q = c_q \dot{E}x_q \quad (6.64)$$

Exergoeconomic analysis, can be undertaken starting with writing the exergoeconomic balance equation as:

$$\dot{C}_4 + \dot{C}_2 = \dot{C}_{Q_{ec}} + \dot{C}_{W_{EC}} + \dot{C}_1 + \dot{C}_3 + \dot{Z}_{EC} \quad (6.65)$$

This equation can be further detailed as:

$$c_4\dot{m}_4ex_4 + c_2\dot{m}_2ex_2 = c_{Q_{ec}}Ex_{\dot{Q}_{EC}} + c_{W_{EC}}\dot{W}_{EC} + c_1\dot{m}_1ex_1 + c_3\dot{m}_3ex_3 + \dot{Z}_{EC} \quad (6.66)$$

One of the performance indicator given by the exergoeconomic analysis is the exergoeconomic factor which can be determined for each component as follow:

$$f_k = \frac{\dot{Z}_k}{\dot{Z}_k + \dot{C}_L} \quad (6.67)$$

The exergoeconomic factor is a ratio of the levelized capital cost per unit time over the total levelized cost of the associated with the same component, i.e. capital cost plus exergy destruction and exergy losses costs.

## 6.5. SOE System Optimization

In a broad context, an optimization is a process of introducing changes to system structure design or operating parameter to improve performance and/or reduce cost. This process is usually bounded with a number of physical and financial limits within which an optimum solution is been sought. For the current study, two major aspects are the target of the optimization: the thermodynamic performance, and the economic potential. However, as these two aspects are competing criteria, commonly observed as increasing one such system efficiency increases also the other such as the cost while the aim is to increase efficiency and reduce cost. In this case a multiobjective optimization.

Though a number of studies have been conducted on the optimization SOFCs, e.g., [154], [155], few recent literature has been found on optimizing SOEC performance [156], [157], some of these studies considered parametric-based optimization rather than implementing an optimization algorithm. Since many variables are involved in determining the performance of SOEC, as clearly presented through the analyses, the optimization becomes more important. These variables include the operating and design parameters that their simultaneous change may differently influence the overall cell performance. Moreover, parametric studies are excellent in showing the overall trends in performance as a result of change in a single variable. However, it may not identify the optimum operating conditions.

Therefore, an optimization algorithm can be implemented to investigate the optimum operating conditions within a set of possibilities.

In any optimization problem, a primary step is defining an objective function expressed in a mathematical form. This function is then, chosen to be either maximized or minimized within a defined domain of variables. This variables domain is called search or design domain. The optimization problems are usually classified based on the number of objectives, if only one objective is to be optimized, the problem called then called single objective optimization problem [158]. However, if more than one objective is to be optimized the problem is called multiobjective optimization problem.

For the current study, the primary objective is to optimize the SOE performance. The objective function can be defined as the exergy efficiency of SOE, while the decision variables are the main operating conditions. The objective function:

$$F(\eta_{\text{exSOE}}) = F(T_{\text{st}}, P_{\text{st}}, J) \quad (6.68)$$

Subjected to the following constraints listed in Table 6.1. The temperature constrains are made to maintain low-to-intermediate operating temperature, as high operating temperature is undesirable. The operating pressure is allowed to vary from atmospheric pressure to a maximum of 700 kPa.

**Table 6.1 List of objective function constraints.**

Parameters	Constraints
Operating temperature (°C)	$500 \leq T_{\text{st}} \leq 950$
Operating Pressure (kPa)	$100 \leq P_{\text{st}} \leq 700$
Current density ( $\text{A m}^{-1}$ )	$5000 \leq J \leq 15000$

Though increasing the operating pressure may result in a favorable performance and lower hydrogen compression work requirement, it is commonly avoided in practical applications as it creates additional stresses on the cell components and thus reduces cells and stacks lifetime. In the case of steam concentration, current density and cell potential, they allowed to vary while maintaining operating in an electrolysis mode.

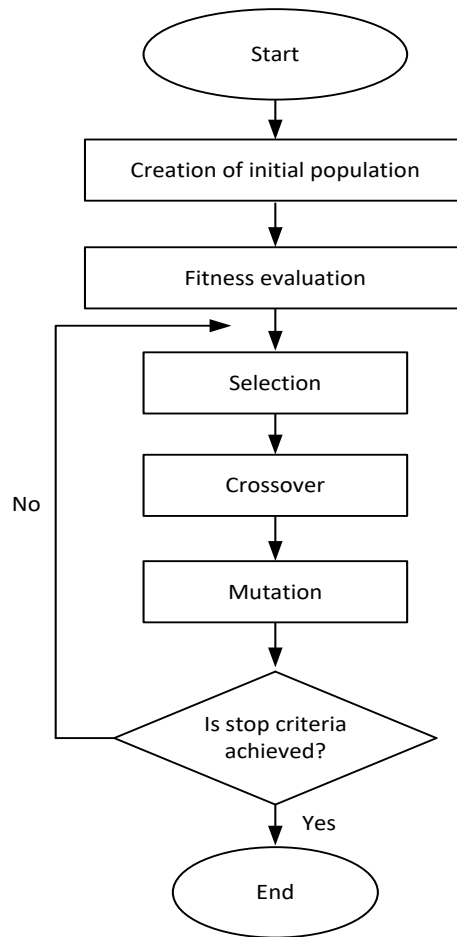


**Figure 6.1 Schematic flow chart of the GA optimization.**

Among different optimization algorithms Genetic Algorithm (GA) is selected for optimizing the efficiency as a function of the above listed variables. GA is inspired by the biological evolution and founded on the natural selection theory. GA method is widely used and characterized by its simple implementation and applicability to complex problems. In this algorithm, an appropriate fitness function is defined such that the solution with a higher fitness is selected [158]. This based on the crossover  $p_c$ , mutation  $p_m$  probabilities, and population size that are previously defined. It is important to realize that GA is a stochastic optimization algorithm and unless these parameters are carefully selected and initiated, the algorithm may not converge or give a misleading result. The operating scheme and flow chart of GA is illustrated in Fig. 6.1.

## 6.6. Scale-up Analysis

The concept and methodology of evaluating the cost of a product and how the price may change with changing the size of the process or manufacturing plant are comprehensively discussed by Turton et al. [153]. They considered the plant capital cost evaluation, the product manufacturing cost evaluation, and engineering economic and the profitability analyses. The effect of capacity on the cost of purchased equipment is given, according to [153], by:

$$\frac{CL_A}{CL_B} = \left(\frac{A}{B}\right)^n \quad (6.69)$$

Here, A and B are the equipment cost attributes, required and base, respectively, CL is the capital cost, and n is the cost exponent. The value of n depends on the type of the equipment and varies between 0.3–0.84. For example, for a reciprocating compressor with motor drive, n is 0.84, for heat exchangers n is about 0.59. The equation (6.69) can be rearranged, by setting  $K = CL_B/B^n$ , thus equation (6.69) can be written as:

$$CL_A = KA^n \quad (6.70)$$

This equation is widely known as the six-tenths rule.

In order to examine the impact of the system scale on the hydrogen production cost, a scale-up analysis is conducted. In this analysis, two hydrogen production representative scales are considered that are small scale and large-scale commercial plant. The small scale is aimed at meeting local distributed hydrogen demand at a capacity of 650 kg per day; while the large-scale unit assumed to have an average daily production of about 10,000 kg. For these scales, the main system layout and primary components are maintained the same while the size of the components is varied. The scale-up analysis is done entirely in Aspen Plus. In addition to the capabilities of Aspen Plus to accurately model complex chemical processes and provide the stream properties and the equipment details, it has two primary features that are the sensitivity study and the process economic analyzer.

## Chapter 7: Results and Discussion

Under the scope of this thesis of solar hydrogen production using high temperature SOECs, the results are discussed based on the experimentation and the numerical modeling studies which have been presented in Chapters 4–6. Since the main objective of this thesis is to examine and develop a photoelectrochemical Solid oxide cell (PSOC), the experimental results of this part is presented first, then, the results of the modeling study of a standalone 1 MWe SOE unit for hydrogen production are presented. Furthermore, the results of the integration of the SOE into solar tower system are discussed in terms of solar-to-hydrogen energy and exergy efficiencies.

### 7.1. Experimental Results

The experimental apparatus and the test procedure have already been presented and discussed in Chapter 4. In this section, the selected cell performance is reported for a combination of different operating temperatures and gas compositions in both operating modes fuel cell and electrolysis cell. These combinations are presented in Table 7.1.

**Table 7.1 The combination of tests performed on two typical cells.**

Cell No.	Temperature	Gas compositions (vol.%) out of 200 ±1.6 sccm	Operating mode
1	750 ± 5 °C	100 H <sub>2</sub>	FC
		50 H <sub>2</sub> /50 H <sub>2</sub> O	FC/EC
		20 H <sub>2</sub> /80 H <sub>2</sub> O	FC/EC
	850 ± 5 °C	50 H <sub>2</sub> /50 H <sub>2</sub> O	FC/EC
		20 H <sub>2</sub> /80 H <sub>2</sub> O	FC/EC
2	750 ± 5 °C	100 H <sub>2</sub>	FC
		50 H <sub>2</sub> /50 H <sub>2</sub> O	FC/EC
		10 H <sub>2</sub> /90 H <sub>2</sub> O	FC/EC
		05 H <sub>2</sub> /95 H <sub>2</sub> O	FC/EC
	850 ± 5 °C	50 H <sub>2</sub> /50 H <sub>2</sub> O	FC/EC
		10 H <sub>2</sub> /90 H <sub>2</sub> O	FC/EC
		05 H <sub>2</sub> /95 H <sub>2</sub> O	FC/EC

#### 7.1.1. Cell Performance

A commercial an electrolyte-supported solid oxide cell (Nextcell) [159] was used for testing in fuel and electrolysis cell modes at various gas compositions. The cell is made of about 150  $\mu\text{m}$  thick Sc-doped zirconia electrolyte layer with about 50  $\mu\text{m}$  thick electrodes

composed of Ni-GDC/Ni-YSZ for hydrogen electrode and LSM-GDC/LSM for oxygen electrode. The cell is installed in a testing station designed for testing button cell and various conditions such as temperature, gas compositions, and reactant rates. An exploded view of the design of the testing station is shown in Fig. 7.1, where the cell can be located in between two current collecting meshes. One is Pt mesh used for the hydrogen electrode side while the other is gold mesh used for the oxygen electrode side.

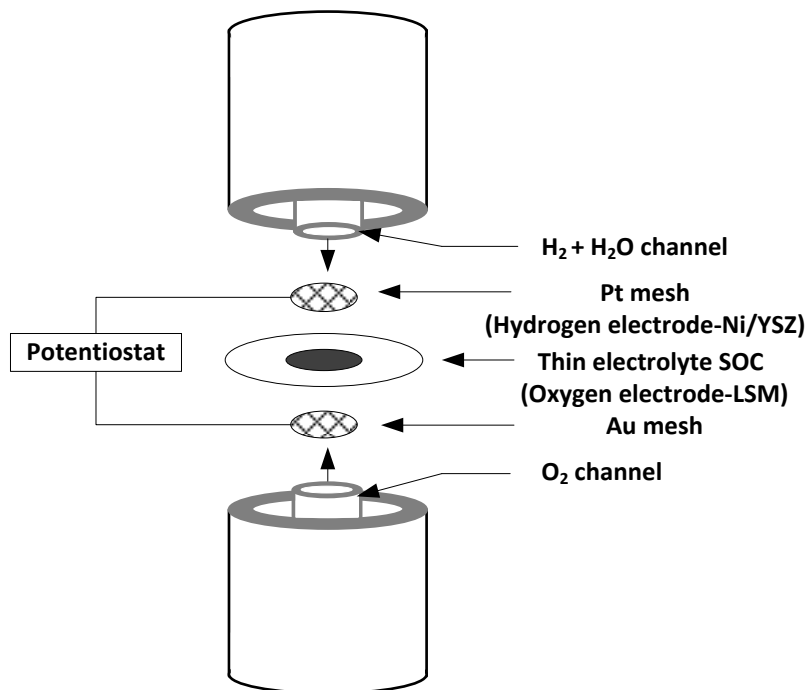


**Figure 7.1** The layout of the button cell installation in the testing fixture.

The cell assembly in the test setup is shown in Fig. 7.1. The button cell is placed inside a high temperature furnace as presented in Chapter 4. Before operating the furnace, appropriate leaking and conductivity tests are performed. Next, the furnace temperature was set to a ramp of  $1^{\circ}\text{C min}^{-1}$  to  $750^{\circ}\text{C}$  in a dry hydrogen flow of  $200 \pm 1.6$  sccm. Alicat mass flow controllers are used to monitor record the changes in mass flow rates. Thermocouples are used to measure the temperature at different locations inside the furnace. The temperature of the cell is evaluated based on a K-type thermocouple which placed about 3 cm from the cell fixture. To achieve the desired humidity ratio, the reactants passed through a water bubbling chamber where the water temperature and gas composition are correlated to make the bubbler output at the required humidity ratio. Over the entire period of the test the voltage values are logged, thus the progress of the cell

activation can be observed. During this time the fuel electrode which composed on NiO/YSZ is reduced to Ni/YSZ. This process is associated with an increase in the cell OCV. Once the cell reached a steady state operating condition, several tests are performed such as OCV measurement over time, J-V curve, and electrochemical impedance spectroscopy (EIS). In the J-V curve measurement, the current is changes gradually, and the corresponding cell potential is recorded. The range of the current is selected such that the cell shall not be permanently damaged due to overloading. Last, the EIS measurement is performed using a potentiostat which applies an alternating current (AC) through the cell and recording the response of the applied AC. The EIS data are presented in a Nyquist plot which represent the complex behavior of the cell impedance. This figure can be analysed to extract some information about the internal phenomena of the cells such as the charge transfer, electrolyte, and electrode resistances. More information on EIS techniques and procedure refer to [160].

Fig. 7.2 shows the J-V-P curve measurement for a cell operating in a fuel cell mode at a 100 vol.% hydrogen fed to the fuel electrode and 100 vol.% air at the oxygen electrode. The total gas flow rates into each electrode compartment are always set to 200 sccm but the compositions at the fuel electrode varied.

The cell starts at an OCV of about 1.3 V and reduces with increasing the current density to reach 0.5 V at a current density of  $0.519 \text{ A cm}^{-2}$ . The measurement continued while the current density reduced from  $0.519 \text{ A cm}^{-2}$  to zero. The cell did not recover the original starting point and the OCV recorded at the end of the test was about 1.16 V. At a current density of  $0.3 \text{ A cm}^{-2}$ , the cell retained a voltage of 0.7 V thus the power density is about  $0.21 \text{ W cm}^{-2}$  higher power density of  $0.24 \text{ W cm}^{-2}$  can be achieved when operating at higher current density of  $0.4 \text{ A cm}^{-2}$  at which the cell has a voltage of 0.6 V. However, the higher the current density the faster the degradation rate. Thus a tradeoff has to be established for the specific type of application. The calculated area specific resistance (ASR) using the equation (6.58) and using the data given in Fig. 7.2 is about  $0.8182 \Omega \text{ cm}^2$ . This value is comparable with that found in literature of  $0.93 \Omega \text{ cm}^2$  [85]. Through typical value is in the range of  $0.40 \Omega \text{ cm}^2$ . This might be related to the high hydrogen concentration and the ASR is evaluated at different reactant concentrations and temperatures.

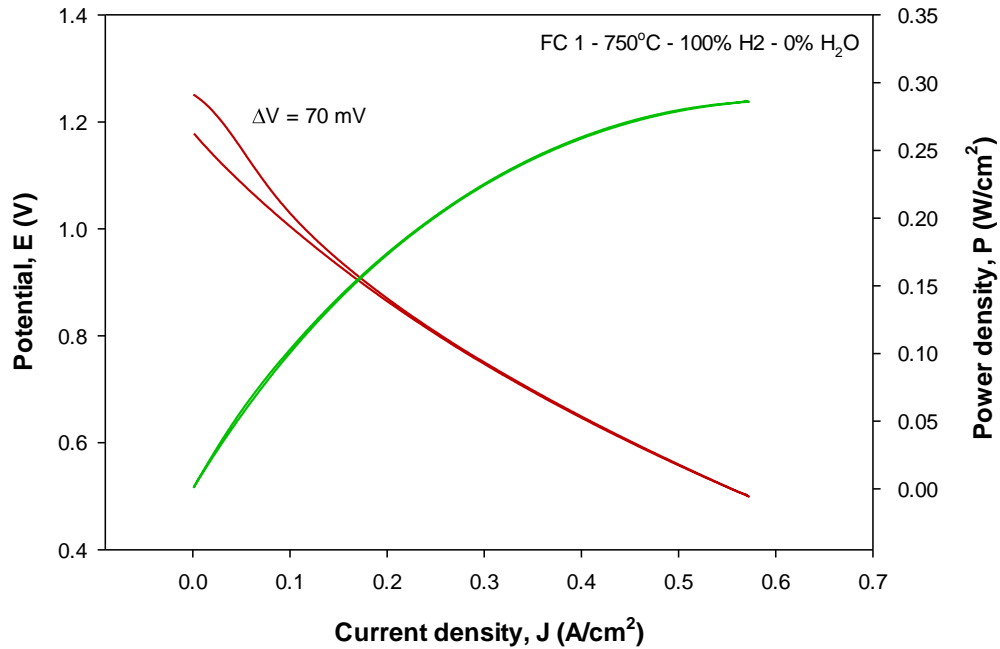


Figure 7.2 The J-V-P curve measurement of the SOFC operating at 100% H<sub>2</sub> and 750°C.

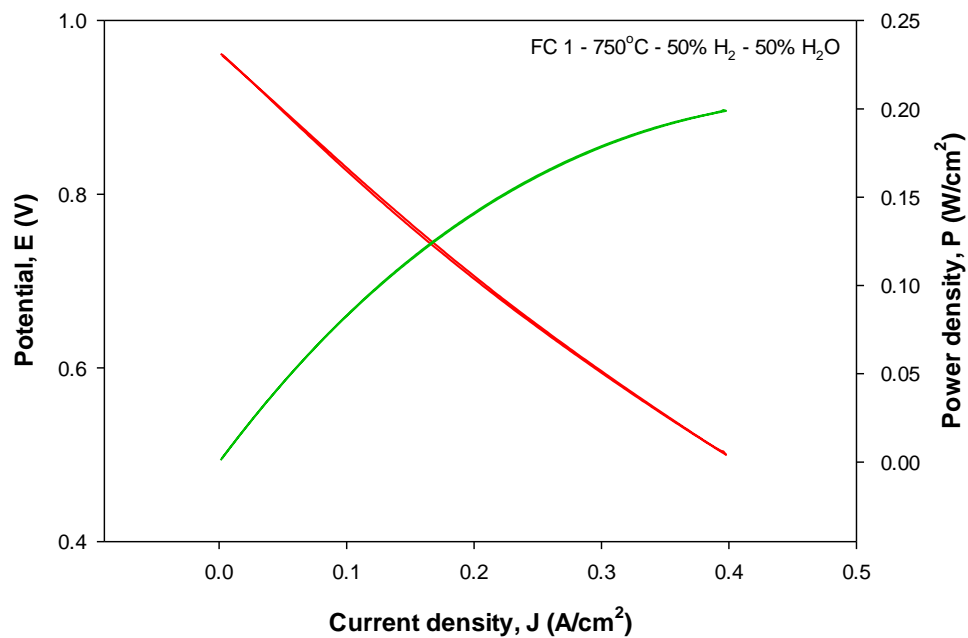
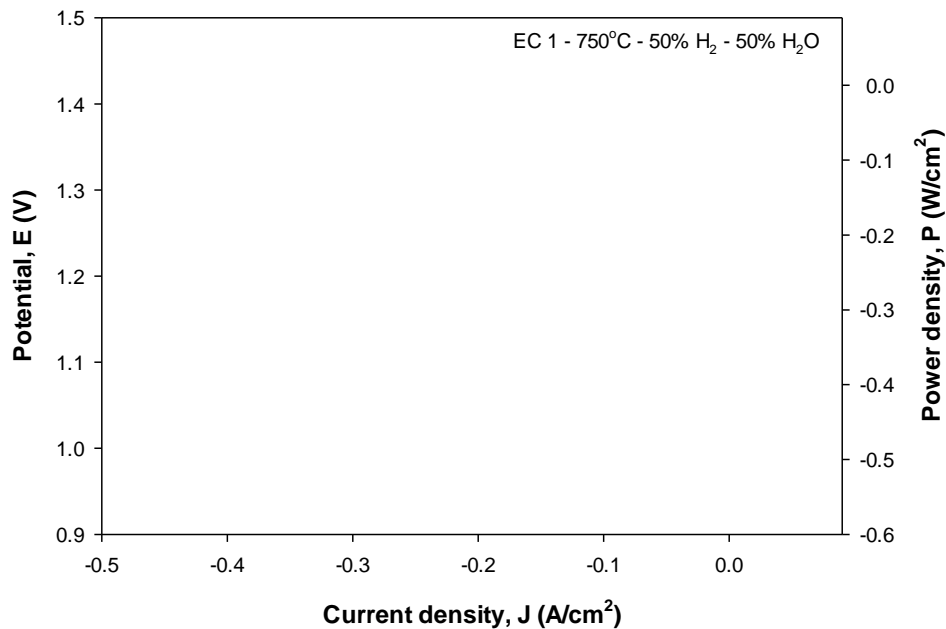


Figure 7.3 The J-V-P curve measurement of the SOFC operating at 50% H<sub>2</sub> - 50% H<sub>2</sub>O and a temperature of 750°C.

In Fig. 7.3 the J-V-P curve is measured again; however, here the reactant composition changed to 50% hydrogen and 50% steam, that is about 100 sccm steam and 100 sccm hydrogen fed to the fuel electrode while the oxygen electrode maintained at 100% air. The curve slope increased reflecting an increase in the ASR of the cell as result of the reduction

in hydrogen in the fuel electrode. At a current density of  $0.3 \text{ A cm}^{-2}$ , the cell has a voltage of  $0.6 \text{ V}$ , producing a power density of  $0.18 \text{ W cm}^{-2}$ .

Fig. 7.4 presents the J-V-P curve measurement at an electrolysis mode with a hydrogen to steam ratio of 1:1 and at a temperature  $750 \text{ }^\circ\text{C}$ . At a current density of  $-0.3 \text{ A cm}^{-2}$ , the cell potential is just over  $1.3 \text{ V}$ . The power density supplied to the cell is about  $0.39 \text{ W cm}^{-2}$ . Figs.7.5 and 7.10 represent the results of the tests listed in Table 7.1. Some of these tests were performed more than once to ensure the typical cell performance or at least on combination is repeated thus same temperature and gas concentration are used.



**Figure 7.4** The J-V-P curve measurement of the SOEC operating at 50%  $\text{H}_2$  - 50%  $\text{H}_2\text{O}$  and a temperature of  $750^\circ\text{C}$ .

Fig. 7.11 summarizes the measurements of the OCV at five different reactant gas compositions and at operating different temperatures. This figure also illustrates the stability of the cell performance before other measurements can be taken. At a temperature of  $750^\circ\text{C}$  and 100% volumetric hydrogen feed to the fuel electrode compartment the cell shows an OCV of  $1.293 \text{ V}$ .

Calculating the Nernst potential based on the equation (6.29) reveals a theoretical OCV value of  $1.294 \text{ V}$  which is in close agreement with the measured value. The discrepancy between the measured and calculated OCV is  $1 \text{ mV}$  that represents an error of  $0.07\%$ . While this minor drop in voltage may be attributed to wiring and other leakage losses, the

close match between the two values can be related to the pure reactants used and the good conductivity of the wiring and current collection system.

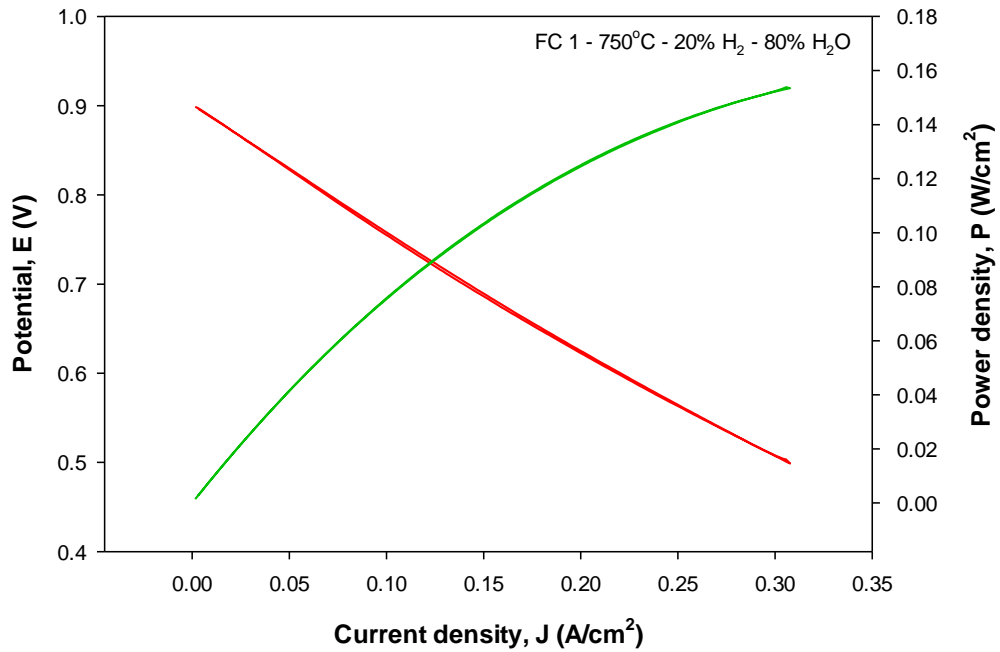


Figure 7.5 The J-V-P curve measurement of the SOFC operating at 20% H<sub>2</sub> - 80% H<sub>2</sub>O and a temperature of 750°C.

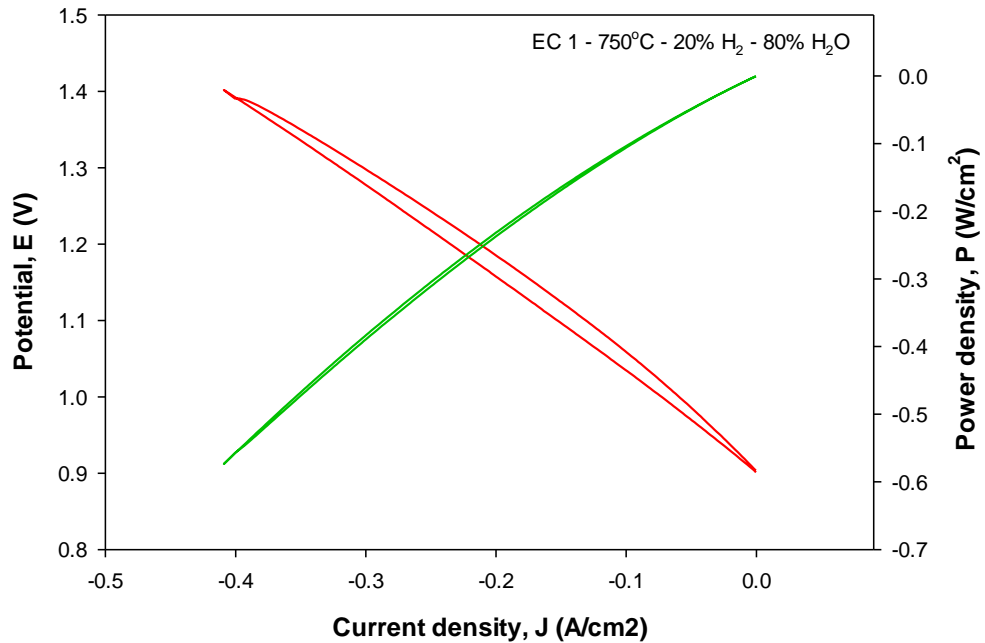


Figure 7.6 The J-V-P curve measurement of the SOEC operating at 20% H<sub>2</sub> - 80% H<sub>2</sub>O and a temperature of 750°C.

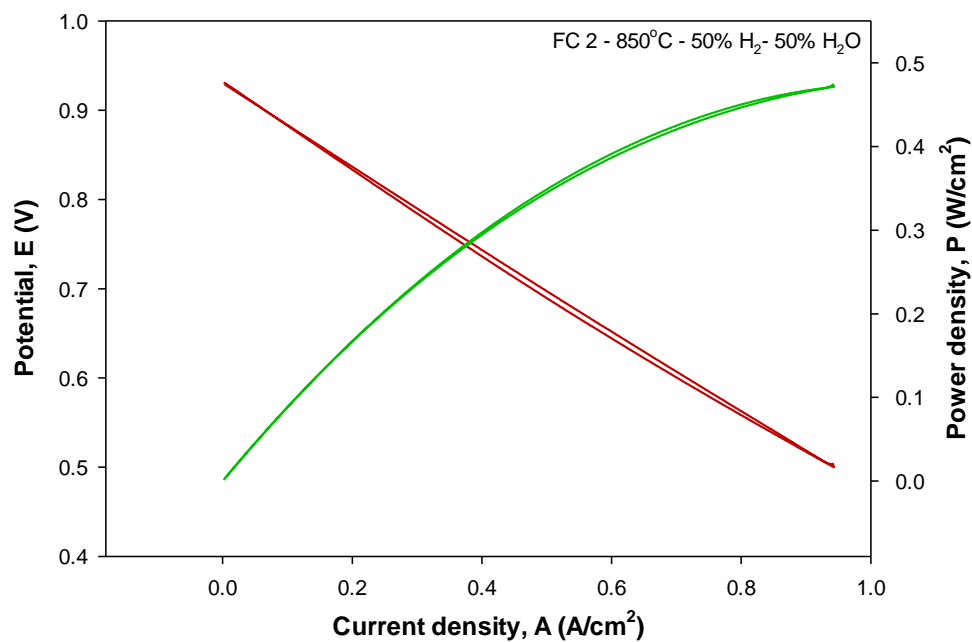


Figure 7.7 The J-V-P curve measurement of the SOFC operating at 50% H<sub>2</sub> - 50% H<sub>2</sub>O and a temperature of 850°C.

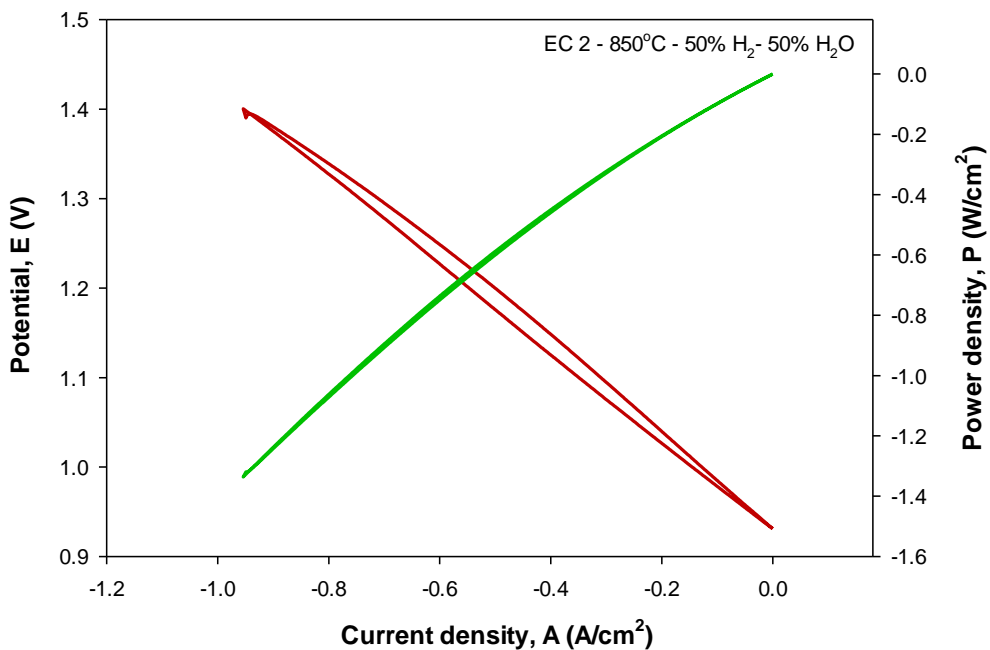


Figure 7.8 The J-V-P curve measurement of the SOEC operating at 50% H<sub>2</sub> - 50% H<sub>2</sub>O and a temperature of 850°C.

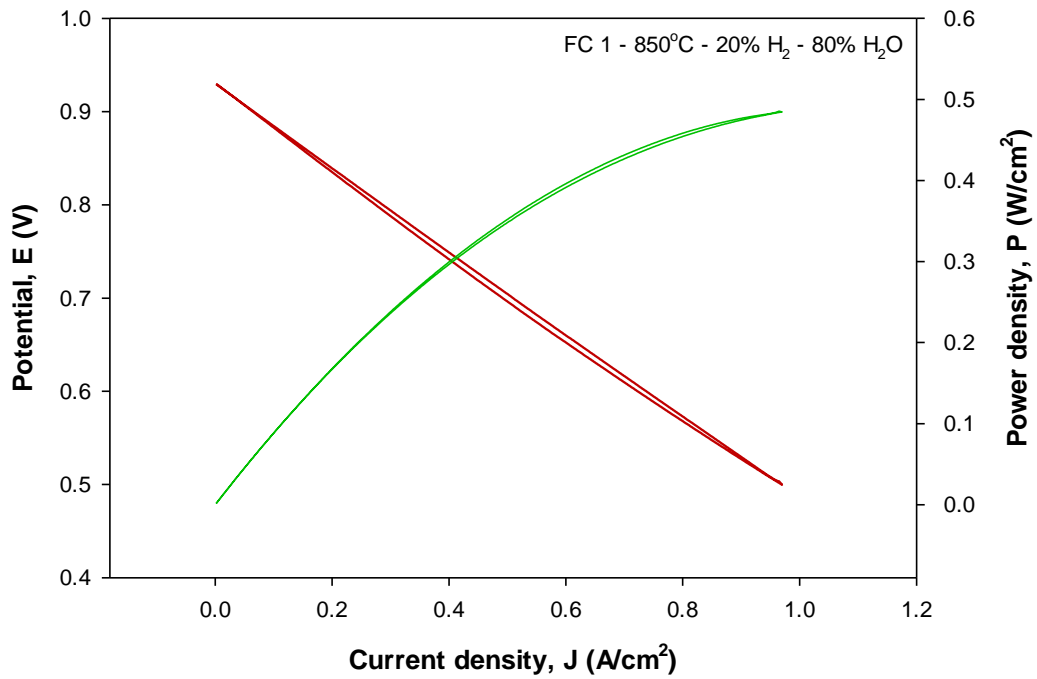


Figure 7.9 The J-V-P curve measurement of the SOFC operating at 20% H<sub>2</sub> - 80% H<sub>2</sub>O and a temperature of 850°C.

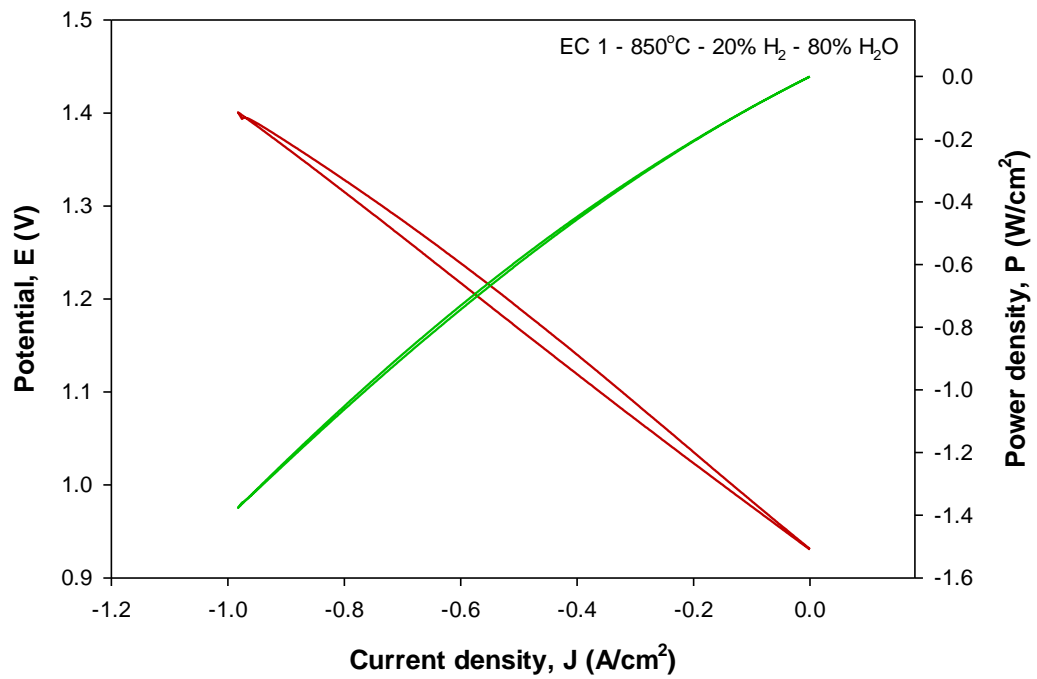
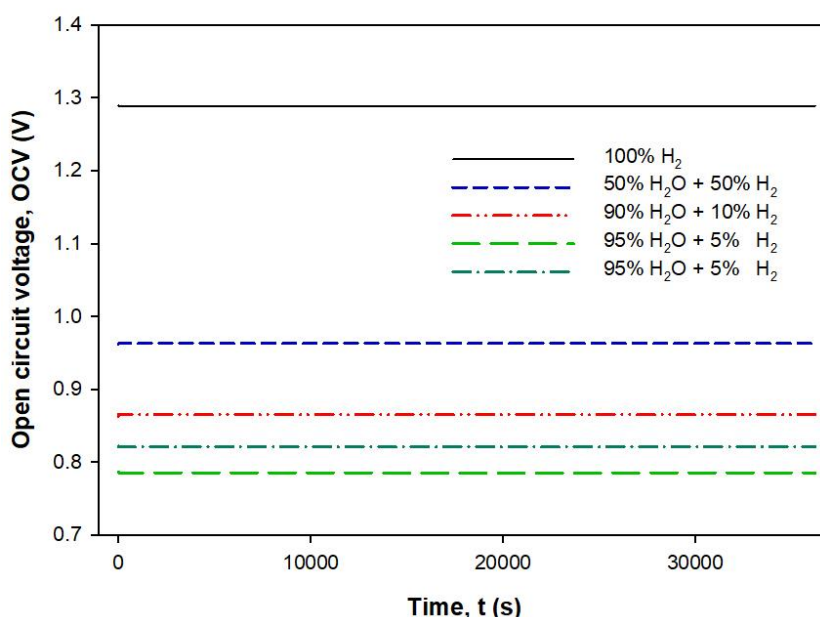


Figure 7.10 The J-V-P curve measurement of the SOEC operating at 20% H<sub>2</sub> - 80% H<sub>2</sub>O and a temperature of 850°C.



**Figure 7.11** The OCV measurements at stable conditions of different reactant gas compositions.

When the hydrogen gas concentration reduced to 50% and the steam increased to 50%, the corresponding cell measured OCV is 0.9628 V. The calculated Nernst potential is 0.9895 V. The difference in potential, in this case, increases to 26.65 mV. Further reduction in the hydrogen concentration to 10% while increasing the steam concentration to 90% led to an OCV of 0.8632 V. Compared with the theoretical value at the same condition of 0.8926 V, the discrepancy increases more than the double to 29.39 mV. Lastly, the OCV measurement made at fuel electrode gas compositions of 5% hydrogen and 95% steam is 0.823 V. The corresponding Nernst potential calculated to be 0.8597 V. While the difference is 36.65 mV.

The measured OCVs are observed to decrease with the reduction in the hydrogen concentration thus the difference between measured and calculated values becoming higher. This can be attributed to the reduction in the cell performance as a result of the passivation of the electrode surface as well as the degradation. Extending the period of operating at high steam concentration can rapidly degrade the cell performance. The cell allowed under 5% hydrogen and 95% steam for few hours, then the measured OCV dropped to 0.7872 V which is about 35.8 mV less than the first read at this composition.

Fig. 7.12 shows the J-V-P curve measurements for a fuel cell mode operating on a dry hydrogen (100 vol.% hydrogen) and at a temperature of 750°C. At a current density of 0.5 A cm<sup>-2</sup>, the cell has a potential of 0.6 V. Thus the power density while operating at this point is 0.3 W/cm<sup>2</sup>. The ASR is evaluated to be about 0.9488 Ω cm<sup>2</sup>. It is also noticed that the cell dose not recover its initial OCV that it was at before scanning.

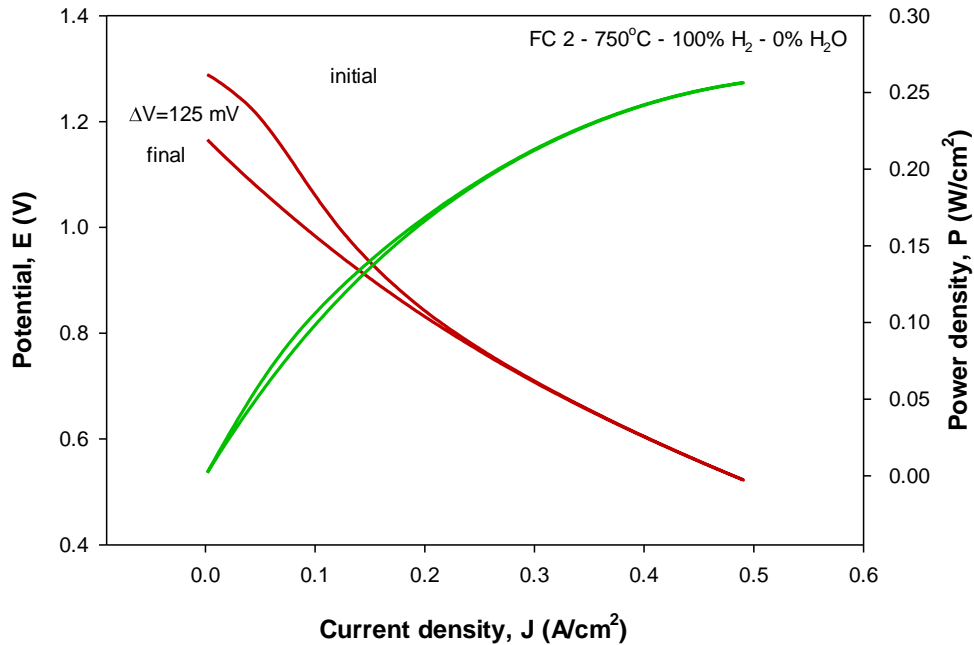


**Figure 7.12** The J-V-P curve measurement while operating in a fuel cell mode at a temperature of 750°C.

In Fig. 7.13, a comparison of the J-V-P curves measured under gas composition of 50% H<sub>2</sub> - 50% H<sub>2</sub>O and temperatures of 750°C and 850°C for two typical cells. This figure shows that the different randomly selected typical cells produces the same performance under the same operating conditions. Though this result is anticipated, it is important to address any discrepancies to avoid misinterpretation of the performance of the modified cells. Fig. 7.13 shows that the cell performance while operating at 850°C is typical. However, there is a noticeable minor variation while testing at 750°C, especially at higher current density.

Fig. 7.14 illustrates the J-V curves of all tests performed on cell number 1 including both modes fuel cell and electrolysis cell. The relative variations as a result of temperature or compositions can be observed. In this figure the error bars are included to show the

uncertainties in each reading based on the equipment accuracy and the calibration procedure presented in Chapter 4. In all these tests, the cell potential is limited 1.4 V in electrolysis mode and a minimum of 0.5 V in fuel cell model.

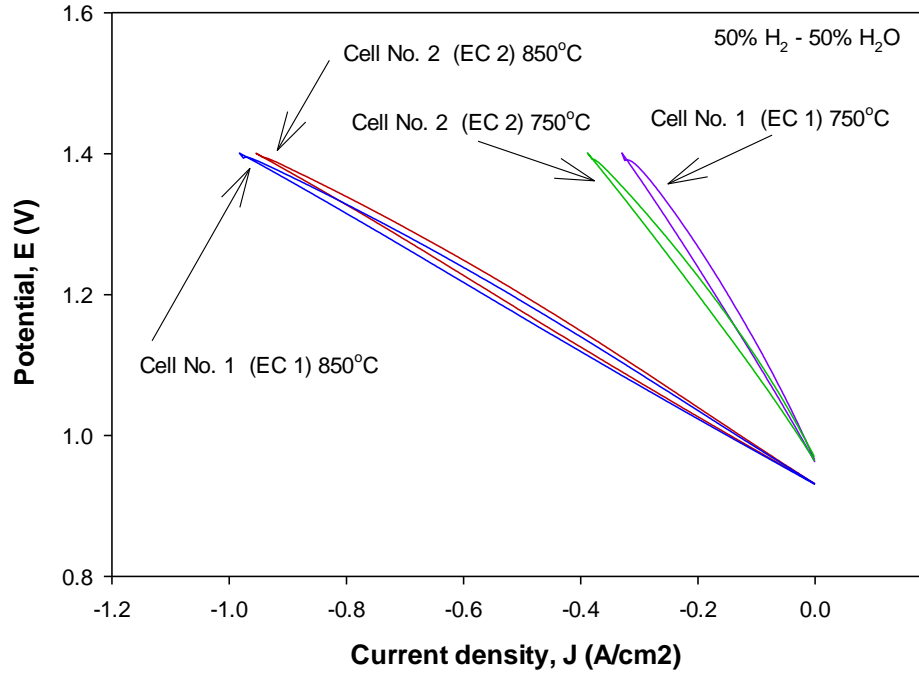


Figure 7.13 Comparisons between the J-V-P of two typical cells tested at exact conditions of 50% H<sub>2</sub> – 50% H<sub>2</sub>O gas compositions and temperatures of 750°C and 850°C

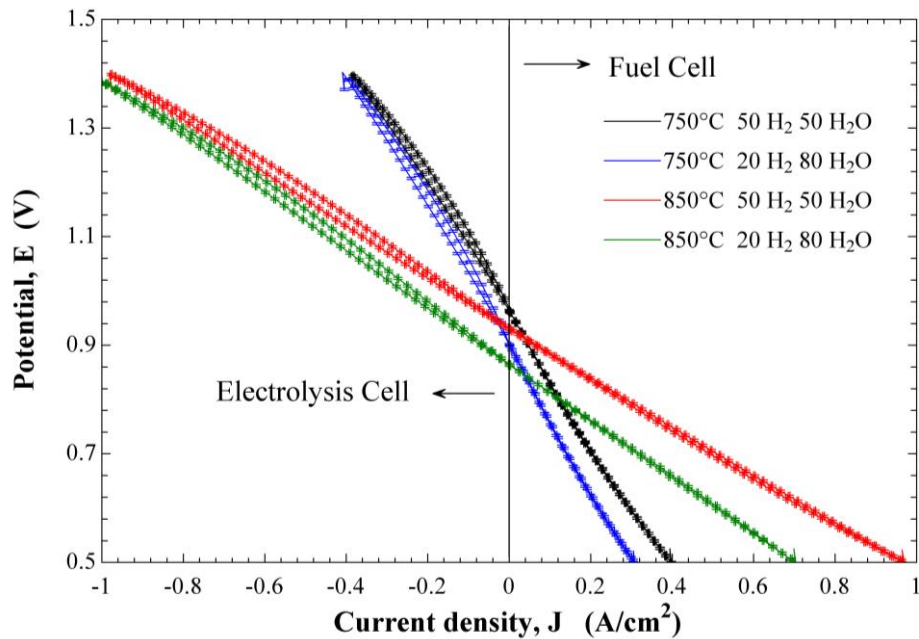


Figure 7.14 J-V curves of the tests performed on cell no. 1 showing the relative changes associated with temperature and composition changes as well as the with associated uncertainties.

The performance of the cell operating in fuel cell mode under three different reactant gas compositions is presented in Fig. 7.15 through the J-V-P curve measurements. The operation at a hydrogen to steam volumetric composition of 1:1 shows an OCV of about 0.9601 V, and with increasing the current density the cell potential reduces to reach a voltage of 0.5 V at a current density of 0.356 A cm<sup>-2</sup>. This corresponds to a power density of 0.178 W cm<sup>-2</sup>. A more practical voltage in the range of 0.7–0.6 V is achieved while drawing a current density in the range of 0.179–0.2536 A cm<sup>-2</sup>, at this range the calculated ASR is about 1.34 Ω cm<sup>2</sup>. As a response to the reduction in the hydrogen concentration from 50% to 10%, the cell potential reduces and the recorded OCV at 10% hydrogen and 90% steam is 0.8608 V. The minimum measured of 0.5 V is at a current density of 0.2461 A cm<sup>-2</sup>. At such low hydrogen concentration, the cell shows a higher ASR calculated to be about 1.5 Ω cm<sup>2</sup>. For the research curiosity, hydrogen concentration is further reduced to 5% while the remaining 95% is water. While it is unlikely such condition would be the desired valued set by an operator for a fuel cell, but it might be the case in some localized area within the cell/stack due geometrical limitation or high current density operating. Therefore, it worth examination. In this case, the cell OCV is about 0.82 V and the cell potential reduces to 0.5 V while operating at current density of 0.1862 A cm<sup>-2</sup>. The calculated ASR is about 1.751 V.

Fig. 7.16 shows the electrolysis tests under fuel electrode gas composition of 50%, 90%, and 95% steam while the remainder was hydrogen. With a maximum cell potential set at 1.4 V, the high steam compositions reacted the maximum potential at current densities of about -4.8 A cm<sup>-2</sup> but at the low compositions of 50% steam (i.e., 1:1 steam to hydrogen ratio) the maximum reached at current density of about -3.3 A cm<sup>-2</sup>. The summary of the relative changes in cell performance due to changing the testing conditions are reported in Fig. 7.17. This figure includes the uncertainties at the high steam concentrations 90%, and 95%. At high the composition of 95% steam and 5% hydrogen, and a temperature of 850°C, the fuel cell curve shows some deviation from expected curve behavior this deviation may attributed to the high temperature and high steam compositions.

The impedance spectra of the SOC are presented in Fig. 7.18, and 7.19 for the temperature of 750°C and 850°C, and gas compositions of 50%, 90%, and 95% steam concentrations.

These figures show further increase in the cell resistance at lower operating temperature. For example, in Fig. 7.18, the ohmic and polarization resistances are given in Table 7.2. There is an increase in both resistances with increasing the steam concentration.

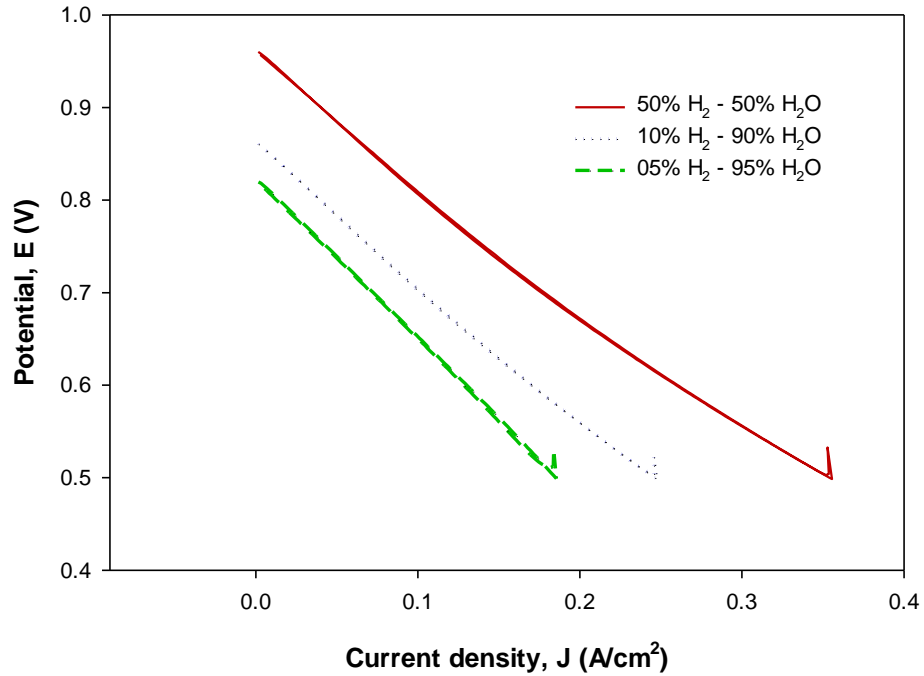


Figure 7.15 The J-V-P curve measurements of a SOFC test at a temperature of 750°C reactants compositions of 50% H<sub>2</sub> - 50% H<sub>2</sub>O, 10% H<sub>2</sub> - 90% H<sub>2</sub>O, and 5% H<sub>2</sub> - 95% H<sub>2</sub>O.

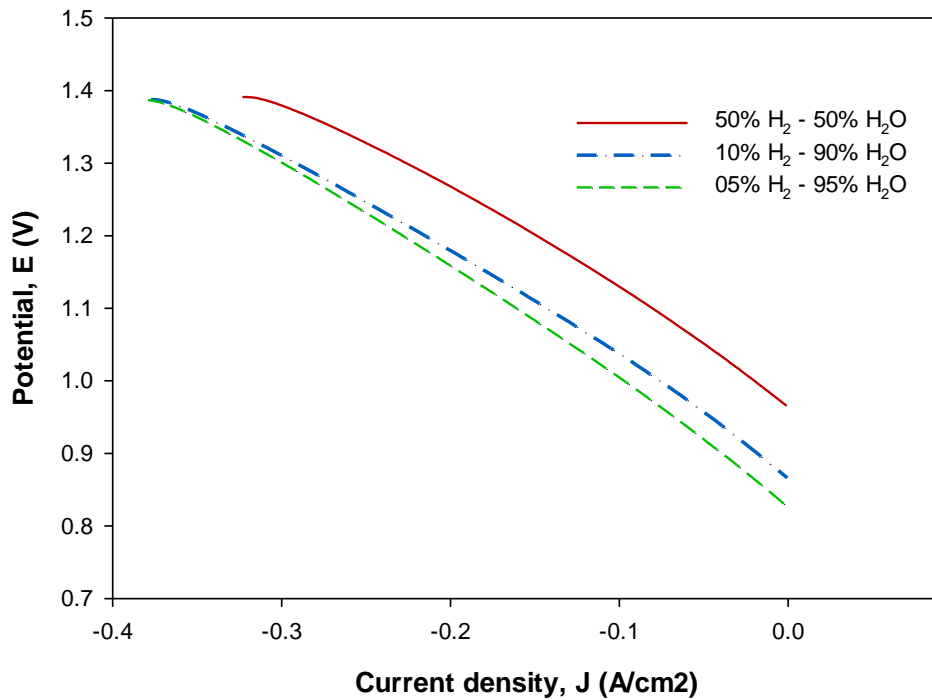


Figure 7.16 The J-V curve measurements of a SOEC test at a temperature of 750°C reactants compositions of 50% H<sub>2</sub> - 50% H<sub>2</sub>O, 10% H<sub>2</sub> - 90% H<sub>2</sub>O, and 5% H<sub>2</sub> - 95% H<sub>2</sub>O.

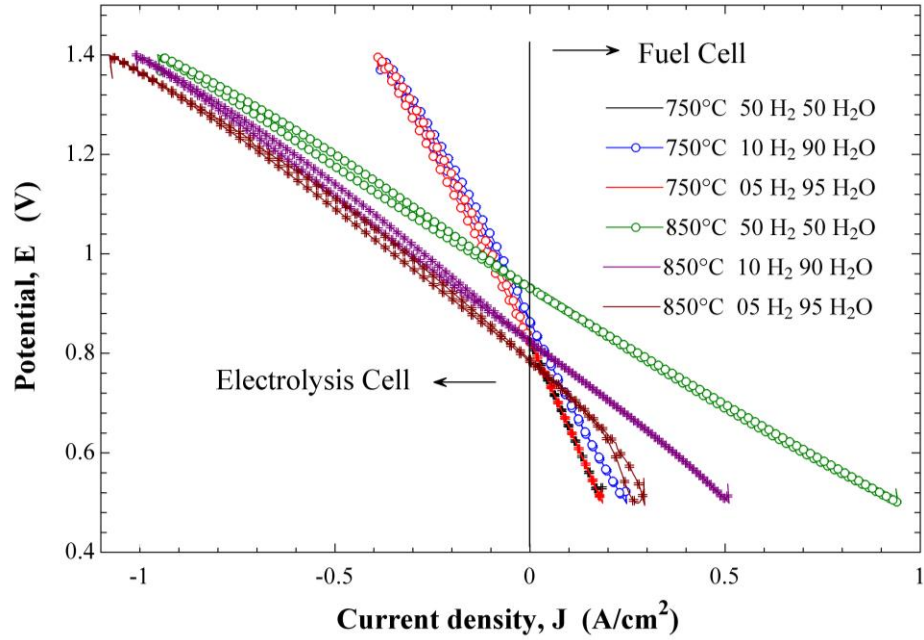


Figure 7.17 J-V curves of the tests performed on cell no. 2 showing the relative changes associated with temperature and composition changes as well as the with associated uncertainties.

Table 7.2 The ohmic and polarization resistances obtained from Fig. 7.18.

Composition	$R_{\text{Ohm}} (\Omega \text{ cm}^2)$	$R_p (\Omega \text{ cm}^2)$
50% H <sub>2</sub> – 50% H <sub>2</sub> O	0.4188	1.118
90% H <sub>2</sub> – 10% H <sub>2</sub> O	0.44608	1.1392
95% H <sub>2</sub> – 05% H <sub>2</sub> O	0.48352	1.14368

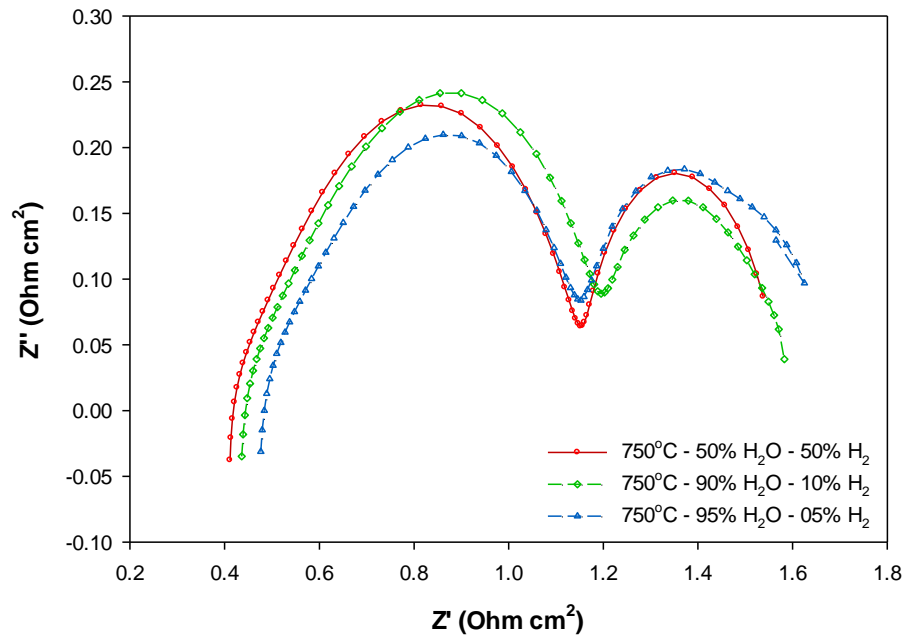
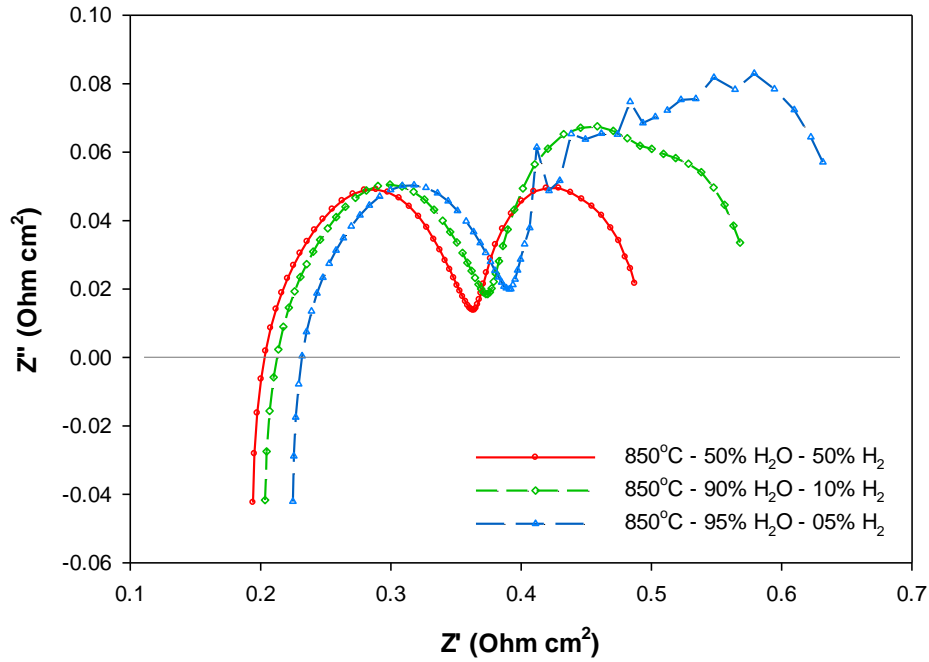


Figure 7.18 The electrochemical impedance spectra at different reactant concentrations while operating at temperature of 750°C.

In the case of 850°C, the concentrations of 50% and 90% showing reasonable performance but at 95% the cell may encounter considerable performance degradation (see Fig. 7.18). The high steam concentration at accelerated high temperature process led to significant reduction in the cell performance and thus damage in the cell structure. The ohmic and polarization resistances are listed in Table 7.3.

**Table 7.3 The ohmic and polarization resistances obtained from Fig. 7.19.**

Composition	$R_{\text{ohm}}$ ( $\Omega \text{ cm}^2$ )	$R_p$ ( $\Omega \text{ cm}^2$ )
50% H <sub>2</sub> – 50% H <sub>2</sub> O	0.2027	0.2847
90% H <sub>2</sub> – 10% H <sub>2</sub> O	0.2124	0.35364
95% H <sub>2</sub> – 05% H <sub>2</sub> O	0.0.2331	0.39912



**Figure 7.19 The electrochemical impedance spectra at different reactant concentrations while operating at a temperature of 850°C.**

Further analysis of the EIS measurements shown in Figs. 7.18, and 7.19 are undertaken to include the complex impedance and the equivalent circuit analysis. In this regard, the Gamry Echem Analyst software was used to model and curve fit an equivalent circuit model into the measured EIS data for cell no. 2 at reactant composition of 1:1 steam to hydrogen and 750°C (shown in red line in the measurements presented in Fig. 7.18). Fig. 7.20 shows the Nyquist plot of the EIS measurements (in dots) and the equivalent circuit curve fit (in solid line). The equivalent circuit model is shown in Fig. 7.21, and the curve

fitting parameters are given in Table 7.4. In this model, R1 represent the ohmic resistance while R2 and R3 are the polarization resistance corresponding to each of the semicircular curves appear in Fig. 7.20. The Yo4 and Yo6 are constant phase elements, and the R. E. and W. E. represents the reference and working electrodes, respectively.

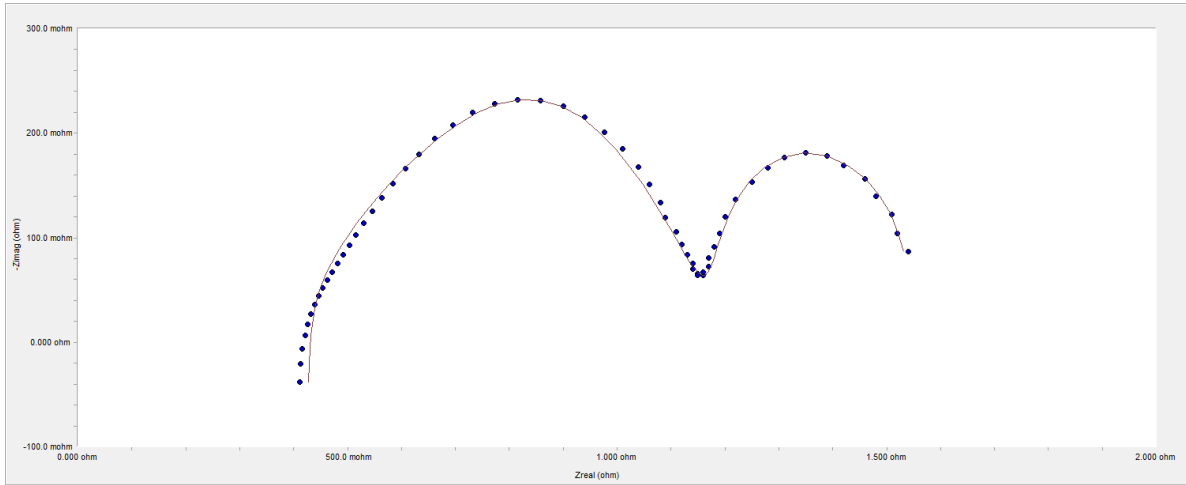


**Figure 7.20** Nyquist curve fitting to the EIS measurements to a representative equivalent circuit model.

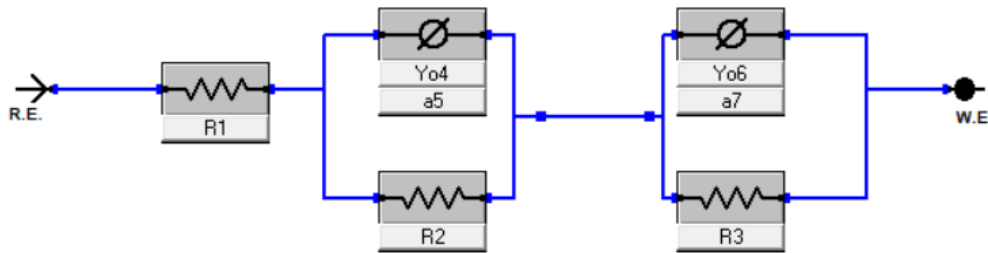


**Figure 7.21** A layout of the equivalent circuit model components.

**Table 7.4** The Equivalent circuit parameters used for model fitting in Fig. 7.20.

Parameter	Value	±Error
R1 (ohm)	418.1E-3	5.592E-3
R2 (ohm)	770.7E-3	18.26E-3
R3 (ohm)	361.7E-3	40.17E-3
Yo4 (S*s <sup>a</sup> )	7.494E-3	1.203E-3
a5	670.4E-3	19.59E-3
Yo6 (S*s <sup>a</sup> )	974.3E-3	125.3E-3
a7	994.6E-3	86.68E-3
Goodness of Fit	748.0E-6	

### 7.1.2. Cell Characterization

The cell structure and material composition is characterized before and after performing the test on the cells. The aim of this characterization is to examine the effect of high steam operating conditions on the cell materials and structure.

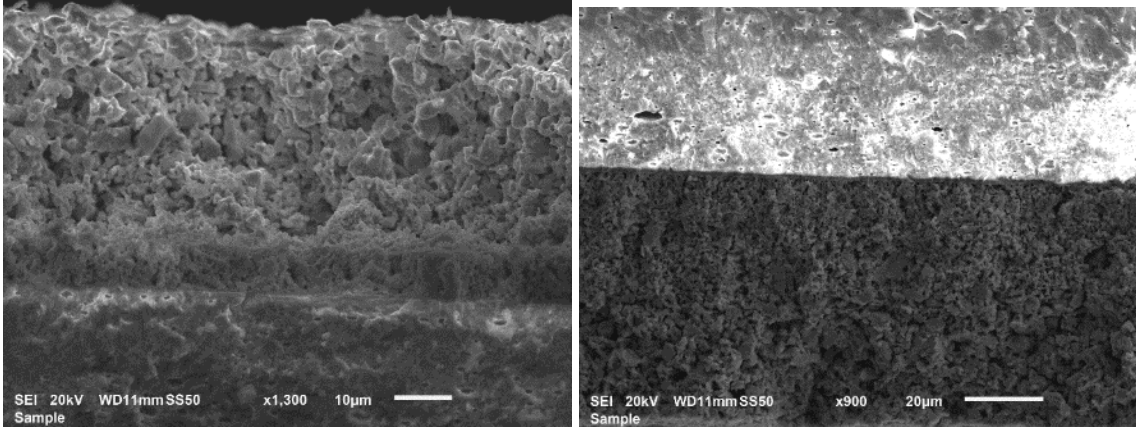


**Figure 7.22** A cross sectional view of the cell structure showing the different electrode layers.

Figs. 7.22 and 7.23 show different views of the cross-sectional structure of the electrolyte and the bi-layers as well as the electrodes functional layers (the interface where the electrochemical reaction takes place). In Figs. 7.24 and 7.25 are showing the material compositions based on the SEM analysis at selected points on the electrolyte and the electrodes. This analysis shows any changes in the material compositions as a result of testing and operating. If there are any materials coming from the test setup or developed during the test procedure it can be recognized and quantified. These figures show homogenous material composition as expected based on the manufacturer data. Also the test short period and the purity of reactants limited the development of unwanted materials.

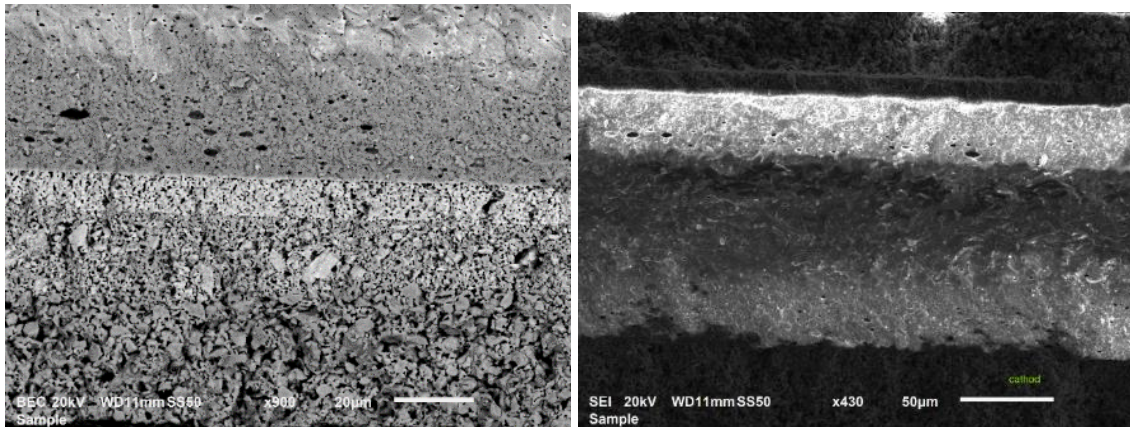


**Figure 7.23** The bilayer used in between the electrolyte and electrodes.

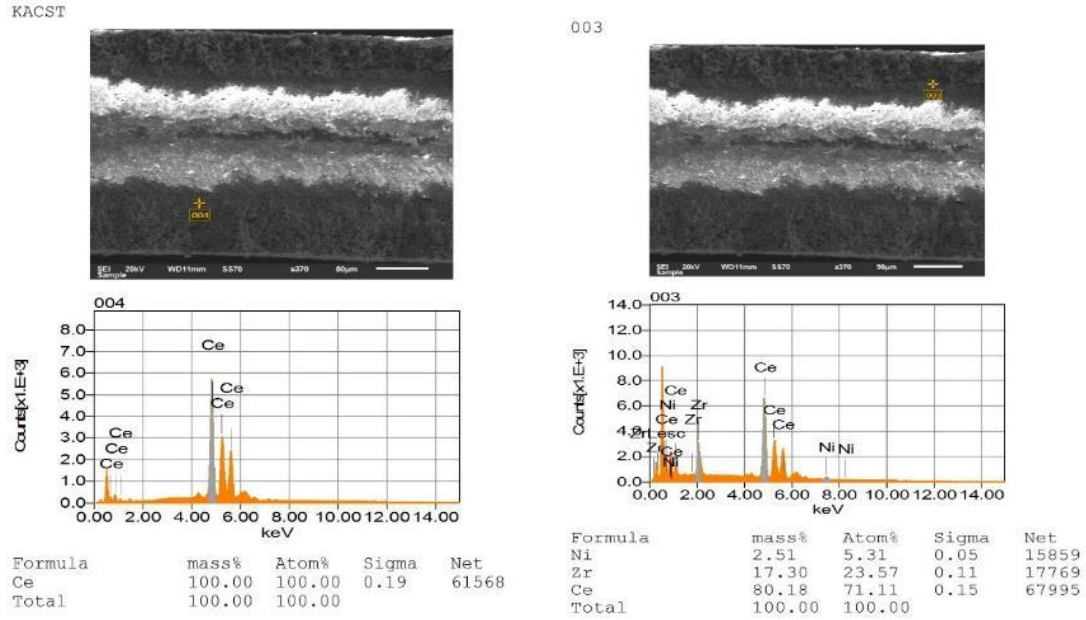


Figure 7.24 Analysis of the material compositions for each layer of the electrolyte.

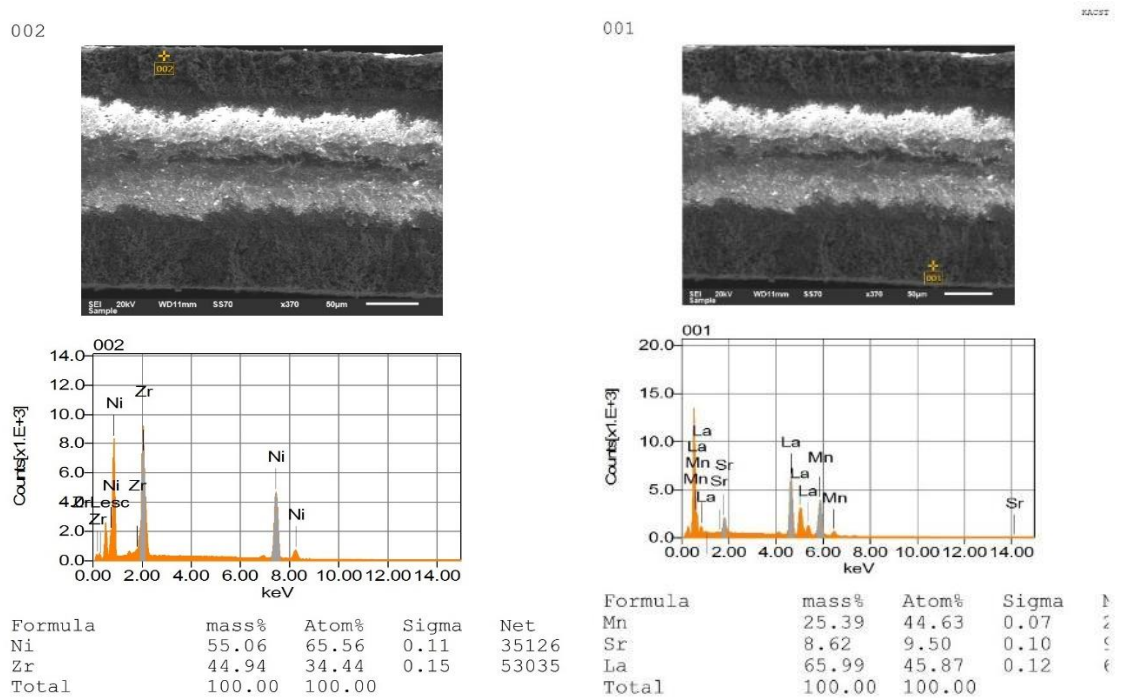
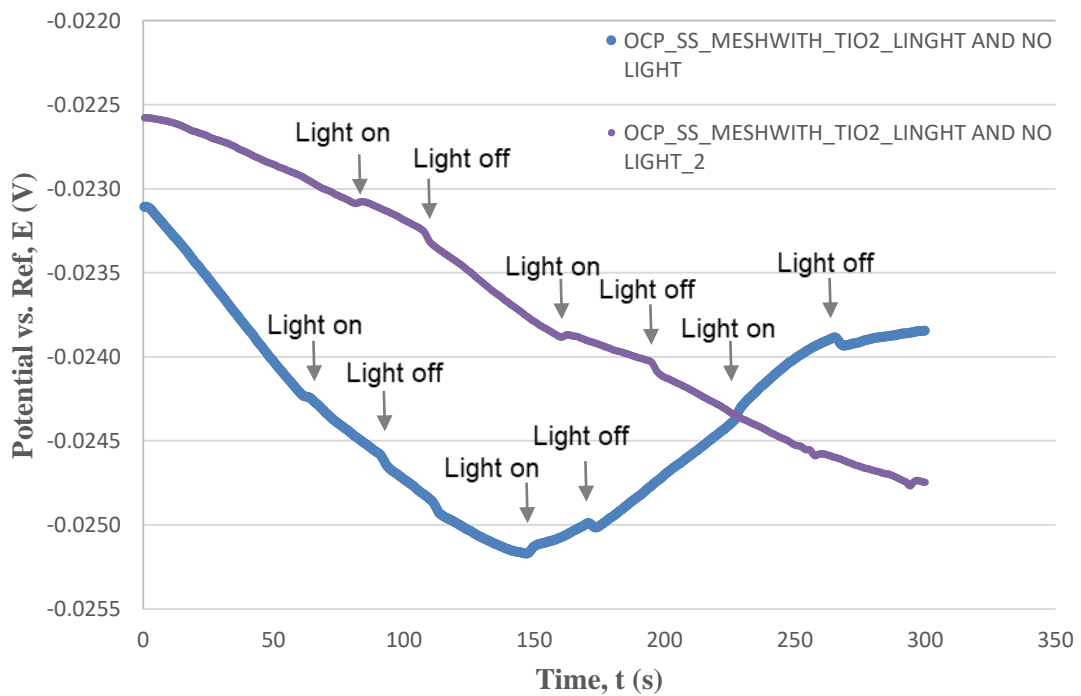


Figure 7.25 Analysis of the material compositions within each electrode.

### 7.1.3. Coated Samples

In Fig.7.26, shows OCV reading on TiO<sub>2</sub> coated stainless steel (SS) mesh. The experimental procedure is presented in Chapter 4. In this figure, the UV light responses are recorded through the OCV. The trend of the curve shows an ongoing redox process that changes with time of the test. For example, the potential reading at the beginning of test in the case on. 1 was -23 mV and reduced to below 25 mV at 150 seconds from the beginning of the test. The potential increased afterward.



**Figure 7.26** OCV reading showing the TiO<sub>2</sub> coated SS mesh under on/off UV light.

The limited excitation induced by UV light may attribute to the small surface area of the mesh compared with other dense structures such as Ni foam. In Fig. 2.27, microphotographs of the Ni foam samples on which the ZnS semiconductor is deposited by electrospinning. These microphotographs show the microstructure of the Ni foam surface after the annealing process. It can be noticed that there are some reminders of the polymer material after annealing which mandate extending the annealing process. Furthermore, noticeable yellowish spots appeared on the surface which indicate that some bonding between the ZnS and the Ni foam has been established.

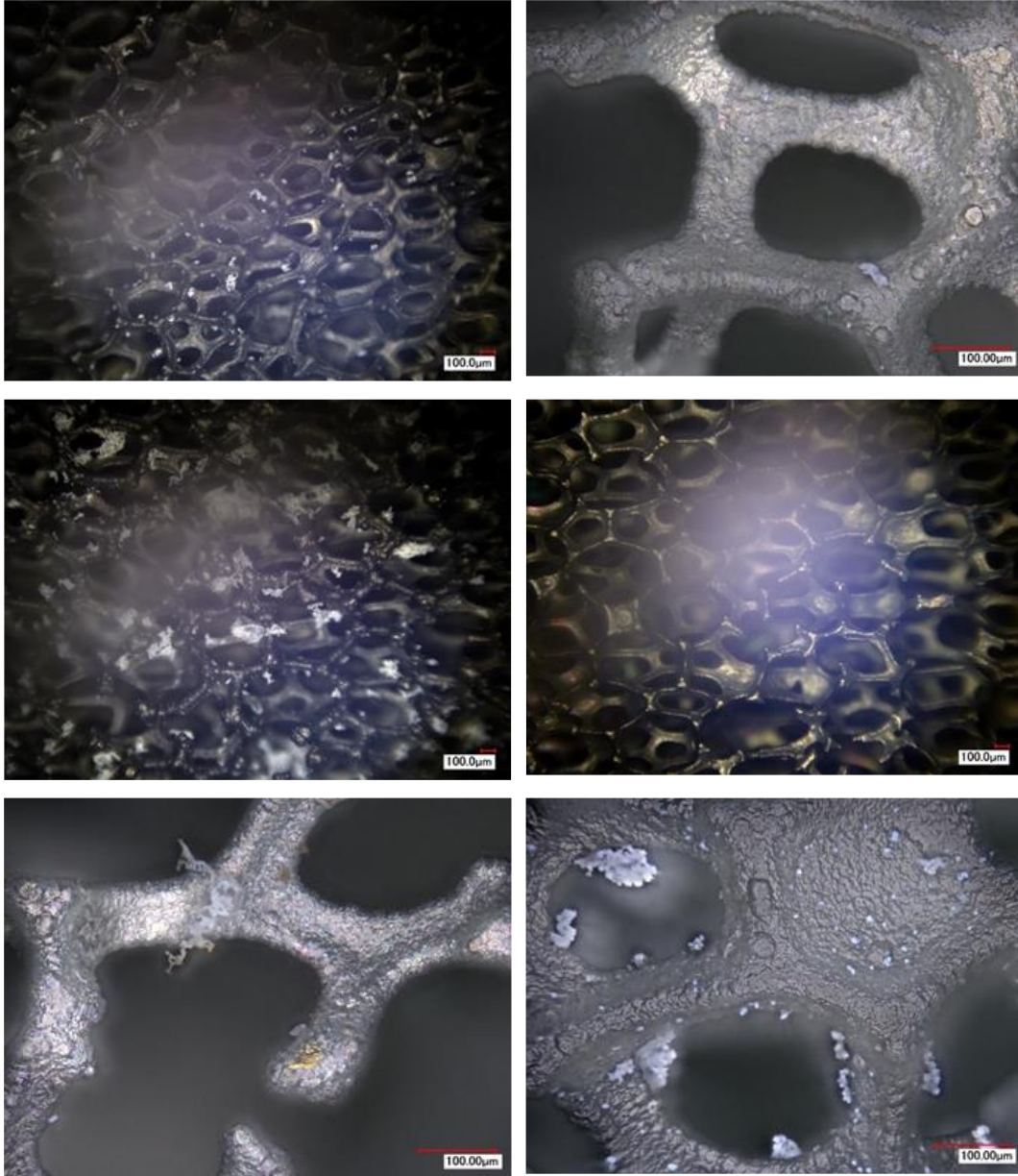


**Figure 7.27** Magnified photos of the surface structure of Ni sample coated with ZnS through the electrospinning process and annealed at a temperature of  $450 \pm 5^\circ\text{C}$ .

## 7.2. Modeling Results

The thermodynamic models developed in Chapter 5 are solved using Engineering Equation Solver (EES). The section of EES motivated by the thermodynamic features that this software has such as the built-in functions of the state properties of the different species. Furthermore, the software provides high quality graphs that facilitate representation. The results of the modeling are presented in the following sections.

### 7.2.1. SOEC Thermal and Electric Energy Requirements

One of the main motivations towards high temperature electrolysis is that the electric energy requirement is expected to decrease with increasing the temperature; thus the electricity-to-hydrogen conversion increases. The theoretical energy requirements for the SOEC are presented in Fig. 7.28 over the electrolyzer operating temperature range from 800 to 1300 K. The required electric energy appears to be about three to four times that needed as thermal energy. While the total energy remains almost constant with operating temperature, electric energy shows a slight decline in favor of the thermal energy that increases with temperature increase.

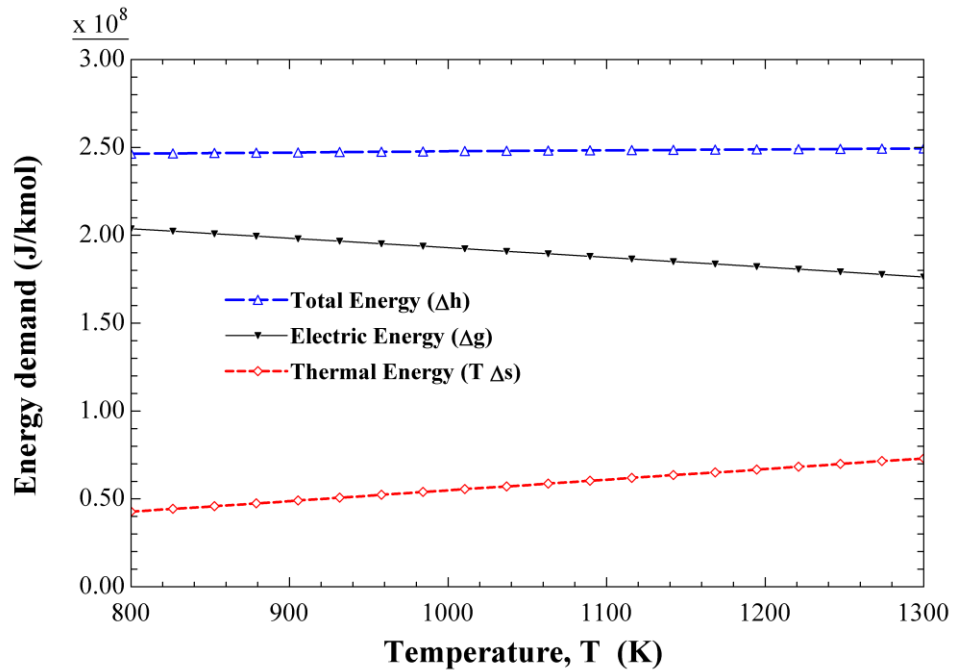


**Figure 7.28** Variations in the SOEC subsystem thermal, electrical, and total energy demand over a range of electrolyzer operating temperature.

This figure presents the theoretical frame of the thermodynamic electrolysis process considering reversible process (no internal losses). However, in the actual case which involves internal irreversibility dissipating energy in the form of heat. This heat reduces the heat requirements from an external source.

The operating and design parameters used in the modeling are presented in Table 7.5. Some of these parameters are altered for validation purposes and to examine the model accuracy, using parameters similar to that reported in the experimental measurements used for

validation. Operating parameters are varied when possible to observe the effect of their change on the SOEC performance.

**Table 7.5 Main parameters used for the base case SOEC model.**

Parameter	Value
Cell operating temperature (K)	1078
Cell operating pressure (Pa)	$101 \times 10^3$
Operating current density, J (A m <sup>-2</sup> )	10000
H <sub>2</sub> O stream composition (molar fraction)	H <sub>2</sub> O 50%, H <sub>2</sub> 50%
Air stream composition (molar fraction)	O <sub>2</sub> 0.21%, N <sub>2</sub> 79%
Anode exchange current density, J <sub>0,a</sub> (A m <sup>-2</sup> )	0.65
Cathode exchange current density, J <sub>0,c</sub> (A m <sup>-2</sup> )	0.25
Calculated effective diffusion coefficient at anode, D <sub>a</sub> <sup>eff</sup> (m <sup>2</sup> s <sup>-1</sup> )	$2 \times 10^{-5}$
Calculated effective diffusion coefficient at cathode, D <sub>c</sub> <sup>eff</sup> (m <sup>2</sup> s <sup>-1</sup> )	$5.11 \times 10^{-5}$
Anode thickness, δ <sub>a</sub> (m)	$17.5 \times 10^{-6}$
Cathode thickness, δ <sub>c</sub> (m)	$12.5 \times 10^{-6}$
Electrolyte thickness, δ <sub>e</sub> (m)	$12.5 \times 10^{-6}$
Anode material	LSM
Cathode material	Ni-YSZ
Electrolyte material	YSZ
Pores diameter, D <sub>por</sub> (m)	$1 \times 10^{-6}$
Porosity	0.3
Tortuosity	5

### 7.2.2. SOEC Model Validation

The present model is validated by reproducing the current density-potential (J-V) curve of an electrolysis cell which reflects the performance of a single cell, as shown in Fig. 7.29. The selected experimental data, as reported by Ebbesen et al. [78], is for SOECs. These cells have typical material and structure as those selected for the SOE system. Fig. 7.29 shows the results produced by the model since they fit well with the experimental measurements which cover current densities between 0–10000 A m<sup>-2</sup> as well as operating temperatures of 1023 K and 1123 K. Furthermore, Table 7.6 compares the OCV and ASR obtained by the current model and that measured by Ebbesen et al. [78].

**Table 7.6 Comparison between the results of the current model and the experimental measurements reported by Ebbesen et al. [78] for SOEC tests at reactants gas composition of 50% H<sub>2</sub>O – 50% H<sub>2</sub>.**

Temperature (K)	Present model results		Experimental measurements [78]	
	OCV (mV)	ASR (Ω cm <sup>2</sup> )	OCV (mV)	ASR (Ω cm <sup>2</sup> )
1023	989	0.44	982	0.41
1123	962	0.20	951	0.19

The difference between the calculated and measured OCVs while operating at 1023 K is 7 mV, which increases when operating at 1123 K to 11 mV. Similar discrepancies were also reported by Ebbesen et al. [78], who reported 10 mV and 12 mV, corresponding to 1023 K and 1123 K, respectively. The difference between calculated and measured ASRs is  $0.03 \text{ } \Omega \text{ cm}^2$  at an operating temperature of 1023 K, and  $0.01 \text{ } \Omega \text{ cm}^2$  when operating at 1123 K. The current model slightly overestimates the ASR, the desired increase that can be justified as an average cell performance with minor degradation over the period of operation.

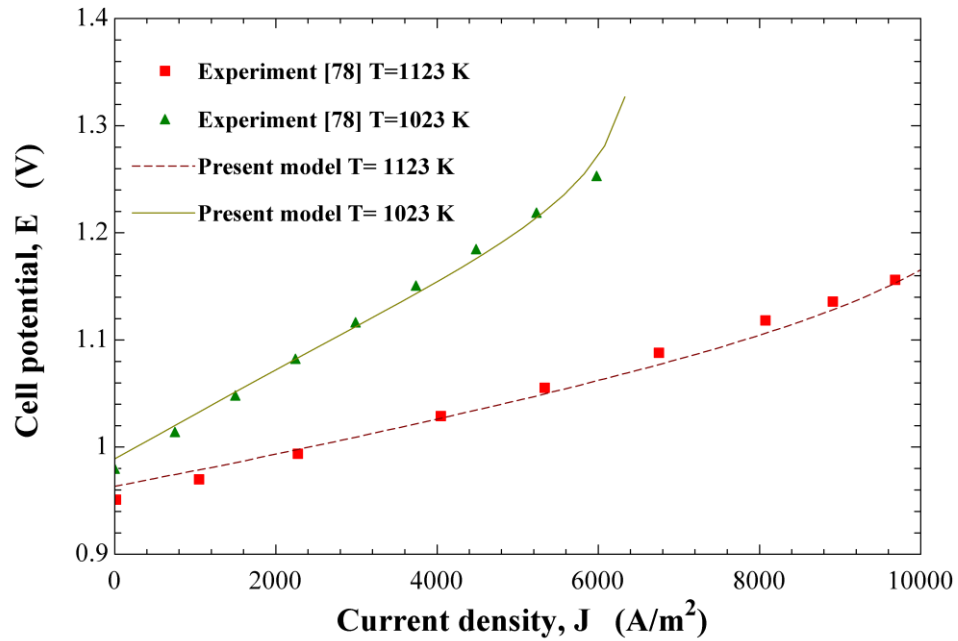


Figure 7.29 Model validation through comparison with the published experimental data [78].

### 7.3. Single Electrolysis Cell Parametric Analysis Results

In Fig. 7.30, the SOEC potentials and power densities are evaluated over a range of operating current densities for three operating temperatures: 973, 1073, and 1173 K. It can be noticed that increasing the operating temperature will significantly reduce the cell power requirements. Operating at higher current densities will also increase cell polarizations although this yields high hydrogen flow rate.

In Fig. 7.31, the cell activation, ohmic, and concentration polarizations are evaluated over a range of operating current densities while operating at 1073 K. It is clearly noticeable that activation polarization dominates all other polarizations, followed by the ohmic polarization. Concentration polarization presents a minimal effect with a small increase

associated with high current densities operation. This behavior is not the norm in SOEC where ohmic polarization tends to dominate other polarizations. However, the reduction in ohmic polarization is mainly attributed to the low electrolyte thickness (12.5 $\mu\text{m}$ ) which resulted in higher ionic conductivity.

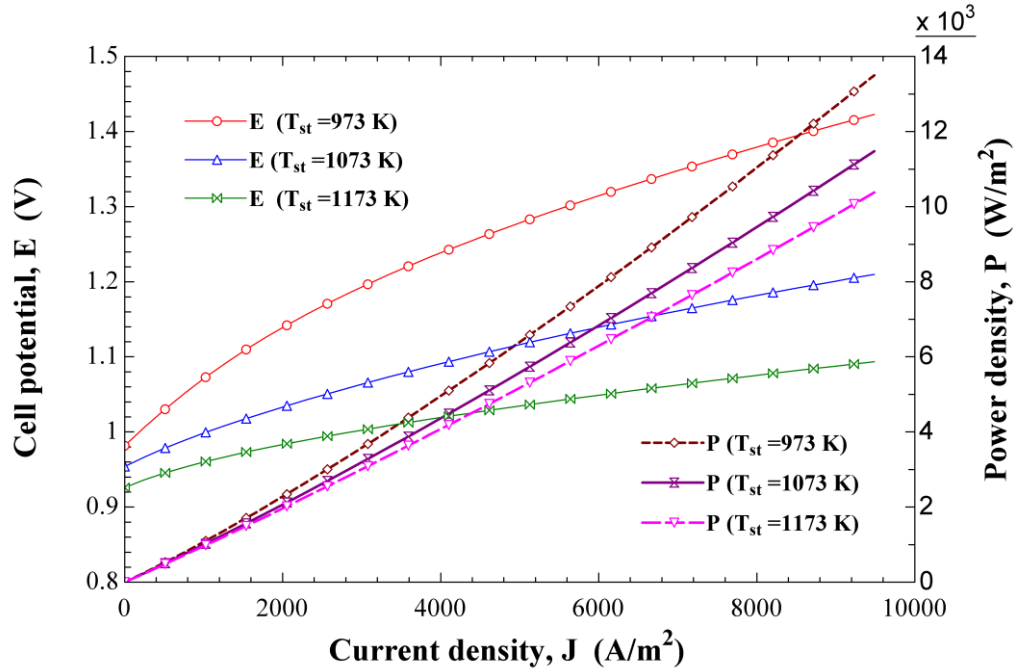


**Figure 7.30 Variations in SOEC voltage and power with current density different operating temperatures.**

Fig. 7.32 shows various polarization curves at low operating temperature. It can be recognized that the cell operation is subjected to a considerable increase in polarizations. Ohmic and concentration polarizations increase almost linearly with increasing cell current density. Comparing Figs. 7.31 and 7.32, ohmic polarization jumps more than twice, reducing the temperature from 1073 to 973 K.

The changes in energy and exergy efficiencies of the SOEC are presented in Fig. 7.33 over a range of operating current densities. The energy efficiency increases with increasing current density reaching 66% at almost 10000 A cm<sup>-2</sup>. The exergy efficiency reached about 82% at the same current density. Considering a practical cell current density in the range of 5000 A m<sup>-2</sup>, the cell then, achieves a conversion efficiency of 56.8 % and exergy efficiency of 81.8%.

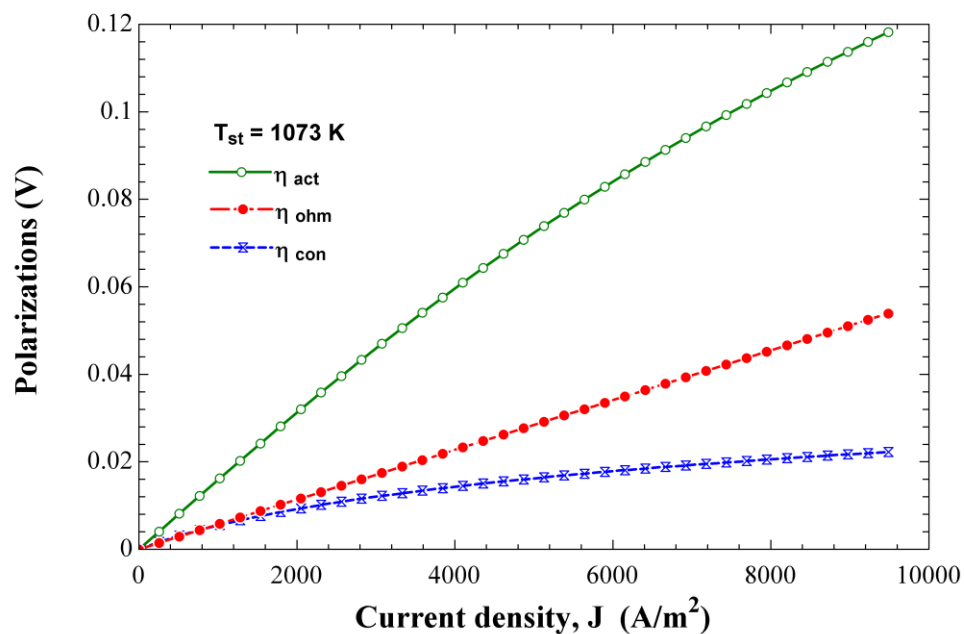


Figure 7.31 Variations in ohmic, activation, and concentration polarizations when electrolysis operates at 1073 K.

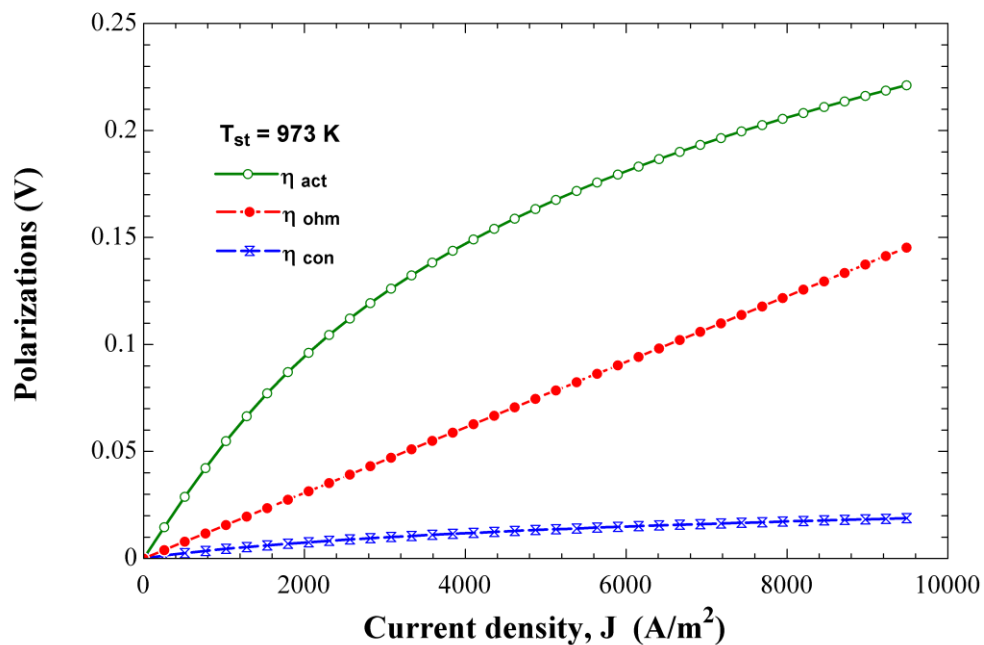


Figure 7.32 Variations in ohmic, activation, and concentration polarizations when electrolysis operates at 973 K.

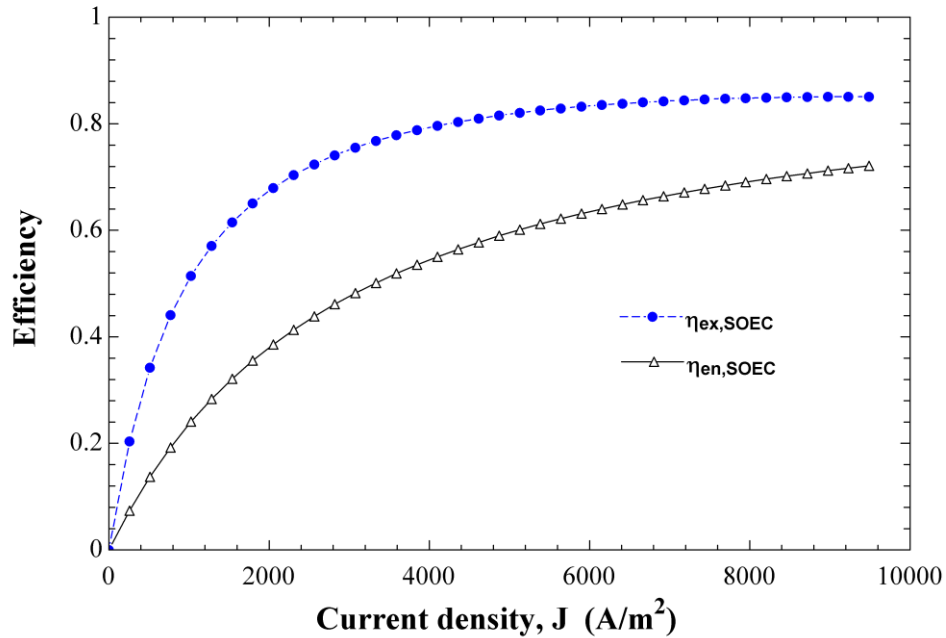


Figure 7.33 Variations in SOEC energy and exergy efficiencies with changing current density.

#### 7.4. Overall SOE System Performance Results

The performance of the SOE system is assessed using both energy and exergy efficiencies as defined for the various cases by equations (6.39-6.46). These efficiencies are formulated based on hydrogen as the primary output of the system. Thus, the hydrogen lower heating value (LHV) is used in addition to ambient temperature and pressure of 293.15 K and 101.325 kPa, respectively. Moreover, the exergy input, exergy output, and the exergy destruction rates are traced along the exergy flow within the SOE system to identify the processes and components that are responsible for higher exergy destruction rates.

In Fig. 7.34, the energy and exergy efficiencies of the SOE system are presented for the two cases of with and without a hydrogen compression unit. These efficiencies reflect the performance of the reference cases considered and illustrated in Figs. 5.1 and 5.2. The SOE system achieves an energy efficiency of 85.15%, which reduces to 79.24% when considering the power requirement for hydrogen compression to 15 MPa. The exergy efficiency is 83.41% and reduces to 77.62% in the case of hydrogen compression. Fig. 7.34 also compares the system efficiencies for the two cases of with and without compressed hydrogen storage as the hydrogen compression reduces the energy efficiency by 5.91% and the exergy efficiency by about 5.79%. Only a few studies have reported the exergy

efficiency of large-scale hydrogen production systems, but the energy efficiency (thermal efficiency) of a nuclear powered SOE plant was reported by Harvego et al. [161] to be 47.1%, considering the nuclear to power production efficiency of 53.2%, thus the efficiency of electricity to hydrogen is about 88.7%, which is satisfactorily comparable with the obtained result.

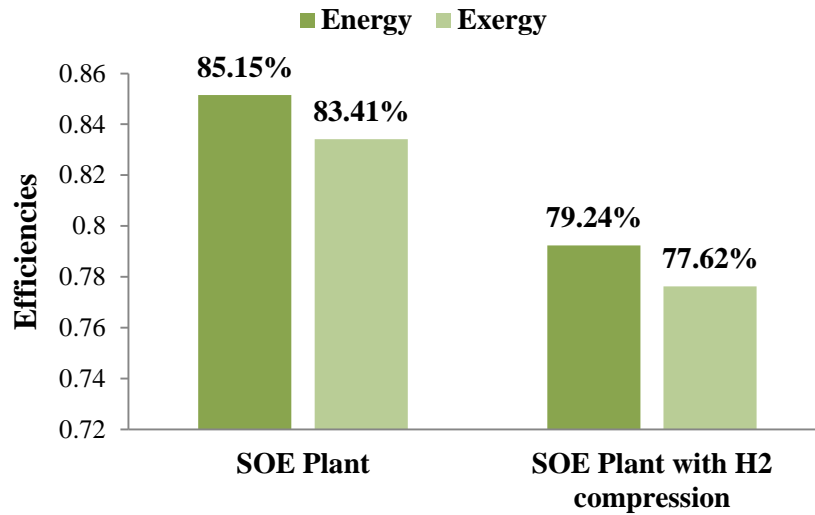


**Figure 7.34** The energy and exergy efficiencies of the SOE system with and without hydrogen compression storage.

Despite the compression penalty, the efficiencies achieved by the SOE system are very high compared to the well-established low temperature electrolyzers whose current state-of-the-art technologies achieve conversion efficiencies of 67% (LHV) [3]. In hydrogen production, storage is a chronic problem, and one which other technologies have to administer. For example, it was estimated that hydrogen handling, including hydrogen compression, to about 2 MPa adds a per kilogram of hydrogen cost of about \$1.88 [3].

Considering the reference case assumptions, as presented in Table 7.5, the SOE system produces hydrogen at a rate of 27.75 kg h<sup>-1</sup> (i.e., 308.7 Nm<sup>3</sup> h<sup>-1</sup>) while consuming a total power of 1.088 MW. Comparing this production rate with an experimentally reported peak production rate of 5.7 Nm<sup>3</sup> h<sup>-1</sup> produced by 18 kW stacks [134], the reported stacks, extrapolating for a power of 1.088 MW, are expected to have a production rate of 28.11 kg h<sup>-1</sup>, which agrees with the value obtained by the present study and serves as a validation of the current holistic model. The peak production value is selected since no degradation

effects are considered in the present work. The minor discrepancy may be attributed to the variations in some design and operating parameters. Another study considered large-scale nuclear hydrogen production [161] that reported a hydrogen production rate of  $2.356 \text{ kg s}^{-1}$  utilizing 329 MWe, which breaks down to about  $26.588 \text{ kg h}^{-1}$  per 1 MWe. These results closely match the present results and support the modular stacks scaling-up to meet high hydrogen demands. Thus, multiple modular units can be deployed and may be partially operated to accommodate seasonal variations in renewable energy resources.

A detailed solution of the reference case is presented in Table 7.7. In this table, a list of the mass flow rate, temperature, pressure, specific enthalpy, specific entropy, and specific exergy for the state points, as numbered in Figs. 5.1-5.2 is provided.

**Table 7.7 The reference case solution listing for each state point the mass flow rate, temperature, pressure, specific enthalpy, specific entropy, and specific exergy.**

State	$\dot{m}$ (kg s <sup>-1</sup> )	$T$ (K)	$P$ (kPa)	$h$ (kJ kg <sup>-1</sup> )	$s$ (kJ kg <sup>-1</sup> K <sup>-1</sup> )	$ex$ (kJ kg <sup>-1</sup> )
0	0.06888	293.2	101.325	84.007	0.2965	0
1	0.06888	293.2	193.139	84.139	0.2966	0.09198
2	0.06888	391.9	191.208	590.327	1.749	80.602
3	0.06888	393.3	187.384	2708	7.160	611.613
4	0.06888	722.3	185.510	3380	8.406	918.698
5	0.06888	863.7	183.655	3684	8.795	1109
6	0.06888	1010	181.818	4014	9.152	1334
7	0.06888	1073	180.000	4159	9.296	1437
8	0.08204	1073	180.000	4296	10.038	1500
9	0.02087	1073	176.400	8809	34.560	3572
10	0.01316	1073	180.000	5012	13.920	1831
11	0.007708	1073	176.400	15290	69.782	6553
12	0.007708	874.1	174.636	12320	66.759	4465
13	0.007708	416.3	172.890	5636	55.983	940.370
14	0.006797	1073	180.000	787.162	1.127	456.758
15	0.06797	1073	176.400	787.160	1.132	455.218
16	0.06797	1091	185.220	806.669	1.138	473.147
17	0.06117	1073	185.220	787.163	1.120	458.938
18	0.06117	739.8	185.220	431.295	0.7226	219.493
19	0.06117	342.4	183.368	40.674	-0.02682	48.574
20	0.007708	301.2	171.161	3975	51.354	635.901
21	0.007708	659.1	1602	9176	53.474	5215
22	0.007708	301.2	1602	3981	42.116	3350
23	0.007708	660.7	15000	9309	44.285	8042

In Fig. 7.35, the output exergy and the exergy destruction rates are plotted in comparison with the total exergy input. Out of the total exergy input that is provided to the system in the form of electricity, 83.4% is converted to hydrogen while 16.6% is destroyed during the conversion process.

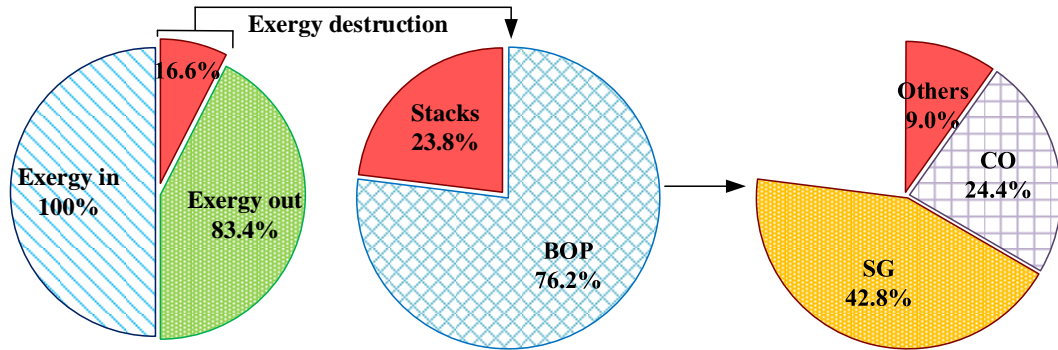


**Figure 7.35 Distribution of exergy output and exergy destruction compared with total exergy input and the relative shares of exergy destruction per main components.**

To gain a deeper insight, the exergy destruction causes are categorized under the two major structures of the SOE system, i.e., the stacks and the BOP. Therefore, it can be observed, as shown in Fig. 7.35, that an exergy destruction share of 23.8% is attributed to the stacks and about 76.2% to the BOP. Further distribution of the exergy destruction shares to the different BOP components is also illustrated. The steam generator is responsible for 42.8% of the total exergy destruction, the AC/DC converter contributes 24.4%, and about 9% is destroyed within the other components such as heat exchangers, pump, and blower. Tracing the exergy destruction within the different components of the SOE system pinpoints the components responsible for the major exergy destruction and losses. Thus, research efforts for the sake of development can be focused on processes where improvement is possible and justified. Fig. 7.35 also indicates that the considerable share of exergy destruction within the BOP is derived by the steam generation process where high exergy content input (electricity) is converted to a lower exergy content form of energy that is heat. Thereby, a significant amount of exergy is destroyed. Assuming steam is externally generated and neglecting the steam generation contribution, the relative contributions in exergy destruction between the stack and the BOP become about 41% and 58%.

#### 7.4.1. Comparison with Conventional Electrolyzers

The outstanding performance of the high temperature SOE can be clearly recognized when compared with conventional low-temperature electrolyzer technologies. The currently well-established low-temperature electrolyzers include two types that are alkaline electrolyzer and PEM electrolyzer. Multiple manufacturers produce these electrolyzers at various scales and hydrogen production capacities. Units of as high as 1–5 MWe and with hydrogen production capacities reaching  $1000 \text{ Nm}^3 \text{ h}^{-1}$  have been recently reported in the literature [162]. In this regard, the capacities, power consumption, and hydrogen production rate of these conventional electrolyzers are compared with the results obtained in the current analysis of high temperature SOE. For example, NEL hydrogen produces alkaline electrolyzers have hydrogen production capacities of  $150\text{--}485 \text{ Nm}^3 \text{ h}^{-1}$  per unit and consumes water feed as a rate of  $0.9 \text{ L Nm}^{-3} \text{ H}_2$  [163]. The efficiency of these systems are given in the range  $3.8\text{--}4.4 \text{ kWh Nm}^{-3} \text{ H}_2$  (i.e., in the range of  $68.1\text{--}78.8\%$  based on LHV). Comparing these figures with that achieved by the SOE, of about  $3.24 \text{ kWh Nm}^{-3} \text{ H}_2$ , illustrates that the SOE considerably outperforms the maximum efficiency of commercial alkaline electrolyzers despite the fact that alkaline electrolyzers have been through significant research and development.

Another example of the commercially available low temperature electrolyzer is PEM electrolyzer. Giner Inc. is a provider of this technology that produces several models with hydrogen production capacities in the range of  $0.03\text{--}1000 \text{ Nm}^3 \text{ H}_2$  [162], [164]. The model Allagash is one of the large PEM electrolyzers units produced by Giner Inc. has a hydrogen production capacity of  $210 \text{ Nm}^3 \text{ H}_2$  while its power consumption is 1 MWe. Comparing this unit with the production rate of the SOE that at 1 MWe produces  $283.8 \text{ Nm}^3 \text{ H}_2$ , proofs that high temperature SOE excels both alkaline and PEM electrolyzer technologies. Furthermore, the remarkable attention and development that are recently directed to high temperature SOE are expected to set this technology far ahead of other hydrogen production technologies.

In the following sections, Figs. 7.36-7.43 present a parametric analysis of the SOE system. The effects of changing one parameter on the SOE system efficiencies, electricity and heat

demand, exergy destructions, and hydrogen production are evaluated and discussed. In these figures, all other parameters are fixed to the reference case, as per Table 7.5.

#### **7.4.2. Effects of Stack Temperature**

The effect of changing the stack operating temperature on the electricity demand of the system and the stack are shown in Fig. 7.36. Furthermore, this figure shows the changes in the stack heat input and output that occur with changing the operating temperature. The operating temperature has a considerable influence on the SOE system electricity and heat requirements. Operating in an exothermic mode (below the thermoneutral state) results in significant increase in total power requirements as a result of the stacks' increasing electricity demand due to the increased irreversibilities (overpotentials). However, the SOE system total electricity demand stabilizes when operating in an endothermic mode (above thermoneutral state), despite the heat that must be externally provided through electric heaters. In the present study, the stacks show a thermoneutral behavior at about 1030 K, below which the heat generated within the stacks is sufficient for the stacks' heating; no external heating is required. Increasing the operating temperature above 1030 K reduces the stacks' electricity demand but increases the heat requirement. Thus the total electricity provided to the SOE system remains the same since the heat is provided by electricity. The reduction in the stacks' electricity demand is attributed to the improved performance of the YSZ-electrolyte cells, specifically the improved conductivity of the YSZ electrolyte at high temperatures that have been reported in the literature [28]. Additionally, Fig. 7.36 presents the variation in the electricity consumed in the BOP heating processes, such as in the steam generator (SG) and in the electric heater (EH). This power reduces to zero with a reduction of the operating temperature to below 960 K, which means the heat produced by the stacks is sufficient for steam generation and for heating incoming streams to the stacks' temperature. This result is supported by the experimental SOE stack test [134], which reported a 15 kW stack test and confirmed that electric heater demands reduce by about 50% when operating just below the thermoneutral voltage.

The variations in the overall SOE system performance with changing the stacks' operating temperature are evaluated in terms of energy and exergy efficiencies over the range from 900–1300 K, as illustrated in Fig. 7.37. This figure considers both cases of with and without

hydrogen compression. The efficiencies change considerably with the change in the mode of operation, either exothermic or endothermic, as presented by equations (6.39 –6.46).

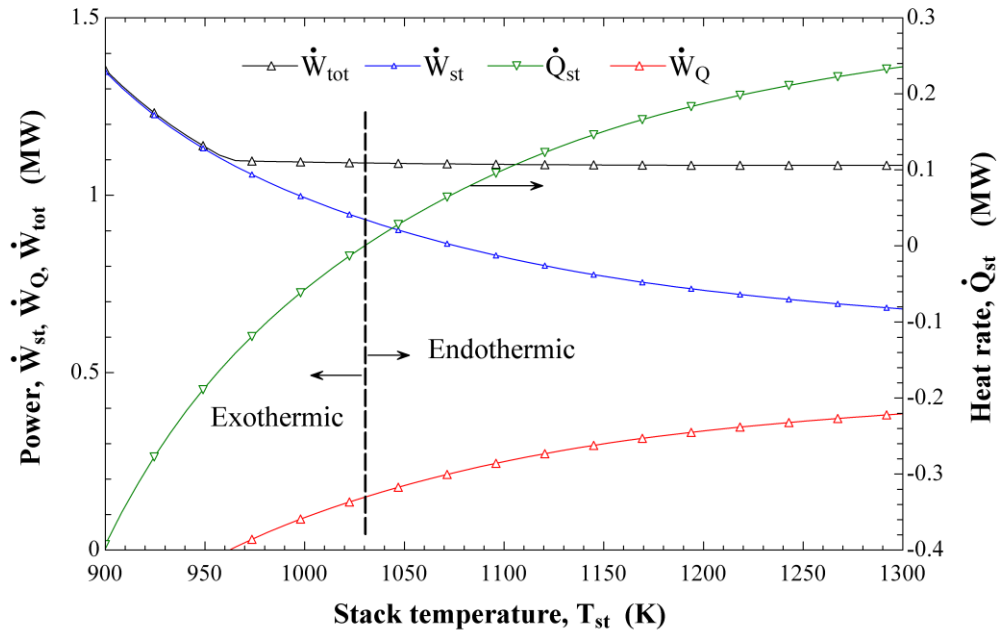


**Figure 7.36** The variations in total power input to the SOE system, the stacks power and power consumed for heating with variations in the stacks operating temperature.

The efficiencies stabilize at high values while operating in endothermic mode; for example, in the case of no hydrogen compression, the energy and exergy efficiencies are at about 85%, and 83%. However, these efficiencies drop sharply with a reduction in stack temperature below 1030 K. In the case of hydrogen compression, similar efficiency profiles result, but about 5–6% less than that of the no compression case.

Further investigation of the operating temperature effects on the SOE system exergetic performance is presented in Fig. 7.38. This figure reflects the improvement in stack performance as a result of increasing the operating temperature. For example, the exergy destruction rate within the stack reduced from about 0.2 MW at 900 K to less than 0.05 MW, a reduction of more than 75%. In regard to the BOP, the exergy destruction rate reduces with increasing the operating temperature but to a lesser extent compared with the stacks. The BOP exergy destruction rate shows a minimum destruction rate when operating between 1120–1180 K.

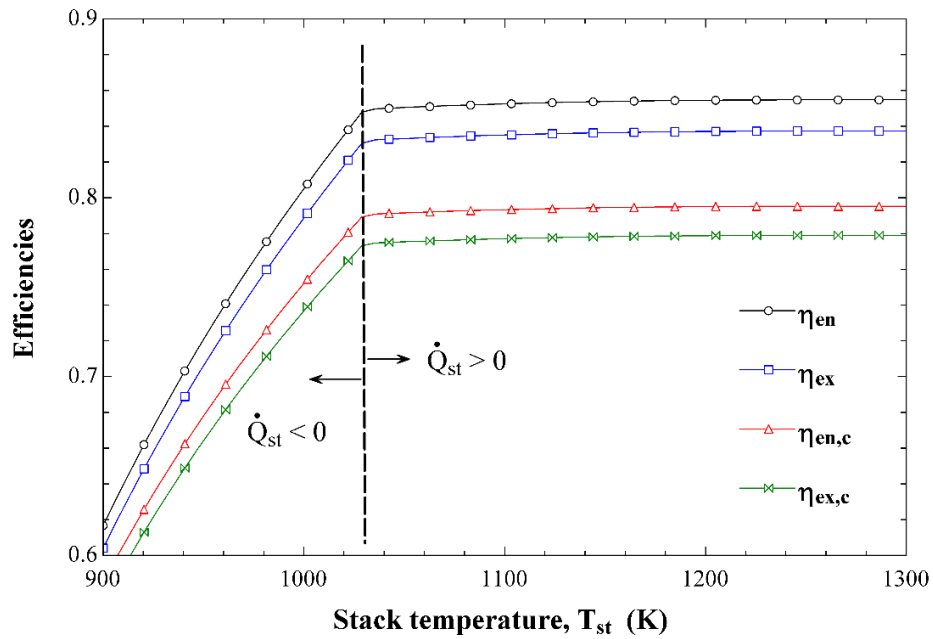


Figure 7.37 The variations in energy and exergy efficiencies of SOE system of the two cases.

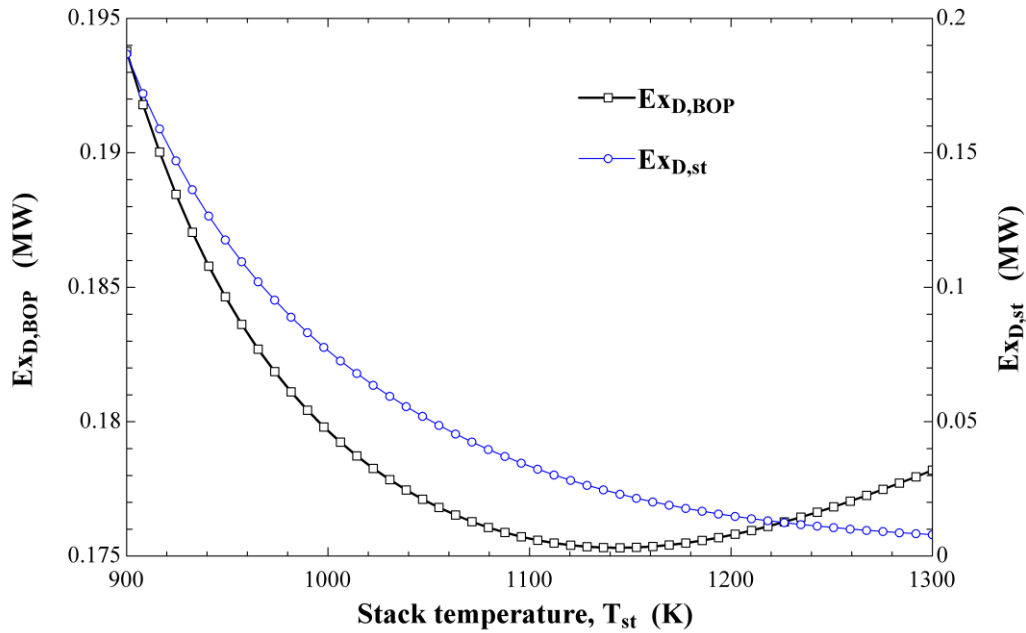


Figure 7.38 Effects of changing the stacks operating temperature on the exergy destruction rates occurs within the stacks and the BOP.

This behavior can be explained as a trade-off between the advantage of increasing the operating temperature that reduces electricity required for heating in the steam generator and the electric heater, and the disadvantage of the exergy losses due to the high

temperature streams leaving the system after the recuperation processes. The changes in exergy destruction rates within the stacks and the BOP with changes in the stack operating temperature are presented for temperatures ranging from 900–1300 K.

### 7.4.3. Effects of Stack Pressure

The effect of the stack operating pressure on energy and exergy efficiencies is shown in Fig. 7.39. The SOE system exergy efficiency is significantly influenced by increasing stack pressure, but the energy efficiency shows limited variation. For example, the exergy efficiency varies from less than 83.5% at ambient pressure to more than 86.5% at a pressure of 8 MPa. However, the energy efficiency reduces from 85.15% at ambient pressure to reach a minimum of about 84.9% at 2 MPa and increases linearly to about 85.2%.

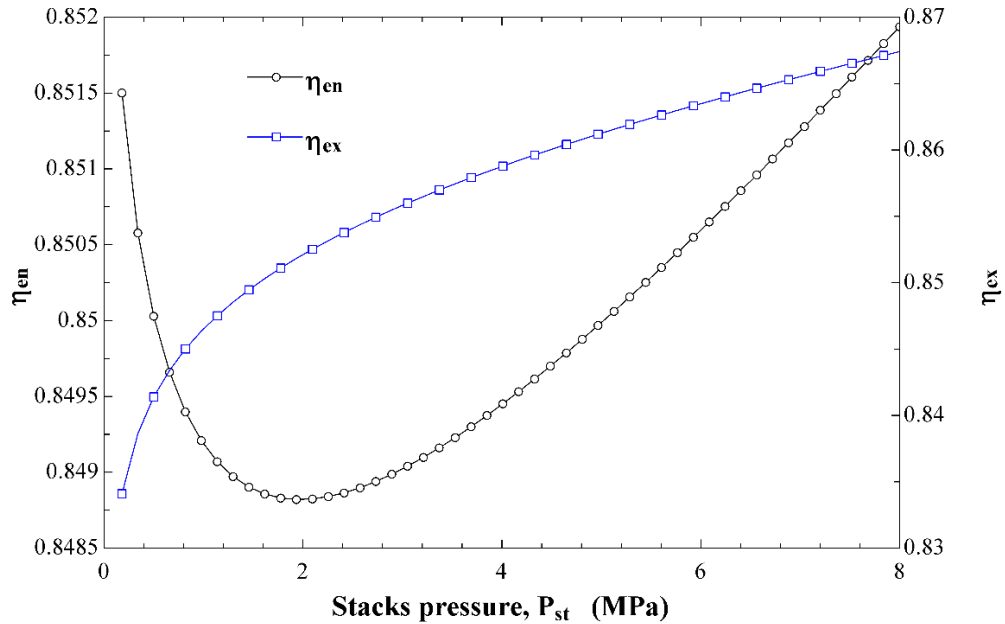


**Figure 7.39** Effects of variations in the stack operating pressure on SOE system energy and exergy efficiencies.

Fig. 7.40 shows the variations in the stacks' heat and electricity demand with the variation in the stack operating pressure. In this case, increasing the stack operating pressure reduces the stack heat demand while the electricity demand increases in a logarithmic profile where the pressure effect is more apparent at lower pressure (up to 4 MPa). However, this effect declines with increasing the pressure.

Fig. 7.41 shows how exergy destruction rates within the stacks and the BOP changes with increasing the stack operating pressure. Increasing the stack operating pressure to about 1 MPa causes a sharp drop in the exergy destruction rate within the BOP by more than 40 kW, after which the BOP exergy destruction levels off at about 94 kW and does not change with a further increase in pressure. The exergy destruction within the stacks does not show significant variations with pressure. The total change was less than 1 kW over the change in pressure from 0.1 MPa to 8 MPa. In regard to the SOE stacks, it can be concluded that the increase in operating pressure has a positive impact on efficiencies and exergy destructions. These results are in agreement with the findings reported in the literature, e.g., [65]–[67].

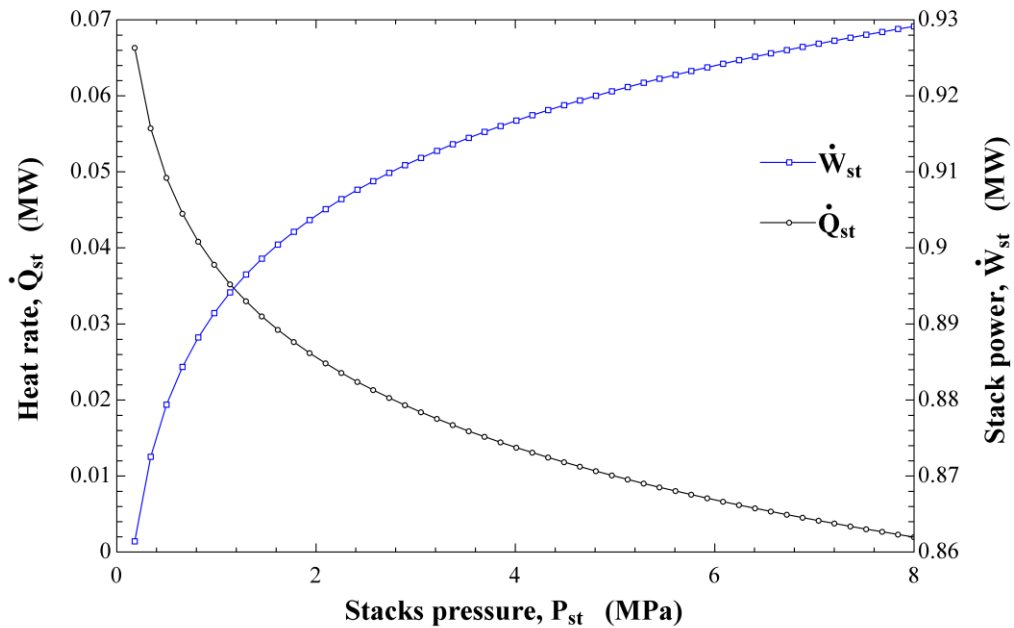


**Figure 7.40** Effects of variations in stack pressure on stacks' heat and power demand.

In the proposed SOE system, the steam generator is a critical component that is responsible for a substantial amount of heat consumption and exergy destruction. Therefore, in Fig. 7.42 the electricity consumption for steam generation and the total SOE system electricity demand are evaluated with increasing the pressure. Though the electricity required for steam generation reduces with increasing the pressure, the total SOE system electricity demand shows a limited reduction. In other words, this trade-off, which might be explained as a gain, may be caused by an improvement in heat transfer characteristics as a result of

increasing the pressure, does not significantly offset the electricity required for compression.

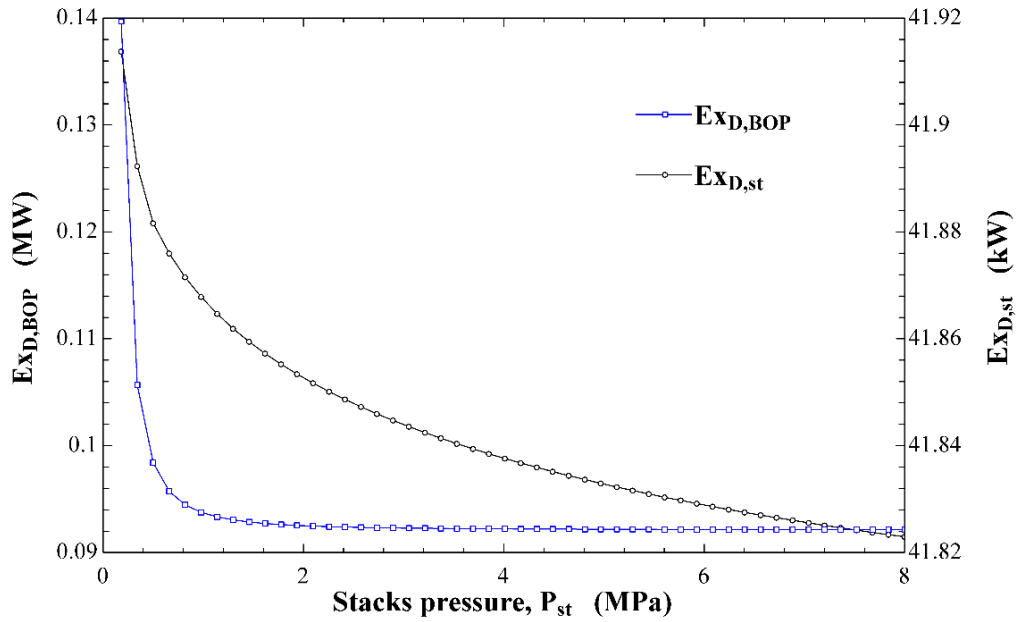


Figure 7.41 Variations exergy distraction rates within the stacks and the BOP with the variation in the stacks operating pressure.

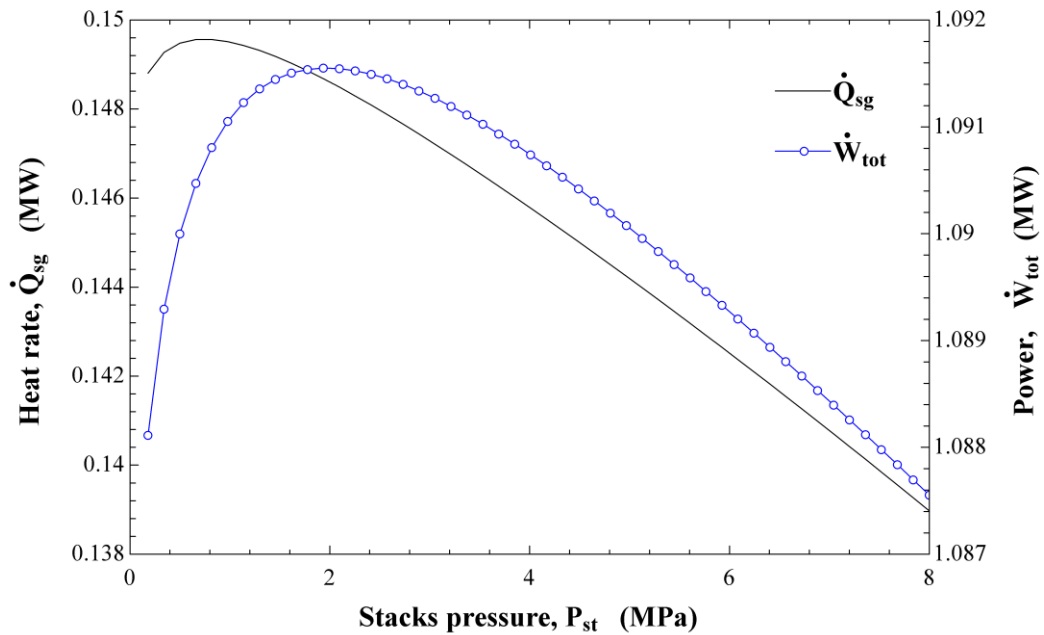


Figure 7.42 Effect of pressure on electric power required for steam generation and total system's electric power demand.

In Fig. 7.43, various pressure drop percentages within the stacks are assumed to observe how these pressure drops influence the overall SOE system energy and exergy efficiencies. Therefore, variation in pressure drop from 0 – meaning no pressure drop – to a maximum of 5% of the stacks’ inlet pressure is considered with respect to the reference case where the stack pressure is set to be 180 kPa. This figure shows a slight linear reduction in efficiencies. However, no significant effect is observed where the maximum variation is less than 0.25%.

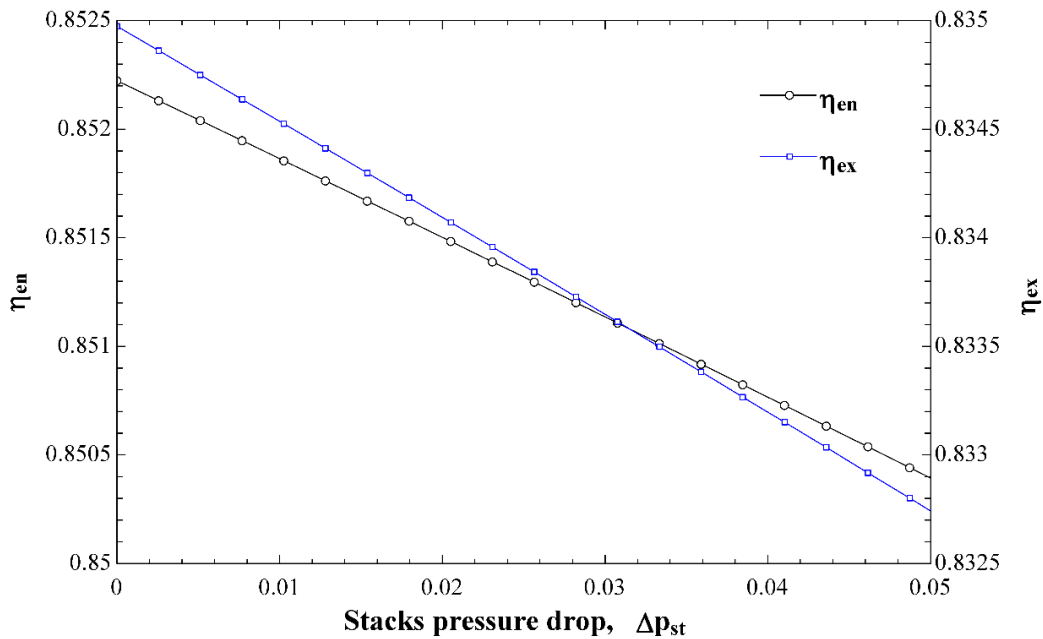


Figure 7.43 Effect of pressure drop within the stacks on the overall SOE system energy and exergy efficiencies.

#### 7.4.4. Effects of Operating Current Density

In Fig. 7.44, the total SOE system power consumption and hydrogen production rate in kg per hour are plotted over a wide range of operating current densities. This figure reflects the design options where an estimate of the power demand and hydrogen production rate can be determined based on the level of technology and practical operating current density of specific type of cells. At a constant power voltage supply, the operating current density linearly increases the power consumption and thus hydrogen production. This is under the assumption that faradaic losses are negligible.

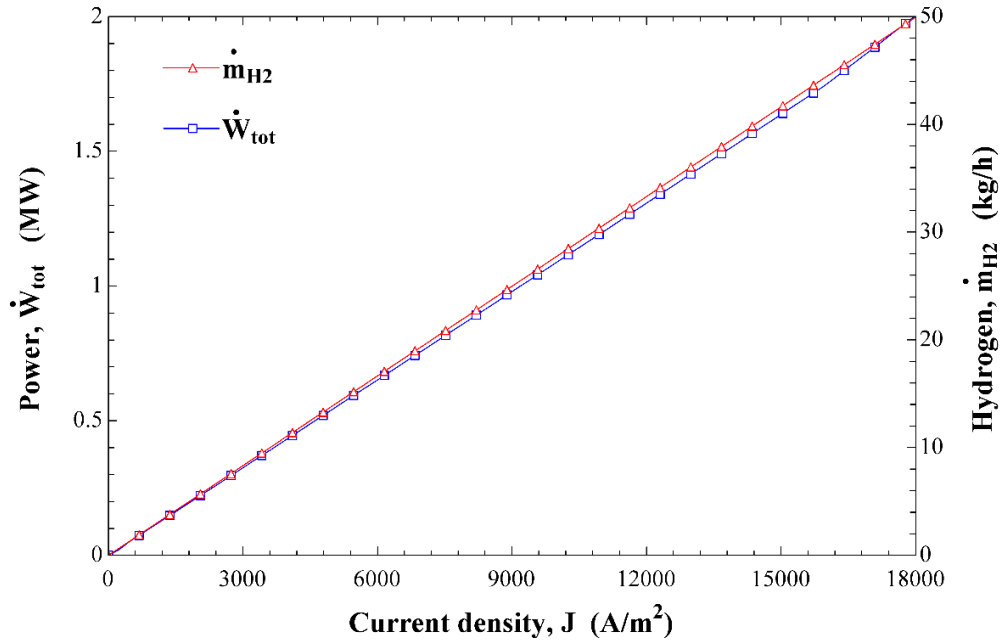


Figure 7.44 Variations in total system electric power demand and hydrogen production with variation in operating current density.

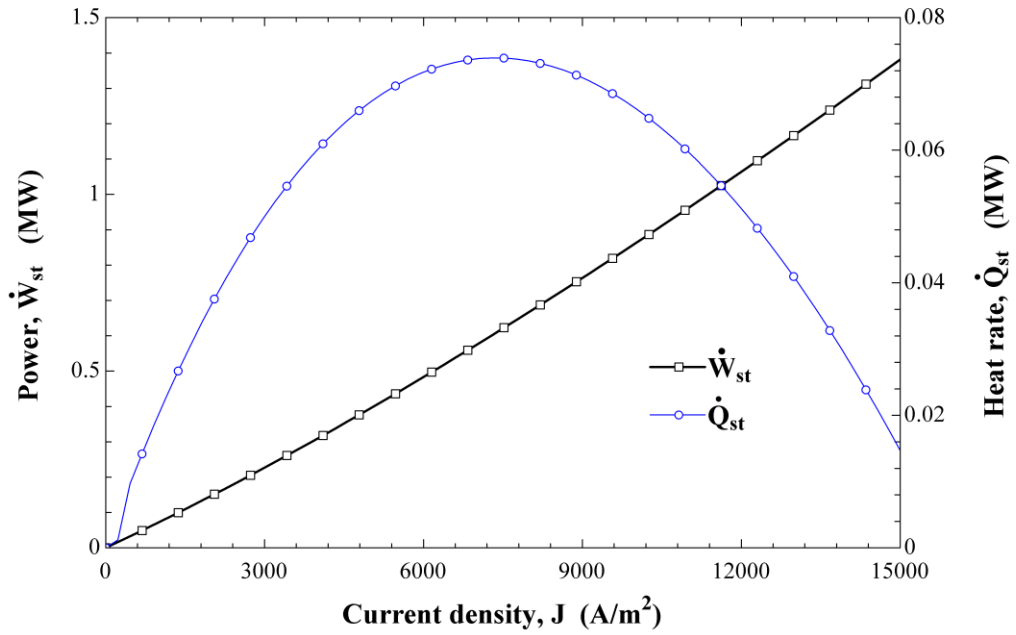
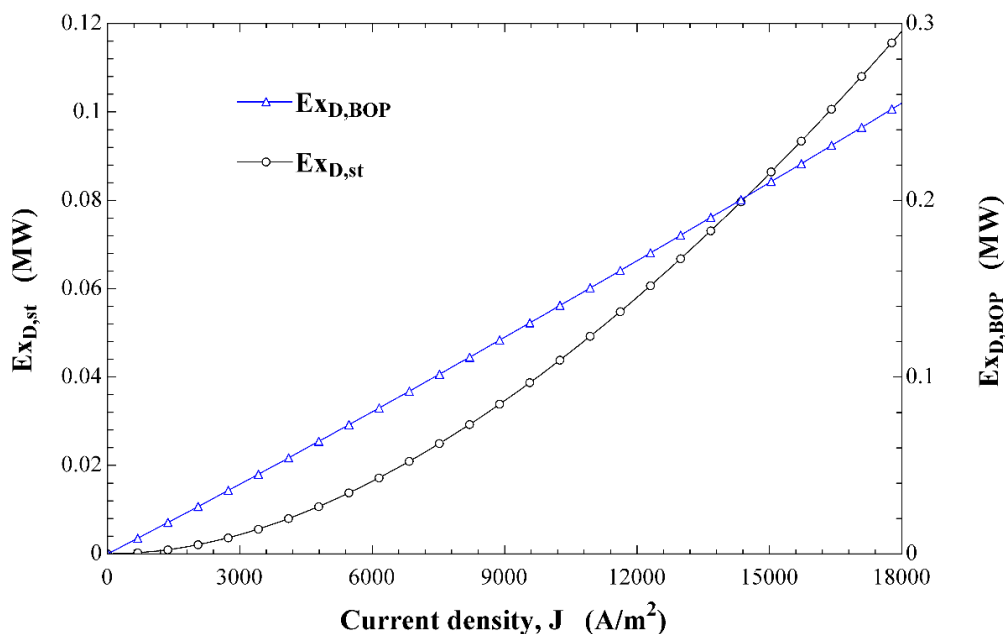


Figure 7.45 Variations in the stacks' heat and power demand with the variations in the operating current density.



**Figure 7.46 Effects of variations in operating current density on exergy destruction rates per stacks and BOP.**

The variations in the stacks' electricity and heat demands are plotted in Fig. 7.45 with changing the current density. For the present study, the electricity increases linearly with the increase in the operating current density, but the heat curve shows a maximum heat requirement point of 0.074 MW at about 7500 A m<sup>-2</sup>. Fig. 7.46 shows variations in exergy destruction rates within the stacks and the BOP with varying the operating current density. The exergy destruction increases proportionally with increasing operating current density. For the range between 6000 A m<sup>-2</sup> and 11000 A m<sup>-2</sup>, the exergy destruction within the SOE stacks varies between 0.016–0.05 MW, while over the same range the exergy destruction within the BOP increased from 0.08 MW to 0.15 MW.

#### **7.4.5. Sensitivity Analysis and Performance Optimization Results**

In order to determine the exergetic performance stability around the reference design point, a sensitivity analysis is conducted to examine the effects of up to 10% variations in the stacks' operating parameters (stack temperature, pressure, and current density) on the overall system exergy efficiencies. Table 7.8 lists the variations in the exergy efficiencies of the SOE considering the two cases presented in Figs. 5.1 and 5.2 (with and without hydrogen compression). These exergy efficiencies are listed corresponding to the

variations in each of the stacks' operating conditions. The design operating temperature, pressure and current density for the reference case are 1073 K, 180 kPa, and 10000 A m<sup>-2</sup>, respectively. The SOE energy and exergy performance under these reference case conditions is presented in Fig. 7.34. In Table 7.8, the deviating conditions are listed, including  $\pm 10\%$  and the corresponding efficiency is then calculated. It can be observed that none of these variations leads to more than 1% change in the exergy efficiencies, which confirms performance stability and tolerance to minor variations in operating conditions.

**Table 7.8 Sensitivity of the exergy efficiencies to  $\pm 10\%$  variations in stack operating temperature, pressure, and current density.**

Vary	-10%	$\eta_{ex}$	$\eta_{ex,c}$	Design	+10%	$\eta_{ex}$	$\eta_{ex,c}$
T <sub>st</sub> (K)	965.7	0.8383	0.7798	1073	1180.3	0.8394	0.7808
P <sub>st</sub> (kPa)	162	0.8388	0.7785	180	198	0.8403	0.7832
J (A m <sup>-2</sup> )	9000	0.8346	0.7766	10000	11000	0.8336	0.7758

For optimization, two different methods are used to assess the optimum SOE exergy efficiency as a function of operating temperature, pressure, and current density. These methods are the conjugate directions method and genetic algorithm. The use of two different methods is to verify that the optimum solution is a global optimum as well as to reduce the risk of the algorithm becoming trapped in a local optimum that could mislead the optimization process. The conjugate direction method is used first, and the optimum exergy efficiency obtained is 87.12%. The optimum operating conditions that achieve this maximum exergy efficiency are identified. Furthermore, the sensitivity of optimum solutions to  $\pm 10\%$  variations are evaluated, as presented in Table 7.9.

**Table 7.9 Results of conjugate directions-based optimization of SOE exergy efficiency and optimum efficiency sensitivity to  $\pm 10\%$  variations in operating conditions.**

Vary	-10%	$\eta_{ex}$	Optimum (87.12%)	+10%	$\eta_{ex}$
T <sub>st</sub> (K)	1128	0.871	1168	1208	0.8711
P <sub>st</sub> (Pa)	7.21E6	0.8697	8.0E6	8.0E6	0.8712
J (A m <sup>-2</sup> )	5000	0.8712	5000	6000	0.8708

In Table 7.10, the results of the genetic algorithm optimization are presented, illustrating the optimum solution to which the algorithm converges and the sensitivity to  $\pm 10\%$  variations. The optimum exergy efficiency is 87.12%, which confirms that already obtained by the conjugate method and ensures that the solution is a global fit. Looking at the operating parameters suggested by the optimization methods to achieve the highest

possible exergy efficiency, the conjugate method suggests a current density of 5000 A m<sup>-2</sup> while genetic optimization suggests 5192 A m<sup>-2</sup>. These values fall in the lower end of the current density range investigated (5000–10000 A m<sup>-2</sup>). For pressure, both methods reached the maximum possible pressure. However, the stack operating temperature was suggested to be between (1149–1168 K), which is a critical parameter, especially considering the present case of standalone operating where electricity provides heating.

**Table 7.10 Results of genetic algorithm optimization of SOE exergy efficiency and optimum efficiency sensitivity to ±10% variations in operating conditions.**

Vary	-10%	$\eta_{ex}$	Optimum (87.12%)	+10%	$\eta_{ex}$
T <sub>st</sub> (K)	1109	0.8708	1149	1189	0.871
P <sub>st</sub> (Pa)	7.21E6	0.8697	8.0E6	8.0E6	0.8711
J (A m <sup>-2</sup> )	5000	0.8711	5192	6192	0.8707

In the SOE system performance stability, the sensitivity analyses show a high stability around the optimum operating conditions with minor variations in exergy efficiency limited to a maximum of 1%.

#### 7.4.6. Exergoeconomic Analysis Results

The exergoeconomic analysis conducted as presented in Chapter 5. Here the results are presented based on the reference case assumptions given in Table 7.11.

**Table 7.11 The financial parameters of the reference case.**

Parameter	Value
Number of years	30
Annual interest rate	5%
Maintenance factor	1.04
Number of hours of operating per year	7886

The capital cost of cost of the equipment is calculated based on literature data [126], [165], [166] for the reference year 2017; and presented for the different components in Table 7.12. The hydrogen cost for the reference case per kg was \$5.71. The effects of the different parameters on the hydrogen cost is presented in the following figures. The cost of the SOE sack is considered a primary factor affecting the hydrogen production cost; therefore, the exergoeconomic factor for SOE stack is traced and considered in all of the following analysis.

**Table 7.12 Capital cost of the SOE system components.**

Parameter	Value
Solid Oxide Electrolysis Cells	92.9 (\$/kW)
Auxiliary units	10% of SOEC cost
Convertor	0.17 (\$/W)
Pump	$91562 \left(\frac{W_P}{445}\right)^{0.67}$
Oxygen circulation blower	10000 \$
Heat exchangers	$2290 (A)^{0.6}$

Figs. 7.47–7.52, showing the variations in the cost in (\$/kg) with the allowable variations in each of these parameters. A general observation that these parameters are leading to a maximum increase in the cost of hydrogen to about \$9/kg. While the minimum is just above \$3/kg. The variations in the exergoeconomic factor appear to have a predictable response dependent on the reduction in exergy destructions. For example, Fig. 7.47 shows the variations in hydrogen production cost and exergoeconomic factor with varying the operating current density. The cost of hydrogen production reduces with the increase of the operating current density. The exergoeconomic factor reduces with the increase of the operating current density. It must be emphasized that the high current density operation increases the utilization and the payback of the SOE unit, but it also increases the cell degradation rate.

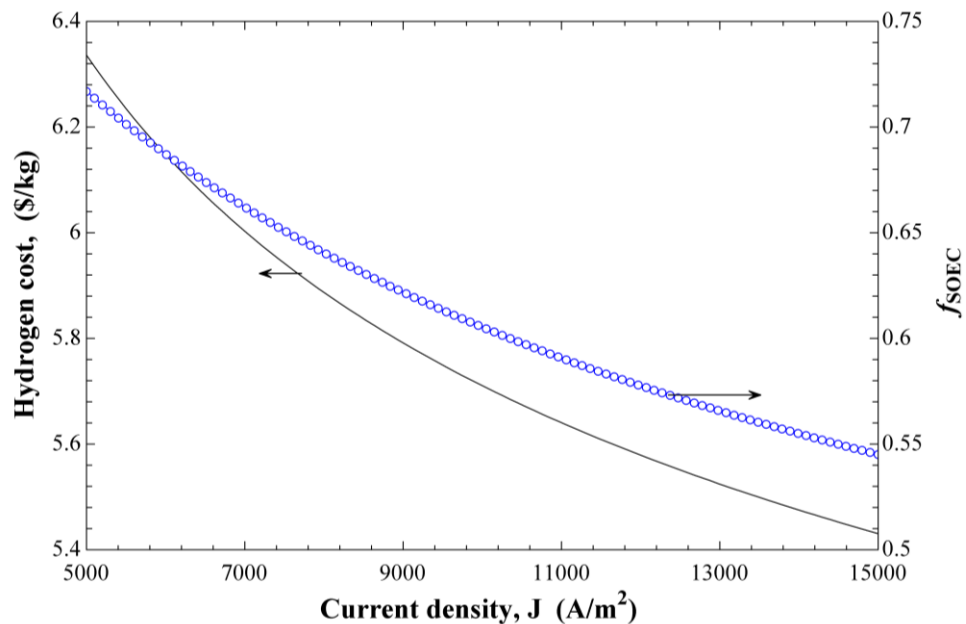


**Figure 7.47 Effect of changing the operating current density on the cost of hydrogen produced and on the exergoeconomic factor of the SOE.**

The effects of varying the stack's operating temperature on the cost of hydrogen and the exergoeconomic factor are shown in Fig. 7.48. The operating temperature has a significant effect on the cost of hydrogen. This is due to the reduced losses and subsequently the required electricity.

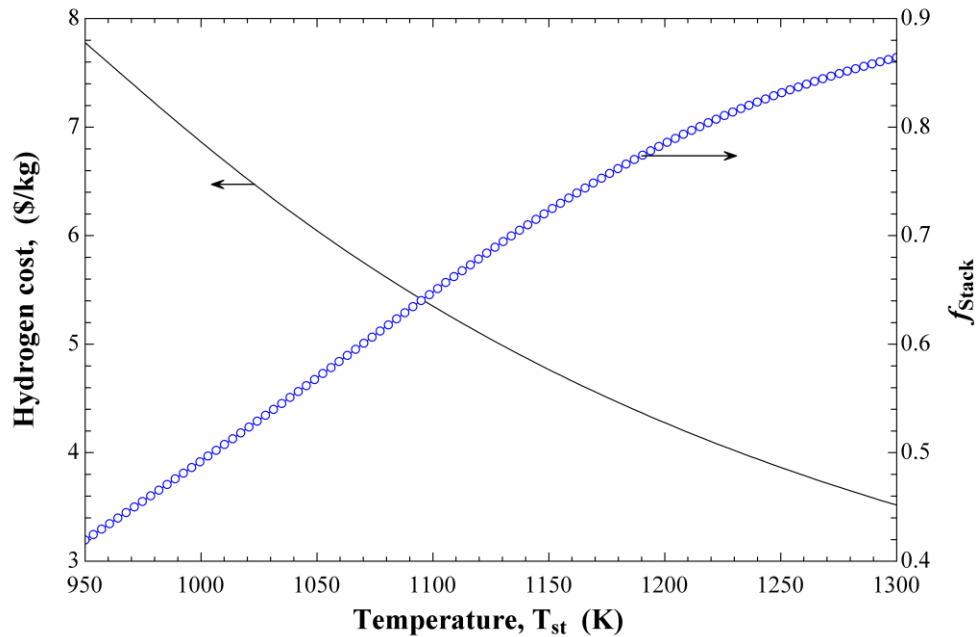


**Figure 7.48** Effect of changing the operating temperature on the cost of hydrogen produced and on the exergoeconomic factor of the SOE.

The impact of changing the stack's operating pressure appeared, as shown in Fig. 7.49, to significantly influence the hydrogen production cost. The figure shows a possible reduction in hydrogen production cost from \$5.71/kg to \$2.25/kg with increasing the operating pressure from pressure around the ambient pressure to over 2 MPa. This cost reduction is about 60% in the \$/kg  $H_2$ , independent of another advantage of delivering higher pressure hydrogen which reduces the compression power requirement in the subsequent storage stage. These findings are consistent with earlier investigations that examined the SOE stacks' performance under elevated pressures. For examples, Jensen et al. [69] concluded that a reduction in the investment cost of 40–50% is possible with increasing the operating pressure to 20 bar, in addition to about 4–5% reduction in operating and maintenance cost.

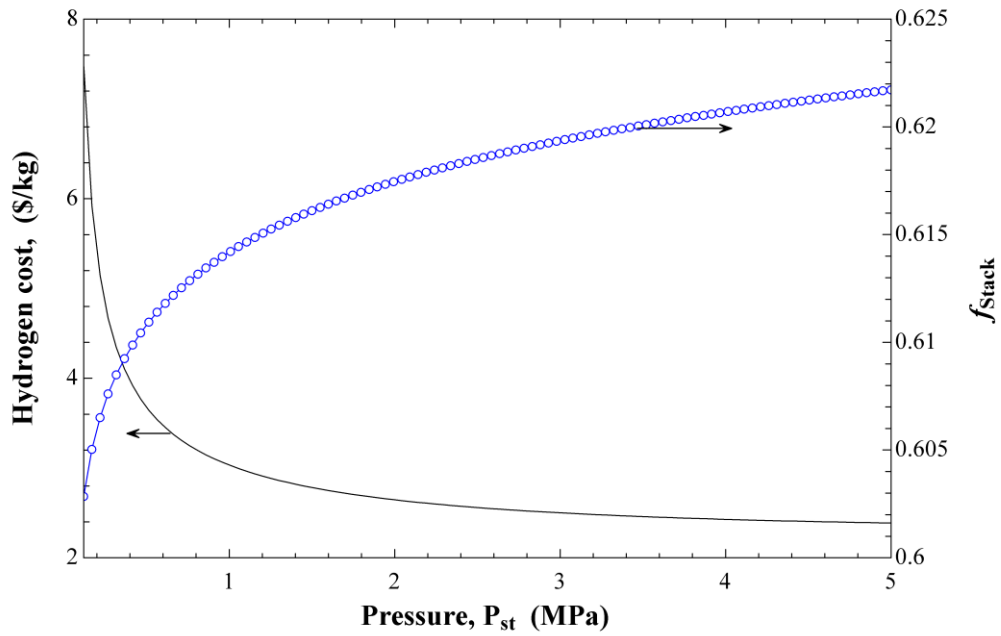


Figure 7.49 Effect of changing the operating current density on the cost of hydrogen produced and on the exergoeconomic factor of the SOE.

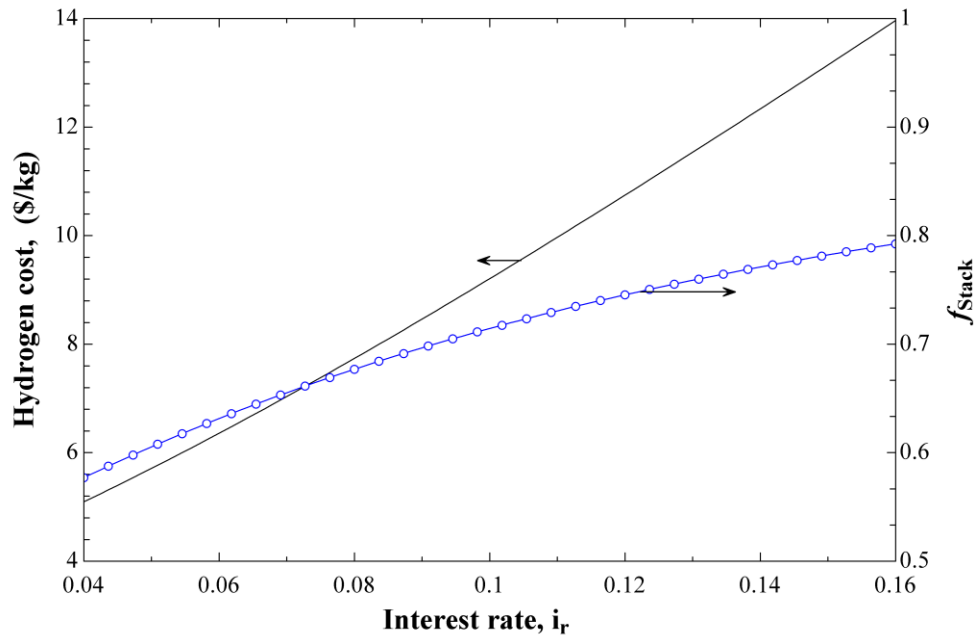


Figure 7.50 Effect of changing the operating current density on the cost of hydrogen produced and on the exergoeconomic factor of the SOE.

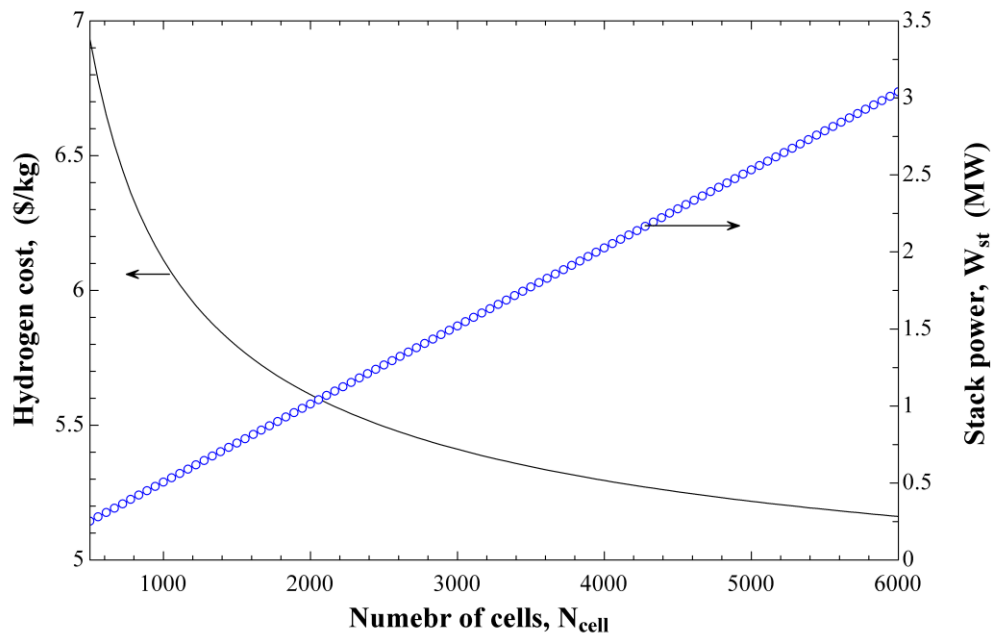


Figure 7.51 Effect of changing the number of cells (scale) on the cost of hydrogen produced and on the exergoeconomic factor of the SOE.

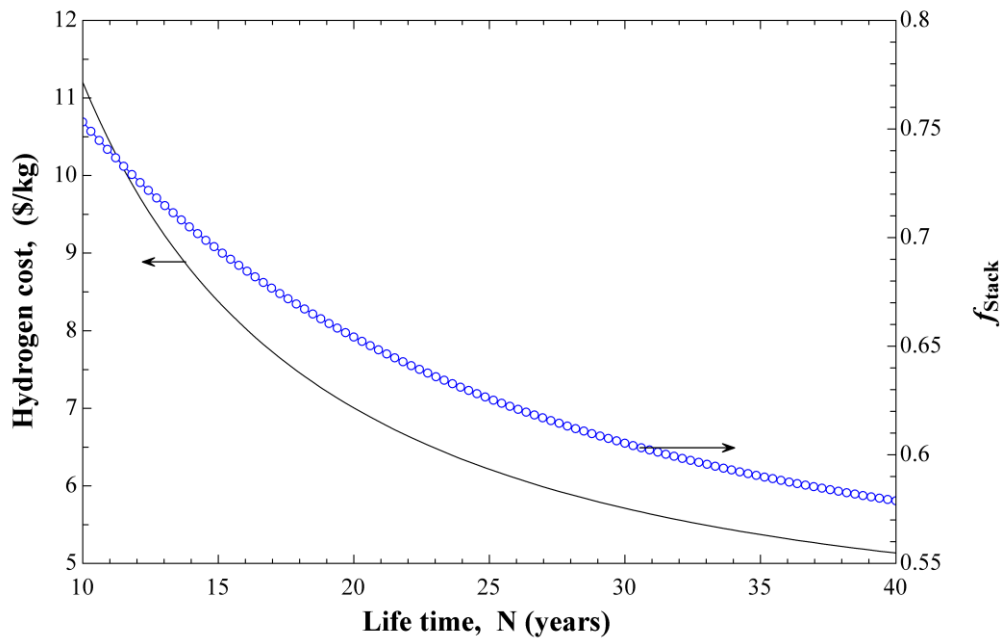


Figure 7.52 Effect of changing the plant life time on the cost of hydrogen produced and on the exergoeconomic factor of the SOE.

## 7.5. Solar Tower Powered SOE Results

In this section, the results corresponding to the performance of the integrated solar tower powered SOE are provided for the different subsystems as presented in Fig. 5.3. These subsystems are: (1) the solar tower, (2) the TES, (3) the S-CO<sub>2</sub> Brayton cycle, and (4) the SOE.

### 7.5.1. Solar Tower Results

The design direct solar radiation is  $850 \text{ W m}^{-2}$ , and total heliostats field area is evaluated to be  $6000 \text{ m}^2$ , to maintain a net electric power of 500 kW as well as the required heat for SOE and TES. The energy efficiency is equivalent to the product of heliostats field and receiver efficiencies; therefore, the energy efficiency of the solar tower, in current analyses, remains constant of about 65.6%. However, the changes in the solar tower operating conditions influence the exergy performance of the solar tower. Fig. 7.53 shows variations in the exergy efficiency of the solar tower with changing the tower outlet temperature (maximum temperature). The solar tower achieves higher exergy efficiency at high temperatures operation. Although, the molten salt mass flow rate reduces significantly. As the tower capable of producing about 8 kg/s at 900 K, it only produces about 3 kg/s when rising the temperature to 1200 K. The solar tower exergy efficiency varies from 37% to 43% with an average of 40% which is reasonably in agreement with the value of about 41.6% reported by Xu et al. [137] for a heliostats field and receiver. The minor difference may result from the more conservative assumption of 87.5% receiver energy efficiency compared with 90% used in [137].

In Fig. 7.54, the variations in the solar tower exergy efficiency and the destruction ratio of the heliostats field are evaluated over changes in ambient temperature. It can be noticed that over an extremes difference of 40 degrees the total variation in exergy efficiency is about 2.5%. The heliostats field exergy destruction rate shows a similar linear variation with maximum exergy destruction at highest ambient temperature. An overview of the solar tower subsystem exergy performance is summarized in Fig. 7.55 which shows how much exergy lost within the heliostats field and the central receiver in relative to the total exergy input to the system. This figure also shows the total net-exergy output from the solar tower. One can notice that only about 40% of the total solar exergy input captured

and transferred to be utilized, while about 40% is lost within the heliostats field and almost 20% within the receiver.

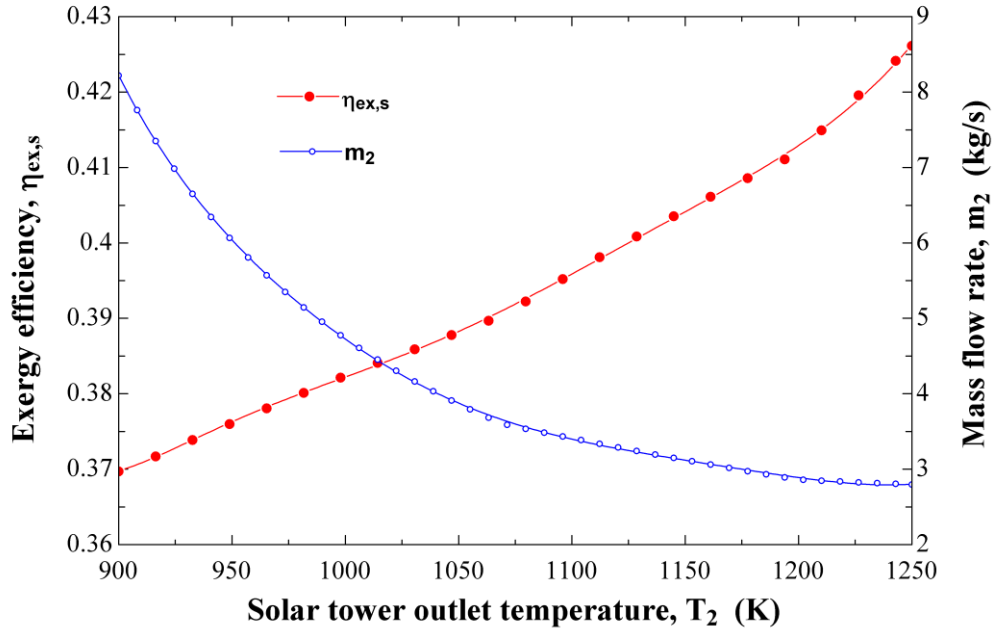


Figure 7.53 Variations in solar tower exergy efficiency and mass flow rate with changing receiver outlet temperature.

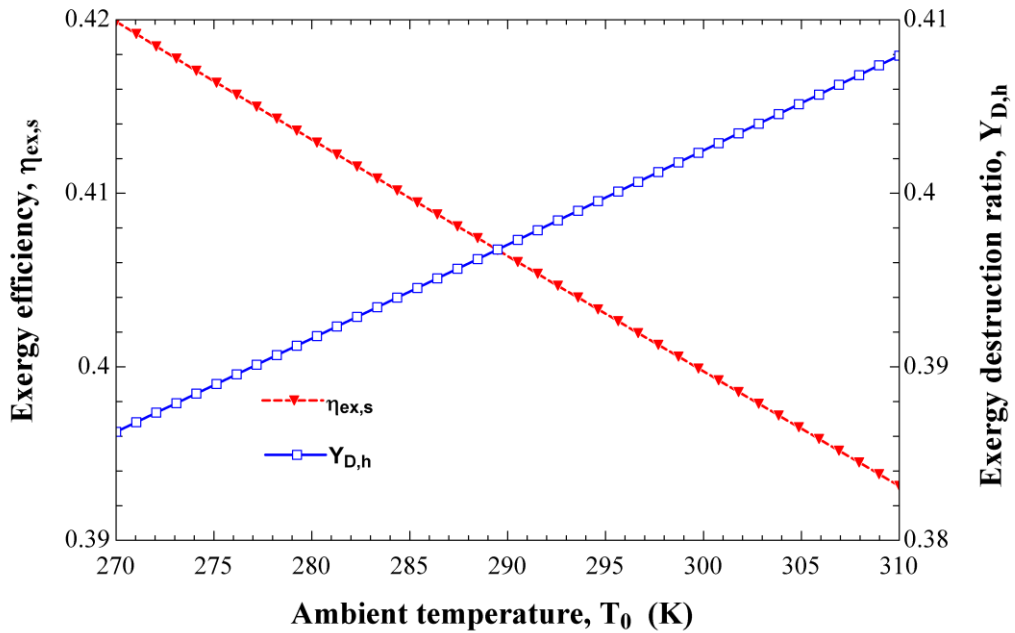
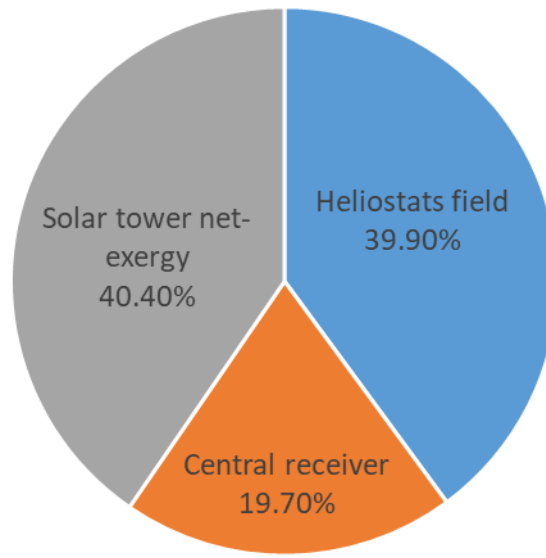


Figure 7.54 Variation in solar tower exergy efficiency and heliostats field exergy destruction ratio with changing ambient temperature.



**Figure 7.55 Exergy destruction ration for the heliostats field and central receiver, and the total net-exergy output from solar tower.**

### 7.5.2. TES Results

A preliminary analysis of the integrated system shows a dependence of the system performance on the solar power outlet temperature, as Carnot cycle concept suggests. Therefore, an overall improvement of the integrated system performance can be achieved with increasing the operating temperature. The selection of fluoride molten salt as HTF permits delivering and maintaining a high temperature  $\sim 1145$  K; which significantly increases S-CO<sub>2</sub> power cycle and SOE conversion efficiencies and eliminates the need to use different storage medium.

A solar multiple of about 2 is assumed to insure solar tower subsystem is large enough to capture during the peak hours the thermal energy required for maintaining the integrated system operating even at night time. As current study focuses on performance, more comprehensive studies must consider economic aspects while setting the plant size. Here, the target net power output is about 500 kW; to be produced by the S-CO<sub>2</sub> Brayton cycle and delivered directly to the SOE. The energy and exergy efficiencies of the TES are defined as the total discharged heat after storage period over the total heat charged, (i.e.,  $Q_{dis}/Q_{ch}$ ), and the total discharged exergy over the total charged exergy, (i.e.,  $Ex_{dis}/Ex_{ch}$ ), respectively. All the units here are energy units e.g., kJ. These definitions consider the three

TES operating modes: charging, storing, and discharging. Therefore, an accurate assessment of heat losses from TES is critical to a meaningful evaluation of TES efficiencies. As several studies investigated TES heat transfer characteristics; e.g., [167]–[169]. All these studies have suggested that the TES temperature linearly declines over storing time as a function of molten salt mass, initial temperature, and design and operation conditions; e.g., insulation material and ambient temperature. Therefore, a linear temperature drop profile is considered in this study, with a maximum temperature drop of 18 degrees over 12 hours. As this assumption appears to be conservative compared with literature reported values of 5–10 degrees for systems with a maximum temperature of 823 K, it is justified since the current TES has a maximum of 1150 K.

Fig. 7.56 shows the hot TES temperature profile over a discharging period of 12 hours. The TES energy and exergy efficiencies achieve a minimum of 97% and 96.5%, respectively, at the end of the discharging period. The average energy efficiency can then be calculated to be about 98.5%. Although, none of the literature reported such an energy efficiency for a TES operating at 1150 K, but a plant currently under construction and implementing 10 hours two tanks TES technology operating at 838 K, reported a storage efficiency of 99% [170].

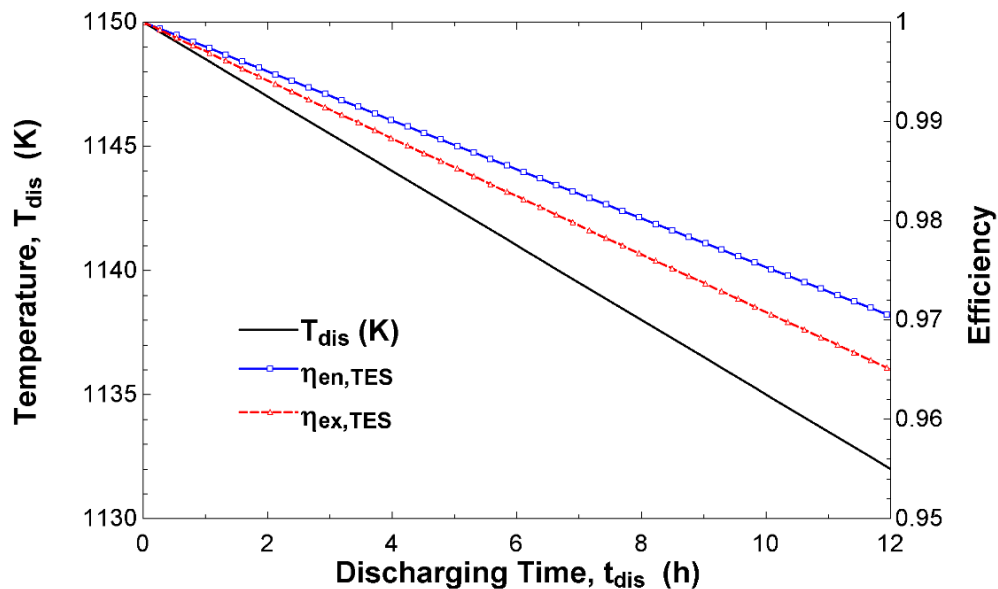
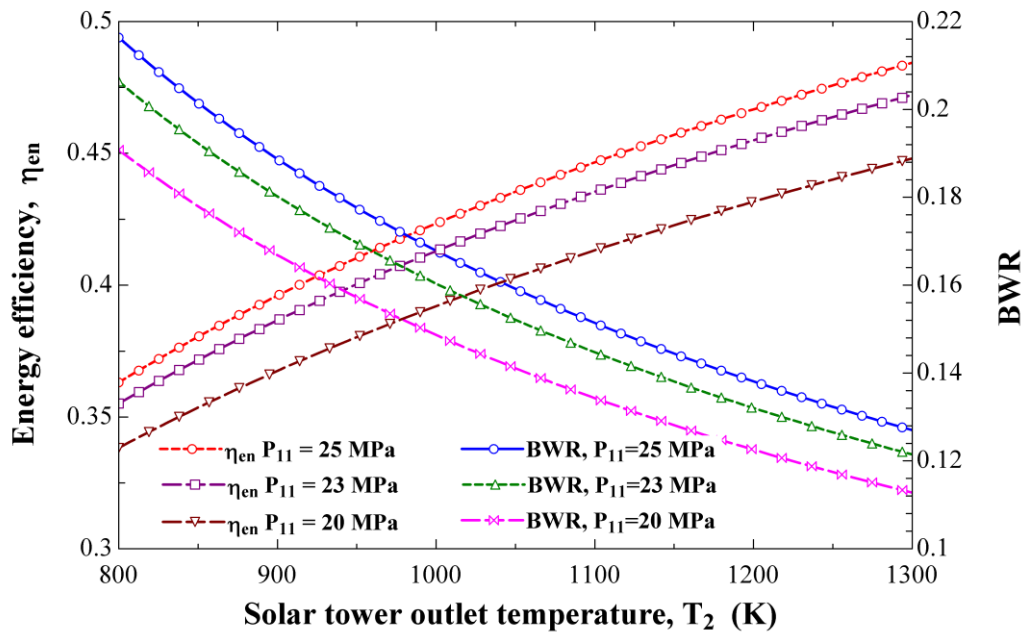


Figure 7.56 The change in the TES temperature over the discharging time as well as the corresponding TES energy and exergy efficiencies.

### 7.5.3. Performance of S-CO<sub>2</sub> Brayton Power Results

The energy efficiency and the back work ratio of the S-CO<sub>2</sub> Brayton power cycle are evaluated at different operating pressures and temperatures, as illustrated in Fig. 7.57. At a turbine inlet pressure of 25 MPa, the cycle energy efficiency varies between 36 to 48% with the variation in solar tower outlet temperatures from 800 to 1300 K. Moreover, the cycle back work ratio is also evaluated over the same range of operating temperatures (800–1300 K) and shows considerable reduction with increasing temperature. Over the entire range, the BWR varies with a factor of 58 to 60%.



**Figure 7.57** The effects of changing the solar tower temperature on the s-CO<sub>2</sub> power cycle performance as illustrated in terms of energy efficiency and BWR for different operating pressures

The effects of the variations in compressor inlet temperature and pressure on the energy and BWR of the S-CO<sub>2</sub> Brayton power cycle are illustrated in Fig. 7.58. The supercritical cycle implies operating above the critical point of the working fluid, CO<sub>2</sub> in this case which has a critical point temperature and pressure of 304 K and 7.1 MPa, respectively. As operating around the critical point is generally disadvantageous and avoided to maintain uniform operation and avoid the sudden significant changes in fluid properties, here operating few degrees above critical point offers significant reduction in compression work and thereby the BWR reduces and the energy efficiency peaks. However, maintaining the

CO<sub>2</sub> working fluid at compressor inlet at such state might create a technical challenge. This is because of the cooling requirements and the small temperature range that above which the BWR increases sharply and below which two phases may form.

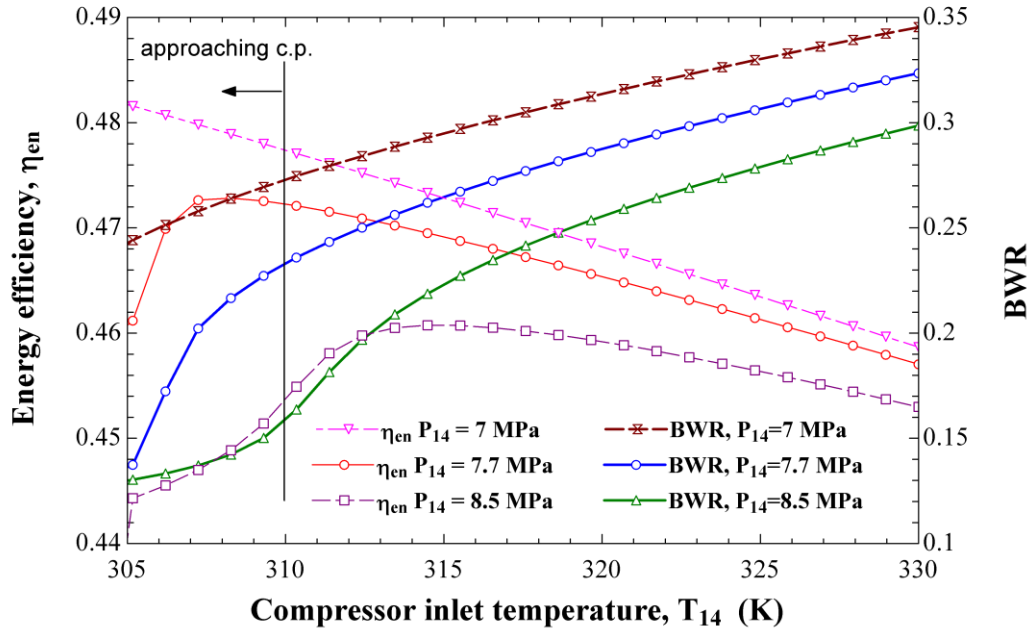


**Figure 7.58** The effects of changing the compressor inlet pressure and temperature on the s-CO<sub>2</sub> power cycle performance as illustrated in terms of energy efficiency and BWR.

The variations of the BWR corresponding to three pressures around the critical point are illustrated in Fig. 7.58. The figure also shows that the energy efficiency of the cycle peaks, for these pressures, between 305 and 310 K. Increasing the pressure led to a reduction in energy efficiency peak and an increase in the temperature at which the peak occurs. Here, increasing the pressure from 7.7 to 8.5 MPa reduces the efficiency by more than 1%. This sensitivity of the S-CO<sub>2</sub> Brayton cycle to the compressor inlet state is a major drawback of this high efficiency cycle.

The evaluation of the exergy destruction through the different cycle components ranks the highest exergy destruction components as follows: the cooler (COL), the heater (HE), the internal heat exchanger (IHE), the compressor (C), and the turbine (T). The exergy destruction ratios, corresponding to cycle exergy input, are illustrated in Fig. 7.59.

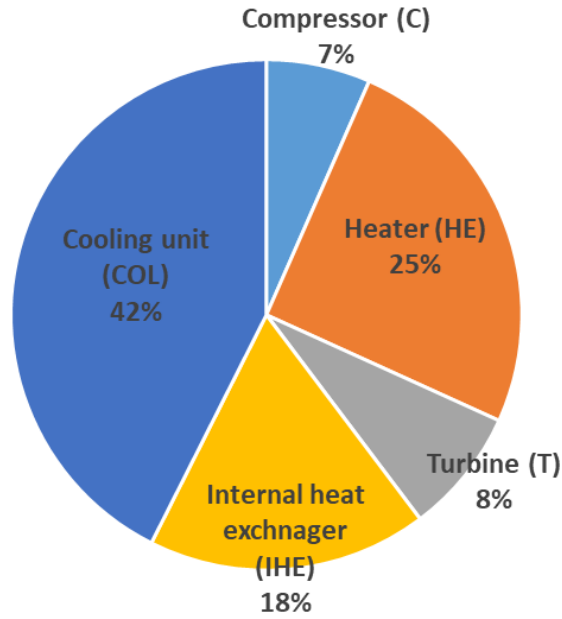


Figure 7.59 Exergy destruction ratios of the s-CO<sub>2</sub> Brayton power cycle components.

#### 7.5.4. Performance of SOE Results

In Fig. 7.60, the simultaneous effects of variations in operating temperature and current density on the cell potential and on the total hydrogen production rate are illustrated. The cell potential drops by about 450 mV with increasing the operating temperature from 900 to 1200 K, as a result, the total hydrogen production rate rises by about 5.5 kg h<sup>-1</sup>, this corresponding to an SOE with a total area of 103.3 m<sup>2</sup>.

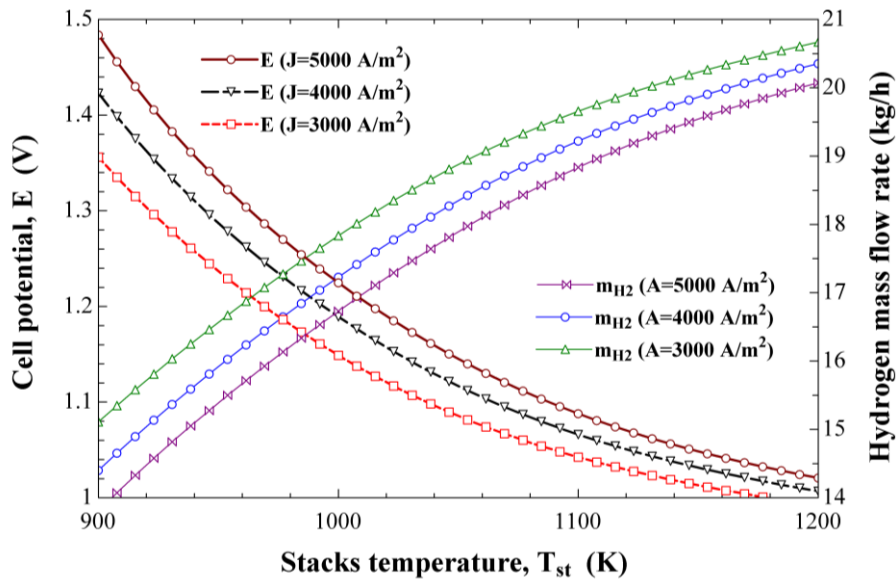


Figure 7.60 Effects of electrolyzer operating temperature and current density on cell potential and total hydrogen production rate.

### 7.5.5. Overall Integrated System Performance Results

The overall integrated system performance based on the base case assumptions and layout presented in Fig. 5.3. Three operating scenarios evolve: (1) operating from the solar field directly, (2) operating from the solar field while charging the TES, and (3) operating from the TES by discharging stored energy during nighttime. Based on these operating scenarios three energy and exergy efficiencies are defined. For instance, in the first case scenario, the energy efficiency is defined as the ratio of hydrogen energy rate (i.e., hydrogen mass flow rate multiplied by the LHV) to the total solar energy hitting the solar field. In the second scenario, the heat rate that is being fed to the TES is taken into account by adjusting the energy output of the system to be the hydrogen energy plus the TES charging rate. In the third scenario, the solar is unavailable thus the energy efficiency is defined as the ratio of the output hydrogen energy to the TES discharged heat rate to operate the system. The definitions of exergy efficiencies followed the same approach. The detailed analysis can be found in [38]. The result of evaluating these energy and exergy efficiencies at the different scenarios are summarized in Table 7.13.

**Table 7.13 Summary of the integrated system energy and exergy efficiencies.**

Efficiency	Solar to hydrogen	Solar to (hydrogen + TES)	Thermal (TES) to hydrogen
Energy	12.7%	56.8%	39.5%
Exergy	13.9%	49.8%	54.1%

### 7.6. SOE Plant Scale-up Results

The results of the Aspen Plus modeled large-scale SOE hydrogen production are presented in this sections. The system flow diagram as modeled in Aspen Plus is given in Fig. 7.61.

In Fig. 7.61, the blue line represents the water stream, the red line represents the oxygen stream, the pink line represents the hydrogen line, and the green line represents a mixture of hydrogen and water vapor. The list of primary equipment is given in Table 7.14. The table shows the cost of these components based on Aspen Process Economic Analyzer. The Aspen Process Economic Analyzer can provide detailed equipment sizing and costing based on the size and type of material of construction.

The solution to the case as given in Fig. 7.61 is presented in the Table 7.15 for the state pointed as numbered in Fig. 7.61. In this case, the hydrogen production rate is 10000 kg

day<sup>-1</sup>. At this scale, the total electric power consumption is 16.29 MW which feeds the stacks and BOP. The total heat rate required by the stacks is 2.024 MW. The sizing of the stack using cells with an active area of 0.0434 m<sup>2</sup>, results in a total number of 25525 cells making a total area of 1108 m<sup>2</sup>.

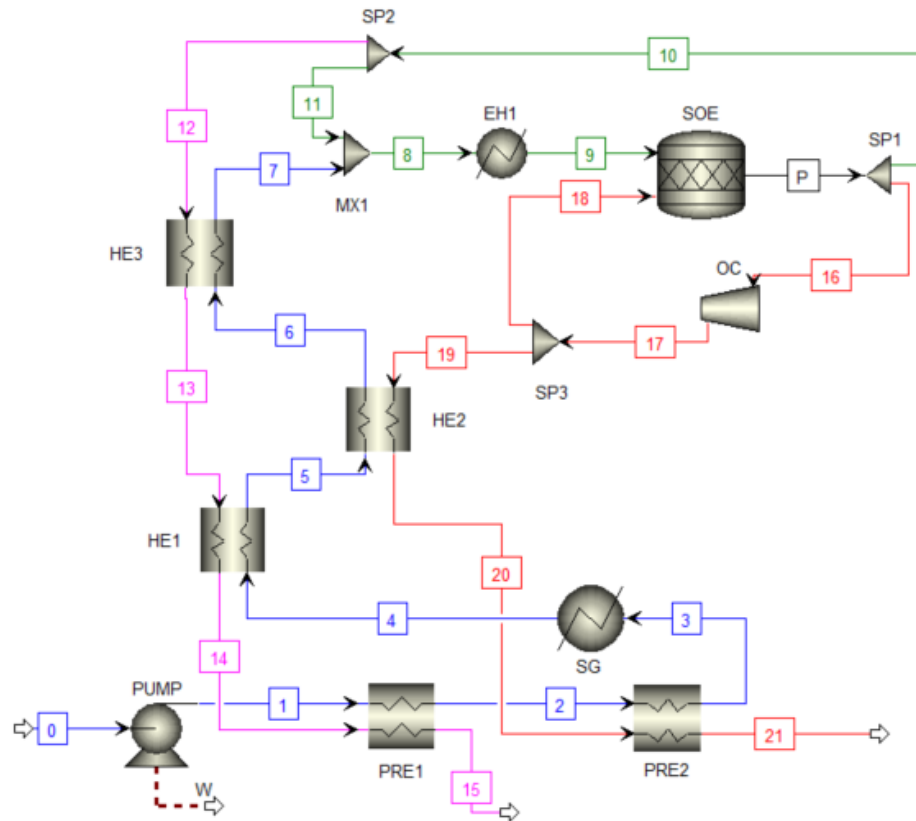


**Figure 7.61** The process flow diagram of the large-scale hydrogen production.

In order to maintain consistency with the small-scale case study presented earlier, the exergoeconomic is used as a mean of evaluating the cost of produced hydrogen. The cost of hydrogen is expected to be in the range of \$4/kg to \$2/kg. This rate is approaching the DoE 2052 target of \$2–3/kg hydrogen production cost from solar tower technology with thermochemical water splitting processes [36]. The relatively limited reduction in the hydrogen cost even at such high production scale is due to the large contribution of the operating cost, i.e., the cost of electricity. This result is in line with earlier investigations that showed that about 70% of the electrolysis hydrogen cost is coming from the cost of electricity [3].

**Table 7.14 List of equipment and their installed cost based on Aspen Plus.**

Equipment	Symbol	Installed cost (\$)
Pump	PUMP	28300
Preheater 1	PRE1	92900
Preheater 2	PRE2	126700
Steam Generator	SG	130000
Heat Exchanger 1	HE1	78400
Heat Exchanger 2	HE2	49800
Heat Exchanger 3	HE3	49200
Mixer chamber	MIX1	-
Electric Heater	EH1	41300
Solid Oxide Electrolyzer	SOE	1094800
Oxygen Blower	OC	18200
Separator1	SP1	-
Separator 2	SP2	-
Separator 3	SP3	-

**Table 7.15 List of stream number and their solution based on Aspen Plus flowsheet given in Fig.7.62.**

Strm.	Material	P	$\dot{m}$	T	ex	h	s
No.	H <sub>2</sub> O/ H <sub>2</sub> /O <sub>2</sub>	kPa	kg h <sup>-1</sup>	K	kJ kg <sup>-1</sup>	kJ kg <sup>-1</sup>	J kg <sup>-1</sup> K <sup>-1</sup>
0	H <sub>2</sub> O	101.325	3722.4	293.2	0	84.007	296.5
1	H <sub>2</sub> O	109.446	3722.4	293.2	8.135	84.019	296.5
2	H <sub>2</sub> O	109.446	3722.4	329.5	35.22	235.962	1034
3	H <sub>2</sub> O	108.351	3722.4	375	72.507	573.357	1718
4	H <sub>2</sub> O	106.184	3722.4	376.4	530.077	2.68E+03	7350
5	H <sub>2</sub> O	105.122	3722.4	723.7	844.291	3.38E+03	8673
6	H <sub>2</sub> O	104.071	3722.4	883.9	1.06E+03	3.73E+03	9108
7	H <sub>2</sub> O	103.030	3722.4	1050	1.32E+03	4.11E+03	9504
8	H <sub>2</sub> O/H <sub>2</sub>	102.000	3722.4	1123	1.45E+03	4.28E+03	9666
9	H <sub>2</sub> O/H <sub>2</sub>	102.000	4423	1123	1.51E+03	4.42E+03	10441
10	H <sub>2</sub> O/H <sub>2</sub>	99.960	1121.4	1123	3.54E+03	9.22E+03	36191
11	H <sub>2</sub> O/H <sub>2</sub>	102.000	704.88	1123	1.83E+03	5.19E+03	14531
12	H <sub>2</sub>	99.960	416.52	1123	6.42E+03	1.61E+04	72815
13	H <sub>2</sub>	98.960	416.52	895.9	3.99E+03	1.26E+04	69466
14	H <sub>2</sub>	97.971	416.52	400.3	187.655	5.40E+03	57757
15	H <sub>2</sub>	96.991	416.52	301.2	-51.349	3.98E+03	53697
16	O <sub>2</sub>	99.960	3675.6	1123	452.013	841.879	1330
17	O <sub>2</sub>	104.958	3675.6	1142	470.842	862.289	1335
18	O <sub>2</sub>	102.000	367.56	1123	453.553	841.880	1325
19	O <sub>2</sub>	104.958	3306.6	1123	455.732	841.881	1317
20	O <sub>2</sub>	104.958	3306.6	743.6	178.603	435.251	875.6
21	O <sub>2</sub>	103.908	3306.6	336.5	4.604	35.351	105

In the near-term, the operating current density and the durability of the cells are very critical factors that can impact the cost of hydrogen production by high temperature electrolysis. However, in the long-term, the development of new material that can efficiently operate at lower temperatures and integrated with other technologies such as solar will be a groundbreaking for the high temperature hydrogen production industry.

## Chapter 8: Conclusions and Recommendations

In this dissertation, the concept of solar hydrogen production through high temperature solid oxide electrolysis is investigated at two scales: (1) the single cell (SOEC) scale and (2) the large-scale SOE system. At the single cell scale, the research pursued the theoretical and experimental development of a novel photoelectrochemical Solid Oxide Cell (PSOC) that can directly convert part of solar energy to photocurrent in order to reduce the required external electricity bias. At the large-scale, the focus was on the development of a standalone SOE system for hydrogen production, utilizing various sources of electricity, notably renewable resources such as solar and wind. The SOE system is also integrated, as a unit, into a solar tower power plant for solar hydrogen production. The performance of these systems is modeled and analyzed through classical thermodynamic approaches, including energy and exergy concepts. Furthermore, sensitivity, optimization, and cost analyses are conducted. The impact of SOE plant scale-up on hydrogen production cost is examined by considering three hydrogen production scales: small, medium, and commercial. The main contributions of this thesis can be summarized in the following points:

- A comprehensive set of experimental results is provided on the performance and characterization of a button cell (NiO-YSZ/NiO-GDC/YSZ/LSM-GDC/LSM).
- Semiconductor selection and application is discussed in the context of the development of a novel PEC, i.e., PSOC for solar hydrogen production application. Two different coating techniques, namely electrospinning and sol-gel methods, have been implemented in order to develop a photoactive layer on current collectors.
- A testing apparatus is designed and built for testing and characterizing PSOCs under light and at different gas reactant compositions and high operating temperatures.
- A standalone SOE system has been conceptually designed, modeled, and optimized for large-scale hydrogen production. The SOE is also integrated into a novel solar tower system for continuous and efficient hydrogen production.

The following sections provide an outline of the main conclusions and recommendations resulting from this work

## 8.1. Conclusions

The following findings are obtained from this thesis study:

- The performance of state-of-the-art SOCs is tested in both SOFC and SOEC operating modes under different operating temperatures and gas compositions. At 100% H<sub>2</sub> and 750°C, the cell OCV was 1.3V, while at a current density of 0.5 A cm<sup>-2</sup>, the cell power density was recorded at 0.28 Wcm<sup>-2</sup>.
- At a hydrogen-to-steam ratio of 1:1 and at a temperature of 750 °C, the cell potential is measured to be 1.3 V, and the cell power density is about 0.39 W cm<sup>-2</sup>.
- The presence of a minimum of about 10 vol.% hydrogen in the fuel electrode was proven to be necessary for cell durability. The cell experienced an accelerated degradation as a result of high steam concentration feeds of 95%, especially while operating at a high temperature of 850°C.
- Despite the accelerated rate of degradation in the cell performance while operating at high steam concentration, the cell micrographs show a high integrity level of the cell makeup.
- The preliminary screening of the candidate semiconductors for the development of the PSOC revealed that TiO<sub>2</sub>, ZnS, and CdS are the most promising semiconductors, based on the requirements set and acting as representatives of various types of semiconductors.
- The sol-gel and electrospinning methods of fabrication process are identified and selected for the development of photoactive layer coating on conductive current collectors.
- The photoactivity of ZnS deposited by electrospinning techniques on Ni foam was detected and measured through OCV measurements. Similarly, the TiO<sub>2</sub> coating layer made by sol-gel on Ni foam was tested under UV light.
- The model predicted an energy efficiency of a single SOEC of 66% at about 10000 A m<sup>-2</sup>. At the same current density, the exergy efficiency reached about 82%.
- The standalone SOE system achieves energy and exergy efficiencies of 85.15% and 83.41%, respectively. For the second case, where power for hydrogen compression to 15 MPa is considered, these efficiencies reduce to 79.24% and 77.62%, respectively.

- Based on the results obtained, SOE outperforms state-of-the-art low-temperature electrolyzers, achieving 3.24 kWh Nm<sup>-3</sup> H<sub>2</sub> compared to the minimum of 3.8 kWh Nm<sup>-3</sup> H<sub>2</sub> achieved by the latter.
- Exergy analysis reveals that 23.8% of the exergy destruction occurs within the stacks while the remainder is destroyed within the BOP components, with about 42.8% occurring within the steam generator, followed by the converter which contributes about 24.4%.
- Sensitivity analysis shows that the SOE system performance remains stable with a 1% maximum variation in energy and exergy efficiencies as a result of ±10% changes in operating conditions from the design point.
- Exergetic optimization shows an optimum SOE system exergy efficiency of 87.12%, which is obtained through two different optimization algorithms. The optimum SOE system exergy efficiency is achieved at operating conditions of 1149 K, 8 MPa, and 5000 A m<sup>-2</sup>. The optimum exergy efficiency remains stable with less than 1% change, corresponding to ±10% changes in operating conditions.
- The overall impact of increasing the operating temperature and pressure on the stacks and BOP exergy performance is positive. However, limits and trade-offs must be established case by case, considering the specific conditions and practically feasible limits.
- At a capacity of 1 MW electric power input, the SOE system produces hydrogen at a rate of 27.75 kg h<sup>-1</sup> and oxygen at a rate of 220.2 kg h<sup>-1</sup>, while the water consumption rate is about 248 kg h<sup>-1</sup>.
- Exergoeconomic analysis concluded an average hydrogen production cost of \$5.71 per kg H<sub>2</sub> for the reference case scale, which may vary, according to technological and economic factors, from \$9 to \$3/kg H<sub>2</sub>.
- The hydrogen production cost can be considerably reduced by increasing the stacks' operating pressure to over 2 MPa.
- Analysis indicates that technological development would have a significant impact on hydrogen production cost, primarily the improvement of cell durability at high current density operation. This is an essential step for near-term SOE commercialization.

- The performance of solar hydrogen production through the integration of current SOE technology into a solar tower power plant is evaluated. The integrated system achieves a solar-to-hydrogen energy efficiency of 12.7% and an exergy efficiency of 13.9%. In the case of operating from the TES, the integrated system energy and exergy efficiencies increased to 39.5%, and 54.1%, respectively.

## 8.2. Recommendations

The following points are the primary recommendations for future research:

- PSOC development is a very promising yet unexplored research direction that can lead to significant improvement in the solar-to-hydrogen efficiency that can be achieved by a PEC.
- Since the interdisciplinary nature of the PSOC involves physics, electrochemistry, and material science, to name a few, in order for this new device to reach its potential, collaborative research efforts, through which the various aspects of a PSOC can be addressed, have to be established.
- In particular, the properties and behavior of semiconductors at high temperatures require investigation with a focus on the chemical and thermal stability of these materials.
- The cell synthesis and fabrication of a photoactive surface or electrode is an additional challenge that must be encountered. For example, two options arise: (1) the development of a single electrode with a photoabsorption capability as well as catalytic activity; or (2) the integration of multi-components/layers, some of which would absorb light while others provide a catalytic site for the redox reaction.
- Different nanostructured inorganic semiconductor materials, such as quantum dots, are worth investigation.
- More specialized coating methods, such as screen printing and sputtering, which can be adapted for the accurate fabrication of a photosensitive surface, should be utilized.
- Systematic testing and characterization should be established in order to identify the key directions and to synchronize the contributions of different areas of expertise.
- In regard to large-scale hydrogen production, more SOE stack testing and design optimization is required. In particular, the development of a prototype SOE unit

should be conducted to examine the degradation level and long-term performance of a SOE unit operating in a standalone mode.

- The integration of SOE technology into renewable systems, such as solar and wind, for hydrogen production is of crucial importance for the realization of sustainable hydrogen production.

## References

- [1] I. Dincer, *Sustainable hydrogen production*, 1st edition. Cambridge, MA: Elsevier, 2016.
- [2] I. Dincer and C. Zamfirescu, “Chapter 2 - Hydrogen and Its Production,” in *Sustainable Hydrogen Production*, Elsevier, 2016, pp. 65–97.
- [3] J. Genovese, K. Harg, M. Paster, and J. Turner, “Current (2009) State-of-the-Art Hydrogen Production Cost Estimate Using Water Electrolysis: Independent Review,” *Natl. Renew. Energy Lab.*, 2009.
- [4] International Energy Agency, “International Energy Agency-Renewables Information 2016,” International Energy Agency, 2016.
- [5] T. A. Boden G. Marland, and R. J. Andres., “Global, Regional, and National Fossil-Fuel CO<sub>2</sub> Emissions. Carbon Dioxide Information Analysis Center.” Oak Ridge National Laboratory, U.S. Department of Energy, 2015.
- [6] M. S. R. Ruedy and K. Lo., “NASA GISS Surface Temperature (GISTEMP) Analysis. In Trends: A Compendium of Data on Global Change. Carbon Dioxide Information Analysis Center.” Oak Ridge National Laboratory, U.S. Department of Energy, 2014.
- [7] K. V. Wong, “Planning and Engineering Strategies to Mitigate Effects of Climate Change,” *J. Energy Resour. Technol.*, vol. 138, no. 1, pp. 014701–014701, 2015.
- [8] G. Luderer *et al.*, “The role of renewable energy in climate stabilization: results from the EMF27 scenarios,” *Clim. Change*, vol. 123, no. 3–4, pp. 427–441, Apr. 2014.
- [9] J. Sathaye *et al.*, “Renewable energy in the context of sustainable development,” 2011.
- [10] O. Edenhofer, Intergovernmental Panel on Climate Change, and Working Group 3, *Renewable energy sources and climate change mitigation: summary for policymakers and technical summary : special report of the intergovernmental panel on climate change*. New York, Cambridge University Press, 2011.
- [11] IRENA, “Renewable capacity statistics 2017,” International Renewable Energy Agency (IRENA), Abu Dhabi, 2017.
- [12] A. McCrone, U. Moslener, F. D’Estais, and C. Gruning, “Global trends in renewable energy investment 2017,” Frankfurt School of Finance & Management gGmbH 2017., 2017.
- [13] I. Dincer, “Green methods for hydrogen production,” *Int. J. Hydrog. Energy*, vol. 37, no. 2, pp. 1954–1971, 2012.
- [14] L. Schlapbach and A. Zuttel, “Hydrogen-storage materials for mobile applications,” *Nature*, vol. 414, no. 6861, pp. 353–8, Nov. 2001.
- [15] B. Rohland, K. Eberle, R. Strobel, J. Scholta, and J. Garche, “Electrochemical hydrogen compressor,” *Electrochimica Acta*, vol. 43, no. 24, 1998.
- [16] P. J. Bouwman *et al.*, “(Invited) Electrochemical Hydrogen Compression,” *ECS Trans.*, vol. 64, no. 3, pp. 1009–1018, Aug. 2014.
- [17] K. Onda, K. Ichihara, M. Nagahama, Y. Minamoto, and T. Araki, “Separation and compression characteristics of hydrogen by use of proton exchange membrane,” *J. Power Sources*, vol. 164, 2007.

- [18] N. A. A. Rusman and M. Dahari, "A review on the current progress of metal hydrides material for solid-state hydrogen storage applications," *Int. J. Hydrog. Energy*, vol. 41, no. 28, pp. 12108–12126, 2016.
- [19] G. F. Naterer, I. Dincer, and C. Zamfirescu, *Hydrogen production from nuclear energy*. Springer, 2013.
- [20] IHS.com, "Hydrogen - Chemical Economics Handbook (CEH)." [Online]. Available: <https://www.ihs.com/products/hydrogen-chemical-economics-handbook.html>. [Accessed: 22-Aug-2017].
- [21] M. Manage, D. Hodgson, N. Milligan, S. Simons, and D. Brett, "A techno-economic appraisal of hydrogen generation and the case for solid oxide electrolyser cells," *Int. J. Hydrog. Energy*, vol. 36, no. 10, pp. 5782–5796, 2011.
- [22] N. E. Carpenter, *Chemistry of sustainable energy*. CRC Press, 2014.
- [23] IEA, "Tracking Clean Energy Progress 2015," International Energy Agency (IEA), Paris, 2015.
- [24] IEA, "IEA Energy Technology Essentials: Hydrogen Production & Distribution," 2007.
- [25] P. Millet and S. Grigoriev, "Water electrolysis technologies," *Renew. Hydrog. Technol. Prod. Purif. Storage Appl. Saf.*, 2013.
- [26] K. Zeng and D. Zhang, "Recent progress in alkaline water electrolysis for hydrogen production and applications," *Prog. Energy Combust. Sci.*, vol. 36, no. 3, pp. 307–326, 2010.
- [27] M. Carmo, D. L. Fritz, J. Mergel, and D. Stolten, "A comprehensive review on PEM water electrolysis," *Int. J. Hydrog. Energy*, vol. 38, no. 12, pp. 4901–4934, 2013.
- [28] X. Li, *Principles of Fuel Cells*. Taylor & Francis, 2005.
- [29] G. F. Naterer, I. Dincer, and C. Zamfirescu, *Hydrogen Production from Nuclear Energy*. London: Springer London, 2013.
- [30] A. AlZahrani, I. Dincer, and X. Li, "A performance assessment study on solid oxide fuel cells for reduced operating temperatures," *Int. J. Hydrog. Energy*, vol. 40, no. 24, pp. 7791–7797, Jun. 2015.
- [31] A. Brisse, J. Schefold, and M. Zahid, "High temperature water electrolysis in solid oxide cells," *Int. J. Hydrog. Energy*, vol. 33, no. 20, pp. 5375–5382, 2008.
- [32] Q. Li, Y. Zheng, W. Guan, L. Jin, C. Xu, and W. G. Wang, "Achieving high-efficiency hydrogen production using planar solid-oxide electrolysis stacks," *Int. J. Hydrog. Energy*, vol. 39, no. 21, pp. 10833–10842, 2014.
- [33] R. Knibbe, A. Hauch, J. Hjelm, S. D. Ebbesen, and M. Mogensen, "Durability of solid oxide cells," *Green*, vol. 1, no. 2, pp. 141–169, 2011.
- [34] P. Moçoteguy and A. Brisse, "A review and comprehensive analysis of degradation mechanisms of solid oxide electrolysis cells," *Int. J. Hydrog. Energy*, vol. 38, no. 36, pp. 15887–15902, 2013.
- [35] A. Steinfeld, "Solar thermochemical production of hydrogen—a review," *Sol. Energy*, vol. 78, no. 5, pp. 603–615, 2005.
- [36] W. Vogel and H. Kalb, *Large-scale solar thermal power: technologies, costs and development*. John Wiley & Sons, 2010.
- [37] M. Romero, R. Buck, and J. E. Pacheco, "An update on solar central receiver systems, projects, and technologies," *J. Sol. Energy Eng.*, vol. 124, no. 2, pp. 98–108, 2002.

- [38] M. Kromer, K. Roth, R. Takata, and P. Chin, “Support for cost analyses on solar-driven high temperature thermochemical water-splitting cycles,” *TIAX LLC Rep.*, no. D0535, 2011.
- [39] K. Rajeshwar, R. D. McConnell, and S. Licht, *Solar hydrogen generation*. Springer, 2008.
- [40] A. A. AlZahrani and I. Dincer, “Design and analysis of a solar tower based integrated system using high temperature electrolyzer for hydrogen production,” *Int. J. Hydrog. Energy*, vol. 41, no. 19, pp. 8042–8056, May 2016.
- [41] C. Zamfirescu and I. Dincer, “Assessment of a new integrated solar energy system for hydrogen production,” *Sol. Energy*, vol. 107, no. 0, pp. 700–713, 2014.
- [42] J. E. Funk and R. M. Reinstrom, “Energy requirements in production of hydrogen from water,” *Ind. Eng. Chem. Process Des. Dev.*, vol. 5, no. 3, pp. 336–342, 1966.
- [43] M. S. Lee, *Theoretical studies of UT-3 thermochemical hydrogen production cycle and development of calcium oxide reactant for UT-3 cycle and carbon dioxide capture*. University of Florida, 2008.
- [44] L. C. Brown, “High Efficiency Generation of Hydrogen Fuels Using Nuclear Power,” GA-C23317, 761612, Feb. 2000.
- [45] G. Naterer *et al.*, “Recent Canadian advances in nuclear-based hydrogen production and the thermochemical Cu–Cl cycle,” *Int. J. Hydrog. Energy*, vol. 34, no. 7, pp. 2901–2917, Apr. 2009.
- [46] G. F. Naterer *et al.*, “Progress of international hydrogen production network for the thermochemical Cu–Cl cycle,” *Int. J. Hydrog. Energy*, vol. 38, no. 2, pp. 740–759, Jan. 2013.
- [47] G. F. Naterer *et al.*, “Advances in unit operations and materials for the CuCl cycle of hydrogen production,” *Int. J. Hydrog. Energy*, vol. 42, no. 24, pp. 15708–15723, Jun. 2017.
- [48] G. F. Naterer, K. S. Gabriel, M. Lewis, and S. Suppiah, “Nuclear Hydrogen Production by Thermochemical Cycles,” *Handb. Hydrog. Energy*, p. 215, 2014.
- [49] O. Yamamoto, “Solid oxide fuel cells: fundamental aspects and prospects,” *Electrochimica Acta*, vol. 45, no. 15, pp. 2423–2435, May 2000.
- [50] S. C. Singhal and K. Kendall, *High-temperature solid oxide fuel cells: fundamentals, design and applications*. Elsevier, 2003.
- [51] W. Doenitz, R. Schmidberger, E. Steinheil, and R. Streicher, “Hydrogen production by high temperature electrolysis of water vapour,” *Int. J. Hydrog. Energy*, vol. 5, no. 1, pp. 55–63, 1980.
- [52] W. Dönitz and E. Erdle, “High-temperature electrolysis of water vapor—status of development and perspectives for application,” *Int. J. Hydrog. Energy*, vol. 10, no. 5, pp. 291–295, 1985.
- [53] H. Arashi, H. Naito, and H. Miura, “Hydrogen production from high-temperature steam electrolysis using solar energy,” *Int. J. Hydrog. Energy*, vol. 16, no. 9, pp. 603–608, 1991.
- [54] H. Zhang, S. Su, X. Chen, G. Lin, and J. Chen, “Configuration design and performance optimum analysis of a solar-driven high temperature steam electrolysis system for hydrogen production,” *Int. J. Hydrog. Energy*, vol. 38, no. 11, pp. 4298–4307, Apr. 2013.

- [55] A. Houaijia, M. Roeb, N. Monnerie, and C. Sattler, "Solar power tower as heat and electricity source for a solid oxide electrolyzer: a case study: Solid oxide electrolyzer," *Int. J. Energy Res.*, vol. 39, no. 8, pp. 1120–1130, Jun. 2015.
- [56] L. Mingyi, Y. Bo, X. Jingming, and C. Jing, "Thermodynamic analysis of the efficiency of high-temperature steam electrolysis system for hydrogen production," *J. Power Sources*, vol. 177, no. 2, pp. 493–499, Mar. 2008.
- [57] J. S. Herring, J. E. O'Brien, C. M. Stoots, G. L. Hawkes, J. J. Hartvigsen, and M. Shahnam, "Progress in high-temperature electrolysis for hydrogen production using planar SOFC technology," *Int. J. Hydrog. Energy*, vol. 32, no. 4, pp. 440–450, Mar. 2007.
- [58] Y. Bo, Z. Wenqiang, X. Jingming, and C. Jing, "Status and research of highly efficient hydrogen production through high temperature steam electrolysis at INET," *Int. J. Hydrog. Energy*, vol. 35, no. 7, pp. 2829–2835, Apr. 2010.
- [59] S. Chan, K. Khor, and Z. Xia, "A complete polarization model of a solid oxide fuel cell and its sensitivity to the change of cell component thickness," *J. Power Sources*, vol. 93, no. 1, pp. 130–140, 2001.
- [60] M. Ni, M. Leung, and D. Leung, "Parametric study of solid oxide steam electrolyzer for hydrogen production," *Int. J. Hydrog. Energy*, vol. 32, no. 13, pp. 2305–2313, Sep. 2007.
- [61] M. Ni, M. Leung, and D. Leung, "Energy and exergy analysis of hydrogen production by solid oxide steam electrolyzer plant," *Int. J. Hydrog. Energy*, vol. 32, no. 18, pp. 4648–4660, Dec. 2007.
- [62] H. Zhang, G. Lin, and J. Chen, "Evaluation and calculation on the efficiency of a water electrolysis system for hydrogen production," *Int. J. Hydrog. Energy*, vol. 35, no. 20, pp. 10851–10858, Oct. 2010.
- [63] J. Nieminen, I. Dincer, and G. Naterer, "Comparative performance analysis of PEM and solid oxide steam electrolyzers," *Int. J. Hydrog. Energy*, vol. 35, no. 20, pp. 10842–10850, 2010.
- [64] J. Laurencin, D. Kane, G. Delette, J. Deseure, and F. Lefebvre-Joud, "Modelling of solid oxide steam electrolyser: Impact of the operating conditions on hydrogen production," *J. Power Sources*, vol. 196, no. 4, pp. 2080–2093, Feb. 2011.
- [65] G. Hawkes, J. O'Brien, C. Stoots, and B. Hawkes, "3D CFD model of a multi-cell high-temperature electrolysis stack," *Int. J. Hydrog. Energy*, vol. 34, no. 9, pp. 4189–4197, May 2009.
- [66] M. Henke, C. Willich, J. Kallo, and K. A. Friedrich, "Theoretical study on pressurized operation of solid oxide electrolysis cells," *Int. J. Hydrog. Energy*, vol. 39, no. 24, pp. 12434–12439, Aug. 2014.
- [67] D. Todd, M. Schwager, and W. Mérida, "Thermodynamics of high-temperature, high-pressure water electrolysis," *J. Power Sources*, vol. 269, pp. 424–429, Dec. 2014.
- [68] Q. Cacciuttolo, J. Vulliet, V. Lair, M. Cassir, and A. Ringuedé, "Effect of pressure on high temperature steam electrolysis: Model and experimental tests," *Int. J. Hydrog. Energy*, vol. 40, no. 35, pp. 11378–11384, Sep. 2015.
- [69] J. E. O'Brien, X. Zhang, G. K. Housley, K. DeWall, and L. Moore-McAteer, "High temperature electrolysis pressurized experiment design, operation, and results," Idaho National Laboratory (INL), 2012.

- [70] S. H. Jensen, X. Sun, S. D. Ebbesen, and M. Chen, "Pressurized Operation of a Planar Solid Oxide Cell Stack," *Fuel Cells*, vol. 16, no. 2, pp. 205–218, Apr. 2016.
- [71] S. H. Jensen, C. Graves, M. Chen, J. B. Hansen, and X. Sun, "Characterization of a Planar Solid Oxide Cell Stack Operated at Elevated Pressure," *J. Electrochem. Soc.*, vol. 163, no. 14, pp. F1596–F1604, Jan. 2016.
- [72] L. S. Mahmud, A. Muchtar, and M. R. Somalu, "Challenges in fabricating planar solid oxide fuel cells: A review," *Renew. Sustain. Energy Rev.*, vol. 72, pp. 105–116, May 2017.
- [73] V. Karakoussis, N. P. Brandon, M. Leach, and R. van der Vorst, "The environmental impact of manufacturing planar and tubular solid oxide fuel cells," *J. Power Sources*, vol. 101, no. 1, pp. 10–26, Oct. 2001.
- [74] N. Mahato, A. Banerjee, A. Gupta, S. Omar, and K. Balani, "Progress in material selection for solid oxide fuel cell technology: A review," *Prog. Mater. Sci.*, vol. 72, pp. 141–337, Jul. 2015.
- [75] S. P. S. Shaikh, A. Muchtar, and M. R. Somalu, "A review on the selection of anode materials for solid-oxide fuel cells," *Renew. Sustain. Energy Rev.*, vol. 51, pp. 1–8, Nov. 2015.
- [76] E. C. Thomsen, G. W. Coffey, L. R. Pederson, and O. A. Marina, "Performance of lanthanum strontium manganite electrodes at high pressure," *J. Power Sources*, vol. 191, no. 2, pp. 217–224, Jun. 2009.
- [77] M. A. Laguna-Bercero, J. A. Kilner, and S. J. Skinner, "Performance and Characterization of (La, Sr)MnO<sub>3</sub>/YSZ and La<sub>0.6</sub>Sr<sub>0.4</sub>Co<sub>0.2</sub>Fe<sub>0.8</sub>O<sub>3</sub> Electrodes for Solid Oxide Electrolysis Cells<sup>†</sup>," *Chem. Mater.*, vol. 22, no. 3, pp. 1134–1141, Feb. 2010.
- [78] M. Mori, Z. Wang, N. Serizawa, and T. Itoh, "Evaluation of SrTi<sub>1-x</sub>CoxO<sub>3</sub> Perovskites (0 ≤ x ≤ 0.2) as Interconnect Materials for Solid Oxide Fuel Cells," *J. Fuel Cell Sci. Technol.*, vol. 8, no. 5, pp. 051010-051010-6, Jun. 2011.
- [79] P. Moçoteguy and A. Brisse, "A review and comprehensive analysis of degradation mechanisms of solid oxide electrolysis cells," *Int. J. Hydrog. Energy*, vol. 38, no. 36, pp. 15887–15902, Dec. 2013.
- [80] S. D. Ebbesen, C. Graves, and M. Mogensen, "Production of Synthetic Fuels by Co-Electrolysis of Steam and Carbon Dioxide," *Int. J. Green Energy*, vol. 6, no. 6, pp. 646–660, Dec. 2009.
- [81] A. Brisse, J. Schefold, and M. Zahid, "High temperature water electrolysis in solid oxide cells," *Int. J. Hydrog. Energy*, vol. 33, no. 20, pp. 5375–5382, Oct. 2008.
- [82] Y. Zheng, Q. Li, T. Chen, W. Wu, C. Xu, and W. G. Wang, "Comparison of performance and degradation of large-scale solid oxide electrolysis cells in stack with different composite air electrodes," *Int. J. Hydrog. Energy*, vol. 40, no. 6, pp. 2460–2472, Feb. 2015.
- [83] A. Nechache, M. Cassir, and A. Ringuedé, "Solid oxide electrolysis cell analysis by means of electrochemical impedance spectroscopy: A review," *J. Power Sources*, vol. 258, pp. 164–181, Jul. 2014.
- [84] E.-C. Shin *et al.*, "Polarization mechanism of high temperature electrolysis in a Ni-YSZ/YSZ/LSM solid oxide cell by parametric impedance analysis," *Solid State Ion.*, vol. 232, pp. 80–96, Feb. 2013.

- [85] S.-D. Kim, J.-H. Yu, D.-W. Seo, I.-S. Han, and S.-K. Woo, "Hydrogen production performance of 3-cell flat-tubular solid oxide electrolysis stack," *Int. J. Hydrog. Energy*, vol. 37, no. 1, pp. 78–83, Jan. 2012.
- [86] F. Petipas, Q. Fu, A. Brisse, and C. Bouallou, "Transient operation of a solid oxide electrolysis cell," *Int. J. Hydrog. Energy*, vol. 38, no. 7, pp. 2957–2964, Mar. 2013.
- [87] M. A. Laguna-Bercero, S. J. Skinner, and J. A. Kilner, "Performance of solid oxide electrolysis cells based on scandia stabilised zirconia," *J. Power Sources*, vol. 192, no. 1, pp. 126–131, Jul. 2009.
- [88] V. Menon, Q. Fu, V. M. Janardhanan, and O. Deutschmann, "A model-based understanding of solid-oxide electrolysis cells (SOECs) for syngas production by H<sub>2</sub>O/CO<sub>2</sub> co-electrolysis," *J. Power Sources*, vol. 274, pp. 768–781, Jan. 2015.
- [89] J. Aicart, M. Petitjean, J. Laurencin, L. Tallobre, and L. Dessemond, "Accurate predictions of H<sub>2</sub>O and CO<sub>2</sub> co-electrolysis outlet compositions in operation," *Int. J. Hydrog. Energy*, vol. 40, no. 8, pp. 3134–3148, Mar. 2015.
- [90] J. Aicart, F. Usseglio-Viretta, J. Laurencin, M. Petitjean, G. Delette, and L. Dessemond, "Operating maps of high temperature H<sub>2</sub>O electrolysis and H<sub>2</sub>O+CO<sub>2</sub> co-electrolysis in solid oxide cells," *Int. J. Hydrog. Energy*, vol. 41, no. 39, pp. 17233–17246, Oct. 2016.
- [91] M. S. Khan, S.-B. Lee, R.-H. Song, J.-W. Lee, T.-H. Lim, and S.-J. Park, "Fundamental mechanisms involved in the degradation of nickel–yttria stabilized zirconia (Ni–YSZ) anode during solid oxide fuel cells operation: A review," *Ceram. Int.*, 2015.
- [92] G. Schiller, A. Ansar, M. Lang, and O. Patz, "High temperature water electrolysis using metal supported solid oxide electrolyser cells (SOEC)," *J. Appl. Electrochem.*, vol. 39, no. 2, pp. 293–301, 2009.
- [93] E. Lay-Grindler *et al.*, "Degradation study by 3D reconstruction of a nickel–yttria stabilized zirconia cathode after high temperature steam electrolysis operation," *J. Power Sources*, vol. 269, pp. 927–936, Dec. 2014.
- [94] A. Fujishima and K. Honda, "Electrochemical Photolysis of Water at a Semiconductor Electrode," *Nature*, vol. 238, no. 5358, pp. 37–38, Jul. 1972.
- [95] J. Bao, "Photoelectrochemical water splitting: A new use for bandgap engineering," *Nat. Nanotechnol.*, vol. 10, no. 1, pp. 19–20, 2015.
- [96] A. A. Ismail and D. W. Bahnemann, "Photochemical splitting of water for hydrogen production by photocatalysis: A review," *Sol. Energy Mater. Sol. Cells*, vol. 128, pp. 85–101, Sep. 2014.
- [97] M. D. Archer, "Photovoltaics and photoelectrochemistry: similarities and differences," *Phys. E Low-Dimens. Syst. Nanostructures*, vol. 14, no. 1, pp. 61–64, 2002.
- [98] M. Gratzel, "Photovoltaic and photoelectrochemical conversion of solar energy," *Philos. Trans. R. Soc. Math. Phys. Eng. Sci.*, vol. 365, no. 1853, pp. 993–1005, Apr. 2007.
- [99] R. van de Krol, Y. Liang, and J. Schoonman, "Solar hydrogen production with nanostructured metal oxides," *J. Mater. Chem.*, vol. 18, no. 20, pp. 2311–2320, 2008.

- [100] X. Shi *et al.*, “Efficient photoelectrochemical hydrogen production from bismuth vanadate-decorated tungsten trioxide helix nanostructures,” *Nat. Commun.*, vol. 5, p. 4775, Sep. 2014.
- [101] C. G. Morales-Guio, L. Liardet, M. T. Mayer, S. D. Tilley, M. Grätzel, and X. Hu, “Photoelectrochemical Hydrogen Production in Alkaline Solutions Using Cu<sub>2</sub>O Coated with Earth-Abundant Hydrogen Evolution Catalysts,” *Angew. Chem. Int. Ed.*, p. n/a-n/a, Nov. 2014.
- [102] V. Preethi and S. Kanmani, “Photocatalytic hydrogen production,” *Mater. Sci. Semicond. Process.*, vol. 16, no. 3, pp. 561–575, Jun. 2013.
- [103] H. Tong, S. Ouyang, Y. Bi, N. Umezawa, M. Oshikiri, and J. Ye, “Nano-photocatalytic Materials: Possibilities and Challenges,” *Adv. Mater.*, vol. 24, no. 2, pp. 229–251, Jan. 2012.
- [104] X. Ye, J. Melas-Kyriazi, Z. A. Feng, N. A. Melosh, and W. C. Chueh, “A semiconductor/mixed ion and electron conductor heterojunction for elevated-temperature water splitting,” *Phys. Chem. Chem. Phys.*, vol. 15, no. 37, pp. 15459–15469, Aug. 2013.
- [105] C. Zhou, J. E. O’Brien, G. Rajan, S. Marsillac, and X. Zhang, “Water Splitting Using High Temperature Solid Oxide Photoelectrochemical Cell and Visible Sunlight: Searching for the Appropriate Semiconductor Materials,” *J. Electrochem. Soc.*, vol. 164, no. 7, pp. H497–H502, 2017.
- [106] Y. P. Varshni, “Temperature dependence of the energy gap in semiconductors,” *physica*, vol. 34, no. 1, pp. 149–154, 1967.
- [107] J. Fleig *et al.*, “Mixed Conductors under Light: On the Way to Solid Oxide Photo-Electrochemical Cells,” *ECS Trans.*, vol. 72, no. 7, pp. 23–33, Apr. 2016.
- [108] G. Walch *et al.*, “A solid oxide photoelectrochemical cell with UV light-driven oxygen storage in mixed conducting electrodes,” *J Mater Chem A*, vol. 5, no. 4, pp. 1637–1649, 2017.
- [109] Omega.com, “Coiled Nickel-Chromium Alloy Resistance Wire.” [Online]. Available: [https://www.omega.ca/pptst\\_eng/NIC60\\_NIC80.html](https://www.omega.ca/pptst_eng/NIC60_NIC80.html). [Accessed: 23-Jan-2018].
- [110] Alliedmineral.com, *Allied Mineral Products*. [Online]. Available: <http://alliedmineral.com/>. [Accessed: 23-Jan-2018].
- [111] Fuelcellmaterial.com, “NEXTCELL-2.5,” 2008. [Online]. Available: [http://www.fuelcellmaterials.com/site/sofc-components/cells-a-substrates?page=shop.product\\_details&flypage=vmj\\_naru.tpl&product\\_id=70&category\\_id=7](http://www.fuelcellmaterials.com/site/sofc-components/cells-a-substrates?page=shop.product_details&flypage=vmj_naru.tpl&product_id=70&category_id=7). [Accessed: 16-Oct-2015].
- [112] Gamry.com, “Potentiostat-Instrument Between Working Electrode/Reference Electrode.” [Online]. Available: <https://www.gamry.com/application-notes/instrumentation/potentiostat-fundamentals/>. [Accessed: 21-Jan-2018].
- [113] Gamry.com, “Gamry Reference 3000 Potentiostat/Galvanostat/ZRA.” [Online]. Available: <https://www.gamry.com/potentiostats/reference-3000/>. [Accessed: 21-Jan-2018].
- [114] Swagelok.com, “Pressure Gauges” [Online]. Available: <https://www.swagelok.com/en/product/Measurement-Devices/Pressure-Gauges>. [Accessed: 21-Jan-2018].

- [115] Alicat.com, “Product Manuals,” *Alicat Scientific*, 22-Jan-2018. [Online]. Available: <https://www.alicat.com/knowledge-base/product-manuals/>. [Accessed: 14-Apr-2018].
- [116] S. Koumi Ngoh and D. Njomo, “An overview of hydrogen gas production from solar energy,” *Renew. Sustain. Energy Rev.*, vol. 16, no. 9, pp. 6782–6792, Dec. 2012.
- [117] R. Hansch, M. R. R. Chowdhury, and N. H. Menzler, “Screen printing of sol–gel-derived electrolytes for solid oxide fuel cell (SOFC) application,” *Ceram. Int.*, vol. 35, no. 2, pp. 803–811, Mar. 2009.
- [118] “CAS No. 546-68-9 | Sigma-Aldrich.” [Online]. Available: <https://www.sigmaaldrich.com/catalog/search?term=546-68-9&interface=CAS%20No.&N=0+&mode=partialmax&lang=en&region=CA&focus=product>. [Accessed: 24-Jan-2018].
- [119] “CAS No. 64-19-7 | Sigma-Aldrich.” [Online]. Available: <https://www.sigmaaldrich.com/catalog/search?term=64-19-7&interface=CAS%20No.&N=0+&mode=partialmax&lang=en&region=CA&focus=product>. [Accessed: 24-Jan-2018].
- [120] “CAS No. 7697-37-2 | Sigma-Aldrich.” [Online]. Available: <https://www.sigmaaldrich.com/catalog/search?term=7697-37-2&interface=CAS%20No.&N=0+&mode=partialmax&lang=en&region=CA&focus=product>. [Accessed: 24-Jan-2018].
- [121] H. W. Coleman and W. G. Steele, *Experimentation, validation, and uncertainty analysis for engineers*. John Wiley & Sons, 2009.
- [122] C. W. Garland, J. W. Nibler, and D. P. Shoemaker, *Experiments in physical chemistry*, 8th ed. Boston: McGraw-Hill Higher Education, 2009.
- [123] B. N. Taylor and C. E. Kuyatt, *Guidelines for evaluating and expressing the uncertainty of NIST measurement results*. Citeseer, 1994.
- [124] S. A. Klein, “Engineering Equation Solver (EES) for Microsoft Windows Operating System: Commercial and Professional Versions,” *Madison WI F-Chart Softw.*, 2002.
- [125] M. S. Sohal and J. S. Herring, “Oxygen Handling and Cooling Options in High Temperature Electrolysis Plants,” Idaho National Laboratory (INL), 2008.
- [126] D. F. Cheddie and R. Murray, “Thermo-economic modeling of an indirectly coupled solid oxide fuel cell/gas turbine hybrid power plant,” *J. Power Sources*, vol. 195, no. 24, pp. 8134–8140, Dec. 2010.
- [127] D. W. Green and R. H. Perry, *Perry’s Chemical Engineers’ Handbook/edición Don W. Green y Robert H. Perry.*, 7 ed. McGraw Hill, 1997.
- [128] Electrosteam.com “Electro-Steam Generator Corp.” 2018. [Online]. Available: <https://www.electrosteam.com/>. [Accessed: 06-Mar-2018].
- [129] Heatric.com, “High Efficiency Heat Exchangers, PCHE Specialists.” [Online]. Available: [https://www.heatric.com/heat\\_exchanger\\_efficiency\\_and\\_effectiveness.html](https://www.heatric.com/heat_exchanger_efficiency_and_effectiveness.html). [Accessed: 22-Mar-2018].
- [130] M. M. Whiston, W. O. Collinge, M. M. Bilec, and L. A. Schaefer, “Exergy and economic comparison between kW-scale hybrid and stand-alone solid oxide fuel cell systems,” *J. Power Sources*, vol. 353, pp. 152–166, Jun. 2017.

- [131] E. A. Harvego, M. G. McKellar, M. S. Sohal, J. E. O'Brien, and J. S. Herring, "Economic Analysis of the Reference Design for a Nuclear-Driven High-Temperature-Electrolysis Hydrogen Production Plant," INL/EXT-08-13799, 933186, Jan. 2008.
- [132] G. Parks, R. Boyd, J. Cornish, and R. Remick, "Hydrogen station compression, storage, and dispensing technical status and costs: Systems integration," National Renewable Energy Laboratory (NREL), Golden, CO., 2014.
- [133] X. Zhang, J. E. O'Brien, R. C. O'Brien, J. J. Hartvigsen, G. Tao, and G. K. Housley, "Improved durability of SOEC stacks for high temperature electrolysis," *Int. J. Hydrog. Energy*, vol. 38, no. 1, pp. 20–28, Jan. 2013.
- [134] C. M. Stoots, J. E. O'Brien, K. G. Condie, and J. J. Hartvigsen, "High-temperature electrolysis for large-scale hydrogen production from nuclear energy – Experimental investigations," *Int. J. Hydrog. Energy*, vol. 35, no. 10, pp. 4861–4870, May 2010.
- [135] H. Barthelemy, M. Weber, and F. Barbier, "Hydrogen storage: Recent improvements and industrial perspectives," *Int. J. Hydrog. Energy*, vol. 42, no. 11, pp. 7254–7262, Mar. 2017.
- [136] S. A. Kalogirou, *Solar energy engineering: processes and systems*. Academic Press, 2013.
- [137] C. Xu, Z. Wang, X. Li, and F. Sun, "Energy and exergy analysis of solar power tower plants," *Appl. Therm. Eng.*, vol. 31, no. 17–18, pp. 3904–3913, Dec. 2011.
- [138] J. E. Pacheco, H. E. Reilly, G. J. Kolb, and C. E. Tyner, "Summary of the solar two test and evaluation program," Sandia National Labs., Albuquerque, NM (US); Sandia National Labs., Livermore, CA (US), 2000.
- [139] D. F. Williams, "Assessment of candidate molten salt coolants for the NGNP/NHI Heat-Transfer Loop," Oak Ridge National Laboratory (ORNL), Oak Ridge, TN (United States), 2006.
- [140] C. K. Ho, "Advances in central receivers for concentrating solar applications," *Sol. Energy*, Apr. 2017.
- [141] G. Conzelmann, M. Petri, C. Forsberg, B. Yildiz, and others, "Configuration and technology implications of potential nuclear hydrogen system applications.," Argonne National Laboratory (ANL), 2005.
- [142] X. Li *et al.*, "High-temperature corrosion behavior of Ni–16Mo–7Cr–4Fe superalloy containing yttrium in molten LiF–NaF–KF salt," *J. Nucl. Mater.*, vol. 464, pp. 342–345, 2015.
- [143] L. C. Olson, J. W. Ambrosek, K. Sridharan, M. H. Anderson, and T. R. Allen, "Materials corrosion in molten LiF–NaF–KF salt," *J. Fluor. Chem.*, vol. 130, no. 1, pp. 67–73, 2009.
- [144] V. Dostal, "A Supercritical Carbon Dioxide Cycle for Next Generation Nuclear Reactors," PhD thesis, MIT, Cambridge, 2004.
- [145] T. Conboy, S. Wright, J. Pasch, D. Fleming, G. Rochau, and R. Fuller, "Performance characteristics of an operating supercritical CO<sub>2</sub> Brayton cycle," *J. Eng. Gas Turbines Power*, vol. 134, no. 11, p. 111703, 2012.
- [146] A. AlZahrani, "Development and Analysis of a Solar-Based Integrated System with a CO<sub>2</sub> Rankine Power Cycle," University of Ontario Institute of Technology (Canada), 2013.

- [147] A. A. AlZahrani and I. Dincer, "Energy and exergy analyses of a parabolic trough solar power plant using carbon dioxide power cycle," *Energy Convers. Manag.*, vol. 158, pp. 476–488, Feb. 2018.
- [148] A. A. R. AlZahrani and I. Dincer, "Rankine cycle power generation system with sc-co<sub>2</sub> working fluid and integrated absorption refrigeration chiller," 2014.
- [149] L. Santini, C. Accornero, and A. Cioncolini, "On the adoption of carbon dioxide thermodynamic cycles for nuclear power conversion: A case study applied to Mochovce 3 Nuclear Power Plant," *Appl. Energy*, vol. 181, pp. 446–463, Nov. 2016.
- [150] Z. Chen, S. Mo, and P. Hu, "Recent progress in thermodynamics of radiation—exergy of radiation, effective temperature of photon and entropy constant of photon," *Sci. China Ser. E Technol. Sci.*, vol. 51, no. 8, pp. 1096–1109, Aug. 2008.
- [151] A. Bejan, G. Tsatsaronis, and M. J. Moran, *Thermal design and optimization*. John Wiley & Sons, 1996.
- [152] X. Li, *Principles of fuel cells*. New York: Taylor & Francis, 2006.
- [153] R. Turton, R. C. Bailie, W. B. Whiting, and J. A. Shaeiwitz, *Analysis, synthesis and design of chemical processes*. Pearson Education, 2008.
- [154] S. Bozorgmehri and M. Hamed, "Modeling and Optimization of Anode-Supported Solid Oxide Fuel Cells on Cell Parameters via Artificial Neural Network and Genetic Algorithm," *Fuel Cells*, vol. 12, no. 1, pp. 11–23, Feb. 2012.
- [155] L. J. Tan, C. Yang, and N. Zhou, "Thermoeconomic Optimization of a Solid Oxide Fuel Cell and Proton Exchange Membrane Fuel Cell Hybrid Power System," *J. Fuel Cell Sci. Technol.*, vol. 11, no. 1, p. 011005, 2014.
- [156] D. G. Milobar, "Analytical Study, One Dimensional Computational Simulation, and Optimization of an Electrode Supported Solid Oxide Electrolysis Cell," 2010.
- [157] O. J. Shariatzadeh, A. Refahi, S. Abolhassani, and M. Rahmani, "Modeling and optimization of a novel solar chimney cogeneration power plant combined with solid oxide electrolysis/fuel cell," *Energy Convers. Manag.*, vol. 105, pp. 423–432, 2015.
- [158] X.-S. Yang, *Engineering optimization: an introduction with metaheuristic applications*. John Wiley & Sons, 2010.
- [159] "NextCell Electrolyte Supported Button Cell," *fuelcellmaterials*. .
- [160] M. E. Orazem and B. Tribollet, *Electrochemical impedance spectroscopy*, vol. 48. John Wiley & Sons, 2011.
- [161] E. A. Harvego, M. G. McKellar, M. S. Sohal, J. E. O'Brien, and J. S. Herring, "Economic Analysis of a Nuclear Reactor Powered High-Temperature Electrolysis Hydrogen Production Plant," no. 43192, pp. 549–558, 2008.
- [162] I. Dincer and A. A. AlZahrani, "4.25 Electrolyzers," in *Comprehensive Energy Systems*, 1st ed., vol. 4, Oxford: Elsevier, 2018, pp. 985–1025.
- [163] Nelhydrogen.com, "Products," 2016. [Online]. Available: <http://nelhydrogen.com/product/a-range/>. [Accessed: 17-Dec-2016].
- [164] Ginerinc.com, "Electrolyzer Stacks, Giner Inc.," 2016. [Online]. Available: <http://www.ginerinc.com/electrolyzer-stacks>. [Accessed: 19-Nov-2016].
- [165] F. Calise, M. Dentice d' Accadia, L. Vanoli, and M. R. von Spakovsky, "Single-level optimization of a hybrid SOFC–GT power plant," *J. Power Sources*, vol. 159, no. 2, pp. 1169–1185, Sep. 2006.

- [166] A. Arsalis, M. R. von Spakovsky, and F. Calise, “Thermoeconomic Modeling and Parametric Study of Hybrid Solid Oxide Fuel Cell-Gas Turbine-Steam Turbine Power Plants Ranging From 1.5 MWe to 10 MWe,” *J. Fuel Cell Sci. Technol.*, vol. 6, no. 1, p. 011015, 2009.
- [167] R. Gabbrielli and C. Zamparelli, “Optimal design of a molten salt thermal storage tank for parabolic trough solar power plants,” *J. Sol. Energy Eng.*, vol. 131, no. 4, p. 041001, 2009.
- [168] C. Suárez, A. Iranzo, F. J. Pino, and J. Guerra, “Transient analysis of the cooling process of molten salt thermal storage tanks due to standby heat loss,” *Appl. Energy*, vol. 142, pp. 56–65, 2015.
- [169] J. Schulte-Fischedick, R. Tamme, and U. Herrmann, “CFD analysis of the cool down behaviour of molten salt thermal storage systems,” in *Proceedings 2nd International Conference on Energy Sustainability*, 2008.
- [170] Nrel.gov, “Concentrating Solar Power Projects - Crescent Dunes Solar Energy Project | Concentrating Solar Power | NREL.” [Online]. Available: [https://www.nrel.gov/csp/solarpaces/project\\_detail.cfm/projectID=60](https://www.nrel.gov/csp/solarpaces/project_detail.cfm/projectID=60). [Accessed: 29-Nov-2017].

# Appendix 1: Fixture Designs

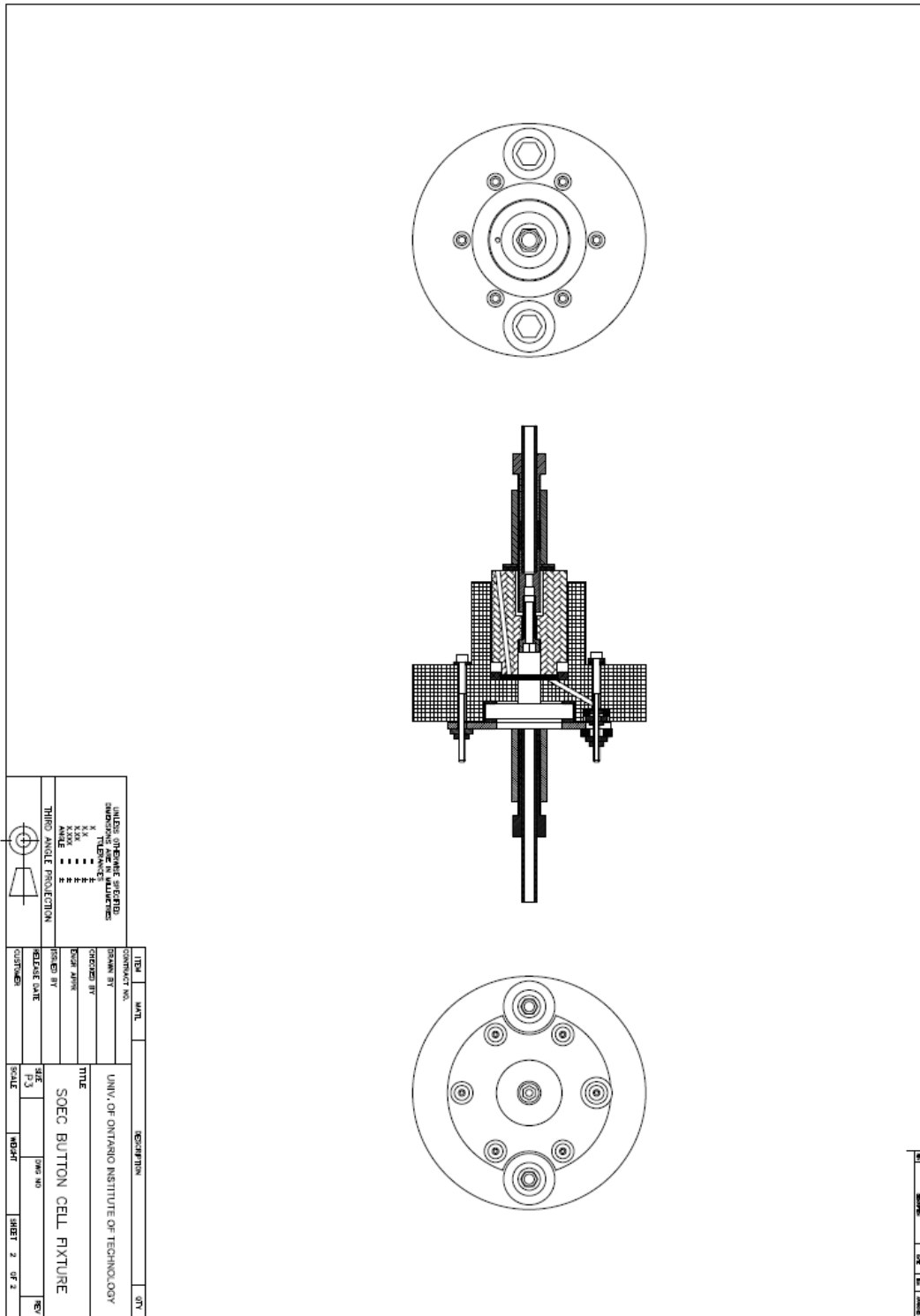


Figure A1.1 Design no. 1A.

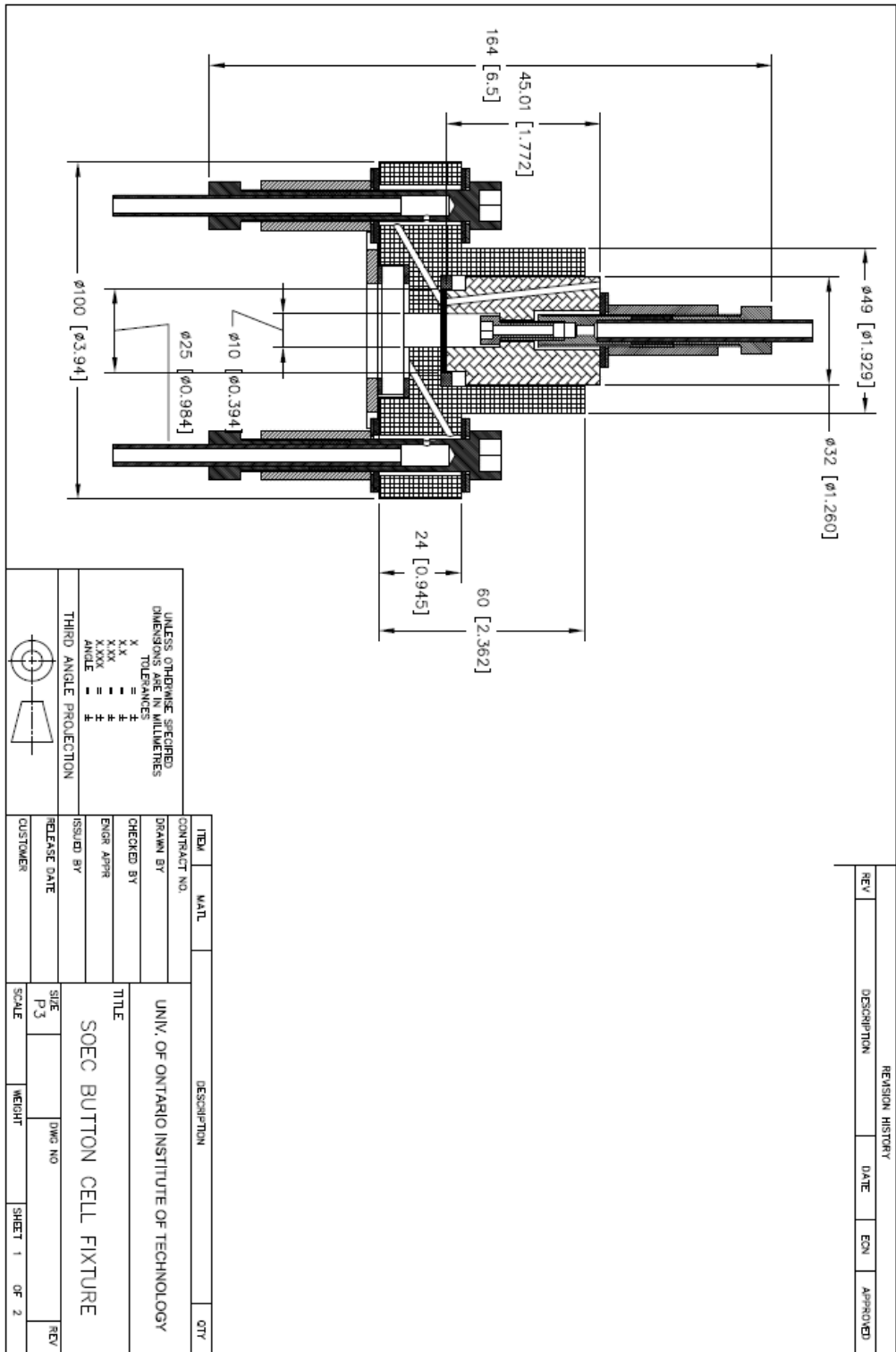


Figure A1.2 Design no. 2A.

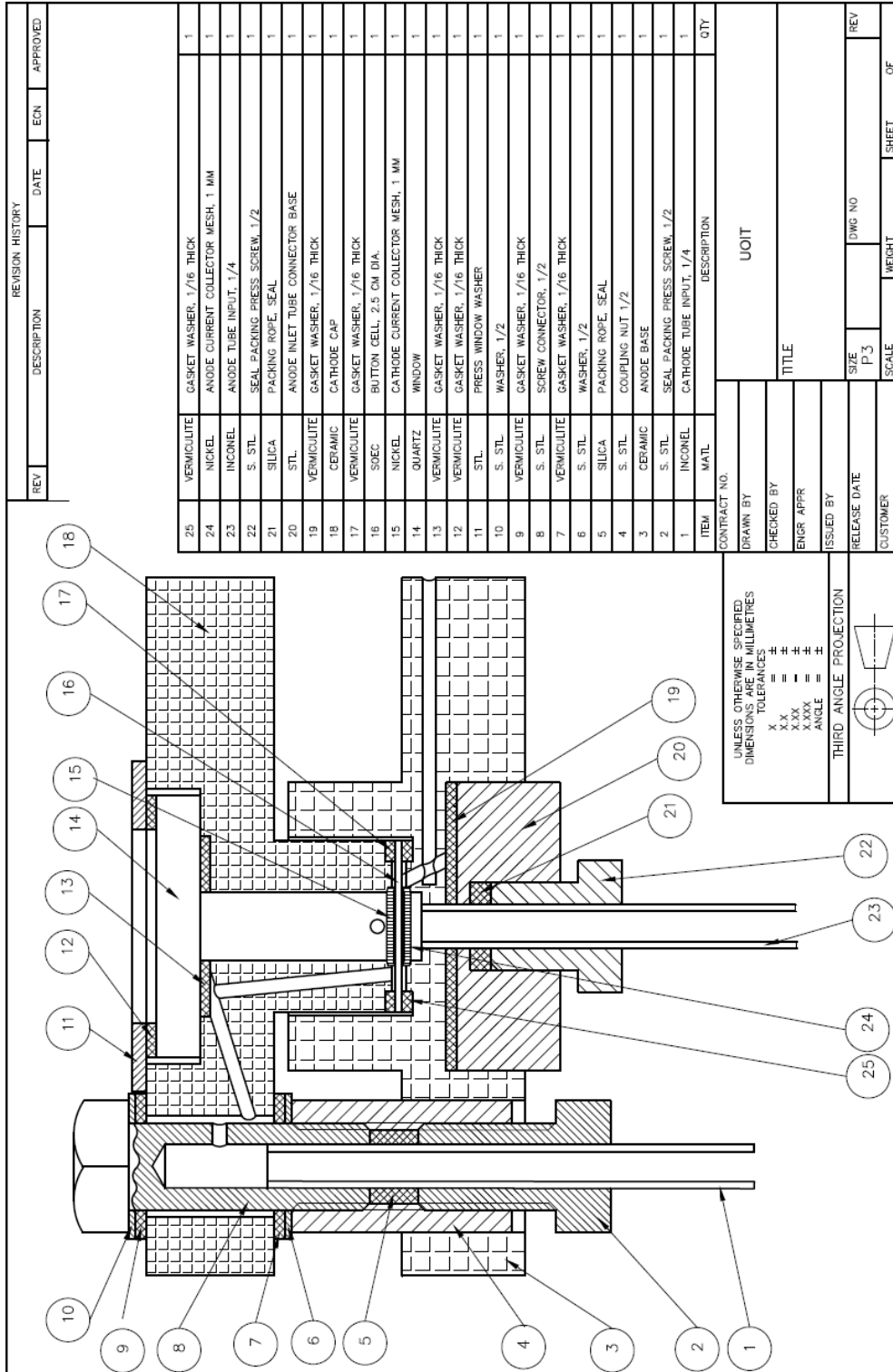


Figure A1.3 Design no. 1B.

## Appendix 2: Uncertainty Calculation Example

In this appendix uncertainty calculations are explained by using an illustrative example based on the data recorded from this thesis work and the calculations conducted to evaluate propagated uncertainties in the calculated values.

The accuracy of the Potentiostat is 0.1% of the range; where the potential range was 2 V, and the current range was 2 A. Thus the absolute uncertainties per voltage and current readings are 0.002 V, and 0.002 A/cm<sup>2</sup>, respectively.

Having the power density calculated as

$$P \pm U_p = (V \pm U_V) \times (J \pm U_J) \quad (\text{A2.1})$$

The partial derivatives of power density are given by

$$U_{P,V} = \frac{\partial P}{\partial V} \quad (\text{A2.2})$$

$$U_{P,J} = \frac{\partial P}{\partial J} \quad (\text{A2.3})$$

The uncertainty in the power density is calculated using the root-square-method, (RSS), as

$$U_p = \sqrt{(U_V)^2 + (U_J)^2} \quad (\text{A2.4})$$

A sample table of measurements of the cell potential with varying operating current density is given in Table A2.1. The Measurements are used to evaluate the cell characteristic J–V curve. In Table A2.1 the measurements are accompanied by the corresponding uncertainties and the evaluated power density with the propagated uncertainty.

**Table A2.1. Potential and current measurements and power density with uncertainties.**

No.	Potential, P (V)	Current density, J (A cm <sup>-2</sup> )	Power density, P (W cm <sup>-2</sup> )
1	0.9617±0.002	0.001105±0.002	0.001063±0.001923
2	0.9603±0.002	0.00267±0.002	0.002564±0.001921
3	0.9579±0.002	0.004545±0.002	0.004354±0.001916
4	0.9556±0.002	0.006323±0.002	0.006042±0.001911
5	0.9533±0.002	0.008032±0.002	0.007657±0.001907
6	0.9509±0.002	0.00985±0.002	0.009366±0.001902
7	0.9485±0.002	0.01162±0.002	0.01102±0.001897
8	0.9459±0.002	0.01344±0.002	0.01272±0.001892
9	0.9436±0.002	0.0152±0.002	0.01434±0.001887
10	0.9412±0.002	0.01695±0.002	0.01595±0.001883
11	0.9387±0.002	0.01871±0.002	0.01757±0.001878
12	0.9363±0.002	0.02046±0.002	0.01916±0.001873
13	0.934±0.002	0.02216±0.002	0.0207±0.001869
14	0.9316±0.002	0.02398±0.002	0.02234±0.001864
15	0.9291±0.002	0.02575±0.002	0.02392±0.001859
16	0.9267±0.002	0.02751±0.002	0.0255±0.001854
17	0.9242±0.002	0.02927±0.002	0.02706±0.001849
18	0.9217±0.002	0.03115±0.002	0.02871±0.001844
19	0.9192±0.002	0.03294±0.002	0.03028±0.00184
20	0.9168±0.002	0.03466±0.002	0.03177±0.001835
21	0.9144±0.002	0.03637±0.002	0.03326±0.00183
22	0.9121±0.002	0.03809±0.002	0.03474±0.001826
23	0.9095±0.002	0.03992±0.002	0.03631±0.001821
24	0.9069±0.002	0.04176±0.002	0.03787±0.001816
25	0.9044±0.002	0.04352±0.002	0.03936±0.001811
26	0.9019±0.002	0.04535±0.002	0.0409±0.001806
27	0.8995±0.002	0.04704±0.002	0.04231±0.001801
28	0.8971±0.002	0.04879±0.002	0.04377±0.001797
29	0.8945±0.002	0.05061±0.002	0.04527±0.001792
30	0.8922±0.002	0.05236±0.002	0.04671±0.001787
31	0.8896±0.002	0.05421±0.002	0.04822±0.001782
32	0.8871±0.002	0.056±0.002	0.04968±0.001778
33	0.8847±0.002	0.05771±0.002	0.05106±0.001773
34	0.8823±0.002	0.05947±0.002	0.05247±0.001769